

Energetic ion dynamics and confinement in 3D saturated MHD configurations

THÈSE N° 6561 (2015)

PRÉSENTÉE LE 29 MAI 2015
À LA FACULTÉ DES SCIENCES DE BASE
CRPP - THÉORIE
PROGRAMME DOCTORAL EN PHYSIQUE

ÉCOLE POLYTECHNIQUE FÉDÉRALE DE LAUSANNE

POUR L'OBTENTION DU GRADE DE DOCTEUR ÈS SCIENCES

PAR

David PFEFFERLÉ

acceptée sur proposition du jury:

Prof. V. Savona, président du jury
Dr W. A. Cooper, Dr J. P. Graves, directeurs de thèse
Dr Y. Liu, rapporteur
Prof. P. Helander, rapporteur
Dr S. Coda, rapporteur



ÉCOLE POLYTECHNIQUE
FÉDÉRALE DE LAUSANNE

Suisse
2015

"You get out of life what you put into it."
— Jerry Yang, Magistrale 2010

To my grandmother, Anna Miriam Clifton Webb.

Abstract

In the following theoretical and numerically oriented work, a number of findings have been assembled. The newly devised VENUS-LEVIS code, designed to accurately solve the motion of energetic particles in the presence of 3D magnetic fields, relies on a non-canonical general coordinate Lagrangian formulation of the guiding-centre and full-orbit equations of motion. VENUS-LEVIS can switch between guiding-centre and full-orbit equations with minimal discrepancy at first order in Larmor radius by verifying the perpendicular variation of magnetic vector field, not only including gradients and curvature terms but also parallel currents and the shearing of field-lines. By virtue of a Fourier representation of the fields in poloidal and toroidal coordinates and a cubic spline in the radial variable, the order of the Runge-Kutta integrating scheme is preserved and convergence of Hamiltonian properties is obtained. This interpolation scheme is crucial to compute orbits over slowing-down times, as well as to mitigate the singularity of the magnetic axis in toroidal flux coordinate systems. Three-dimensional saturated MagnetoHydroDynamics (MHD) states are associated with many tokamak phenomena including snakes and Long-Lived Modes (LLMs) in spherical or more conventional tokamaks, and are inherent to stellarator devices. The VMEC equilibrium code conveniently reproduces such 3D magnetic configurations. Slowing-down simulations of energetic ions from Neutral Beam Injection (NBI) predict off-axis deposition of particles during LLM MHD activity in hybrid-like plasmas of the Mega-Ampère Spherical Tokamak (MAST). Co-passing particles helically align in the opposite side of the plasma deformation, whereas counter-passing and trapped particles are less affected by the presence of a helical core. Qualitative agreement is found against experimental measurements of the neutron emission. Two opposing approaches to include Resonant Magnetic Perturbations (RMPs) in fast ion simulations are compared, one where the vacuum field caused by the RMP current coils is added to the axisymmetric MHD equilibrium, the other where the MHD equilibrium includes the plasma response within the 3D deformation of its flux-surfaces. The first model admits large regions of stochastic field-lines that penetrate the plasma without alteration. The second assumes nested flux-surfaces with a single magnetic axis, embedding the RMPs in a 3D saturated ideal MHD state but excluding stochastic field-lines within the last closed flux-surface. Simulations of fast ion populations from NBI are applied to MAST $n = 3$ RMP coil configuration with 4 different activation patterns. At low beam energies, particle losses are dominated by parallel transport due to the stochasticity of the field-lines, whereas at higher energies, losses are accredited to the 3D structure of the perturbed plasma as well as drift resonances.

Key words: curvilinear coordinates, MHD equilibrium, guiding-centre drift theory, full-orbit simulations, non-canonical phase-space Lagrangian, fast ion confinement, neutral beam injection, saturated ideal internal kink, helical core, resonant magnetic perturbations

Résumé

Le nouveau code VENUS-LEVIS est programmé pour résoudre le mouvement de particules énergétiques en présence de champs magnétiques 3D avec la plus grande précision possible. Par le truchement d'une formulation Lagrangienne non-canonique, les équations du centre guide et les équations du mouvement cyclotronique sont exprimées en coordonnées curvilignes, profitant de l'existence de fonctions de flux magnétique. Le passage des unes aux autres équations du mouvement est déclenché par un critère qui vérifie la variation perpendiculaire du champ magnétique, comprenant non seulement le calcul du gradient et de la courbure du champ mais également la contribution due au courant parallèle et au cisaillement des lignes de champ. Grâce à la représentation du champ magnétique en séries de Fourier dans la direction poloïdale et toroïdale et à l'aide de splines cubiques dans la direction radiale, l'ordre du schéma d'intégration Runge-Kutta est préservé et la convergence numérique des propriétés hamiltoniennes des équations du mouvement est obtenue. Le schéma d'interpolation est crucial pour calculer les orbites de particules rapides sur des temps de simulation longs, ainsi que pour s'affranchir de la singularité de l'axe magnétique due au système de coordonnées. Dans les tokamaks ou stellarateurs, de nombreux phénomènes sont convenablement interprétés comme étant des états tridimensionnels saturés de la magnétohydrodynamique (MHD), en particulier lesdits "serpents" ou lesdits modes à longue durée de vie. Ces équilibres MHD sont fidèlement reproduits à l'aide du code VMEC. En présence de modes à longue durée de vie dans les plasmas hybrides de MAST, les ions chauds s'alignent dans la région opposée à la déformation hélicoïdale du plasma, contrairement aux particules thermales qui se déposent autour de l'axe magnétique. Les simulations reproduisent qualitativement les mesures expérimentales d'émission de neutrons. Deux approches distinctes sont comparées pour inclure les perturbations magnétiques résonnantes (PMR) dans les simulations d'ions rapides. Avec la première approche, le champ PMR dans le vide est algébriquement superposé au champ d'équilibre MHD axisymétrique, ce qui prévoit la formation d'îlots magnétiques et de régions où les lignes de champs sont ergodiques. Avec la deuxième approche, les PMR sont incluses dans le calcul tridimensionnel de l'équilibre MHD, dont les surfaces de flux sont déformées en surface sans produire d'îlots ni de stochasticité. L'effet de PMR est étudié sur des populations d'ions rapides provenant de l'injection de neutres dans MAST en appliquant une périodicité $n = 3$. À basse énergie, la perte de particules provient du transport parallèle et de la diffusion des lignes de champ. À haute énergie, les pertes sont dues à la structure 3D de la configuration magnétique ainsi qu'au mouvement résonnant des ions.

Mots clefs : coordonnées curvilignes, équilibre MHD, équations du centre guide, orbites de particules chargées, Lagrangien non-canonique dans l'espace de phase, confinement des ions rapides, injection de neutres, déplacement interne idéalement saturé, coeur hélicoïdal, perturbations magnétiques résonnantes

Contents

Abstract (English/Français)	i
1 Introduction	1
1.1 Energy crisis, solutions and the importance of scientific research	1
1.2 Nuclear fusion and plasmas	2
1.3 Magnetic confinement, plasma heating and energetic particles	3
1.4 Thesis orientation, goals and contribution	6
1.5 Outline	7
2 Magnetic representations and plasma equilibrium	9
2.1 Representations and magnetic coordinates	9
2.2 Field-line equations from variational principles	10
2.3 Ideal MHD equilibrium	12
2.3.1 Axisymmetry, nested flux-surfaces and Grad-Shafranov equation	13
2.3.2 Three-dimensional ideal MHD equilibria	17
2.3.3 Straight-field line Boozer coordinates	19
2.4 Stellarator symmetry	21
2.5 Conclusions	23
3 Particle motion and guiding-centre drift	25
3.1 Full particle motion	25
3.1.1 The magnetic field as a generator of rotation	25
3.1.2 In a constant magnetic field	26
3.1.3 Particle drift due to constant force (electric field)	27
3.2 Full-orbit equations in curvilinear coordinates	28
3.2.1 Conservation properties	30
3.3 Drift theory	30
3.3.1 First-order guiding-centre drift equations	30
3.3.2 Conservation properties	36
3.4 Particle motion in a purely sheared magnetic field and limits of the drift approximation	37
3.5 Field variation estimator	42
3.5.1 Toroidal coordinates with geometric toroidal angle	45
3.5.2 Field variation constituents in MHD equilibrium fields	46
3.5.3 Field variation map of various devices	48
3.6 Full-orbit to guiding-centre switching	51
3.6.1 From particle to guiding-centre variables	54
3.6.2 From guiding-centre to particle variables	55
3.6.3 Small vector displacements in curvilinear coordinates	57

Contents

3.7	Conclusions	58
4	VENUS-LEVIS and numerical methods	61
4.1	Code description	62
4.2	Spline-Fourier interpolation	66
4.2.1	Fourier recomposition	67
4.2.2	Radial cubic splines	68
4.2.3	Spline boundary conditions	70
4.2.4	Grid substitution	73
4.2.5	Interpolated integrals	73
4.3	External fields (vacuum fields)	74
4.4	Neutral Beam Injection module	76
4.5	Monte-Carlo collision operators	76
4.6	MAST neutron camera synthetic diagnostic	80
4.6.1	Neutron production rate or emissivity in VENUS-LEVIS	81
4.7	Hybrid kinetic-MHD model	84
4.7.1	MINERVA fields and perturbations with toroidal rotation	85
4.7.2	Fast ion contribution via δf PIC scheme without rotation (preliminary)	87
4.8	Conclusions	93
5	NBI fast ion redistribution in saturated ideal internal kink	95
5.1	Phenomenology and modelling	95
5.1.1	Helical core equilibrium solution from VMEC	98
5.2	Particle orbits in helical cores, drift surfaces and drift islands	105
5.3	Slowing-down simulations of NBI distributions	110
5.3.1	Comparison with experimental neutron camera data	114
5.4	Conclusions	116
6	Effect of Resonant Magnetic Perturbation on NBI fast ion confinement	119
6.1	Coil configuration and compatibility with stellarator symmetry	120
6.2	Plasma response and magnetic field structure of the contrasting RMP models	124
6.3	Slowing-down simulations, saturated loss rates and energy dependency of even parity coil configuration	127
6.4	Prompt losses, diffusion and resonances	130
6.5	Conclusions	132
7	Final remarks and perspectives	135
7.1	Perspectives and future expansions	136
7.1.1	Code development	136
7.1.2	Physics applications	137
A	Mathematical complements	139
A.1	Curvilinear coordinates	139
A.1.1	General definitions and properties	139
A.1.2	Special case of \mathbb{R}^3	144
A.1.3	Examples	146

A.2 Lagrangian and Hamiltonian formalism	149
A.2.1 Phase-space Lagrangian and non-canonical Hamilton equations of motion	151
A.2.2 Lagrange and Poisson brackets	152
A.2.3 Liouville theorem and other properties	153
B MHD equilibria	155
B.1 Axisymmetric representations	155
B.1.1 Analytic Solov'ev equilibrium	155
B.1.2 Axisymmetric straight field-line coordinates (MINERVA, PEST)	157
B.2 3D representations with nested flux surfaces	158
B.2.1 VMEC/ANIMEC coordinates	158
B.3 Stellarator symmetry jargon	159
C Orbit equations	163
C.1 Relativistic non-canonical phase-space Lagrangian Guiding-centre Drift Equations	163
C.1.1 Guiding-centre Drift Equations in straight field-line coordinates	166
Bibliography	180
Acronyms	181
Acknowledgements	183
Curriculum Vitae	185

1 Introduction

1.1 Energy crisis, solutions and the importance of scientific research

The world's population is growing and its basic needs are increasing: access to food, water and supplies, shelter, heat and safety, communication, trade and business, social interaction, leisure time, etc. Unless major societal and political crisis leading to war, natural disasters or disease, the human population and its desire for comfort will continue to increase. The median quality of life, in industrialised countries at least, has significantly improved thanks to technology. Over the past century, we have become exponentially dependent on its use. It seems difficult nowadays to imagine reverting back to more rudimentary lifestyles. The problem is that it takes an increasing amount of energy to produce and maintain the objects that we use on a daily basis, like computers, telephones, washing-machines, televisions, vehicles etc. Our capacity to generate energy is limited to what is available on our planet and what comes from the sun. It also depends on how we are able to transform these natural resources into usable power, in particular electricity. The majority of our electrical energy comes from burning fossil fuels, such as petrol, gas or coal. The chemical process behind combustion is simple to initiate and control. The heat released per cubic meter of fuel is good and currently cheap. Reserves of fossil fuels are however being depleted and, according to Shafiee and Topal (2009), we will have exhausted proven reserves of oil, coal and gas within approximately 35, 107 and 37 years respectively. Given modern extraction techniques (hydrofracturing, directional drilling) and latest reserve evaluations, depletion times are probably longer (100-300 years). Combustion of fossil fuels produces large amounts of CO_2 which tends to enhance the green-house effect in the atmosphere, contributing to the destabilisation of the world's climate. It is thus doubly important to break away from fossil fuels in favour of sustainable and renewable sources of energy. The economy of many countries is based on the trade of oil and petrol. Companies make huge profit on deciding the produced quantities and the price of these goods. It will take political courage and determination to convince people of the urgency of the situation and implement long-term measures. Sooner or later though, the energy crisis will have to be faced. This is why scientific research is vital in order to develop cleaner methods, improve conversion efficiency, optimise the distribution and rationalisation of electricity, etc.

Green renewable energies, such as wind turbines, solar panels, geothermal energy and water dams are important for sustainable development. They appeal to many countries who seek energy independence. The advantage of renewable energies is that their source, i.e. the sun, rainfall and wind is free, and the conversion in energy usually does not imply waste, except for the construction and dismantling of the facilities. The cost to produce solar panels, wind turbines, geothermal stations and dams as well as to maintain them is high, even if heavily subsidised. The energy harvested per green power unit is relatively low and depends on the

Chapter 1. Introduction

ambient weather conditions. The latter fluctuate and are often out of phase with the power demand. The implementation of wind turbines or solar panels close to cities and villages often triggers resistance from the local population because they occupy a lot of space and denature the landscape. From these inconveniences, it seems unlikely that green energies will totally cover our needs in electricity. Green energies should certainly constitute a large fraction of our energy budget, but a baseline energy source is required.

Nuclear fission has been used now for over 70 years as a baseline source of electricity in many countries including France, Japan, USA and Switzerland. The splitting of heavy atoms such as Uranium releases extraordinary amounts of energy, several orders of magnitude more than chemically based processes. With only a few grams of Uranium, nuclear power plants produce the same amount of energy as fossil-fuel power plants with tons of gas or coal. Compared to the massive release of CO_2 and other pollutants from combustion of fossil fuels, the amount of nuclear waste is relatively small. However, a fraction of the waste is extremely radioactive, which means they must be handled and stored with great care for many thousands of years (permanently). Nuclear waste can potentially be made into nuclear bombs, thus increasing the risk of nuclear weapon proliferation. Fission technology is well advanced and has the highest security standards in developed countries. However, the risk of setting the fission chain-reaction off-balance and losing control cannot be reduced to zero. The consequences of accidents are usually catastrophic, as the 3 most critical incidents of Three-mile Island, Chernobyl and Fukushima have demonstrated. Many developed countries like Germany and Switzerland have recently decided to break away from nuclear fission power within the next 30 years and strongly encourage renewable energies. However, replacing a few nuclear power sites each producing 1GW=1000MW of electricity with solar panels and wind turbines producing an average of a few MW individually seems objectively unrealistic, especially in countries like Switzerland where there is little open-space available. Unless major breakthroughs in the research and development of green energies are realised or unless deflation of electrical power consumption is sustained, those countries will necessarily have to import their energy from their neighbours, in particular France whose production comes primarily from nuclear fission (76%, according to the International Energy Agency's Key World Energy Statistics 2014).

1.2 Nuclear fusion and plasmas

Active research to exploit sources of energy that have both a low ecological imprint and a high power efficiency is ongoing. An ideal source of energy would harvest the huge energy radiated by a nuclear reaction but without producing radioactive wastes and without the dangers of a chain reaction. This is the solution offered by nuclear fusion. Fusion is, as the name suggests, the opposite reaction of fission; light atoms are brought together to form heavier ones, which releases huge amounts of energy due to the deficit mass between the final products and reactants. Although it is possible to fuse any elements of the periodic tables (and this is how all elements are created in stars and supernovae), on earth the easiest fusion reaction to initiate and sustain is between deuterium-tritium atoms. The latter are both isotopes of hydrogen, the most abundant element in the universe (73% of matter according to Carroll et al. (1996)). Deuterium is found in small quantities in sea water but tritium must be derived from chemical

1.3. Magnetic confinement, plasma heating and energetic particles

and nuclear processes involving lithium. The production of tritium is why fusion is not yet an ideal renewable source of energy. Although quite abundant, the reserves of lithium will eventually be depleted in roughly 1000 years.

The state of matter in which fusion reactions are most likely to occur is called a plasma, where the ions and electrons of deuterium and tritium atoms have separated, forming a neutral soup of charges. While fission is self-sustained by a chain reaction, fusion is achieved only if this plasma is extremely dense, hot and subject to high pressure. In stars like our sun, gravity increases the pressure and density to create the right conditions for fusion, by compressing hydrogen ions close enough to surpass their electric repulsion. Gravity on earth is too weak to recreate the same conditions; fusion on earth can only take place at very high temperatures. Techniques comprise intense shock-waves and implosions, a realm of research called inertial fusion, and a more controlled approach called magnetic confinement, where the plasma is heated while levitating in a constricting magnetic field. In such fusion devices, the reaction between two deuterium ions produces highly energetic helium ions, called alpha-particles, as well as neutrons. Neutrons exit the vacuum chamber, since they are insensitive to the confining electromagnetic field, and are stopped by outer blankets. The deposited energy is used to generate electricity via traditional steam turbines.

Although a very active field of research over the past 50 years, the difficulty to confine a hot plasma and achieve fusion has discouraged scientists as well as partially turned away support from governmental institutions. Unfortunately, it is clear from numerous plasma experiments and theoretical predictions that the larger the device the easier it is to reach and sustain fusion. The costs involved in building a fully operational fusion energy producing power plant grow in proportion to their size, so large investments are necessary to perfect the technology and guarantee the success of the fusion project. Laboratories throughout the world are working towards this common goal, joining forces in a project called the International Thermonuclear Experimental Reactor (ITER). This experimental device, currently in construction in Cadarache (France), will demonstrate the feasibility of fusion on earth at the horizon of 2030. Many issues are to be addressed and huge challenges will have to be overcome. This is why scientific research, like the one documented in this thesis, is important not only for academic reasons but to support efficient design and technological progress.

1.3 Magnetic confinement, plasma heating and energetic particles

Plasmas, although globally neutral fluids, are strongly susceptible to (electro)magnetic fields. Magnetic confinement exploits this principle to contain ionised plasma in a finite volume of space by applying strong magnetic fields, thus avoiding contact and heat transfers with surrounding objects. Early designs of linear plasma devices were found to be rather ineffective because of plasma loss through the ends. Spherical geometries suffer a similar issue by virtue of the *Hairy-Ball* theorem (algebraic topology), stipulating that it is not possible to comb a hairy ball flat without forming at least one cowlick¹. The simplest geometry on which the confining magnetic field can lie continuously without singularities is on a torus. This abstract

¹There is no non-vanishing continuous tangent vector field on a sphere.

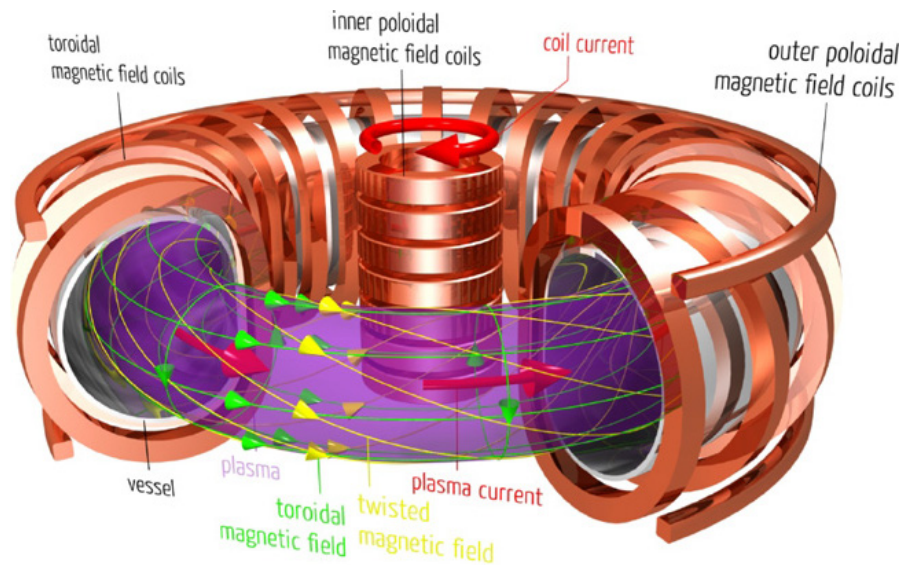


Figure 1.1 – Tokamak confinement of a nuclear fusion plasma: the twisted magnetic field lines (yellow) required to confine the high temperature plasma (purple) are created by the currents in a set of planar coils (copper colour) and an induced current flowing in the conductive plasma itself. Courtesy of Max-Planck Institut für Plasmaphysik.

mathematical fact has motivated the conception of toroidal fusion devices. Ignition and steady-state burning plasmas are in principle easier to obtain in larger devices with stronger confining fields. Building large machines is very costly, so research focuses on the optimisation of magnetic confinement and modes of operation, targeting steady-state burning plasmas with minimal power input.

A first category, called tokamaks like Tokamak à Configuration Variable (TCV) in Lausanne (Switzerland), Mega-Ampère Spherical Tokamak (MAST) in Culham (UK), Joint European Torus (JET) in Culham (UK) or ITER, use an axisymmetric set of coils to generate a strong toroidal magnetic field (see figure 1.1). In order to confine the plasma, a poloidal magnetic field is generated by inducing a toroidal plasma current. The induction limits the duration of tokamak pulses (or shots) from a few seconds in small devices to 15 minutes in JET and possibly over an hour in ITER.

Another category, called stellarators like W7X soon in operation in Greifswald (Germany), relies on a complex design of external current coils to wind the magnetic field around the plasma, thus avoiding the necessity of induced currents to obtain global confinement (see figure 1.2). The duration of stellarator pulses are in principle limitless.

A large portion of the challenge in both types of devices is to optimise plasma confinement; many instabilities emanate from the interplay between the electromagnetic fields and complex motion of particles. This usually leads to significant loss of density and decrease of temperature, degrading the conditions for fusion. The internal dynamics and interactions of ions and electrons inside a plasma are well understood in the framework of MagnetoHydroDynamics (MHD). The (kinetic) closure is similar to the description of fluids or gases in thermodynamics but with the inclusion of the Lorentz force. The MHD model performs well on the bulk of the

1.3. Magnetic confinement, plasma heating and energetic particles

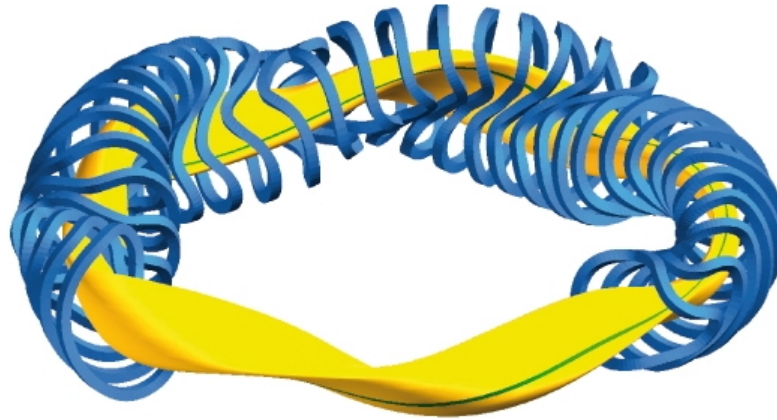


Figure 1.2 – Coil configuration of Wendelstein-7X (W7X) stellarator device (blue) and representation of the confined plasma (yellow). Courtesy of Max-Planck Institut für Plasmaphysik.

plasma and provides a robust theoretical background for many macroscopic instabilities such as kink modes, sawteeth, ballooning modes, Alfvén eigenmodes, etc. MHD alone is however limited when it comes to incorporating some effects from non-thermal and energetic particles. The MHD model predicts that the plasma fluid is tied to magnetic flux-surfaces. This property is not compatible with the fact that hot particles have rather large radial excursions. More importantly, MHD assumes that particles collide many times over a transit period along the magnetic field lines. However, fast particles in modern tokamaks are essentially collisionless over these scales.

Plasma heating is essential to reach ignition densities and temperatures, and plays a key role in maintaining and controlling the conditions for burning plasmas. Ohmic heating being insufficient, because the collisionality in the plasma decreases with its temperature, additional heating systems are required. Neutral Beam Injection (NBI) or Ion Cyclotron Resonance Heating (ICRH) create significant populations of energetic particles which transfer energy to the bulk plasma via collisional processes over slowing-down timescales. From the point of view of MHD, hot particles modify the net plasma pressure and, depending on their origin, are the main source of anisotropy inside the plasma. ICRH enhances the magnetic moment of particles, which causes the perpendicular pressure to rise. NBI provides thrust along the toroidal direction, which mainly results in higher parallel pressure. Fast particles undergo characteristic bounce or transit motion (trapped or passing orbits), precession around the toroidal direction or more exotic potato or super-banana trajectories. They are expected to resonate with spatial/time disturbances of the fields, hence strengthening or damping a certain range of modes. Even if one disregards the complex microscopic turbulence, the physical situation is ultimately non-linear. Analytic progress is made in simple cases, like axisymmetric geometry, linearized electromagnetic perturbations, simple fast ion distributions, etc., but it is necessary to deal with more realistic situations, like helical tokamak core, stellarator geometry, full-field perturbations (especially relevant for high beta plasmas).

The efficient design of those heating systems thus requires accurate modelling of the dynamics of fast ions so that their interaction with the background thermal plasma can be realistically studied. More generally, accurate modelling of magnetic confinement physics phenomena

constitutes a necessary step to explain experimental observations in current machines and make predictions for future fusion devices. Computer codes of increasing complexity are being developed to solve fast particle motion in various magnetic configurations. The physics investigated by these numerical tools is disputably richer and more realistic compared to simple but complementary analytic models. From the engineer's point of view, quantitative and trustworthy numerical solutions are indispensable to the safe and efficient design of fusion devices, anticipating power deposition, heat load, mechanical stress, etc. High energy particles striking the containment vessel can cause severe wall damage and compromise the integrity of the plasma facing components. The loss of hot particles in fusion reactor devices, amongst other mechanisms, can be enhanced by the onset of MHD unstable modes, by a bifurcation of the equilibrium to a helical state, or by the perturbation of the equilibrium with the application of Resonant Magnetic Perturbation (RMP) coils to control Edge Localised Modes (ELMs).

1.4 Thesis orientation, goals and contribution

Many studies have been conducted on the topics of fast particle driven Alfvén modes and fast particle losses due to small perturbations from axisymmetry (RMPs, Test Blanket Module (TBM), magnetic ripple, etc.) but less research has focused on the interaction between non-thermal particles and 3D tokamak equilibria. The opportunity exists to investigate this subject in depth, extending the possibilities of existing codes but also exploring new approaches. Our research thus focuses on robust analytic and numerical techniques for capturing the fast ion dynamics in 3D magnetic equilibria. The thesis reviews the theoretical background related to solving charged particle motion in toroidal magnetic fields, with perhaps a slightly alternate viewpoint than in the main literature. The techniques derived are then applied to study the interactions of hot ions with 3D equilibrium and externally applied fields, in order to establish their confinement properties as well as their impact as a source of free energy for instabilities. In particular, the investigation of two physical phenomena will guide our work; first, the evidence of exotic fast ion redistribution in the Long-Lived Mode (LLM) of MAST, second, the impact of RMP simulation models on fast ion losses. These topics are addressed with a desire for specific physical insight so that the methods can become general, exploiting various mathematical methods such as curvilinear coordinates and Lagrangian/Hamiltonian mechanics. The conceptual findings and analytic derivations presented are all implemented in a new orbit code called VENUS-LEVIS. A number of interfaces between VENUS-LEVIS and MHD codes such as VMEC, ANIMEC, MINERVA or TERPSICHORE are developed to yield a robust and flexible platform for integrated modelling applications. Numerical results are compared with experimental measurements in MAST and JET and predictions are made for ITER and W7X. The manuscript details the modelling approach and the results obtained. The document is meant to be more than just a simple gathering of publications. Little is devoted to explaining the conception and technicality of the code. The interested users are encouraged to read the documentation found alongside the source files or contact the author (main developer) for explanations related to VENUS-LEVIS itself.

1.5 Outline

The thesis is organised as follows. A short theoretical review of the representation of stationary magnetic fields is presented in chapter 2. Curvilinear coordinates, whose usage is briefly recalled in appendix A.1, are employed to highlight the geometry and symmetries of the magnetic configuration. The concepts of integrable field-lines, flux-surfaces, axisymmetric/three-dimensional MHD equilibrium are discussed. The VMEC code, which comes with a few limitations, is used to generate 3D MHD equilibria.

Chapter 3 addresses the motion of charged particles in general magnetic fields, focusing on full-orbit equations in curvilinear coordinates and their convenient reduction to Guiding-centre Drift Equations (GCDE). Derivations will rely on non-canonical phase-space Lagrangian techniques, for which a complementary discussion is found in appendix A.2. The limitations and inadequacy of first-order GCDE is exposed by solving particle motion in a purely sheared magnetic field. A criterion to identify where this problem can occur in fusion relevant MHD equilibria is proposed. A procedure to switch between particle and guiding-centre variables with minimal discrepancy using this criterion is shown.

The new orbit-solving code called VENUS-LEVIS is presented in chapter 4. The important interpolation scheme based on cubic splines and Fourier reconstruction is shown to preserve smoothness and continuity of the equations of motion. The routines for initialising fast ions according to NBI are upgraded to the flux-surface geometry of three-dimensional equilibria. Monte-Carlo operators are derived for Coulomb collisions with the background plasma. The neutron camera virtual diagnostic provides a comparison with experimental signals related to fast ion transport phenomena. Considered as a bonus topic, the hybrid kinetic-MHD interface between the MINERVA stability code and VENUS-LEVIS is presented. The formulation of linear Vlasov equation as well as the delta-f treatment of the fast ion distribution is mentioned in prevision of future work.

The redistribution of fast ion from NBI is studied in chapter 5 in MAST saturated ideal internal kink. LLM phenomena are reproduced with the helical core solution of VMEC. The effect of helical cores on fast ion orbits is assessed in both guiding-centre and full-orbit approaches, focusing on the portrayal of helical drift-surfaces. Slowing-down simulations show off-axis density, current and heat deposition of NBI particles, which is a consequence of the 3D geometry and exotic drifts. Excellent qualitative match is obtained with experimental neutron camera signals, proving that the main transport mechanism has been correctly captured.

Chapter 6 focuses on the modelling of RMPs, for which two approaches are compared. One where the vacuum field is added on the unperturbed equilibrium and another where the RMP is embedded in the 3D equilibrium generated with VMEC. Fast particle losses are assessed in the presence of RMPs and various loss mechanisms are identified.

Chapter 7 will synthesise our modelling approach, summarise main results and expand on the open questions that can be addressed using the methods discussed in this thesis and the VENUS-LEVIS code.

2 Magnetic representations and plasma equilibrium

The important concepts related to the analytic and numerical representation of stationary magnetic configurations are summarised in this chapter. Cartesian coordinates can always be used to represent the magnetic field, but it is usually more convenient to express it in a set of curvilinear coordinates, taking advantage of the natural geometry and spatial symmetries. Curvilinear coordinates and their properties being central to our approach, a short review of their manipulation is provided in appendix A.1.

2.1 Representations and magnetic coordinates

The solenoidal nature of the magnetic field, i.e. $\nabla \cdot \mathbf{B} = 0$, is related to the fact that the magnetic field derives from a vector potential; $\mathbf{B} = \nabla \times (\mathbf{A} + \nabla G)$, where G is an arbitrary function that is added without effect on the magnetic field (property called gauge invariance). With the help of curvilinear coordinates, the vector potential and the magnetic field are generically written in covariant components (up to a gauge term) as

$$\mathbf{A} = A_j \nabla u^j \quad \mathbf{B} = \nabla A_j \times \nabla u^j \quad \nabla A_j = (\partial_i A_j) \nabla u^i$$

where u^i is an arbitrary set of curvilinear coordinates and $\partial_i \equiv \frac{\partial}{\partial u^i}$ and the Einstein summation convention¹ is employed (and will be throughout the manuscript). This way of representing the magnetic field is convenient because it is automatically divergenceless. The contravariant components of the magnetic field are

$$B^k = \mathbf{B} \cdot \nabla u^k = \partial_i A_j (\nabla u^i \times \nabla u^j) \cdot \nabla u^k = \partial_i A_j \varepsilon^{ijk} = \partial_i A_j \frac{\varepsilon^{ijk}}{\sqrt{g}}$$

where $\varepsilon^{ijk} = \nabla u^i \cdot (\nabla u^j \times \nabla u^k) = \varepsilon^{ijk} / \sqrt{g}$ is the Levi-Civita tensor. The covariant representation of the magnetic field is used to express, via Ampère's law, the current density as

$$\mathbf{B} = B_j \nabla u^j \quad \mathbf{j} / \mu_0 = \mathbf{J} = \nabla \times \mathbf{B} = \nabla B_j \times \nabla u^j.$$

By Stokes theorem, the components of the vector potential are related to the magnetic flux,

$$\Phi_\Sigma = \int_\Sigma \mathbf{B} \cdot d\boldsymbol{\sigma} = \oint_{\partial\Sigma} \mathbf{A} \cdot d\mathbf{l}$$

which quantifies the flow of magnetic field-lines across a given surface Σ . Flux functions arise from a meaningful choice of Σ surfaces, following the natural alignment of field-lines

¹Terms with repeated upper and lower indices are summed, for example $v_i A^{ij} w_j \equiv \sum_i \sum_j v_i^j A^{ij} w_j$.

Chapter 2. Magnetic representations and plasma equilibrium

and directions of symmetry. The use of flux functions (or stream functions) is the basis for magnetic coordinates.

The Clebsch representation (Cary and Brizard, 2009; D’Haeseleer, 1991) is one of the simplest examples. This coordinate system is based on the existence of functions (α, β, l) , in which the vector potential and magnetic field have the following simple form

$$\bar{A} = \alpha \nabla \beta \text{ or } -\beta \nabla \alpha \qquad \bar{B} = \nabla \alpha \times \nabla \beta = \frac{1}{\sqrt{g}} \frac{\partial \mathbf{x}}{\partial l}.$$

Originally appearing in hydrodynamics, α and β are called Euler potentials. l is a parallel coordinate that is scaled to measure the length along the magnetic field-lines. In doing so, the Jacobian of the coordinate system corresponds to the inverse of the magnetic strength, $(\nabla \alpha \times \nabla \beta) \cdot \nabla l = 1/\sqrt{g} = B(\alpha, \beta, l)$. Indeed, the field-line equation is redundantly expressed as

$$\frac{\bar{B}}{B} = \sqrt{g} \nabla \alpha \times \nabla \beta = \frac{\partial \mathbf{x}}{\partial l}.$$

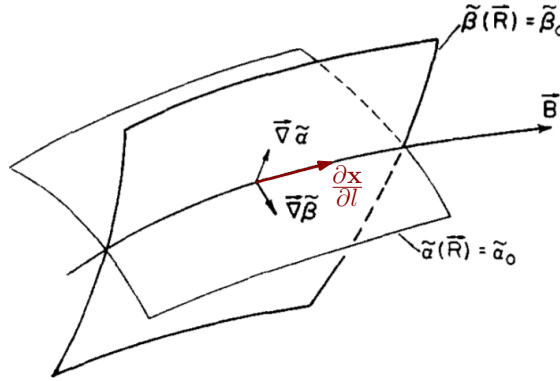


Figure 2.1 – The path of the magnetic field-line is represented by the crossing of constant $\alpha = \alpha_0$ and $\beta = \beta_0$. Courtesy of D’Haeseleer (1991).

As deduced from figure 2.1, smooth magnetic coordinates α and β originate from the alignment of field-lines on distinct surfaces (and vice-versa). Although elegant, the Clebsch representation is generally not practical because the α and β potentials are difficult to express and may not even be smooth functions in the case of stochastic field-lines. Clebsch coordinates however constitute a prototype of canonical coordinates (Meiss and Hazeltine, 1990) for the formulation of Hamiltonian Guiding-centre Drift Equations (GCDE).

2.2 Field-line equations from variational principles

An overlooked aspect of magnetic fields (and again a consequence of $\nabla \cdot \bar{B} = 0$) is that the governing equations of field-lines are equivalent to those of Hamiltonian systems. As highlighted by various references (Abdullaev, 2013; Morrison, 2000) as well as in the book by D’Haeseleer (1991, section 9.4), but in the particular framework of non-canonical Lagrangian techniques

2.2. Field-line equations from variational principles

by Cary and Littlejohn (1983), field-line equations derive from a variational principle

$$S = \int \mathbf{A} \cdot d\mathbf{x} = \int d\lambda \left(\mathbf{A} \cdot \frac{d\mathbf{x}}{d\lambda} \right) \quad \delta S = 0 \quad \Rightarrow \quad (\nabla \times \mathbf{A}) \times \frac{d\mathbf{x}}{d\lambda} = \mathbf{B} \times \frac{d\mathbf{x}}{d\lambda} = 0$$

where $\mathbf{x}(\lambda)$ is the parametrisation of the field-line with respect to an arbitrary parameter λ . By taking the vector product of this equation with \mathbf{B}/B^2 , the field-line equation is more easily identified as

$$\frac{d\mathbf{x}}{d\lambda} = \frac{\mathbf{B}}{B} \underbrace{\left(\frac{d\mathbf{x}}{d\lambda} \cdot \frac{\mathbf{B}}{B} \right)}_{dl/d\lambda} \iff \frac{d\mathbf{x}}{dl} = \frac{\mathbf{B}}{B}$$

where l is the length along the curve. The fact that the field-line action S can be represented as the integral of a phase-space Lagrangian suggests that a non-canonical treatment can be applied (see appendix A.2.1) in order to recover various Hamiltonian properties. For example, by virtue of Darboux theorem (Littlejohn, 1982), the Lagrangian can be (locally) cast into a canonical form by finding an appropriate coordinate transformation (and using a specific gauge), i.e. the action can be transformed into

$$S = \int A_i dx^i = \int p dq - h(p, q, t) dt.$$

where (p, q, t) are canonical coordinates, functions of \mathbf{x} . The field-line equations in canonical coordinates are written as usual Hamilton equations

$$\frac{dp}{dt} = -\frac{\partial h}{\partial q} \quad \frac{dq}{dt} = \frac{\partial h}{\partial p}.$$

In the context of toroidal systems, one can imagine promoting the toroidal angle as the system's time, $t \equiv \phi$. By doing so, the toroidal covariant component of the vector potential plays the role of the Hamiltonian $h = -A_\phi$ (Abdullaev, 2013; Cary and Littlejohn, 1983). This Hamiltonian, identified with one of the vector potential's component, formally depends on the three coordinates of space \mathbf{x} but, via the Darboux transformation, is actually seen to depend on one degree of freedom q and its conjugate p and one variable playing the role of time. The description of field-lines is therefore equivalent to Hamiltonian systems with $1 + 1/2$ degrees of freedom. It is well-known that systems with $N > 1$ degrees of freedom are generally non-integrable (non-separable) and can behave chaotically. This implies that field-lines are intrinsically chaotic systems to the contrary of what is taught in textbooks where they are simplistically pictured as closed curves. If the magnetic field possesses a symmetry, i.e. a dummy coordinate ζ , the field-line equations become integrable (separable). The ζ -invariance of the vector potential is equivalent to time-independence of the identified Hamiltonian, $\Psi_p = -A_\zeta$. The latter quantity is conserved along the trajectory of field-lines (as a Noether charge), which implies that field-lines lie on iso-contours of Ψ_p in the (p, q) plane. By virtue of Hamilton-Jacobi theory of action-angle variables, a specific set of canonical magnetic coordinates $(P, Q, t) \equiv (\Psi_t, \eta, \zeta)$ can be found where η is the phase-space (poloidal) angle and $\Psi_t = \frac{1}{2\pi} \oint \mathbf{A} \cdot d\mathbf{x}$ is the phase-space action (Poincaré integral invariant). Ψ_t corresponds to the magnetic flux across a surface in the $\zeta = \text{const}$ plane enclosed by the contour $\Psi_p = \text{const}$. In

this action-angle coordinate system, the magnetic representation reduces to

$$\mathbf{A} = \Psi_t \nabla \eta - \Psi_p(\Psi_t) \nabla \zeta \qquad \mathbf{B} = \nabla \Psi_t \times \nabla \eta + \frac{d\Psi_p}{d\Psi_t} \nabla \zeta \times \Psi_t$$

and the field-line equations read

$$\frac{d\eta}{d\zeta} = \frac{\partial \Psi_p}{\partial \Psi_t} = \iota(\Psi_t) \qquad \frac{d\Psi_t}{d\zeta} = -\frac{\partial \Psi_p}{\partial \eta} = 0.$$

In this phase-space, field-lines lie on constant Ψ_t (and Ψ_p) surfaces. In action-angle coordinates where ζ is periodic, these surfaces represent nested tori. In real-space, these canonical flux-surfaces may have more complex geometries as depicted on figure 2.2, but will still correspond topologically to tori or Klein bottles (Kruskal and Kulsrud, 1958). The function $\iota(\Psi_t) = 1/q(\Psi_t)$ is called the iota-profile and measures the pitch (slope) of the field-lines on each toroidal iso-surface in the (η, ζ) plane

$$\frac{\mathbf{B} \cdot \nabla \eta}{\mathbf{B} \cdot \nabla \zeta} = \frac{B^\eta}{B^\zeta} = \iota = \frac{1}{q}.$$

The independence of the iota-profile with respect to η (and ζ) is a defining property of so-called straight field-line coordinates (Boozer, 1982) and vice-versa, straight field-lines coordinates are in effect canonical field-line coordinates.

Straight field-line coordinates are used in various plasma theories in order to separate the parallel and perpendicular dynamics, for example in the study of MagnetoHydroDynamics (MHD) stability, hybrid kinetic-MHD or gyro-kinetics. As it will be discussed in later section 2.3.2, it is not straight-forward to obtain canonical straight field-line coordinates in general three-dimensional systems; the existence of flux-surfaces depends on a symmetry of the field-line Hamiltonian.

2.3 Ideal MHD equilibrium

A magnetic equilibrium refers to a stationary magnetic field that, in addition to being a solenoidal vector field, respects the MHD force balance $\mathbf{j} \times \mathbf{B} = \nabla p$. This apparently simple equation reflects something quite fundamental, namely the containment of pressure, i.e. thermal agitation of particles, via magnetism. MHD, as the description of a state of plasma by a magnetised fluid, embeds the microscopic/kinetic phenomena into the macroscopic layout of the magnetic field. The MHD model also suggests that, although the plasma remains a neutral fluid, the pressure gradient coexists with plasma current, i.e. internal flow of electric charges.

In the context of toroidal fusion devices, it makes sense to consider the situation where the plasma is hot and dense in the centre but cold and sparse near the walls. In this case, the pressure gradient is inwards, compensated by the tension that the magnetic field creates by bending, shearing and wrapping the field-lines around the constant pressure surfaces. On the occasion of symmetry, magnetic equilibria are such that both the magnetic field-lines and

current-lines lie on flux and pressure surfaces.

2.3.1 Axisymmetry, nested flux-surfaces and Grad-Shafranov equation

Axisymmetry is a topological constraint that implies that physical quantities, like the components of the magnetic field, do not depend on the toroidal angle ϕ . The natural coordinate system to work in is the cylindrical system (R, ϕ, Z) . For any physical function f , axisymmetry corresponds mathematically to

$$\left. \frac{\partial}{\partial \phi} \right|_{R,Z} f = \mathbf{e}_\phi \cdot \nabla f \equiv 0 \quad \iff \quad f = f(R, Z)$$

where it is stressed that the partial derivative implies varying only ϕ .

The coordinate system does not necessarily need to be cylindrical, for example, one could choose $(u^1(R, Z), u^2(R, Z), \phi)$. Coordinates u^1 and u^2 are mapping functions of R and Z so that, by virtue of $\mathbf{e}_\phi \cdot \nabla u^M = \partial u^M / \partial \phi = 0$, they automatically form valid dual basis vectors with respect to ϕ (see appendix A.1). In this coordinate system (but also in cylindrical coordinates), the vector potential is written generically as

$$\mathbf{A} = A_N(u^1, u^2) \nabla u^N - \Psi(u^1, u^2) \nabla \phi. \quad (2.1)$$

The minus sign in front of Ψ highlights its role as the field-line Hamiltonian, as discussed in previous section 2.2. The magnetic field, which derives from this specific vector potential, possesses, thanks to axisymmetry, a reduced expression

$$\mathbf{B} = \nabla \times \mathbf{A} = \partial_M A_N \nabla u^M \times \nabla u^N + \nabla \phi \times \nabla \Psi = \underbrace{\frac{\partial_M A_N}{\sqrt{g}} \mathbf{e}_\phi}_{B^\phi(u^M)} + \nabla \phi \times \nabla \Psi$$

where $\sqrt{g} = \mathbf{e}_{u^1} \cdot (\mathbf{e}_{u^2} \times \mathbf{e}_\phi) = [\nabla u^1 \cdot (\nabla u^2 \times \nabla \phi)]^{-1}$ is the Jacobian of the yet unspecified coordinate system. It is then seen that the magnetic field is always perpendicular to the gradient of the Ψ function,

$$\mathbf{B} \cdot \nabla \Psi = \frac{\partial_M A_N}{\sqrt{g_u}} \mathbf{e}_\phi \cdot \nabla \Psi + (\nabla \phi \times \nabla \Psi) \cdot \nabla \Psi = 0.$$

On each fixed ϕ plane, magnetic field-lines lie on contours of constant Ψ as depicted on figure 2.2. By revolution around the axis of these 2D curves, toroidal iso-surfaces called *flux-surfaces* are created. Like on topographic maps, the 2D contours close around the *hills* or *craters* of Ψ (formally extrema or *O*-points) forming, in 3D, toroidal nested flux-surfaces. The saddle points of Ψ creates so-called *X*-points where the contour lines seem to intersect (homoclinic point) but where the magnetic field is purely toroidal. Wherever $\nabla \Psi$ is zero (extrema, saddle points and regions of constant Ψ), the magnetic field (if any) is purely toroidal.

From the fact that $\mathbf{e}_\phi \cdot \nabla \Psi = 0$, it appears that $\nabla \Psi$ is a perfect candidate for a dual basis

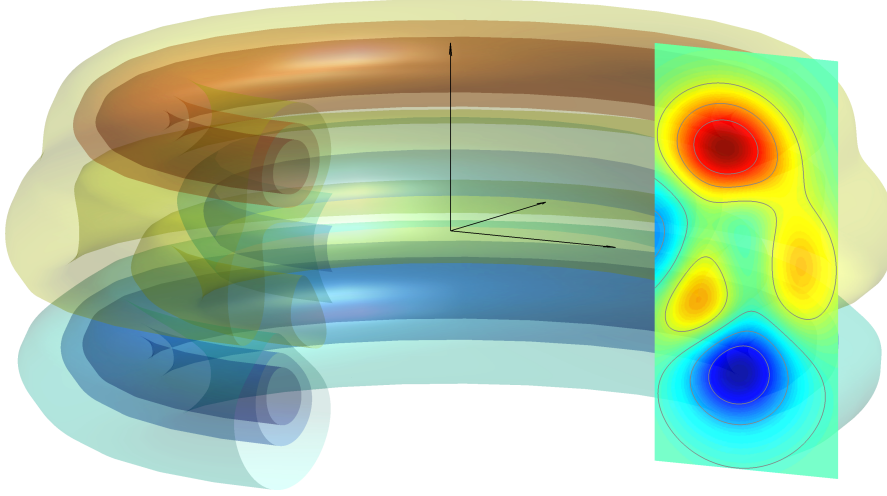


Figure 2.2 – Map of the magnetic flux Ψ , its contours on a poloidal cross-section and iso-surfaces created by revolution around the cylindrical axis.

vector and Ψ can be promoted to a coordinate, say $u^1 \equiv \Psi$. The second coordinate, renamed $\chi(R, Z) = u^2$ for the remaining of this section, will give the position along each contour lines (for example length). The χ function is somewhat arbitrary and irrelevant for the moment; it must at least satisfy $\mathbf{e}_\chi = \sqrt{g} \nabla \phi \times \nabla \Psi$. In the case of closed contours and nested toroidal flux surfaces, it is usually defined so to represent a poloidal angle. It is important to notice that the coordinate system only makes sense if $\nabla \Psi$ is different than zero. In this toroidal coordinate system, the presence of flux-surfaces is the tautological consequence of $B^\Psi = \mathbf{B} \cdot \nabla \Psi = 0$.

From the orthogonality of the cylindrical basis vectors $\nabla \phi = \mathbf{e}_\phi / R^2$, the contravariant basis vector display partial orthogonality $\nabla \phi \cdot \nabla \Psi = 0 = \nabla \phi \cdot \nabla \chi$. With this property, the magnetic field reads

$$\mathbf{B} = \underbrace{\frac{1}{\sqrt{g}} \mathbf{e}_\chi}_{B^\chi} + B^\phi \mathbf{e}_\phi = B_\Psi(\Psi, \chi) \nabla \Psi + B_\chi(\Psi, \chi) \nabla \chi + B_\phi(\Psi, \chi) \nabla \phi \quad \text{where } B_\phi = B^\phi R^2. \quad (2.2)$$

By Ampère's law, the contravariant components of the current are derived from the magnetic field as

$$\mathbf{j} / \mu_0 = \mathbf{J} = \nabla \times \mathbf{B} = \frac{\partial B_\phi}{\partial \chi} \nabla \chi \times \nabla \phi - \frac{\partial B_\phi}{\partial \Psi} \nabla \phi \times \nabla \Psi + \left(\frac{\partial B_\chi}{\partial \Psi} - \frac{\partial B_\Psi}{\partial \chi} \right) \nabla \Psi \times \nabla \chi.$$

In particular, the toroidal component of the current is

$$J_\phi = R^2 J^\phi = R^2 (\nabla \times \mathbf{B}) \cdot \nabla \phi = R^2 \nabla \cdot (\mathbf{B} \times \nabla \phi) = R^2 \nabla \cdot \left(\frac{\nabla \Psi}{R^2} \right) = \Delta^* \Psi. \quad (2.3)$$

The elliptic operator Δ^* is a 2D cylindrical version of the Laplacian. In this context, $\Delta^* \Psi = J_\phi$ resembles the Poisson equation where Ψ would be identified as the electrostatic potential and J_ϕ as the charge density. The contours of Ψ on the $R - Z$ plane are drawn, in the presence of

toroidal currents, in the same way as 2D equipotential lines in the presence of free charges. This picture is useful to explain various divertor configurations in tokamaks (Abdullaev, 2013). The operator Δ^* is written with respect to cylindrical coordinates (R, Z) as

$$\Delta^* \Psi = R^2 \nabla \phi \cdot [\nabla \times (\nabla \phi \times \nabla \Psi)] = R^2 \nabla \cdot \left(\frac{\nabla \Psi}{R^2} \right) = R \frac{\partial}{\partial R} \left(\frac{1}{R} \frac{\partial \Psi}{\partial R} \right) + \frac{\partial^2 \Psi}{\partial Z^2}$$

and with a change of variables $\Psi = \sqrt{R}U$ (Pataki et al., 2013) as

$$\Delta^* (\sqrt{R}U) = \sqrt{R} \left(\frac{\partial^2 U}{\partial R^2} + \frac{\partial^2 U}{\partial Z^2} - \frac{3}{4} \frac{U}{R^2} \right).$$

If the existence of toroidal magnetic flux-surfaces is a pure consequence of axisymmetry and the smoothness of Ψ , it is not specified how this function behaves and acquires points of extrema or saddle points yet. The MHD force balance further constrains the field to represent a plasma equilibrium

$$\mathbf{j} \times \mathbf{B} = \nabla p. \quad (2.4)$$

By projecting this equation on the magnetic field (parallel force balance), it is noted that, unless the magnetic field has no poloidal component (i.e. $\nabla \Psi = 0$), fluid pressure $p(\Psi, \chi)$ is necessarily a flux function

$$\nabla p \cdot \mathbf{B} = 0 \iff \left(\frac{\partial p}{\partial \Psi} \nabla \Psi + \frac{\partial p}{\partial \chi} \nabla \chi \right) \cdot (B^\chi \mathbf{e}_\chi + B^\phi \mathbf{e}_\phi) = 0 \iff B^\chi \frac{\partial p}{\partial \chi} = 0 \iff p = p(\Psi).$$

The force balance equation contracted with \mathbf{j} implies that the current-lines also lie on flux surfaces

$$\nabla p \cdot \mathbf{j} = 0 \iff \mathbf{j} \cdot \nabla \Psi = 0 \iff \frac{\partial B_\phi}{\partial \chi} = 0 \iff B_\phi = F(\Psi).$$

Notice that the argument can be reversed; if the current density lies on flux-surfaces ($j^\Psi = 0$) then a flux function $p(\Psi)$ exists such that $\mathbf{j} \times \mathbf{B} = \nabla p$. Therefore, axisymmetric MHD equilibrium labels a class of magnetic fields whose current density lies on toroidal flux-surfaces. Members of this class are (uniquely) represented by the Ψ function. Another way of demonstrating the alignment of current lines on flux-surfaces is to consider the force balance in the toroidal direction

$$\mathbf{e}_\phi \cdot \nabla p = \frac{\partial p}{\partial \phi} = 0 = (\mathbf{j} \times \mathbf{B}) \cdot \mathbf{e}_\phi = j^\Psi B^\chi \sqrt{g} \iff j^\Psi = 0.$$

The magnetic field and plasma current density are invariantly expressed in terms of F and Ψ as

$$\mathbf{B} = F \nabla \phi + \nabla \phi \times \nabla \Psi = \frac{F}{R^2} \mathbf{e}_\phi + \frac{1}{\sqrt{g}} \mathbf{e}_\chi \quad \mathbf{J} = J_\phi \nabla \phi - F' \nabla \phi \times \nabla \Psi = J^\phi \mathbf{e}_\phi - \frac{F'}{\sqrt{g}} \mathbf{e}_\chi \quad (2.5)$$

Chapter 2. Magnetic representations and plasma equilibrium

where $F' = dF/d\Psi$. From the normal projection of the force balance equation

$$\mu_0 p' = \mu_0 \nabla p \cdot \mathbf{e}_\Psi = (\mathbf{J} \times \mathbf{B}) \cdot \mathbf{e}_\Psi = \left(-J^\phi - \frac{FF'}{R^2} \right) \frac{\mathbf{e}_\chi \times \mathbf{e}_\phi \cdot \mathbf{e}_\Psi}{\sqrt{g}}, \quad (2.6)$$

the Ψ function (or $U = \Psi/\sqrt{R}$) complies to the so-called Grad-Shafranov equation

$$\Delta^* \Psi + \mu_0 \frac{dp}{d\Psi} R^2 + \frac{1}{2} \frac{dF^2}{d\Psi} = 0 \quad \left(\frac{\partial^2}{\partial R^2} + \frac{\partial^2}{\partial Z^2} \right) U = \frac{3}{4} \frac{U}{R^2} - \mu_0 R \frac{dp}{dU} - \frac{1}{2R} \frac{dF^2}{dU} \quad (2.7)$$

which is a 2D non-linear elliptic partial differential equation, constraining the functional form of Ψ . $F(\Psi)$ and $p(\Psi)$ are arbitrary functions that are prescribed either from theoretical considerations or from experimental profiles for equilibrium reconstruction. Nearly every plasma physics institute have their own Grad-Shafranov equilibrium solver as a quick method to reconstruct the magnetic configuration in a tokamak. The Grad-Shafranov equation is singular at the separatrix but is valid on either side of this point. It is used to represent the plasma in regions near the divertors (Abdullaev, 2013). The Grad-Shafranov equation can also be generalised to helical symmetry (White and Chance, 1984).

Simple analytic solutions are found. For example, Solov'ev (1968) assumed a constant current profile and a linear pressure profile with respect to Ψ . The Solov'ev solution, although missing many features of real tokamak plasmas, is a useful analytic MHD equilibrium used in the VENUS-LEVIS code for quick tests and benchmarks. The resulting magnetic field is discussed in detail in appendix B.1.1.

Grad-Shafranov equation with toroidal rotation

In axisymmetry, toroidal rotation $\mathbf{V} = \Omega \mathbf{e}_\phi = R^2 \Omega \nabla \phi$ can be included into the Grad-Shafranov equation. The ideal MHD force balance is composed of an extra term due to the toroidal flow

$$\mathbf{j} \times \mathbf{B} = \nabla p + \rho_M (\mathbf{V} \cdot \nabla) \mathbf{V}$$

where $\rho_m = m_i n$ is the ion mass density. The fluid velocity term actually represents a centripetal force

$$(\mathbf{V} \cdot \nabla) \mathbf{V} = \Omega \frac{\partial}{\partial \phi} (\Omega \mathbf{e}_\phi) = \Omega^2 \frac{\partial^2 \mathbf{r}}{\partial \phi^2} = -\Omega^2 R \mathbf{e}_R = -\Omega^2 R \nabla R.$$

From ideal Ohm's law, the presence of toroidal flow implies a radial electric field proportional to the angular rotation

$$\mathbf{E} + \mathbf{V} \times \mathbf{B} = 0 \stackrel{(2.2)}{\iff} \mathbf{E} = \Omega \frac{\mathbf{e}_\chi \times \mathbf{e}_\phi}{\sqrt{g}} = \Omega \nabla \Psi \quad (2.8)$$

which, by Faraday's law, happens to be a flux function

$$\nabla \times \mathbf{E} = 0 \iff -\frac{\partial \Omega}{\partial \chi} \nabla \Psi \times \nabla \chi = 0 \iff \frac{\partial \Omega}{\partial \chi} = 0 \iff \Omega = \Omega(\Psi).$$

The force balance is thus written

$$\mathbf{j} \times \mathbf{B} = \nabla p - m_i n \Omega^2 R \nabla R = \nabla p - \frac{m_i \Omega^2 R}{2T} p \nabla R$$

where pressure is assumed to be $p = (n_i + n_e)T = 2nT$. Considering the toroidal projection of the force balance, it is concluded that $j^\Psi = 0 = \frac{\partial B_\phi}{\partial \chi}$, i.e. the current density lies on flux-surfaces and the covariant toroidal component of the magnetic field is a flux function (as it is the case without rotation). The magnetic field is still cast in the form $\mathbf{B} = F(\Psi)\nabla\phi + \nabla\phi \times \nabla\Psi$ where $F(\Psi)$ is the current density profile (see equation 2.5). Taking the poloidal projection of the force balance, one obtains

$$\mathbf{e}_\chi \cdot (\mathbf{j} \times \mathbf{B}) = 0 \iff \frac{\partial p}{\partial \chi} = \frac{m_i n \Omega^2}{2} \frac{\partial R^2}{\partial \chi} = p \frac{m_i \Omega^2}{4T} \frac{\partial R^2}{\partial \chi}$$

which implies that part of the pressure gradient is compensated by the centripetal force. To make easy progress, we assume either that the plasma density or the temperature is a flux function, i.e.

$$\begin{aligned} n(\Psi) &\iff p(\Psi, \chi) = p_0(\Psi) + \Gamma(R^2 - R_0^2) & \Gamma(\Psi) &= \frac{m_i n \Omega^2}{2} \\ T(\Psi) &\iff p(\Psi, \chi) = p_0(\Psi) e^{\Lambda(R^2 - R_0^2)} & \Lambda(\Psi) &= \frac{m_i \Omega^2}{4T} \end{aligned}$$

Finally, two versions of the Grad-Shafranov equation in the presence of toroidal rotation are derived. By considering the normal projection of the force balance and using the right-hand side of (2.6) as well as the definition of Δ^* (2.3), we obtain

$$n(\Psi) \iff \Delta^* \Psi + FF' + \mu_0 R^2 [p'_0 + \Gamma'(R^2 - R_0^2)] = 0 \quad (2.9)$$

$$T(\Psi) \iff \Delta^* \Psi + FF' + \mu_0 R^2 \left[\frac{p'_0}{p_0} + \Lambda'(R^2 - R_0^2) \right] p = 0 \quad (2.10)$$

2.3.2 Three-dimensional ideal MHD equilibria

The stochastic nature of field-lines spoils the existence of flux-surfaces in three-dimensions, as discussed in section 2.2. There is no equivalent of the Grad-Shafranov equation for general 3D fields unless imposing a symmetry. Conversely, the assumption of ideal flux-surfaces leads to singularities on the surfaces where the rotational transform is a rational number (Boozer, 1981). The problem of finding 3D MHD equilibria is thus addressed using different physical paradigms and/or iterative algorithms.

For example, the PIES code (Krommes and Reiman, 2009) employs an iterative scheme to adjust the plasma current and magnetic field until the MHD force balance equation is satisfied; given the initial guess of the magnetic field (e.g. vacuum fields or resulting from the previous iteration) and imposing that $\mathbf{B} \cdot \nabla p$, the diamagnetic (perpendicular) current is calculated from the force balance and the Pfirsch-Schlüter current (parallel) from $\nabla \cdot \mathbf{j} = 0$. The magnetic field is then solved via Ampère's law $\nabla \times \mathbf{B} = \mu_0 \mathbf{j}$. This method generates regions with magnetic

Chapter 2. Magnetic representations and plasma equilibrium

islands and stochastic fields.

Another approach, considered by the HINT2 code (Harafuji et al., 1989; Suzuki et al., 2006), is to relax an initial magnetic configuration into an equilibrium by solving resistive MHD equations. The relaxation process is first carried out by adjusting the pressure to satisfy a vanishing gradient along the field lines. Then a set of MHD equations are solved with the fixed pressure distribution and artificial resistivity. This method also produces regions with magnetic islands and stochastic fields which would be equivalent to using saturated states from the MHD initial value code XTOR (Lütjens et al., 2009).

Magnetic configurations can be represented when pressure gradients are absent assuming full relaxation of the plasma (Taylor, 1974) for which $(\nabla \times \mathbf{B}) \times \mathbf{B} = 0$. Solutions to this equation belong to a class of force-free fields called Beltrami fields which satisfy $\nabla \times \mathbf{B} = \mu(\mathbf{x})\mathbf{B}$ (Dewar et al., 2008). This idea is exploited by the SPEC code (Hudson et al., 2012) to partition the plasma in multiple regions of relaxed constant pressure plasma and connect them with layers of infinite current sheets with pressure steps.

To construct 3D equilibria without explicitly solving MHD differential equations, a number of codes such as VMEC (Hirshman et al., 1986a; Hirshman and Whitson, 1983), ANIMEC (Cooper et al., 2009) or SIESTA (Hirshman et al., 2011) use a steepest gradient method applying the MHD energy minimisation principle by Kruskal and Kulsrud (1958). The saturated MHD states in this thesis were generated with VMEC so the remaining of this section will present the key concepts, the benefits and constraints of this approach. The main idea is to find a 3D vector field \mathbf{B} and a 3D scalar pressure p such that the total energy W is minimal. W is composed of magnetic energy W_m and fluid energy W_f as

$$W = W_m + W_f \quad W_m = \int_V \frac{B^2}{2\mu} dv \quad W_f = \int_V dU = \int_V e dm = \int_V e\rho dv$$

where V is the total volume of the plasma, μ is the magnetic permeability of the medium (μ_0 in isotropic plasmas), dU is the internal energy of an infinitesimal volume dv of the plasma, e is the specific internal energy and ρ is the mass density of the fluid plasma. Describing the plasma as an ideal gas with specific heat capacity \hat{c}_v , the internal energy of an infinitesimal plasma volume dv is $dU = \hat{c}_v dN k_B T = \hat{c}_v p dv$. After defining the adiabatic index $\gamma = 1 + 1/\hat{c}_v$, the plasma energy is written in terms of thermal pressure and the magnetic field strength as

$$W = \int_V dv \left(\frac{B^2}{2\mu} + \frac{p}{\gamma - 1} \right). \quad (2.11)$$

Candidly minimising W without a proper variational principle will lead to the trivial result $\mathbf{B} = 0$ and $p = 0$. In the context of fusion devices where the magnetic configuration is toroidal, the original principal proposed by Kruskal and Kulsrud (1958) was stated as follows: given functions $\mathbf{B}(\mathbf{x})$, $p(\mathbf{x})$ and $\Psi(\mathbf{x})$ that satisfy constraints

1. Ψ depicts toroidally nested surfaces with $\Psi = 0$ on the magnetic axis (minimum) and $\Psi = \Psi_{edge}$ on a perfectly conducting boundary (maximum),
2. \mathbf{B} is a solenoidal field ($\nabla \cdot \mathbf{B} = 0$) that is aligned on constant Ψ surfaces, i.e. $\mathbf{B} \cdot \nabla \Psi = 0$,

3. $\int_{\Psi \leq c} \mathbf{B} \cdot \nabla \zeta \, dv = c$, where ζ is a toroidal angle coordinate and $\int_{\Psi \leq c} \mathbf{B} \cdot \nabla \eta \, dv = \psi_p(c)$, where η is a poloidal angle coordinate; poloidal and toroidal flux, Ψ_p and Ψ are related flux functions,
4. $\int_{\Psi \leq c} p^{1/\gamma} \, dv = M(c)$, where $M(c)$ is a flux-function called mass profile reflecting mass conservation of isentropic fluid elements ($p\rho^{-\gamma} = \text{const}$ and $\rho \, dv = dm$),

then, W is stationary functional if and only if

1. $p = p(\Psi)$ is a function of Ψ ,
2. $\nabla p = (\nabla \times \mathbf{B}) \times \mathbf{B}$, the magnetic configuration satisfies MHD force balance.

The minimisation process is guided towards a solution of the MHD force balance via smartly designed physical (holonomic) constraints. The equilibrium solutions thus represent a specific class of MHD states, where the flux-surfaces are toroidally nested with a single magnetic axis. From the Hamiltonian interpretation of field-line equations of section 2.2, imposing flux-surfaces implies integrability of field-line equations. This is equivalent to implicitly forcing the field-line Hamiltonian to possess a direction of symmetry. It is thus conjectured that an independent (dummy) variable exists in the 3D MHD solutions arising from the above minimisation principle. This statement is important for the interpretation of drift-surface in later sections 5.2. The variational principle is evidently valid up to the last-closed flux-surface, beyond which Ψ is an ill-defined function (separatrix). In axisymmetry, using this variational principle can be shown to be equivalent to solving the Grad-Shafranov equations.

The VMEC code is based on the above variational principle (Hirshman and Whitson, 1983), converging towards an MHD equilibrium via a steepest gradient method. Flux-surfaces and the field components are Fourier decomposed into a fixed number of modes, yielding valuable control over the resulting spectrum. This method also allows full control over the plasma profiles, which are provided as inputs to the code (as opposed to the other methods where the profiles are results of the equilibrium calculation). In the free-boundary version of VMEC (Hirshman et al., 1986a), the geometry of the last-closed flux-surface is included in the minimisation process. The boundary conditions are provided by vacuum fields generated by external currents. This version is widely used in the stellarator community, in particular, for the optimisation of the coil design of stellarators like Wendelstein-7X (W7X). VMEC does not predict magnetic islands nor is it meant to handle stochastic regions. However, it is a very convenient tool to obtain a robust MHD equilibrium, in the sense that the force balance equation is numerically respected down to machine precision.

2.3.3 Straight-field line Boozer coordinates

The Boozer coordinate system, noted (s, θ, φ) , is a particularly useful case of straight field-line coordinate systems to represent 3D MHD equilibria. Among other interesting properties, its Jacobian, i.e. the measure of infinitesimal volume elements, is a flux function divided by B^2 . The radial variable $s = \Phi/\Phi_b$ is chosen as the normalised toroidal magnetic flux, θ is a poloidal

Chapter 2. Magnetic representations and plasma equilibrium

angle and φ a toroidal angle. The covariant components of the vector potential are pure flux functions, defining a canonical representation of field-lines as discussed in section 2.2,

$$\mathbf{A} = \Phi(s)\nabla\theta - \Psi(s)\nabla\varphi. \quad (2.12)$$

where Ψ is the poloidal magnetic flux. The magnetic field in the contravariant representation becomes

$$\mathbf{B} = \nabla\varphi \times \nabla\Psi + \nabla\Phi \times \nabla\theta = \nabla s \times (\Phi'\nabla\theta - \Psi'\nabla\varphi) = \frac{1}{\sqrt{g}} (\Psi' \mathbf{e}_\theta + \Phi' \mathbf{e}_\varphi). \quad (2.13)$$

As expected in a straight field-line coordinate system, the q -profile is indeed a flux function $q(s) = B^\varphi / B^\theta = \Phi' / \Psi'$.

The toroidal angle φ is not the geometrical angle ϕ , but differs by a periodic function as $\phi = \varphi + \eta(s, \theta, \varphi)$. This loads the metric tensor with off-diagonal terms ($g_{s\varphi}, g_{\theta\varphi} \neq 0$) even in axisymmetric cases. In compensation, the covariant components of the magnetic field are conveniently written as (Boozer, 1982; D'Haeseleer, 1991)

$$\mathbf{B} = B_s(s, \theta, \varphi)\nabla s + \mathcal{J}(s)\nabla\theta - \mathcal{I}(s)\nabla\varphi. \quad (2.14)$$

where \mathcal{I} is the poloidal current and \mathcal{J} is the toroidal current. In this way, the magnetic field strength has a direct relationship with the Jacobian

$$B^2 = \frac{\mathcal{J}\Psi' - \mathcal{I}\Phi'}{\sqrt{g}} > 0 \quad (2.15)$$

which is the defining property of Boozer coordinates. Despite the negative sign in equation (2.15), the right-hand side term is always positive. The Jacobian can be either negative or positive depending on the right-handedness of the coordinate system.

The current is found as

$$\nabla \times \mathbf{B} = \mathbf{J} = \left(\mathcal{J}' + \frac{\partial B_s}{\partial \varphi} \right) \nabla\varphi \times \nabla s + \left(\mathcal{I}' - \frac{\partial B_s}{\partial \theta} \right) \nabla s \times \nabla\theta. \quad (2.16)$$

The MHD force balance equation $\mathbf{J} \times \mathbf{B} = \mu_0 \nabla p$ implies that

$$\mathcal{J}'\Phi' - \mathcal{I}'\Psi' = \mu_0 p' \sqrt{g} - \left(\frac{\partial B_s}{\partial \theta} \Psi' + \frac{\partial B_s}{\partial \phi} \Phi' \right)$$

This equation, integrated over the poloidal and toroidal angles, produces an interesting relation between current derivatives, the pressure gradient and the flux volume (geometry)

$$\mathcal{J}'\Phi' - \mathcal{I}'\Psi' = \frac{\mu_0 p'}{4\pi^2} \iint_{00}^{2\pi 2\pi} \sqrt{g} d\theta d\varphi \quad \text{i.e.} \quad \frac{d\mathcal{J}}{d\Psi} - \frac{d\mathcal{I}}{d\Phi} = \frac{\mu_0}{4\pi^2} \frac{dp}{d\Phi} \frac{dV}{d\Psi} = \frac{\mu_0}{4\pi^2} \frac{dp}{d\Psi} \frac{dV}{d\Phi} \quad (2.17)$$

where V is the volume contained inside the flux-surface s ,

$$V(s) = \iiint_{000}^{s2\pi2\pi} \sqrt{g} ds d\theta d\varphi. \quad (2.18)$$

TERPSICHORE (Anderson et al., 1990) is a code based on Boozer coordinates to investigate MHD stability in 3D equilibria. TERPSICHORE converts VMEC coordinates into the list of flux functions $\Psi', \Phi', \mathcal{I}, \mathcal{J}$ and provides a Fourier decomposition in Boozer coordinates of $R_{mn}, B_{mn}^2, B_{s,mn}, \sqrt{g}$ in cosine functions and Z_{mn} and η_{mn} in sine functions (thus implying stellarator symmetry, see section 2.4). VENUS-LEVIS, the orbit code proposed in this thesis to solve the dynamics of fast particles, was initially designed to trace particles in this coordinate system, for which the guiding-centre equations are the same as in the ORBIT code (White and Chance, 1984). The interpolation of Boozer metric elements has been improved with the spline-Fourier technique described in section 4.2 and is used to follow full-orbits in straight field-line coordinates.

2.4 Stellarator symmetry

The coil design of most toroidal fusion devices respects a discrete symmetry identified by Dewar and Hudson (1998), called stellarator symmetry. It is demonstrated hereafter and in appendix B.3 that the magnetic field inside the plasma satisfies stellarator symmetry if the coil configuration is stellarator symmetric. The list of acquirable states is thus conveniently reduced, facilitating interpretation and representation of 3D MHD equilibria as well as helping the convergence of VMEC. For the various applications within this thesis, stellarator symmetry has been imposed. Compatible coil configurations had to be provided, which is not particularly evident with Resonant Magnetic Perturbations (RMPs), as discussed in section 6.1. Minimal work would be required to relax the stellarator symmetric condition and produce more general simulations. Results are nevertheless not expected to differ significantly. It is however pointed out that a certain loss of generality occurs and care must be taken in interpreting theoretical results. In real machines, stellarator symmetry is as improbable as axisymmetry; those solutions may not necessarily be stable under non-stellarator symmetric perturbations caused, for example, by small imperfections.

The definitions, jargon and notation concerning stellarator symmetry are specified in appendix B.3. Briefly summarising, a stellarator-symmetric (SS) scalar f denotes a function such that $f(R, -\phi, -Z) = \pm f(R, \phi, Z)$. A SS vector \mathbf{A} is a vector field such that $A_R(R, -\phi, -Z) = \pm A_R(R, \phi, Z)$, $A_\phi(R, -\phi, -Z) = \mp A_\phi(R, \phi, Z)$ and $A_Z(R, -\phi, -Z) = \mp A_Z(R, \phi, Z)$. The vector product of two SS polar-vectors or two SS axial-vectors is a SS polar-vector (see equations B.6). The vector product of a SS polar-vector and a SS axial-vector is a SS axial-vector (see equations B.12 and B.14).

Ideal MHD equilibrium equations satisfy the following propositions

1. the current density \mathbf{J} is a SS vector \iff the magnetic field \mathbf{B} is a SS vector.

Proof: ∇ is a SS polar-vector and $\nabla \times \mathbf{B} = \mu_0 \mathbf{J}$.

Chapter 2. Magnetic representations and plasma equilibrium

2. the current density \mathbf{J} is a SS vector \iff the plasma pressure p is a SS scalar.

Proof: $\mathbf{J} \times \mathbf{B} = \nabla p$ and point (1) implies that ∇p is a SS polar-vector.

Given stellarator symmetry, it does not seem that there is an equation implying that \mathbf{B} (nor \mathbf{J}) should be either a SS axial-vector or a SS polar-vector. However, if \mathbf{B} were a SS polar-vector, it would mean that both $B_\phi(R, 0, 0) = -B_\phi(R, 0, 0) = 0$ and $B_Z(R, 0, 0) = -B_Z(R, 0, 0) = 0$, i.e. the magnetic field is purely radial on the half-line $R > 0$, at $\phi = 0$ and $Z = 0$. This would obviously spoil the existence of toroidal flux-surfaces. Hence, in the applications of this thesis, we only consider the case where \mathbf{B} (and \mathbf{J}) are SS axial-vectors. The existence of stellarator symmetric flux surfaces implies that the pressure is a SS scalar². There is then an equivalence between the transformation $I : (R, \phi, Z) \rightarrow (R, -\phi, -Z)$ and the transformation in flux-coordinates $S : (s, u, v) \rightarrow (s, -u, -v)$ (no restriction in the definition of poloidal and toroidal angle). The mapping from flux-coordinates to cylindrical coordinates is necessarily expressed as $R \sim \cos(mu - nv)$, $Z \sim \sin(mu - nv)$ and $\phi - v \sim \sin(mu - nv)$. The modulus of B and J (SS scalars) become $|B|(s, u, v) \sim \cos(mu - nv)$, the covariant components (idem for contravariant components) of the magnetic field respect

$$[B_s(s, -u, -v), B_u(s, -u, -v), B_v(s, -u, -v)] = [-B_s(s, u, v), B_u(s, u, v), B_v(s, u, v)]$$

and are thus expressed as $B_s \sim \sin(mu - nv)$ and $B_{u,v} \sim \cos(mu - nv)$.

Under the assumption of stellarator symmetry, VMEC necessarily produces a mapping between cylindrical coordinates and flux coordinates as

$$R(s, u, v) = \sum_{m,n} R_{mn}(s) \cos(mu - nv) \quad (2.19)$$

$$Z(s, u, v) = \sum_{m,n} Z_{mn}(s) \sin(mu - nv) \quad (2.20)$$

$$\phi(s, u, v) = v. \quad (2.21)$$

where $s = \Phi/\Phi_{edge} = \rho^2$ is the radial variable proportional to the toroidal flux, u is a poloidal variable and $v = \phi$ the geometric toroidal angle. This implies that the configuration is up-down symmetric on the specific poloidal cross-section at $\phi = v = 0$. The same properties apply to the output of TERPSICHORE in Boozer straight field-line coordinates (s, θ, φ) .

By 2π -periodicity, stellarator symmetry with respect to $\phi = v = 0$, denoted I_0 by Dewar and Hudson (1998), implies stellarator symmetry with respect to $\phi = v = \pi$, denoted I_π . If the coil configuration has a certain toroidal periodicity, i.e. $B(\phi + \frac{2\pi}{n}) = B(\phi)$, there are $2n$ reference angles for stellarator symmetry; $I_{\frac{k\pi}{n}}$ where $k = 0, \dots, 2n - 1$. In VMEC configuration space, stellarator symmetric solutions come in pairs of energy extrema (maximum or minimum, depending on the up-down symmetry of the coil configuration at the reference angle).

²It is not clear if in general, one could say that a SS scalar pressure implies the existence of stellarator symmetric flux-surfaces.

2.5 Conclusions

In summary, this chapter highlights the fact that field-line equations are equivalent to non-integrable Hamiltonian systems. In this context, flux-surfaces arise from a symmetry condition, either explicitly in the case of axisymmetry or implicitly in the case of VMEC. The latter implements the variational principle by Kruskal and Kulsrud (1958) where nested flux-surfaces are a prerequisite. Flux coordinates are convenient to express the magnetic field in terms of physical quantities such as current density and magnetic flux. Physical insight is gained in exchange to the algebraic complexity of curvilinear coordinates. For numerical applications, a balance between these two aspects will be found, as seen in the next chapters.

Stellarator symmetry is assumed with little loss of generality, in effect reducing by a factor 2 the amount of Fourier coefficients to represent 3D MHD equilibria. This free optimisation is exploited in the spline-Fourier interpolation scheme described in section 4.2. Stellarator symmetry is an inflexible condition on the coil configuration and requires conscious interpretation, as it will be seen in section 6.1 on the investigation of RMPs.

3 Particle motion and guiding-centre drift

The motion of charged particles in magnetic fields is discussed in this chapter with the goal of expressing the equations of motion in coordinate systems related to the natural layout of the magnetic field, in particular in the case of MagnetoHydroDynamics (MHD) equilibria. Because the general gyro-motion is often superfluous to solve, so-called Guiding-centre Drift Equations (GCDE) are established in order to follow the average drift of the particle without solving the full gyro-motion. While a formal derivation of GCDE is not shown (slightly out of the scope of the present thesis), a means of verifying the GCDE applicability will be proposed by estimating the scale over which the magnetic field is varying. This measure will be used as a trigger to switch between full-orbit or GCDE.

Original results from this section are partly published in Pfefferlé et al. (2014) and in a recently accepted contribution (Pfefferlé et al., 2015a).

3.1 Full particle motion

3.1.1 The magnetic field as a generator of rotation

The motion of a charged particle in a magnetic field \mathbf{B} is dictated by the well-known Lorentz force. The usual vector differential equation can be arranged as

$$\dot{\mathbf{v}} = \frac{q}{m} \mathbf{v} \times \mathbf{B} = -\boldsymbol{\omega} \times \mathbf{v} \iff \begin{pmatrix} \dot{v}_x \\ \dot{v}_y \\ \dot{v}_z \end{pmatrix} = - \begin{pmatrix} 0 & -\omega_z & \omega_y \\ \omega_z & 0 & -\omega_x \\ -\omega_y & \omega_x & 0 \end{pmatrix} \begin{pmatrix} v_x \\ v_y \\ v_z \end{pmatrix} \quad \text{i.e.} \quad \frac{d\mathbf{v}}{dt} = -\tilde{\boldsymbol{\omega}} \mathbf{v} \quad (3.1)$$

where $\boldsymbol{\omega} = q\mathbf{B}/m$. This expression suggests that the infinitesimal variation of the velocity vector \mathbf{v} is caused by the action of an antisymmetric (skew-symmetric) matrix $\tilde{\boldsymbol{\omega}}$. Furthermore, if the velocity vector \mathbf{v} is embedded in an antisymmetric matrix $\tilde{\mathbf{v}}$ similarly to $\boldsymbol{\omega}$ in $\tilde{\boldsymbol{\omega}}$, it can be verified that

$$[\tilde{\boldsymbol{\omega}}, \tilde{\mathbf{v}}] = \tilde{\boldsymbol{\omega}} \tilde{\mathbf{v}} - \tilde{\mathbf{v}} \tilde{\boldsymbol{\omega}} = \widetilde{\boldsymbol{\omega} \times \mathbf{v}} \quad \frac{d\tilde{\mathbf{v}}}{dt} = -[\tilde{\boldsymbol{\omega}}, \tilde{\mathbf{v}}]$$

In the framework of Lie group theory, this differential equation defines a Lie algebra in the adjoint representation where $\tilde{\boldsymbol{\omega}}$ represents the infinitesimal action of a group. The skew-symmetric matrix $\tilde{\boldsymbol{\omega}}$ is identified as a generator of the Lie algebra and it turns out that the Lie algebra $\mathfrak{so}(3)$ formed by 3×3 skew-symmetric matrices is associated with the rotation group $SO(3) \equiv \{3 \times 3 \text{ matrices with } \det = 1\}$. This abstract affirmation basically means that *the Lorentz force instantaneously generates rotation*. The particle motion corresponds, without solving

Chapter 3. Particle motion and guiding-centre drift

it, to the infinite sum of small rotations around the axis generated by the vector $\boldsymbol{\omega}$. Since the velocity vector \boldsymbol{v} is instantaneously rotated around $\boldsymbol{\omega}$, its norm is constant

$$\frac{d}{dt} v^2 = 2\boldsymbol{v} \cdot \frac{d\boldsymbol{v}}{dt} = 2\boldsymbol{v} \cdot (\boldsymbol{v} \times \boldsymbol{\omega}) = 0 \iff v = \text{const.}$$

The trajectory $\boldsymbol{x}(t)$, that is constructed from the tangent velocity vector $d\boldsymbol{x}/dt = \boldsymbol{v}$, is a (topological) corkscrew or a distorted helix with the main axis being the direction of the magnetic field.

To make further contact with the helical geometry of the trajectory, we write the differential equation for the unit tangent vector $\boldsymbol{T}(l) = \boldsymbol{v}/v$ as a function of the arc-length along the particle trajectory $l = vt$ (invariance of v). It is known from Frenet-Serret formulas that the variation of the unit tangent vector $d\boldsymbol{T}/dl$ is always in the direction of the normal unit vector \boldsymbol{N} and is proportional to the local curvature κ . By (3.7) and Frenet-Formulas, we obtain

$$\kappa \boldsymbol{N} = \frac{d\boldsymbol{T}}{dl} = -\frac{\boldsymbol{\omega} \times \boldsymbol{T}}{v}.$$

The local curvature of the trajectory κ is identified as

$$\kappa = \frac{1}{R} = \left| \frac{d\boldsymbol{T}}{dl} \right| = \frac{\omega}{v^2} |\boldsymbol{v} \times \boldsymbol{n}| = \frac{\omega}{v^2} \sqrt{v^2 - v_{\parallel}^2} = \frac{v_{\perp}/\omega}{v_{\parallel}^2/\omega^2 + v_{\perp}^2/\omega^2}$$

where $\boldsymbol{n} = \boldsymbol{\omega}/\omega$ and $v_{\parallel} = \boldsymbol{v} \cdot \boldsymbol{n}$. The expression of κ on the far right is distinctively recognised as the curvature of a helix with radius $\rho_{\perp} = v_{\perp}/\omega$ and pitch $h = 2\pi\rho_{\parallel} = 2\pi v_{\parallel}/\omega$. The instantaneous gyro-radius or Larmor radius, is the normal vector multiplied by the *local* radius of the helix

$$\boldsymbol{\rho}_{\perp} = \rho_{\perp} \boldsymbol{N} = -\frac{\boldsymbol{\omega} \times \boldsymbol{v}}{\omega^2} = \frac{m}{q} \frac{\boldsymbol{v} \times \boldsymbol{B}}{B^2} \quad (3.2)$$

The Larmor radius vector corresponds to the trajectory's centre of rotation. In fusion relevant magnetic fields, the Larmor radius is a tiny characteristic length scale. The mass over charge ratio $m/q = 1.044 \cdot 10^{-8} \text{kg/C}$ is small for Hydrogen ions and a thousand times smaller for electrons. This implies that the ion Larmor radius is proportional to a factor of $\sqrt{2m/q} = 1.445 \cdot 10^{-4}$ as a function of energy (in electron Volts). The latter has to be in the *keV* range to yield a Larmor radius of a few centimetres in a 1T magnetic field. These numerical considerations indicate that low energy or light particles (electrons) are tangled with field-lines. This justifies the separation of their fast motion along field-lines and slow drift across with a formalism known as guiding-centre drift theory.

3.1.2 In a constant magnetic field

To make contact with the predicted helical trajectories, the motion of a particle is solved in the simple situation where both the direction and the modulus of the magnetic field are kept constant. Without loss of generality, the coordinate system can be chosen with the z axis aligning in the direction of the magnetic field. In this case, the equation of motion in the

parallel direction is simply $v_z = \text{const} = v_{||}$. The motion in the Oxy plane is solved from (3.1) as

$$\frac{d}{dt} \mathbf{v}_{\perp} = -\omega \underbrace{\begin{pmatrix} 0 & -1 \\ 1 & 0 \end{pmatrix}}_{\tilde{\boldsymbol{\epsilon}}} \mathbf{v}_{\perp} \iff \mathbf{v}_{\perp}(t) = e^{-\omega t \tilde{\boldsymbol{\epsilon}}} \mathbf{v}_0$$

where $\tilde{\boldsymbol{\epsilon}}$ is the unit 2×2 antisymmetric matrix. Noticing that $\tilde{\boldsymbol{\epsilon}}^2 = -\mathbf{I}$, hence $\tilde{\boldsymbol{\epsilon}}^{-1} = -\tilde{\boldsymbol{\epsilon}}$, the exponential of the anti-symmetric matrix $\tilde{\boldsymbol{\epsilon}}$ written as a power series reduces to a rotation matrix in \mathbb{R}^2

$$\begin{aligned} e^{\alpha \tilde{\boldsymbol{\epsilon}}} &= \mathbf{I} + \alpha \tilde{\boldsymbol{\epsilon}} + \frac{1}{2} \alpha^2 \tilde{\boldsymbol{\epsilon}}^2 + \frac{1}{3!} \alpha^3 \tilde{\boldsymbol{\epsilon}}^3 + \dots = \sum_{n=0}^{\infty} \frac{\alpha^n \tilde{\boldsymbol{\epsilon}}^n}{n!} = \mathbf{I} \sum_{n=0}^{\infty} \frac{\alpha^{2n} (-1)^n}{2n!} + \tilde{\boldsymbol{\epsilon}} \sum_{n=0}^{\infty} \frac{\alpha^{2n+1} (-1)^n}{(2n+1)!} \\ &= \mathbf{I} \cos \alpha + \tilde{\boldsymbol{\epsilon}} \sin \alpha = \begin{pmatrix} \cos \alpha & -\sin \alpha \\ \sin \alpha & \cos \alpha \end{pmatrix} = R(\alpha) \end{aligned}$$

Thus, the initial perpendicular velocity vector \mathbf{v}_0 is rotated at the frequency of $\omega = qB/m$ called the gyro-frequency (clockwise for an ion, counter-clockwise for an electron)

$$\mathbf{v}_{\perp}(t) = \begin{pmatrix} \cos(\omega t) & \sin(\omega t) \\ -\sin(\omega t) & \cos(\omega t) \end{pmatrix} \mathbf{v}_0 = R(-\omega t) \mathbf{v}_0$$

The particle motion is found after integration of $\mathbf{v}_{\perp}(t)$ over time as

$$\mathbf{x}_{\perp}(t) = e^{-\omega t \tilde{\boldsymbol{\epsilon}}} \underbrace{(-\tilde{\boldsymbol{\epsilon}}^{-1}) \frac{\mathbf{v}_0}{\omega}}_{\boldsymbol{\rho}_0} + \mathbf{X} = \begin{pmatrix} \cos(\omega t) & \sin(\omega t) \\ -\sin(\omega t) & \cos(\omega t) \end{pmatrix} \boldsymbol{\rho}_0 + \mathbf{X} = R(-\omega t) \boldsymbol{\rho}_0 + \mathbf{X}$$

It corresponds to the rotation of a vector $\boldsymbol{\rho}_0$, corresponding to the Larmor radius, around a fixed position \mathbf{X} called the guiding-centre. The Larmor radius is found as

$$\boldsymbol{\rho}_0 = \tilde{\boldsymbol{\epsilon}} \frac{\mathbf{v}_0}{\omega} = \frac{\tilde{\boldsymbol{\omega}} \mathbf{v}_0}{\omega^2} = \frac{\boldsymbol{\omega} \times \mathbf{v}_0}{\omega^2} = \frac{m}{qB} \mathbf{b} \times \mathbf{v}_0 \qquad \rho_0 = \frac{m v_{\perp}}{qB}$$

where $\mathbf{b} = \mathbf{B}/B$ and v_{\perp} is the initial velocity in the Oxy plane.

3.1.3 Particle drift due to constant force (electric field)

In addition to a constant magnetic field, let us assume that a constant force is added to the equations of motion

$$\frac{d\mathbf{v}}{dt} = -\boldsymbol{\omega} \times \mathbf{v} + \frac{\mathbf{F}}{m} = -\omega \tilde{\boldsymbol{\epsilon}} \mathbf{v} + \mathbf{f}$$

where $\mathbf{f} = \mathbf{F}/m$ is the "specific" force (force per unit mass). This matrix differential equation admits a fixed point solution $\bar{\mathbf{v}}$ where $d\bar{\mathbf{v}}/dt = 0$. For this case, the particle simply drifts at a

constant speed

$$\bar{\mathbf{v}} = \frac{\tilde{\boldsymbol{\epsilon}}^{-1} \mathbf{f}}{\omega} = -\frac{\tilde{\boldsymbol{\epsilon}} \mathbf{f}}{\omega} = \frac{\mathbf{f} \times \boldsymbol{\omega}}{\omega^2} = \frac{\mathbf{F} \times \mathbf{b}}{qB}$$

without undergoing rotation. The constant drift is eliminated from the equations of motion with a change of reference frame $\mathbf{v} = \mathbf{u} + \bar{\mathbf{v}}$, $d\mathbf{v}/dt = d\mathbf{u}/dt$,

$$\frac{d\mathbf{u}}{dt} = -\boldsymbol{\omega} \times \mathbf{u} - \frac{\omega}{\omega} \tilde{\boldsymbol{\epsilon}} \tilde{\boldsymbol{\epsilon}}^{-1} \mathbf{f} + \mathbf{f} \iff \mathbf{u}(t) = R(-\omega t) \mathbf{u}_0, \quad \mathbf{v}(t) = R(-\omega t) (\mathbf{v}_0 - \bar{\mathbf{v}}) + \bar{\mathbf{v}}$$

Hence, the particle motion in this reference frame is that of a particle in a constant magnetic field,

$$\mathbf{x}(t) = R(-\omega t) \boldsymbol{\rho}_L + \mathbf{X}(t) \quad , \quad \mathbf{X}(t) = \bar{\mathbf{v}} t + \mathbf{X}_0$$

where the guiding-centre is drifting at a constant speed perpendicularly to both the magnetic field and the force field.

This drift is particularly relevant in the case of a force created by a constant electric field, $\mathbf{F} = q\mathbf{E}$. The associated "electric" drift depends neither on the particle mass, neither on the particle charge

$$\mathbf{V}_E = \frac{\mathbf{E} \times \mathbf{b}}{B} \tag{3.3}$$

such that even a massless charged particle undergoes a perpendicular drift to the field-lines in the presence of an electric field. This electric drift has many implications, which will not be discussed in this manuscript. However, it must be remembered, when reducing the particle motion to its guiding-centre, that the drift $\mathbf{E} \times \mathbf{b}/B$ must be included in the definition of the parallel and perpendicular velocity. This is equivalent to stating that the frame of reference in which to perform gyro-average procedures is the one where the perpendicular electric field is cancelled due to the non-relativistic Lorentz transformation $\mathbf{E}' = \mathbf{E} + \mathbf{v} \times \mathbf{B}$. This remark is particularly important to establish guiding-centre equations in rotating plasmas, where the guiding-centre position is solved in the laboratory frame but the magnetic moment and parallel velocity are defined in the rotating frame.

3.2 Full-orbit equations in curvilinear coordinates

The derivation of the equations of motion of a charged particle in an electromagnetic field is a standard textbook problem, but rarely is it carried out in curvilinear coordinates.

It is often worth expressing the electromagnetic fields in flux coordinates because the components are related to simple flux functions and other physically relevant quantities (poloidal or toroidal current, q-profile, pressure gradient). The parallel and perpendicular dynamics are more naturally separated in a toroidal set of coordinates than in the Cartesian system. Formulating the fields in curvilinear coordinates finally relieves the numerical difficulties related to discretisations and mesh creation in exchange for the algebraic yet analytic manip-

3.2. Full-orbit equations in curvilinear coordinates

ulation of geometric elements (metric). This is especially relevant in general 3D magnetic equilibria, where the numerical evaluation of the field components requires either heavy mesh-based interpolation schemes in the 3 directions of space, or a well-posed representation of the physical fields via a smart choice of coordinates. The formulation, certainly suitable for tokamaks, is of high interest for solving full-orbits in complex stellarator equilibria.

If general coordinates (u^1, u^2, u^3) locate the particle, the contravariant components of its velocity are $v^i = \dot{u}^i = \dot{\mathbf{x}} \cdot \nabla u^i$. The Lagrangian associated with this charged particle is

$$\mathcal{L}(u^i, v^i, t) = \frac{1}{2} m \mathbf{v}^2 + q \mathbf{A}(u^i, t) \cdot \mathbf{v} - q \Phi_E(u^i, t) = \frac{1}{2} m g_{mn} v^m v^n + q A_k v^k - q \Phi_E \quad (3.4)$$

where A_k are the covariant components of the electromagnetic vector potential, Φ_E the electrostatic potential and $g_{mn} = \frac{\partial \mathbf{x}}{\partial u^m} \cdot \frac{\partial \mathbf{x}}{\partial u^n}$ the covariant components of the metric tensor.

The Euler-Lagrange equations $\frac{d}{dt} \left(\frac{\partial \mathcal{L}}{\partial v^j} \right) = \frac{\partial \mathcal{L}}{\partial u^j}$ yield

$$g_{jk} \dot{v}^k + \frac{d g_{jk}}{dt} v^k + \frac{q}{m} \frac{d A_j}{dt} = \frac{1}{2} \frac{\partial g_{mn}}{\partial u^j} v^m v^n + \frac{q}{m} \frac{\partial A_k}{\partial u^j} v^k - \frac{q}{m} \frac{\partial \Phi_E}{\partial u^j}. \quad (3.5)$$

Expanding $\frac{d}{dt} = \partial_t + v^m \partial_m$ and re-arranging a few terms, the equations of motion become

$$g_{jk} \dot{v}^k + v^m v^n \frac{1}{2} (2 \partial_m g_{nj} - \partial_j g_{mn}) = \frac{q}{m} v^k (\partial_k A_j - \partial_j A_k) + \frac{q}{m} (-\partial_t A_j - \partial_j \Phi_E) - v^k \cancel{\partial_t g_{jk}}.$$

Situations where the metric elements vary explicitly with respect to time are discarded hereafter since, for most applications, the coordinate system is derived from a stationary magnetic configuration such as an MHD equilibrium¹.

Formulating the equations of motion with the anti-symmetric Levi-Civita symbol ϵ^{lmn} , using the symmetry properties of the metric tensor and identifying the last term as the electric field, the previous equation is re-expressed as

$$g_{jk} \dot{v}^k + v^m v^n \frac{1}{2} (\partial_m g_{nj} + \partial_n g_{jm} - \partial_j g_{mn}) = \frac{q}{m} \epsilon_{jkl} v^k \epsilon^{lmn} \partial_m A_n + \frac{q}{m} E_j. \quad (3.6)$$

The first term on the right-hand side $\epsilon^{lmn} \partial_m A_n = \sqrt{g} B^l$ corresponds to the curl of the vector potential, i.e. the magnetic field. The second term on the left-hand side is recognised as the Christoffel symbol of first kind $\Gamma_{j,mn} = \frac{1}{2} (\partial_m g_{nj} + \partial_n g_{jm} - \partial_j g_{mn})$ (see equation (A.18)) compensating for inertial forces due to the curvilinear coordinate system. This result is the one expected from the derivation of geodesic equations of motion of charged particle in the theory of general relativity (equivalence principle).

Summarising, the equations of motion are written for the covariant components as

$$\dot{v}_j = g_{jk} \dot{v}^k = \frac{q}{m} (\epsilon_{jkl} v^k B^l + E_j) - v^m v^n \Gamma_{j,mn}$$

¹If axisymmetry applies, the description of toroidally rotating plasmas is also free of explicit time variation of metric elements.

Chapter 3. Particle motion and guiding-centre drift

where $\varepsilon_{ijk} = \sqrt{g}\varepsilon_{ijk}$ is the Levi-Civita tensor, or for the contravariant components as

$$\dot{v}^i = \frac{q}{m} \left(g^{ij} \varepsilon_{jkl} v^k B^l + E^i \right) - v^m v^n \Gamma_{mn}^i = \frac{q}{m} \left(\varepsilon^{ijk} v_j B_k + E^i \right) - v^m v^n \Gamma_{mn}^i \quad (3.7)$$

or, in a recognisable vector form (relaxation of formal notation for Christoffel symbol from Γ_{mn}^i to Γ) as

$$\dot{\mathbf{v}} = \frac{q}{m} (\mathbf{v} \times \mathbf{B} + \mathbf{E}) - \mathbf{v} \cdot \Gamma \cdot \mathbf{v}.$$

3.2.1 Conservation properties

The equations of motion of charged particles also verify Hamiltonian conservation properties in curvilinear coordinates. These properties are useful to test correct implementation and convergence of numerical simulations. In particular, the particle's energy is a constant of motion in time-independent electromagnetic fields,

$$\frac{\mathcal{H}(x^i, v^i)}{q} = \frac{1}{2} \frac{m}{q} g_{ij} v^i v^j + \Phi_E, \quad (3.8)$$

and for axisymmetric systems, the particle's toroidal momentum is conserved

$$\frac{P_\phi}{q} = A_\phi + \frac{m}{q} g_{\phi j} v^j = -\Psi + \frac{m}{q} R^2 \dot{\phi}. \quad (3.9)$$

where Ψ is the poloidal magnetic flux as in equation (2.1).

Without a third constant of motion, the motion of charged particle in time-independent axisymmetric magnetic fields is in principle non-integrable (Dragt and Finn, 1976). In the limit of an infinite field strength or a zero Larmor radius, the equations of motion reduce to integrable field-line equations (see section 2.2). Departure from integrability is first answered by adiabatic theory, which results in the invariance of the magnetic moment $\mu = m v_\perp^2 / 2B$ (Lichtenberg and Lieberman, 2010, section 2.3) or (Abdullaev, 2013, section 4.1). The adiabatic treatment of charged particle full-motion is at the basis of guiding-centre drift theory, discussed in the next section. Non-adiabaticity eventually leads to stochastic full-orbits even in time-independent axisymmetric fields. However, the transition to chaos is smooth in the sense of the KAM theorem, which guarantees persistent periodic orbits and near-confinement at large Larmor radii (Cambon et al., 2014). This property is in favour of tokamak confinement, where the magnetic fields only slightly depart from axisymmetry.

3.3 Drift theory

3.3.1 First-order guiding-centre drift equations

In simulations of charged particles travelling through electromagnetic fields, it is convenient not to follow their spiralling trajectory whenever the field is slowly and smoothly varying with respect to the fast gyro-motion around the field-lines. If the gyro-radius is much smaller

than typical spatial variation lengths and the gyro-frequency much faster than characteristic timescales, it is possible to reduce the 6-dimensional phase-space of those particles (position and velocity) down to 4 (guiding-centre position and parallel velocity) via gyro-averaging techniques, invoking the (adiabatic) invariance of the magnetic moment, $\mu = E_{\perp}/B = mv_{\perp}^2/2B$ where m is the particle mass, v_{\perp} is its velocity perpendicular to the magnetic field and $B = |\mathbf{B}|$ the magnetic field strength. At zero order in Larmor radius, the description of particle motion is that of field-lines; particles simply stream along them at a given parallel speed. At first order, particles steadily spin around their so-called guiding-centre, the latter slowly drifting across field-lines because of the variations in the electromagnetic field. Numerically, solving the slow drift of the guiding-centre is far less demanding than resolving the particle's full orbit; time-steps are at most of the order of the gyro-period in guiding-centre simulations, whereas they are at least two orders of magnitude smaller in the full-orbit case. The guiding-centre equations become increasingly accurate at low energies and for small Larmor radii, whereas tight gyro-motion is more difficult to resolve.

Guiding-centre equations were first expressed by Morozov and Solov'ev (1966) averaging the rapidly varying terms out of the equations of motion. The Russian findings were similarly confirmed in a review by Northrop and Rome (1978). The disadvantage of directly gyro-averaging full-orbit equations is that the resulting equations completely lack important physical conservation properties like energy conservation in a time-independent system or conservation of toroidal momentum in axisymmetric fields. A number of authors have thus proposed Hamiltonian perturbation techniques to derive guiding-centre drift equations where the terms that appeared to be of higher order in the gyro-expansion were preserved to correctly satisfy conservation properties (Boozer, 1980; Littlejohn, 1979, 1981). The difficulty in Hamiltonian perturbation theory is to construct appropriate canonical coordinate transformations (Meiss and Hazeltine, 1990; White and Chance, 1984), which originate for certain classes of magnetic field configurations in the establishment of straight field-line coordinates (Boozer, 1982). Canonical coordinates are certainly useful in analytic derivations for devices where the symmetry is apparent, for example in axisymmetric tokamaks or helically symmetric stellarators, but they are not very practical for numerical applications. Generalisations including full-field perturbations or non-axisymmetric systems have been found (Cooper et al., 2011a; Wang, 2006; White and Zakharov, 2003) and have, for example, been applied to general 3D stellarator geometry (Jucker et al., 2012; Rome, 1995). Physical intuition is somewhat obscured by the technicality of the coordinate transformations preserving the canonical structure, such that, in practice, Hamiltonian formulations are used for specific cases and are often only advantageous over non-canonical formulations in conjunction with symplectic integration techniques (White et al., 2013) or in axisymmetry (Wingen et al., 2006).

The non-canonical phase-space Lagrangian technique developed by Littlejohn (1981, 1983) is probably the best suited and most elegant to obtain guiding-centre equations of motion in arbitrary coordinate system, yet retaining essential Hamiltonian properties such as energy conservation in time-independent magnetic fields, toroidal momentum conservation in axisymmetric systems, Liouville equation, Noether theorem, etc. The details on how to construct the phase-space Lagrangian can be found in the review by Cary and Brizard (2009). A systematic derivation to arbitrary order of the guiding-centre transformation is found in the

Chapter 3. Particle motion and guiding-centre drift

work by Burby et al. (2013). These non-canonical phase-space techniques are at the basis of gyro-kinetic theory (Brizard and Hahm, 2007; Krommes, 2010).

A derivation of guiding-centre equations including relativistic effects and pressure anisotropy is done in appendix C.1. For the dynamics of ions in fusion devices, the relativistic approach is superfluous. Leaving out anisotropy for the moment, the important steps are repeated in order to compare various choices of the fourth coordinate. It is also verified that the resulting equations of motion are implicitly identical. The starting point is the first-order non-canonical phase-space guiding-centre Lagrangian proposed by Littlejohn (1983)

$$\frac{\mathcal{L}_{GC}}{q} = l = \mathbf{A}^* \cdot \dot{\mathbf{X}} - \frac{\mathcal{H}_{GC}}{q} = \left(\mathbf{A} + \frac{m}{q} v_{\parallel} \frac{\mathbf{B}}{B} \right) \cdot \dot{\mathbf{X}} - h = (\mathbf{A} + \rho_{\parallel} \mathbf{B}) \cdot \dot{\mathbf{X}} - h \quad (3.10)$$

and the Hamiltonian defined as

$$\frac{\mathcal{H}_{GC}}{q} = h = \frac{1}{2} \frac{m}{q} v_{\parallel}^2 + \frac{\mu}{q} B + \Phi_E = \frac{1}{2} \frac{q}{m} \rho_{\parallel}^2 B^2 + \frac{\mu}{q} B + \Phi_E \quad (3.11)$$

where \mathbf{X} is the position of the guiding centre, q and m the charge and mass of the considered particle, $\rho_{\parallel} = mv_{\parallel}/qB$ the parallel gyro-radius, v_{\parallel} the parallel velocity, $\mu = mv_{\perp}^2/2B$ the (adiabatically) conserved magnetic moment associated with the fast gyro-motion, v_{\perp} the perpendicular velocity, $\mathbf{A}(\mathbf{X}, t)$ and $\mathbf{B}(\mathbf{X}, t) = \nabla \times \mathbf{A}$ the magnetic vector potential and magnetic field, $\Phi_E(\mathbf{X}, t)$ the electrostatic potential.

To obtain the guiding-centre Lagrangian above, Littlejohn (1983) assumes that the field variation is much weaker than the particle's instantaneous Larmor radius (see equation 3.2), presupposing that gradients and curvature are $O(\epsilon)$ in the guiding-centre expansion². Secondly (and more importantly), the amplitude of the electric field is assumed to be of order $O(\epsilon)$, which means that the electric drift is zero in the limit of a massless charged particle. Cary and Brizard (2009) recommend including the zeroth-order electric drift in the definition of the magnetic moment. This idea is related to choosing a reference frame in which the electric field has been cancelled by a Lorentz transformation, as for example in the case of toroidal rotation (Brizard, 1995). For the applications of this thesis, where only stationary magnetic equilibrium are considered, the zeroth-order electric field is irrelevant.

As discussed in the appendix on non-canonical phase-space Lagrangian techniques A.2.1 and for the relativistic example of appendix C.1, the equations of motion for any choice of variables are written

$$\dot{z}^{\alpha} = [\Omega^{-1}]^{\alpha\beta} (\partial_{\beta} h + \partial_t A_{\beta}^*)$$

where the Lagrange brackets are expressed as $\Omega_{\alpha\beta} = \partial_{\alpha} A_{\beta}^* - \partial_{\beta} A_{\alpha}^*$.

²The expansion parameter is said to correspond to the ratio m/q , but is essentially related to the Larmor radius.

As a function of parallel gyro-radius

Given the guiding-centre Lagrangian (3.10), $(\rho_{\parallel}, \mathbf{X})$ is a suitable choice of four variables. The modified vector potential is defined as $\mathbf{A}^*(\rho_{\parallel}, \mathbf{X}, t) = \mathbf{A}(\mathbf{X}, t) + \rho_{\parallel} \mathbf{B}(\mathbf{X}, t)$ and the Lagrange brackets

$$\Omega_{\alpha\beta} = \begin{pmatrix} 0 & \partial_{\rho_{\parallel}} A_j^* \\ -\partial_{\rho_{\parallel}} A_i^* & \partial_i A_j^* - \partial_j A_i^* \end{pmatrix} = \begin{pmatrix} 0 & B_j \\ -B_i & B^{*k} \varepsilon_{kij} \end{pmatrix} \quad [\Omega^{-1}]^{\alpha\beta} = \frac{1}{B_l B^{*l}} \begin{pmatrix} 0 & -B^{*j} \\ B^{*i} & -B_k \varepsilon^{kij} \end{pmatrix}$$

where $\mathbf{B}^*(\rho_{\parallel}, \mathbf{X}, t) = \nabla \times \mathbf{A}^* = \mathbf{B} + \rho_{\parallel} \nabla \times \mathbf{B}$ is the modified magnetic field, $\varepsilon_{kij} = \varepsilon_{kij} \sqrt{g}$ and $\varepsilon^{kij} = \varepsilon^{kij} / \sqrt{g}$ the Levi-Civita tensor as in equation (A.28) with \sqrt{g} the Jacobian of the space-coordinate system. The phase-space derivatives of the Hamiltonian read

$$\partial_{\rho_{\parallel}} h = \frac{\rho_{\parallel} q}{m} B^2 = v_{\parallel} B \quad \text{and} \quad \partial_i h + \partial_t A_i^* = -E_i + \left(\frac{\mu}{q} + v_{\parallel} \rho_{\parallel} \right) \partial_i B + \rho_{\parallel} \partial_t B_i \equiv -E_i^*,$$

where the modified electric field \mathbf{E}^* was defined and the parallel velocity is formally a function of the phase-space variables $v_{\parallel}(\rho_{\parallel}, \mathbf{X}, t)$. The equations of motion are written

$$\begin{pmatrix} \dot{\rho}_{\parallel} \\ \dot{X}^i \end{pmatrix} = \frac{1}{B_l B^{*l}} \begin{pmatrix} 0 & -B^{*j} \\ B^{*i} & -B_k \varepsilon^{kij} \end{pmatrix} \begin{pmatrix} v_{\parallel} B \\ -E_j^* \end{pmatrix}$$

i.e.

$$\dot{\rho}_{\parallel} = \frac{E_j^* B^{*j}}{B_l B^{*l}} = \frac{\mathbf{E}^* \cdot \mathbf{B}^*}{B B_{\parallel}^*} \quad (3.12a)$$

$$\dot{X}^i = v_{\parallel} \frac{B B^{*i}}{B_l B^{*l}} + \frac{\varepsilon^{ijk} B_k E_j^*}{\sqrt{g} B_l B^{*l}} = \left[v_{\parallel} \frac{\mathbf{B}^*}{B_{\parallel}^*} + \frac{\mathbf{E}^* \times \mathbf{b}}{B_{\parallel}^*} \right]^i \quad (3.12b)$$

where $\mathbf{b} = \mathbf{B}/B$ and $B_{\parallel}^* = \mathbf{b} \cdot \mathbf{B}^* = B_l B^{*l}/B$.

Using the decomposition $\dot{\mathbf{X}} = \mathbf{b}(\dot{\mathbf{X}} \cdot \mathbf{b}) - \mathbf{b} \times (\mathbf{b} \times \dot{\mathbf{X}})$, the guiding-centre drift velocity can be cast into the a form where the Larmor-radius terms are neatly ordered and various drift terms from the literature are identified. In this case, we obtain

$$\dot{\mathbf{X}} = v_{\parallel} \mathbf{b} + \mathbf{V}_E + \mathbf{V}_B + \mathbf{V}_P \quad (3.13)$$

where \mathbf{V}_E is the electric drift, \mathbf{V}_B is the gradient and curvature drift, \mathbf{V}_P is a form of polarisation drift. These first-order drifts are perpendicular to the field-lines and are found as

$$\mathbf{V}_E = \frac{\mathbf{E} \times \mathbf{b}}{B_{\parallel}^*} \quad \mathbf{V}_B = \mathbf{b} \times \left(\frac{\mu}{q} \nabla B + v_{\parallel} \rho_{\parallel} \boldsymbol{\kappa} \right) / B_{\parallel}^* \quad \mathbf{V}_P = \rho_{\parallel} \frac{\mathbf{b} \times \partial_t \mathbf{B}}{B_{\parallel}^*} \quad (3.14)$$

where the definition of magnetic curvature $\boldsymbol{\kappa} = \mathbf{b} \cdot \nabla \mathbf{b} = -\mathbf{b} \times (\nabla \times \mathbf{b})$ was used (D'Haeseleer, 1991, chapter 4.3). It is noticed that the parallel projection of the guiding-centre velocity exactly matches the parallel velocity $\mathbf{b} \cdot \dot{\mathbf{X}} = v_{\parallel}$, which is correct in guiding-centre theory only to first order in Larmor radius (see equation 3.32 in later section 3.4). We also recall that the electric drift of equation (3.14) should not be confused with the zeroth-order drift of equation

Chapter 3. Particle motion and guiding-centre drift

(3.3). The ordering considered for the guiding-centre expansion requires all drifts of equation (3.14) to be of order $O(\epsilon)$ (Littlejohn, 1983); \mathbf{V}_E in (3.14) and \mathbf{V}_E in (3.3) are technically of different nature.

The set of GCDE (3.12) is implemented in the numerical code VENUS-LEVIS described in later chapter 4.1. The advantage is that anisotropy as well as other relevant physics (parallel perturbed vector potential) can be trivially included in the redefinition of ρ_{\parallel} as discussed in appendix C.1.

As a function of parallel velocity

The most common choice of variables for guiding-centre drift theory (Boozer, 1980; Cary and Brizard, 2009) and the original choice in the work by Littlejohn (1983) is $(v_{\parallel}, \mathbf{X})$ because of the convenient separation of the Hamiltonian into a kinetic term $mv_{\parallel}^2/2$ and an effective potential $\Phi_E^{\dagger} = \mu B/q + \Phi_E$. In this case, the modified vector potential is the function $\mathbf{A}^{\dagger}(v_{\parallel}, \mathbf{X}, t) = \mathbf{A} + \frac{m}{q} v_{\parallel} \mathbf{B}/B$ and the Lagrange brackets are

$$\Omega_{\alpha\beta} = \begin{pmatrix} 0 & \partial_{v_{\parallel}} A_j^{\dagger} \\ -\partial_{v_{\parallel}} A_i^{\dagger} & \partial_i A_j^{\dagger} - \partial_j A_i^{\dagger} \end{pmatrix} = \begin{pmatrix} 0 & \frac{m}{q} \frac{B_j}{B} \\ -\frac{m}{q} \frac{B_j}{B} & B^{\dagger k} \epsilon_{kij} \end{pmatrix} \quad [\Omega^{-1}]^{\alpha\beta} = \frac{qB}{mB_l B^{\dagger l}} \begin{pmatrix} 0 & -B^{\dagger j} \\ B^{\dagger i} & -\frac{m}{q} \frac{B_k}{B} \epsilon^{kij} \end{pmatrix}$$

where the modified magnetic field has a more elaborate expression than \mathbf{B}^*

$$\mathbf{B}^{\dagger}(v_{\parallel}, \mathbf{X}, t) = \nabla \times \mathbf{A}^{\dagger} = \mathbf{B} + \frac{m}{q} v_{\parallel} \nabla \times \left(\frac{\mathbf{B}}{B} \right) = \mathbf{B} + \rho_{\parallel} \nabla \times \mathbf{B} - \rho_{\parallel} \nabla B \times \mathbf{b}$$

and the parallel gyro-radius is now a function of the phase-space variables $\rho_{\parallel}(v_{\parallel}, \mathbf{X}, t)$. The phase-space derivatives of the Hamiltonian now yield

$$\partial_{v_{\parallel}} h = \frac{m}{q} v_{\parallel} \quad \text{and} \quad \partial_i h + \partial_t A_i^{\dagger} = \partial_i \Phi_E^{\dagger} + \partial_t A_i^{\dagger} = -E_i + \frac{\mu}{q} \partial_i B + \rho_{\parallel} \partial_t B_i - \rho_{\parallel} \frac{B_i}{B} \partial_t B \equiv -E_i^{\dagger},$$

such that the equations of motion are written as

$$\begin{pmatrix} \dot{v}_{\parallel} \\ \dot{X}^i \end{pmatrix} = \frac{qB}{mB_l B^{\dagger l}} \begin{pmatrix} 0 & -B^{\dagger j} \\ B^{\dagger i} & -\frac{m}{q} \frac{B_k}{B} \epsilon^{kij} \end{pmatrix} \begin{pmatrix} \frac{m}{q} v_{\parallel} \\ -E_j^{\dagger} \end{pmatrix}$$

i.e.

$$\dot{v}_{\parallel} = \frac{qB}{mB_l B^{\dagger l}} E_j^{\dagger} B^{\dagger j} = \frac{q}{m} \frac{\mathbf{E}^{\dagger} \cdot \mathbf{B}^{\dagger}}{B_{\parallel}^{\dagger}} \quad (3.15a)$$

$$\dot{X}^i = v_{\parallel} \frac{B B^{\dagger i}}{B_l B^{\dagger l}} + \frac{\epsilon^{ijk} B_k E_j^{\dagger}}{\sqrt{g} B_l B^{\dagger l}} = \left[v_{\parallel} \frac{\mathbf{B}^{\dagger}}{B_{\parallel}^{\dagger}} + \frac{\mathbf{E}^{\dagger} \times \mathbf{b}}{B_{\parallel}^{\dagger}} \right]^i \quad (3.15b)$$

Although it is clear that $\mathbf{B}^{\dagger} \neq \mathbf{B}^*$ and $\mathbf{E}^{\dagger} \neq \mathbf{E}^*$, it is easily verified that $B_{\parallel}^{\dagger}(v_{\parallel}, \mathbf{X}, t) = (\mathbf{B} + \rho_{\parallel} \nabla \times \mathbf{B} - \rho_{\parallel} \nabla B \times \mathbf{b}) \cdot \mathbf{b} = (\mathbf{B} + \rho_{\parallel} \nabla \times \mathbf{B}) \cdot \mathbf{b} = B_{\parallel}^*(\rho_{\parallel}, \mathbf{X}, t)$ and that the equations of motion for the guiding-centre position (3.12b) and (3.15b) are algebraically the same.

As a function of energy

With a choice of variables (σ, U, \mathbf{X}) where $\sigma = \text{sign}(v_{\parallel})$ (positive or negative branch) and $U = h$ (units of eV, positive for ions and negative for electrons), the parallel velocity can be written as a function of energy and the guiding-centre position as

$$v_{\parallel}(\sigma, U, \mathbf{X}, t) = \sigma \sqrt{\frac{2q}{m} \left(U - \Phi_E - \frac{\mu}{q} B \right)} \quad \partial_U v_{\parallel} = \frac{q}{m v_{\parallel}} \quad \partial_{i,t} v_{\parallel} = -\frac{q}{m v_{\parallel}} \left(\partial_{i,t} \Phi_E + \frac{\mu}{q} \partial_{i,t} B \right)$$

The phase-space Lagrangian technique leads to correct equations of motion, although it is not strictly rigorous nor practical to use the Hamiltonian as a variable (difficulty in distinguishing the positive or negative branch of v_{\parallel} , singularity of $v_{\parallel} = 0$). The modified vector potential is $\mathbf{A}^{\ddagger}(\sigma, U, \mathbf{X}, t) = \mathbf{A} + \frac{m}{q} v_{\parallel} \mathbf{B}/B = \mathbf{A} + \rho_{\parallel} \mathbf{B}$ and the Lagrange brackets are

$$\Omega_{\alpha\beta} = \begin{pmatrix} 0 & \partial_U A_j^{\ddagger} \\ -\partial_U A_i^{\ddagger} & \partial_i A_j^{\ddagger} - \partial_j A_i^{\ddagger} \end{pmatrix} = \begin{pmatrix} 0 & \frac{B_j}{v_{\parallel} B} \\ -\frac{B_j}{v_{\parallel} B} & B^{\ddagger k} \varepsilon_{kij} \end{pmatrix} \quad [\Omega^{-1}]^{\alpha\beta} = \frac{v_{\parallel} B}{B_l B^{\ddagger l}} \begin{pmatrix} 0 & -B^{\ddagger j} \\ B^{\ddagger i} & -\frac{B_k}{v_{\parallel} B} \varepsilon^{kij} \end{pmatrix}$$

where the modified magnetic field has the following expression

$$\mathbf{B}^{\ddagger}(\sigma, U, \mathbf{X}, t) = \nabla \times \mathbf{A}^{\ddagger} = \mathbf{B} + \nabla \times (\rho_{\parallel} \mathbf{B}) = \mathbf{B} + \rho_{\parallel} \nabla \times \mathbf{B} + \frac{1}{v_{\parallel}} \left[-\nabla \Phi_E - \left(\frac{\mu}{q} + \rho_{\parallel} v_{\parallel} \right) \nabla B \right] \times \mathbf{b}$$

The Hamiltonian being a function of U only, its phase-space derivatives are trivial

$$\partial_U h = 1 \quad \text{and} \quad \nabla \mathcal{H} + \partial_t \mathbf{A}^{\ddagger} = \partial_t \mathbf{A} + \rho_{\parallel} \partial_t \mathbf{B} + \frac{1}{v_{\parallel}} \left[-\partial_t \Phi_E - \left(\frac{\mu}{q} + v_{\parallel} \rho_{\parallel} \right) \partial_t B \right] \mathbf{b}$$

such that the equations of motion become

$$\begin{pmatrix} \dot{U} \\ \dot{X}^i \end{pmatrix} = \frac{v_{\parallel} B}{B_l B^{\ddagger l}} \begin{pmatrix} 0 & -B^{\ddagger j} \\ B^{\ddagger i} & -\frac{B_k}{v_{\parallel} B} \varepsilon^{kij} \end{pmatrix} \begin{pmatrix} 1 \\ \partial_t A_j^{\ddagger} \end{pmatrix}$$

As expected, the equations of motion for the guiding-centre position is algebraically identical to (3.12b) and (3.15b)

$$\dot{\mathbf{X}} = v_{\parallel} \frac{\mathbf{B}^{\ddagger}}{B_{\parallel}^{\ddagger}} + \frac{\partial_t \mathbf{A}^{\ddagger} \times \mathbf{b}}{B_{\parallel}^{\ddagger}} = v_{\parallel} \frac{\mathbf{B}^*}{B_{\parallel}^*} + \frac{\mathbf{E}^* \times \mathbf{b}}{B_{\parallel}^*} \quad (3.16)$$

and the time-variation of the energy variable is equal to minus the partial time derivative of the Lagrangian (3.10)

$$\dot{U} = \frac{dh}{dt} = -v_{\parallel} \frac{\partial_t \mathbf{A}^{\ddagger} \cdot \mathbf{B}^{\ddagger}}{B_{\parallel}^{\ddagger}} = -\partial_t \mathbf{A}^{\ddagger} \cdot \dot{\mathbf{X}} = -\partial_t l. \quad (3.17)$$

The interest of this choice of variables is for the case of time-independent fields. As highlighted by Littlejohn (1983, equation 11), the energy is a constant of motion and the guiding-centre

position respects a fairly simple equation of motion,

$$\frac{d\mathbf{X}}{dt} = v_{\parallel} \frac{\mathbf{B}^{\ddagger}}{B_{\parallel}^{\ddagger}} \iff \frac{d\mathbf{X}}{dl} = \frac{\mathbf{B}^{\ddagger}}{B^{\ddagger}} \quad (3.18)$$

where l is the (unimportant) length along the trajectory found by solving

$$\frac{dl}{dt} = \frac{v_{\parallel} B^{\ddagger}}{B_{\parallel}^{\ddagger}} = \frac{v_{\parallel}}{\mathbf{b} \cdot \mathbf{b}^{\ddagger}} = \frac{v_{\parallel}}{1 - O(\rho_{\parallel}^2)}$$

Equation (3.18) is useful for the analytic treatment of linear delta- f hybrid kinetic-MHD, where orbits are solved in equilibrium fields (see section 4.7). At a more conceptual level, equation (3.18) is in fact a field-line equation for the modified magnetic field \mathbf{B}^{\ddagger} . This analogy makes sense only if $v_{\parallel} \neq 0$ and is therefore only valid for passing particles. The formalism of section 2.2 can be applied to solve the topology of passing orbits (called drift-lines from now on) without actually solving the equations of motion. In this context, the modified guiding-centre vector potential is identified as a perturbed field-line phase-space Lagrangian for which the drift-line action is written

$$S = \int (\mathbf{A} + \epsilon \rho_{\parallel} \mathbf{B}) \cdot d\mathbf{X} = \int \left(\mathbf{A} + \epsilon \sigma \sqrt{\frac{2mU}{q}} \sqrt{1 - \Phi_E/U - \lambda B \frac{\mathbf{B}}{B}} \right) \cdot d\mathbf{X}$$

where $\lambda = \mu/qU \in [0, 1]$ is a convenient normalisation of the magnetic moment (adiabatic constant of motion) and ϵ an expansion parameter reminding that the approach is valid at first-order in Larmor radius (consistent with the guiding-centre approximation). The description of drift-lines is in general chaotic by virtue of the equivalence between the above action and that of a Hamiltonian system with $1 + \frac{1}{2}$ degree of freedom (again valid only in the case of passing particles). If symmetry of the fields is assumed, drift-line equations are integrable and the drift-lines will inevitably follow so-called drift-surfaces, in analogy with field-lines laying on flux-surfaces. If flux-surfaces exist, classical perturbation theory (Lichtenberg and Lieberman, 2010) can be used to calculate the drift-surfaces to any desired degree of accuracy and, in the case of resonances, secular perturbation theory to describe the occurrence of drift-islands. The idea of using canonical perturbation theory upon the drift-line Lagrangian is used by de Rover et al. (1996) to calculate the orbit width of deeply-passing relativistic electrons in a simple case of axisymmetric tokamak equilibria. It is also used in work by Heyn et al. (2012) investigating the confinement of passing alpha-particles in the presence of Resonant Magnetic Perturbations (RMPs). The presence of drift-surfaces and drift-islands in saturated helical states is interpreted in section 5.2 as a direct consequence of equation (3.18).

3.3.2 Conservation properties

Conservation properties arise from the Lagrangian treatment of the guiding-centre equations of motion (Noether theorem). Constants of motion are used for testing the correct implementation of the equations and numerical convergence of the solved orbits. In the case of

3.4. Particle motion in a purely sheared magnetic field and limits of the drift approximation

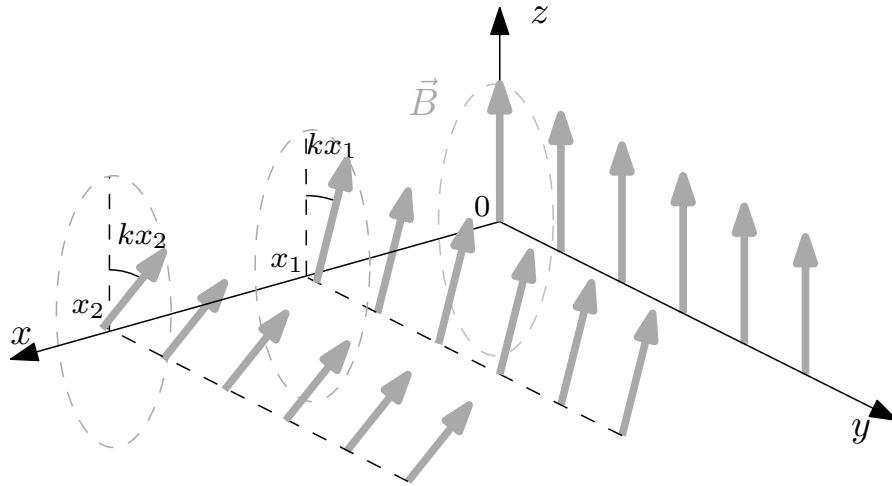


Figure 3.1 – Schematic picture of the purely-sheared magnetic field

time-independent fields, the energy of the guiding-centre \mathcal{H}_{GC} is a conserved quantity

$$\frac{\mathcal{H}_{GC}(X^i, \rho_{||})}{q} = \frac{1}{2} \frac{m}{q} v_{||}^2 + \frac{\mu}{q} B + \Phi_E \quad (3.19)$$

In the case of axisymmetry $\partial_\phi \equiv 0$, the toroidal momentum P_ϕ of the guiding-centre is a conserved quantity

$$\frac{P_\phi(X^i, \rho_{||})}{q} = A_\phi + \frac{mB_\phi}{qB} v_{||}$$

where A_ϕ and B_ϕ are the covariant components in the toroidal direction of the vector potential and the magnetic field. The considered quantities have therefore units of flux. Axisymmetric magnetic fields that satisfy the ideal MHD equilibrium equations can always be written in terms of flux functions as $\mathbf{B} = F(s)\nabla\phi + \nabla\phi \times \nabla\Psi(s)$ (see section 2.3.1), where $F(s)$ is the poloidal current and $\Psi(s)$ the poloidal magnetic flux labelled by the radial variable s , such that toroidal momentum simplifies to³

$$\frac{P_\phi}{q} = -\Psi(s) + \rho_{||}F(s). \quad (3.20)$$

3.4 Particle motion in a purely sheared magnetic field and limits of the drift approximation

As an example of magnetic deformations that are ignored by the leading order terms of the guiding-centre approximation, it is instructive to solve the motion of a charged particle in a

³In the presence of toroidal plasma rotation, the toroidal velocity must be added to the toroidal canonical momentum.

Chapter 3. Particle motion and guiding-centre drift

constant, curvature-free but sheared magnetic field⁴

$$\mathbf{B}(x, y, z) = B_0 [\sin(kx)\mathbf{e}_y + \cos(kx)\mathbf{e}_z]. \quad (3.21)$$

As seen in figure 3.1, the field-lines are straight in the $y - z$ plane, but the pitch varies for different x . This magnetic field is such that its modulus, B , is constant and $\nabla \times \mathbf{B} = k\mathbf{B}$. Hence, there are no gradients, $\nabla B = \mathbf{0}$, and no curvature (D’Haeseleer, 1991, chapter 4.3)

$$\boldsymbol{\kappa} = (\mathbf{b} \cdot \nabla)\mathbf{b} = -\mathbf{b} \times (\nabla \times \mathbf{b}) = -\frac{\mathbf{B}}{B^2} \times (\nabla \times \mathbf{B}) + \frac{\mathbf{B}}{B^3} \times (\nabla B \times \mathbf{B}) = \mathbf{0} \quad (3.22)$$

where $\mathbf{b} = \mathbf{B}/B$. If the direction of the magnetic field is rapidly changing with respect to the coordinate x and if this variation compares with the particle’s Larmor radius, the first order GCDE break down. Indeed, applying equations (3.15) on this particular magnetic field, the guiding-centre motion is written

$$\begin{cases} \dot{v}_{\parallel} = 0 \\ \dot{\mathbf{X}} = v_{\parallel} \mathbf{b} \end{cases} \iff \begin{cases} v_{\parallel}(t) = v_0 \\ \mathbf{X}(t) = v_0 t \mathbf{b} \end{cases}$$

such that it does not depend on the value of the shearing parameter k . As it will be demonstrated in this section, the full particle motion is strongly dependent on k . Eventually, above a certain threshold in k , the motion is not even constrained to the initial parallel axis.

Up to a gauge choice, the vector potential is $\mathbf{A} = \mathbf{B}/k$. The Lagrangian of such particle is written

$$\mathcal{L}(x, y, z, \dot{x}, \dot{y}, \dot{z}) = \frac{1}{2} m v^2 + q \mathbf{A} \cdot \mathbf{v} = \frac{1}{2} m (\dot{x}^2 + \dot{y}^2 + \dot{z}^2) + \frac{qB_0}{k} [\dot{y} \sin(kx) + \dot{z} \cos(kx)] \quad (3.23)$$

The problem is integrable by virtue of the three constants of motion that can be deduced from the symmetries of the above Lagrangian:

$$\begin{aligned} \frac{\partial \mathcal{L}}{\partial y} = 0 &\iff \frac{\partial \mathcal{L}}{\partial \dot{y}} = P_y = m \dot{y} + \frac{qB_0}{k} \sin(kx) = \text{const} \\ \frac{\partial \mathcal{L}}{\partial z} = 0 &\iff \frac{\partial \mathcal{L}}{\partial \dot{z}} = P_z = m \dot{z} + \frac{qB_0}{k} \cos(kx) = \text{const} \\ \frac{\partial \mathcal{L}}{\partial t} = 0 &\iff \mathcal{H} = \frac{1}{2} m (\dot{x}^2 + \dot{y}^2 + \dot{z}^2) = \text{const} \end{aligned}$$

Exploiting the freedom to chose the origin and orientation of the y and z axis, there is no loss in generality to consider the case represented on figure 3.2 where, at $t = 0$,

$$x(0) = 0 \quad y(0) = \frac{m u_0}{q B_0} = \rho_0 \quad z(0) = 0 \quad \dot{x}(0) = u_0 \quad \dot{y}(0) = 0 \quad \dot{z}(0) = v_0$$

i.e. the particle is initially at a distance ρ_0 in the y direction from the origin, with an initial perpendicular velocity of $v_{\perp,0} = u_0$ in the x direction and an initial parallel velocity of $v_{\parallel,0} = v_0$ in the z direction. Without field-line shearing ($k = 0$), these initial conditions would lead to

⁴It is immediately verified that this is a valid magnetic field, i.e. $\nabla \cdot \mathbf{B} = 0$. It corresponds to a trivial force-free field where $\nabla \times \mathbf{B} = k\mathbf{B}$.

3.4. Particle motion in a purely sheared magnetic field and limits of the drift approximation

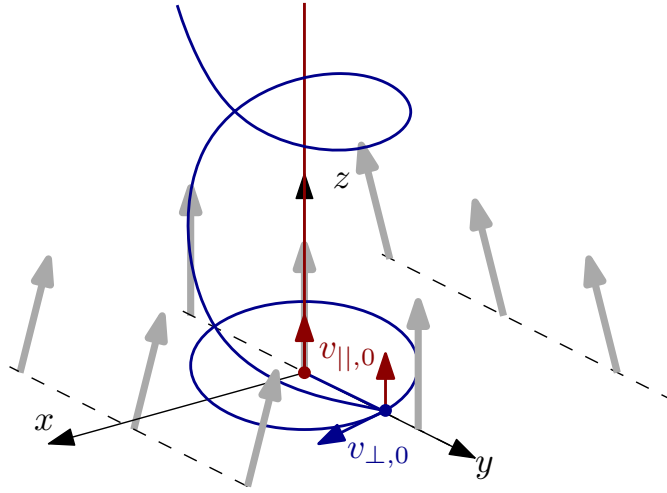


Figure 3.2 – Schematic drawing of the initial conditions and particle motion in the case of low shearing parameter k .

a standard helical trajectory along the z -axis, where the centre of the gyro-motion (guiding-centre) starts on the origin and moves along z at a constant velocity v_0 as expected.

With $k \neq 0$, the constants of motion are set to $P_y = 0$, $P_z = mv_0 + \frac{qB_0}{k}$ and $\mathcal{H} = \frac{1}{2}mv^2 = \frac{1}{2}m(u_0^2 + v_0^2)$. The non-linear coupled system of equations describing the motion of a charged particle respecting those initial conditions becomes

$$\dot{y} = -\frac{qB_0}{mk} \sin(kx) = -\omega_0 \frac{\sin(kx)}{k} \quad (3.24a)$$

$$\dot{z} = v_0 + \frac{qB_0}{mk} [1 - \cos(kx)] = v_0 + \frac{k}{2}\omega_0 \frac{\sin^2(\frac{k}{2}x)}{\left(\frac{k}{2}\right)^2} \quad (3.24b)$$

$$\dot{x}^2 + \omega_0^2 \left(1 + \frac{kv_0}{\omega_0}\right) \frac{\sin^2(\frac{k}{2}x)}{\left(\frac{k}{2}\right)^2} = u_0^2 \quad (3.24c)$$

where $\omega_0 = qB_0/m$ is the usual gyro-frequency. Equation (3.24c) is similar to that of a non-linear pendulum, for which the solution is entirely expressed in terms of elliptic integrals. Figure 3.3 draws the trajectory of the particle in (x, \dot{x}) phase-space. The colours represent the effective potential corresponding to lines of constant energy. It is seen that if the perpendicular initial velocity is high enough, the motion can be unbound in the x direction, above (or below) the lightest blue lines forming the X -point at $x = L/2 = \pi/k$. In the special case where $v_0 = -\omega_0/k$, the velocity along x becomes constant, i.e. $x(t) = u_0 t$ and the trajectory is actually circular in the $y-z$ plane, i.e. $y(t) = \frac{\omega_0}{k^2 u_0} \cos(ku_0 t)$ and $z(t) = -\frac{\omega_0}{k^2 u_0} \sin(ku_0 t)$ with a radius of $4\pi^2 L^2 / \rho_0$.

For $k \rightarrow 0$, equations (3.24a-3.24c) properly reduce to those of a charged particle in a constant magnetic field pointing in the z -direction, for which the solution is the well-known helical motion $x(t) = \rho_0 \sin(\omega_0 t)$, $y(t) = \rho_0 \cos(\omega_0 t)$ and $z(t) = v_0 t$.

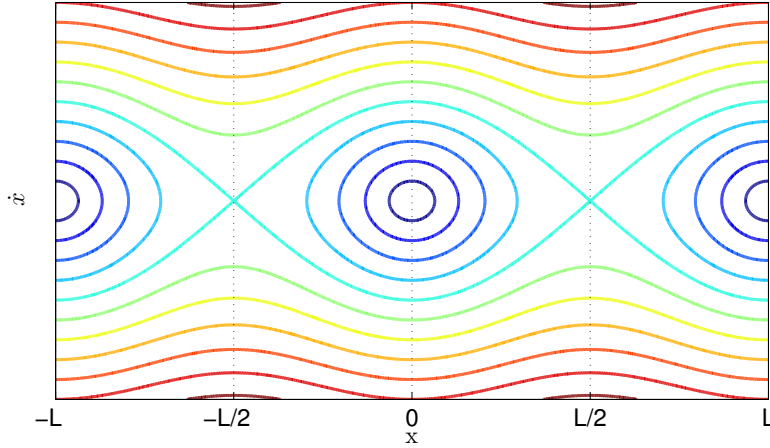


Figure 3.3 – Trajectory in the (x, \dot{x}) phase-space and effective potential according to (3.24c). Beyond the lightest blue line, the motion is unbounded in the x direction.

For intermediate $k \neq 0$, the motion in the x -direction is bounded ($\exists t_M \mid \dot{x}(t_M) = 0$) under the condition that

$$\left| \sin\left(\frac{k}{2}x_M\right) \right| = u_M = \frac{u_0}{\omega_0} \frac{k/2}{\sqrt{1 + \frac{kv_0}{\omega_0}}} < 1 \iff \rho_0 < \frac{L}{\pi} \sqrt{1 + \frac{kv_0}{\omega_0}}, \quad (3.25)$$

where x_M is the maximum amplitude in the x -direction. This condition demonstrates that if the Larmor radius ρ_0 is somewhat larger than the characteristic length $L/\pi = 2/k$ of the shear, particles do not necessarily perform a closed gyro-motion (blue curves on figure 3.3) but may progress along the x -direction indefinitely (red curves on figure 3.3).

Let us focus on the case where the motion is bounded in x (and de facto in y), which corresponds to the situation of closed gyro-orbits (blue contours on figure 3.3). The average particle drift along x and y is thus zero, i.e. $\langle \dot{x} \rangle = 0 = \langle \dot{y} \rangle$. The period of this bounded motion is given by

$$\begin{aligned} T &= \int_0^T dt = \oint \frac{dx}{\dot{x}} = 2 \int_{-x_M}^{x_M} \frac{dx}{\sqrt{u_0^2 - \frac{4\omega_0^2}{k^2} \left(1 + \frac{kv_0}{\omega_0}\right) \sin^2\left(\frac{k}{2}x\right)}} \\ &= \frac{4}{u_0} \int_0^{x_M} \frac{dx}{\sqrt{1 - \sin^2\left(\frac{k}{2}x\right) / \sin^2\left(\frac{k}{2}x_M\right)}} = \frac{8}{ku_0} \int_0^{u_M} \frac{du}{\sqrt{1-u^2} \sqrt{1-u^2/u_M^2}} \\ &= \frac{8u_M}{ku_0} \int_0^1 \frac{d\tau}{\sqrt{1-u_M^2\tau^2} \sqrt{1-\tau^2}} = \frac{4K(u_M)}{\omega_0 \sqrt{1 + \frac{kv_0}{\omega_0}}} \xrightarrow{k \rightarrow 0} \frac{2\pi}{\omega_0} \end{aligned} \quad (3.26)$$

where $K(k)$ is the complete elliptic integral of first kind.

Since there is no average motion in x and y , the average velocity along the z -axis exactly corresponds to the average particle drift. The latter is in the direction of the magnetic field at

3.4. Particle motion in a purely sheared magnetic field and limits of the drift approximation

the guiding-centre position ($x = 0$ and $y = 0$). This drift is given by

$$\begin{aligned}
 \langle \dot{z} \rangle &= \frac{1}{T} \int_0^T \dot{z} dt = v_0 + \frac{2\omega_0}{kT} \oint \frac{\sin^2\left(\frac{k}{2}x\right)}{\dot{x}} dx = v_0 + \frac{16\omega_0 u_M^3}{k^2 u_0 T} \int_0^1 \frac{\tau^2 d\tau}{\sqrt{1-u_M^2 \tau^2} \sqrt{1-\tau^2}} \\
 &= v_0 + \frac{k u_0^2}{2\omega_0} \frac{1}{1 + \frac{k v_0}{\omega_0}} \left[1 - \frac{1}{K(u_M)} \int_0^1 \frac{\sqrt{1-u_M^2 \tau^2}}{\sqrt{1-\tau^2}} d\tau \right] \frac{1}{u_M^2} \\
 &= v_0 + \frac{k u_0^2}{4\omega_0} \frac{1}{1 + \frac{k v_0}{\omega_0}} \left[1 - \frac{E(u_M)}{K(u_M)} \right] \frac{2}{u_M^2} \tag{3.27}
 \end{aligned}$$

where $E(k)$ is the complete elliptic integral of second kind.

First-order guiding-centre equations predict a constant parallel velocity of v_0 . By expanding at leading order in the shearing parameter k , we find a correction to the parallel guiding-centre velocity of

$$\langle \dot{z} \rangle \xrightarrow{k \rightarrow 0} -v_0 \frac{k u_0^2}{4\omega_0}. \tag{3.28}$$

This correction should not be confused with the averaged quantity $\langle v_{\parallel} \rangle$. As the particle swirls around the z -axis, it "sees" a varying magnetic field. The average parallel velocity, i.e. the average of the projection of the particle's velocity on \mathbf{B} , corresponds to

$$\langle v_{\parallel} \rangle = \langle \mathbf{b} \cdot \dot{\mathbf{x}} \rangle = \langle \sin(kx) \dot{y} + \cos(kx) \dot{z} \rangle.$$

Using (3.24a-3.24b) and after some algebra, the average parallel velocity as a function of k is written

$$\begin{aligned}
 \langle v_{\parallel} \rangle - v_0 &= \frac{1}{T} \int_0^T dt \left[-\frac{\omega_0}{k} \sin^2(kx) - \frac{\omega_0}{k} \cos^2(kx) + \left(v_0 + \frac{\omega_0}{k} \right) \cos(kx) \right] - v_0 \\
 &= -\left(1 + \frac{k v_0}{\omega_0} \right) \frac{2\omega_0}{kT} \int_0^T \sin^2\left(\frac{k}{2}x\right) dt = -\frac{k u_0^2}{4\omega_0} \left[1 - \frac{E(u_M)}{K(u_M)} \right] \frac{2}{u_M^2} \xrightarrow{k \rightarrow 0} -\frac{k u_0^2}{4\omega_0}. \tag{3.29}
 \end{aligned}$$

Therefore, at leading order, there is a fundamental (and conceptual) difference between the average particle drift and the average parallel velocity

$$\langle \dot{z} \rangle - \langle v_{\parallel} \rangle \xrightarrow{k \rightarrow 0} \frac{k u_0^2}{2\omega_0} = \frac{k\mu}{q} = \frac{\mu B}{m\omega_0} \mathbf{b} \cdot (\nabla \times \mathbf{b}). \tag{3.30}$$

From first-order guiding-centre theory $\dot{\mathbf{X}} \approx v_{\parallel} \mathbf{b} + \mathbf{v}_{\perp, \text{drift}}$, the particle drift along the parallel direction is expected to be equal to the parallel guiding-centre velocity. This paradoxical result is referred to as the Baños drift (equation (37) Baños, 1967), for which an interpretation is given by Northrop and Rome (1978, appendix B) as well as by Cary and Brizard (2009, p.718). In this example of magnetic fields with no gradient nor curvature, the guiding-centre equations must be extended with second order terms in order to encompass the Baños drift due to shearing of

Chapter 3. Particle motion and guiding-centre drift

field-lines. In a Hamiltonian formalism, this can be performed starting with the second order guiding-centre Lagrangian derived by Littlejohn (1983, equations (32-33)),

$$\mathcal{L} = (q\mathbf{A} + mv_{\parallel}\mathbf{b}) \cdot \dot{\mathbf{X}} - \left[\frac{1}{2}mv_{\parallel}^2 + \mu B + \frac{1}{2}\frac{m}{q}\mu v_{\parallel}\mathbf{b} \cdot (\nabla \times \mathbf{b}) \right], \quad (3.31)$$

which yields an Euler-Lagrange equation that coincides with (3.28)

$$\mathbf{b} \cdot \dot{\mathbf{X}} = v_{\parallel} + \frac{1}{2}\frac{\mu}{q}\mathbf{b} \cdot (\nabla \times \mathbf{b}). \quad (3.32)$$

where the correction due to field-line shearing and parallel currents appears at the same order as other drift terms stemming from gradients or field-line curvature. The guiding-centre motion along the field-lines is thus different than the gyro-averaged parallel velocity. The latter variable v_{\parallel} is interpreted in the guiding-centre phase-space as a pivot variable that includes the parallel curl of the magnetic field and the shearing of field-lines. This simple example where the Baños drift plays a crucial role motivated the implementation of full-orbit equations in the VENUS-LEVIS code as well as a means of switching between guiding-centre and full-orbit formulations as discussed in the next sections.

3.5 Field variation estimator

In most orbit simulations, first-order GCDE are used on the basis that the magnetic field is slowly varying with respect to the Larmor radius. As seen in the example of the previous section, there are situations, especially in three-dimensional configurations, where the field variation is large and where the primary assumptions of the guiding-centre approximation are not cleanly satisfied. Being able to quantify the field variation is important in order to assess the applicability of GCDE.

The guiding-centre approximation is often loosely justified by assuming that the scale length of the magnetic field is large compared with the gyroradius, or simply that gradients in the magnetic strength are weak, $B/|\nabla_{\perp}B| \gg \rho_L$. It is reminded that there are situations where gradients of B and even curvature are absent, but the variation of the field can still be strong, as demonstrated with the purely sheared magnetic field in section 3.4. GCDE are typically derived by expanding the magnetic field around the position of the guiding-centre $\mathbf{x} = \mathbf{X} + \boldsymbol{\rho}_{\perp}$, where \mathbf{x} is the position of the particle, \mathbf{X} the position of the guiding-centre and $\boldsymbol{\rho}_{\perp}$ a vector of the size of the Larmor radius perpendicular to the magnetic field. At first order, the magnetic field is approximated as

$$\mathbf{B}(\mathbf{x}) \approx \mathbf{B}(\mathbf{X}) + (\boldsymbol{\rho}_{\perp} \cdot \nabla)\mathbf{B}(\mathbf{X}).$$

Such an expansion can be qualified as reasonable as long as the variation of the field over $\boldsymbol{\rho}_{\perp}$ is much smaller than the field itself, i.e.

$$\frac{|\delta\mathbf{B}|}{|\mathbf{B}|} = \frac{|\mathbf{B}(\mathbf{x}) - \mathbf{B}(\mathbf{X})|}{|\mathbf{B}|} \approx \frac{|(\boldsymbol{\rho}_{\perp} \cdot \nabla)\mathbf{B}|}{|\mathbf{B}|} \sim O(\epsilon) \ll 1.$$

This criterion should be respected when using first-order GCDE. Hereafter, an explicit computation of the field variation is detailed for general magnetic fields and in curvilinear coordinates.

First, it is useful to express the Larmor radius as the perpendicular projection of an arbitrary vector, $\boldsymbol{\rho}_\perp = P\boldsymbol{\rho} = (I - \mathbf{b}\mathbf{b})\boldsymbol{\rho}$. Then, the idea is to view the desired scalar quantity as a bi-linear form

$$K(\boldsymbol{\rho}, \mathbf{X}) = |(\boldsymbol{\rho}_\perp \cdot \nabla)\mathbf{B}|^2 = [(P\boldsymbol{\rho}) \cdot \nabla\mathbf{B}] \cdot [\nabla\mathbf{B} \cdot (P\boldsymbol{\rho})] = \hat{\rho}^i \hat{M}_{ij} \hat{\rho}^j \quad (3.33)$$

The *hat* notation is meant to stress that the components $\hat{\rho}_i$ are those of the vector $\boldsymbol{\rho}$ expressed in an orthonormal (Cartesian) basis. The importance of this statement will become clear later. The spectral theorem states that an orthonormal basis of eigenvectors always exists for matrix M . In other words, $\boldsymbol{\rho}$ becomes an eigenvector if rotated correctly. This also means that the maximum of $K(\boldsymbol{\rho}, \mathbf{X})$ with respect to $\boldsymbol{\rho}$, i.e. the maximum eigenvalue λ_{max} of matrix M , will correspond to the maximum variation of the magnetic field in the perpendicular direction. In standard Cartesian coordinates $(x^1, x^2, x^3) = (x, y, z)$, M is written

$$\hat{M}_{ij} = \hat{P}_i^m \frac{\partial \hat{B}_l}{\partial x^m} \frac{\partial \hat{B}^l}{\partial x^k} \hat{P}_j^k = [P^T D^T D P]_{ij}$$

where $\hat{B}^i = \hat{B}_i$ are the Cartesian components of the magnetic vector field and $\hat{P}_j^i = \delta_j^i - \frac{\hat{B}^i \hat{B}_j}{B^2}$.

For the purely-sheared magnetic field example given in equation (3.21), the Jacobian matrix \hat{M} reduces to

$$\hat{M}_{ij} = k^2 B_0^2 \begin{pmatrix} 1 & 0 & 0 \\ 0 & 0 & 0 \\ 0 & 0 & 0 \end{pmatrix},$$

and the maximum eigenvalue is $\lambda_{max} = k^2 B_0^2$, which implies that a linear expansion in Larmor radius does notice the shearing of field-lines and the presence of parallel currents.

Representing the field and its derivatives in Cartesian coordinates is not always convenient because those coordinates are not native to the geometry of the system. Cylindrical or flux coordinates are preferred for applying this criterion in the case of toroidal magnetic fields that are relevant to tokamak and stellarator physics. As explained in appendix A.1.1, if (u^1, u^2, u^3) are those coordinates, the Jacobian matrix $\nabla\mathbf{B}$ in equation (3.33) is a covariant derivative,

$$\nabla\mathbf{B} = \frac{\partial}{\partial u^j} (B^i \mathbf{e}_i) \nabla u^j = \frac{\partial B^i}{\partial u^j} \mathbf{e}_i \nabla u^j + B^k \frac{\partial \mathbf{e}_k}{\partial u^j} \nabla u^j = (\partial_j B^i + \Gamma_{jk}^i B^k) \mathbf{e}_i \nabla u^j = B_{;j}^i \mathbf{e}_i \nabla u^j \quad (3.34)$$

or alternatively

$$\nabla\mathbf{B} = B_{i;j} \nabla u^i \nabla u^j = (\partial_j B_i - \Gamma_{ij}^k B_k) \nabla u^i \nabla u^j = (\partial_j B_i - \Gamma_{ij,k} B^k) \nabla u^i \nabla u^j \quad (3.35)$$

where $\mathbf{e}_i = \frac{\partial \mathbf{x}}{\partial u^i}$ the covariant basis, ∇u^i the contravariant basis, B^i the contravariant and B_i covariant components of the magnetic field, $\Gamma_{ij,k}$ is recognised as the Christoffel symbol of

Chapter 3. Particle motion and guiding-centre drift

first type and $\Gamma_{jk}^i = g^{il}\Gamma_{jk,l}$ of second type. The scalar product in curvilinear coordinates is now expressed as a contraction with the metric tensor, $\mathbf{a} \cdot \mathbf{b} = a^i b^j g_{ij} = a_i b_j g^{ij} = a_i b^i = a^i b_i$. The tensor M becomes (multiple possibilities)

$$M^{ij} = P^{ik} B_{,k}^l g_{lm} B_{,n}^m P^{nj} = P^{ik} B_{l;k} g^{lm} B_{m;n} P^{nj}$$

with $P^{ab} = g^{ab} - \frac{B^a B^b}{B^2}$.

If the M tensor is diagonalised in the curvilinear basis, the amplitude of the variations will be expressed along a non-orthonormal basis, which is not desired. The tensor must first be transformed to an orthonormal basis before diagonalisation

$$K(\boldsymbol{\rho}, \mathbf{X}) = \hat{\rho}^k \hat{\mathbf{e}}_k \cdot \mathbf{e}_i M^{ij} \mathbf{e}_j \cdot \hat{\mathbf{e}}_l \hat{\rho}^l = \hat{\rho}^k \frac{\partial x_k}{\partial u^i} M^{ij} \frac{\partial x_l}{\partial u^j} \hat{\rho}^l.$$

The relevant matrix to diagonalise is thus composed of the following product of matrices

$$\hat{M}_{ij} = [\Lambda P^T D^T G D P \Lambda^T]_{ij} = [V^T G V]_{ij} \quad (3.36)$$

with $V = D P \Lambda^T$, $\Lambda_{ij} = \frac{\partial x_i}{\partial u^j}$, $D_{,j}^i = B_{,j}^i$ and $G_{ij} = g_{ij}$ (or $D_{ij} = B_{i;j}$ and $G^{ij} = g^{ij}$). The maximum eigenvalue of \hat{M} , $\lambda_{max}(\mathbf{X}) = \max[\text{eig}(\hat{M})]$, will then provide the local estimate of the maximum variation of the magnetic field in Cartesian coordinates. It is straightforward to find the eigenvalues of \hat{M} . One is zero due to the projection in the perpendicular direction, i.e. $\det(\hat{M}) = 0$. The remaining pair is obtained via the quadratic equation $\lambda^2 - \text{trace}(\hat{M})\lambda + b = 0$,

$$\lambda_{\pm} = \frac{1}{2} \text{trace}(\hat{M}) \pm \frac{1}{2} \sqrt{\text{trace}(\hat{M})^2 - 4b}$$

where $b = M_{11}M_{22} - M_{12}^2 + M_{11}M_{33} - M_{13}^2 + M_{22}M_{33} - M_{23}^2$. λ_+ is evidently the maximum eigenvalue and is noticed to be bounded inferiorly by $\text{trace}(\hat{M})$ (quicker to evaluate).

Finally putting all the pieces together, the criterion that must verify GCDE is

$$\frac{|(\boldsymbol{\rho}_{\perp} \cdot \nabla) \mathbf{B}|}{B} = \frac{\sqrt{\lambda_{max}} \rho_{\perp}}{B} = \frac{m v_{\perp}}{q B^2} \sqrt{\lambda_{max}} = \sqrt{\frac{2m}{q} \frac{\mathcal{H}_{\perp}}{q}} \frac{\sqrt{\lambda_{max}}}{B^2} = \sqrt{\frac{2\lambda_{max}}{B^3} \frac{m \mu}{q}} \ll 1. \quad (3.37)$$

where m is the particle mass, q its charge, $v_{\perp} = \rho_{\perp} q B / m$ the perpendicular velocity, $\mathcal{H}_{\perp} = \frac{1}{2} m v_{\perp}^2$ the energy in the perpendicular direction and $\mu = m v_{\perp}^2 / 2B = \mathcal{H}_{\perp} / B$ the magnetic moment, which is an adiabatic constant of the particle motion.

Applied to toroidal devices where the magnetic field strength $B \approx B_0 R_0 / R$, the field variation approximately corresponds to the gradient of the magnetic field, which is $\sqrt{\lambda_{max}} \approx B_0 / R_0$ on axis. Considering fusion alphas (${}^4\text{He}^{+2}$) for example, the factor $\sqrt{2m/q} \approx 2.04 \cdot 10^{-4} [\text{kg/C}]^{1/2}$ and $\sqrt{\mathcal{H}_{\perp}/q} = \sqrt{3.5 \text{ MeV}/2} = 1.323 \cdot 10^{-3} [\text{eV}]^{1/2}$ so criterion (3.37) coarsely corresponds to $0.27 / B_0 R_0 \ll 1$. The ratio $0.27 / B_0 R_0$ represents a few percent in tokamaks with a large major radius and a strong magnetic field like ITER. In spherical tokamaks like MAST where $R_0 = 0.8\text{m}$ and $B_0 = 0.5\text{T}$, the variation length-scale due to gradients corresponds to 10% of the Larmor radius for alpha particles at 80keV. As it is argued in this paper, not only gradients give rise to

field variations but also curvature, parallel currents and the shearing of field-lines. Therefore, the value of $\sqrt{\lambda_{max}}$ is higher than $|\nabla B|$ and the range of “valid” energies for first-order guiding-centre theory is all the more reduced (i.e. quadratically).

Applied to the purely-sheared magnetic field of equation (3.21), the criterion reads

$$k\rho_{\perp} = \frac{kv_{\perp}}{\Omega_C} \ll 1,$$

meaning that the error between the guiding-centre and the average particle trajectory is of order kv_{\perp}/Ω_C , as intuitively expected from the discussion of full-orbits in section 3.4 and from the drift ordering. It is noted that first-order GCDE do not account for such field variations due to parallel currents and field-line shearing although they appear in criterion (3.37) at linear order in a Larmor radius expansion. A second-order treatment of the guiding-centre Lagrangian would compensate for Baños drifts arising from this field variation.

Criterion (3.37) is used in VENUS-LEVIS as a trigger to switch between GCDE and full-orbit equations in the algorithm presented in section 3.6. It is also applied in section 5.1.1 to the case of Neutral Beam Injection (NBI) fast particles in a Mega-Ampère Spherical Tokamak (MAST) helical core equilibrium in order to inspect the regions of strong field variation and reveal the features of this magnetic configuration.

3.5.1 Toroidal coordinates with geometric toroidal angle

The field variation can be estimated with algebraic expressions of reasonable length in curvilinear coordinates where the toroidal angle is equal to the geometric angle. Derivatives of the magnetic field can be evaluated either in the covariant or the contravariant representation. For example, the matrix of interest $\hat{M} = V^T G V$ is written

$$M_{mn} = V_{im} g^{ij} V_{jn} \qquad V_{im} = B_{i;j} P^{jk} \frac{\partial x_m}{\partial u^k} \qquad (3.38)$$

where $x_m = x^m = (x, y, z)$ are Cartesian coordinates, u^k curvilinear coordinates. The perpendicular projection is written as the following contravariant tensor

$$P^{jk} = g^{jk} - \frac{B^j B^k}{B^2},$$

the covariant derivative is

$$B_{i;j} = \partial_j B_i - \Gamma_{ij}^k B_k = \partial_j B_i - \Gamma_{ij,l} B^l,$$

and the Christoffel symbol of first type is expressed as

$$\Gamma_{ij,l} = \frac{\partial R}{\partial u^l} \frac{\partial^2 R}{\partial u^i \partial u^j} + \frac{\partial Z}{\partial u^l} \frac{\partial^2 Z}{\partial u^i \partial u^j} + R \left[\frac{\partial R}{\partial u^i} \delta_j^3 \delta_l^3 + \frac{\partial R}{\partial u^j} \delta_i^3 \delta_l^3 - \frac{\partial R}{\partial u^l} \delta_i^3 \delta_j^3 \right]. \qquad (3.39)$$

Another option is to lean on

$$M_{mn} = V_m^i g_{ij} V_n^j \quad V_m^i = B_{;j}^i P^{jk} \frac{\partial x_m}{\partial u^k} \quad (3.40)$$

where the covariant derivative is the mixed tensor

$$B_{;j}^i = \partial_j B^i + \Gamma_{jk}^i B^k$$

and the Christoffel symbol of second type is used

$$\Gamma_{jk}^i = \frac{\partial u^i}{\partial R} \frac{\partial^2 R}{\partial u^j \partial u^k} + \frac{\partial u^i}{\partial Z} \frac{\partial^2 Z}{\partial u^j \partial u^k} + \frac{1}{R} \delta_3^i \delta_j^3 \frac{\partial R}{\partial u^k} + \frac{1}{R} \delta_3^i \delta_k^3 \frac{\partial R}{\partial u^j} - R \delta_j^3 \delta_k^3 \frac{\partial u^i}{\partial R}. \quad (3.41)$$

In theory, the two options (3.38-3.40) yield identical results but in practice, computing equation (3.40) is numerically more stable around the singular magnetic axis. In flux coordinates, divergent metric terms such as $\partial^2 R / \partial u^j \partial u^k$ are naturally multiplied by terms going to zero like $\partial u^i / \partial R$ in the Christoffel symbol of second type Γ_{jk}^i . Such cancellation happens later in the matrix multiplication of (3.38) which makes it more prone to truncation errors.

3.5.2 Field variation constituents in MHD equilibrium fields

The criterion (3.37) is valid for any type of magnetic field. In the context of MHD equilibria, it is instructive to identify its main constituents. The linearisation of the magnetic field around the guiding-centre position involves the derivative of the vector field in the form of a Jacobian matrix $\nabla \mathbf{B} = \partial_i B_j$ (working in Cartesian coordinates for simplicity). The entries of this matrix are not all independent and some of them can be written in terms of known differential operators such as the divergence, curl or gradient, $\nabla \cdot \mathbf{B} = 0$, $\nabla \times \mathbf{B} = \mathbf{J}$ and ∇B . The force balance equation $\mathbf{J} \times \mathbf{B} = \mu_0 \nabla p$ is also used to draw links among the matrix components.

For example, using the vector identity $\nabla B = \frac{1}{2} \nabla (\mathbf{B} \cdot \mathbf{B}) / B = \mathbf{b} \cdot \nabla \mathbf{B} + \mathbf{b} \times (\nabla \times \mathbf{B})$, the parallel field variation is expressed as a gradient term

$$\mathbf{b} \cdot \nabla \mathbf{B} = \nabla B + \frac{(\nabla \times \mathbf{B}) \times \mathbf{B}}{B} = \frac{1}{B} (B \nabla B + \mu_0 \nabla p) = \frac{1}{B} \nabla \left(\frac{B^2}{2} + \mu_0 p \right).$$

where the force balance equation was used to introduce ∇p . The perpendicular component of this gradient term is equal to the magnetic curvature,

$$\boldsymbol{\kappa} = \mathbf{b} \cdot \nabla \mathbf{b} = \frac{\mathbf{b} \cdot \nabla \mathbf{B}}{B} - \mathbf{b} \left(\frac{\mathbf{b} \cdot \nabla B}{B} \right) = \frac{1}{B^2} \nabla_{\perp} \left(\frac{B^2}{2} + \mu_0 p \right).$$

By considering only perpendicular field variations $\boldsymbol{\rho}_{\perp}$, the criterion (3.37) does not take curvature into account. The projector P can be simply replaced by the unity matrix I in equation (3.33) to include $\boldsymbol{\kappa}$.

Another point of view is to separate the Jacobian matrix into symmetric and anti-symmetric parts as $\partial_i B_j = \frac{1}{2} (\partial_i B_j + \partial_j B_i) + \frac{1}{2} (\partial_i B_j - \partial_j B_i)$. The anti-symmetric part can be expressed as

the current (curl of the magnetic field) by

$$\partial_i B_j - \partial_j B_i = (\delta_i^m \delta_j^n - \delta_i^n \delta_j^m) \partial_m B_n = \epsilon_{ijk} \underbrace{\epsilon^{kmn} \partial_m B_n}_{[\nabla \times \mathbf{B}]^k} = \epsilon_{ijk} J^k$$

The linear derivative of criterion (3.37) is thus broken up into

$$\boldsymbol{\rho} \cdot \nabla \mathbf{B} = [\boldsymbol{\rho} \cdot \nabla \mathbf{B}]_A + [\boldsymbol{\rho} \cdot \nabla \mathbf{B}]_S = \frac{1}{2} \boldsymbol{\rho} \times (\nabla \times \mathbf{B}) + \frac{1}{2} (\boldsymbol{\rho} \cdot \nabla \mathbf{B} + \nabla \mathbf{B} \cdot \boldsymbol{\rho}).$$

Considering only perpendicular Larmor radii written $\boldsymbol{\rho}_\perp = -\mathbf{b} \times (\mathbf{b} \times \boldsymbol{\rho})$, the anti-symmetric part becomes

$$\begin{aligned} [\boldsymbol{\rho}_\perp \cdot \nabla \mathbf{B}]_A &= -[\mathbf{b} \times (\mathbf{b} \times \boldsymbol{\rho})] \times (\nabla \times \mathbf{B}) = \mathbf{J} \times [\mathbf{b} \times (\mathbf{b} \times \boldsymbol{\rho})] = \mathbf{b} [\mathbf{J} \cdot (\mathbf{b} \times \boldsymbol{\rho})] - (\mathbf{b} \times \boldsymbol{\rho}) (\mathbf{J} \cdot \mathbf{b}) \\ &= \mathbf{b} \left(\boldsymbol{\rho} \cdot \frac{\mathbf{J} \times \mathbf{B}}{B} \right) + J_\parallel \boldsymbol{\rho} \times \mathbf{b} = \mu_0 \frac{\boldsymbol{\rho} \cdot \nabla p}{B} \mathbf{b} + J_\parallel \boldsymbol{\rho} \times \mathbf{b} \end{aligned}$$

revealing the importance of parallel currents in the evaluation of the perpendicular field variation.

The symmetric part has the property that its trace is zero, by virtue of $\partial_i B^i \equiv \nabla \cdot \mathbf{B} = 0$. One diagonal component can thus be expressed in terms of the other two. Three components depend on ∇B . Hence, out of the six elements of the symmetric part of the Jacobian matrix, two cannot be associated to any of the curl, divergence nor gradient differential operators.

Parallel currents in axisymmetric MHD equilibria

The parallel current can be expressed in terms of pressure and current density profiles in axisymmetric MHD equilibria via the Grad-Shafranov equation (2.7). The magnetic field and the current are reminded to be

$$\mathbf{B} = F(\Psi) \nabla \phi + \nabla \phi \times \nabla \Psi \quad \mathbf{J} = \nabla \times \mathbf{B} = \Delta^* \Psi \nabla \phi - \frac{dF}{d\Psi} \nabla \phi \times \nabla \Psi$$

where $\Delta^* \Psi = -\mu_0 \frac{dp}{d\Psi} R^2 - F \frac{dF}{d\Psi}$ results from the Grad-Shafranov equation, $dp/d\Psi$ is the pressure gradient with respect to the poloidal flux Ψ and $dF/d\Psi$ the gradient of the poloidal current. The parallel current therefore reduces to

$$\frac{\mathbf{J} \cdot \mathbf{B}}{B^2} = \frac{1}{B^2 R^2} \left(F \Delta^* \Psi - \frac{dF}{d\Psi} |\nabla \Psi|^2 \right) = -\mu_0 \frac{dp}{d\Psi} \frac{F}{B^2} - \frac{dF}{d\Psi} \quad (3.42)$$

where $B^2 = (F^2 + |\nabla \Psi|^2)/R^2$ was used.

Parallel currents in 3D MHD equilibria

In 3D ideal MHD equilibria, parallel currents can be shown to be locally infinite on rational surfaces (Boozer, 1981; Grad, 1967). This is an unresolved issue for ideal MHD equilibrium codes such as VMEC. Resistive effects would relax these singular current sheets in creating

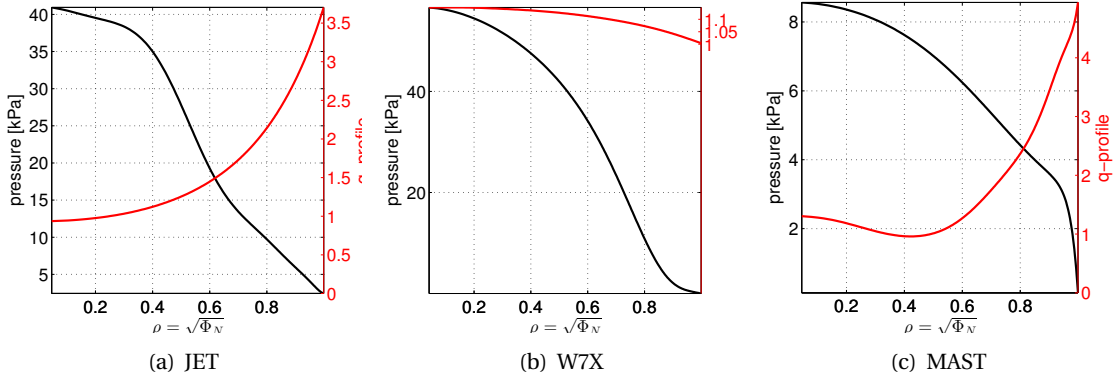


Figure 3.4 – Pressure and q-profile of the devices considered

magnetic islands and reconnection. This topic is slightly out of scope of this thesis.

Using Boozer coordinates to represent the magnetic field as in equation (2.14) and current density as in (2.16), the parallel current conveniently reduces to

$$\frac{\mathbf{J} \cdot \mathbf{B}}{B^2} = \frac{\mathcal{I}' \mathcal{J} - \mathcal{I} \mathcal{J}'}{\mathcal{J} \Psi' - \mathcal{I} \Phi'} + \frac{\frac{\partial B_s}{\partial \theta} \mathcal{J} + \frac{\partial B_s}{\partial \phi} \mathcal{I}}{\mathcal{J} \Psi' - \mathcal{I} \Phi'}$$

where \mathcal{I} and \mathcal{J} are respectively poloidal and toroidal current, Ψ and Φ poloidal and toroidal magnetic flux. The denominator, corresponding to $\sqrt{g}B^2$, is reminded to be non-zero. The first term is a secular parallel current. The second term is the resonant part leading to infinite Pfirsch-Schlüter currents. The derivative of the poloidal current \mathcal{I}' or toroidal current \mathcal{J}' can be interchanged by using relation (2.17) in favour of the derivative of pressure and volume p' and V' . The parallel current is thus expressed as

$$\frac{\mathbf{J} \cdot \mathbf{B}}{B^2} - \frac{\frac{\partial B_s}{\partial \theta} \mathcal{J} + \frac{\partial B_s}{\partial \phi} \mathcal{I}}{\mathcal{J} \Psi' - \mathcal{I} \Phi'} = \frac{\mathcal{I}'}{\Phi'} + \frac{\mu_0 \mathcal{J} p'}{4\pi^2 \Phi' \sqrt{g} B^2} \frac{V'}{\mathcal{I} - \mathcal{J}} = \frac{d\mathcal{I}}{d\Phi} + \frac{\mu_0}{4\pi^2} \frac{dp}{d\Phi} \frac{dV}{d\Phi} \frac{\mathcal{J}}{\mathcal{I} - \mathcal{J}} \quad (3.43)$$

$$= \frac{\mathcal{I}'}{\Psi'} + \frac{\mu_0 \mathcal{I} p'}{4\pi^2 \Psi' \sqrt{g} B^2} = \frac{d\mathcal{I}}{d\Psi} + \frac{\mu_0}{4\pi^2} \frac{dp}{d\Psi} \frac{dV}{d\Psi} \frac{\mathcal{I}}{\mathcal{I} - q\mathcal{I}} \quad (3.44)$$

where $q = 1/\iota$ is the q-profile (iota-profile) and V is the volume contained inside the flux-surface s .

3.5.3 Field variation map of various devices

Criterion (3.37) is applied to various experimental fusion devices to map the field variation that a particle feels with a given Larmor radius. The goal is to illustrate the range of energies above which first-order guiding-centre equations become approximate for solving the motion of fast ions. Various constituents are also displayed to identify from what kind of derivative terms the field variation consists of. It is reminded that only a fraction of each constituent will appear in the final criterion since $|X + Y| \leq |X| + |Y|$. Figure 3.4 displays the pressure and q-profile that were used to generate the equilibria with VMEC.

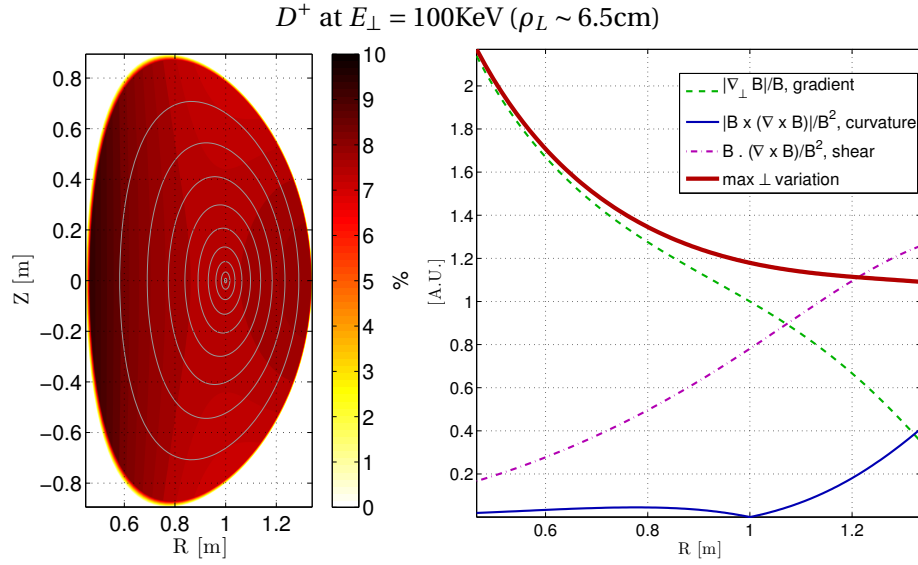


Figure 3.5 – (left) Field variation criterion (3.37) applied to Solov’ev MHD equilibrium with $B_0 = 1\text{ T}$, $R_0 = 1\text{ m}$, $\Psi_{edge} = 0.05\text{ Wb}$, $a = 0.4$, $e = 2$ for a deuterium ion at $E_{\perp} = 100\text{ keV}$. (right) inverse scale-length of the total perpendicular field variation and various derivatives that enter in its composition at mid plane as a function of the major radius.

First, we consider a low aspect ratio Solov’ev analytic MHD equilibrium (see appendix B.1.1 for more details) where the magnetic field on axis is set to $B_0 = 1\text{ [T]}$, the major radius $R_0 = 1\text{ [m]}$, the magnetic flux at the last closed flux-surface $\Psi_{edge} = 0.05\text{ [Wb]}$, the minor radius $a = 0.4\text{ [m]}$ and the elongation $e = 2$. These parameters approximately correspond to a MAST plasma. As seen on figure 3.5, the field variation reaches 7 – 8% of the total field strength everywhere in the plasma for a deuterium ion at $E_{\perp} = 100\text{ keV}$. On the high-field side, the variation is mainly due to the perpendicular gradient of B , as depicted by the green curve nearly aligning with the red curve (maximum variation in the perpendicular direction) on the right plot of figure 3.5. On the low-field side, the gradient fades and the field variation is caused by parallel currents (purple curve). According to equation (3.42) and the fact that $dp/d\Psi = -\text{const}$ and $F(\Psi) = F_0$ for Solov’ev equilibrium, the parallel current is proportional to $1/B^2 \sim R^2$. Curvature, which arises from perpendicular currents (in blue), is relatively low compared to the other components. GCDE are acceptable for the study of hot particles below this range of energies, typically NBI, but may not be applicable for Ion Cyclotron Resonance Heating (ICRH) nor fusion alphas in the MeV range.

In a standard JET equilibrium with a monotonic q -profile starting at $q_0 \approx 1$, the field variation is between 5 – 7% for an alpha particle at $E_{\perp} = 3.5\text{ MeV}$, as seen on figure 3.6. The low variation due to the strong magnetic field and the large aspect ratio justifies the use of GCDE for the study of fusion ions in this device. The main component arises again from gradients (green curve on figure 3.6). The field variation in the core bulges due to parallel currents, caused by a large $dF/d\Psi$ term in equation (3.42). This is related to having low magnetic shear and a q -profile close to unity in the core (see figure 3.4). Perpendicular current is weak in this example, explained by the low value of $\beta \sim 0.6\%$. According to the criterion (3.37), GCDE are fairly adequate to track fast particles such as fusion alphas in JET. Most guiding-centre codes

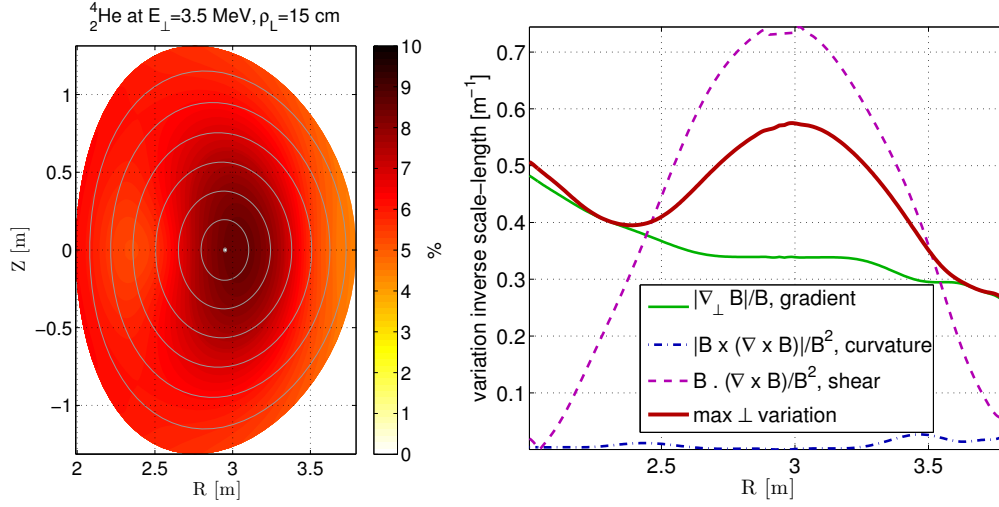


Figure 3.6 – (left) Field variation criterion (3.37) of a typical Joint European Torus (JET) equilibrium with $B_0 = 2.5\text{T}$, $R_0 = 2.95\text{m}$, $\Psi_{edge} = 10\text{Wb}$ and $I_{tor} = 1.9\text{MA}$ for a fusion alpha at $E_{\perp} = 3.5\text{MeV}$. (right) inverse scale-length of the total perpendicular field variation and various derivatives that enter in its composition at mid-plane as a function of major radius.

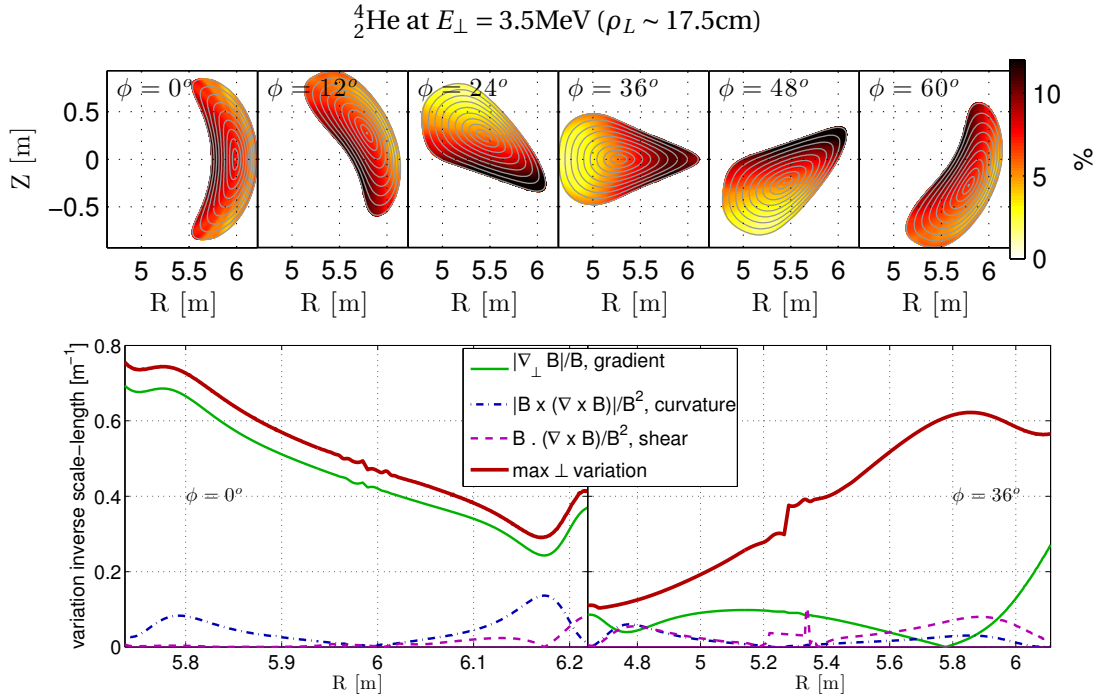


Figure 3.7 – (top) Field variation criterion (3.37) at various toroidal angles within a low shear W7X plasma with $B_0 = 2.38\text{ [T]}$, $R_0 = 5.62\text{ [m]}$, $\Psi_{edge} = 1.9\text{Wb}$ for a fusion alpha at $E_{\perp} = 3.5\text{MeV}$. (bottom) inverse scale-length of the total perpendicular field variation across the mid-plane at $\phi = 0^{\circ}$ (left bottom plot) and $\phi = 36^{\circ}$ (right bottom plot) where the configuration is up-down symmetric.

however do not include the Baños drift from parallel currents.

In the complex geometry of a standard W7X plasma, the field variation for alpha particles

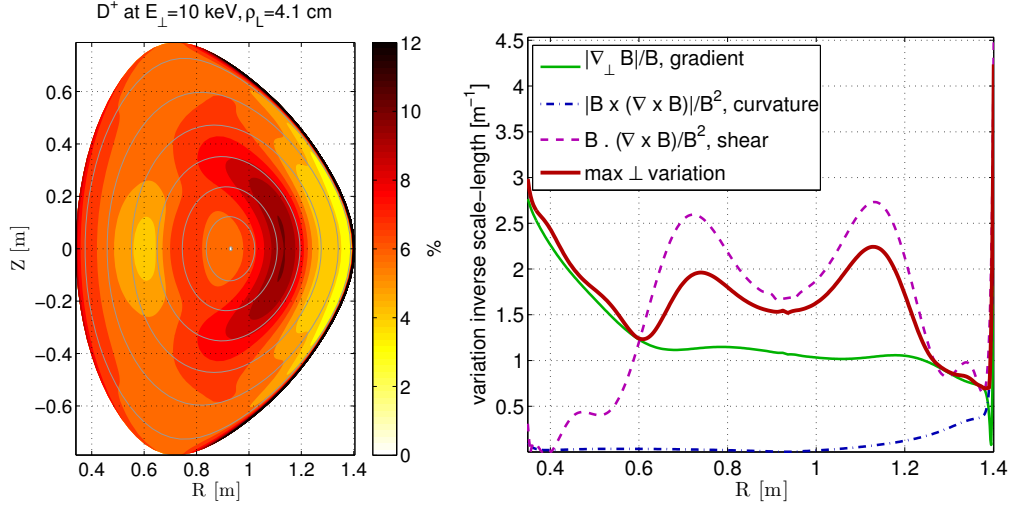


Figure 3.8 – (left) Field variation criterion (3.37) of a MAST hybrid scenario plasma with $B_0 = 0.5T$, $R_0 = 0.93m$, $\Psi_{edge} = 0.68Wb$ and $I_{tor} = 545kA$ for a deuterium ion at $E_{\perp} = 10keV$. (right) inverse scale-length of the total perpendicular field variation and various derivatives that enter in its composition at mid-plane as a function of major radius.

at $E_{\perp} = 3.5MeV$ can be as low as 2 – 3% in some regions (high-field side at $\phi = 36^{\circ}$) but can reach 10 – 12% in others (high-field side at $\phi = 0^{\circ}$ or low-field side at $\phi = 36^{\circ}$), as seen on the top plot of figure 3.7. At $\phi = 0^{\circ}$, the variation is caused by the strong gradient related to the narrow width of the plasma, as shown on the left bottom plot of figure 3.7. At $\phi = 36^{\circ}$, neither the gradient nor the curl terms account for the field variation on the low-field side, which suggests that the origin is geometric. Indeed, the shape of the flux-surfaces varies quite dramatically from one toroidal angle to the other, forming a sharp cusp at $\phi = 36^{\circ}$. The reason for such a large field variation despite weak curvature, gradient and shearing is worth being further explored (possibly the effect of field-line torsion). Nevertheless, it seems reasonable to use GCDE in W7X to solve the motion of rapid ions such as fusion alphas.

In MAST hybrid scenario plasmas, the field variation is already large compared to the Larmor radius of a deuterium ion at the energy of $E_{\perp} = 10keV$, as seen on figure 3.8. This is mostly due to the low aspect ratio and the low magnetic field of $B_0 = 0.5T$. The perpendicular gradients (green curve) contribute almost entirely to the field variation in the outer regions. Parallel currents have an enhancing effect in the core where the low-shear q -profile is near unity. This example indicates that GCDE may not be applicable to trace fast particles in MAST, at least not when the perpendicular energy is in the order of 10keV. It will be verified in chapter 5 that for NBI, GCDE correctly replicate the dynamics of passing particles. For ICRH and fusion products, a higher order guiding-centre scheme or a full-orbit approach is necessary.

3.6 Full-orbit to guiding-centre switching

Solving the full-orbit equations is computationally heavy. Worse, the smaller the Larmor radius, the harder it is to resolve the small gyration of the particle around the field-lines and a

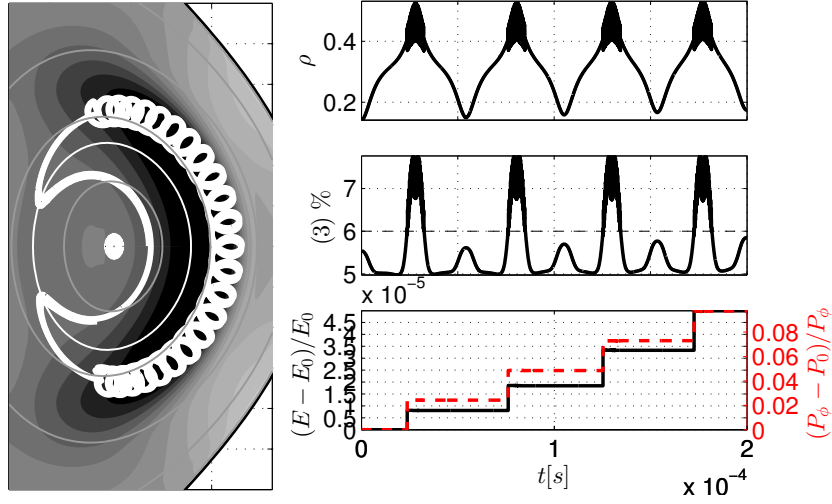


Figure 3.9 – Banana orbit (white curve on the left plot) in a MAST axisymmetric equilibrium of a D^+ ion with $\mathcal{H} = 10$ KeV, $v_{\parallel 0}/v = 0.5$ and $\rho_0 = 0.14$ computed using GCDE/full-orbit switching given a threshold for criterion (3.37) of 6%. The background colours in the left plot highlight the field variation felt by the particle (dark black patch is above the threshold) and light grey lines depict flux surfaces. The top right plot shows the evolution of the particle’s radial coordinate $\rho = \sqrt{\Phi/\Phi_e}$, where Φ is the poloidal magnetic flux (Φ_e its value on the last closed flux-surface). The middle right plot displays the field variation from equation (3.37) felt at the guiding-centre position (black). The bottom right plot shows the relative error in energy (solid black line) and relative error in toroidal momentum (dashed red line) in time.

full-orbit calculation becomes less precise than using a guiding-centre formulation. It is useful to be able to switch instantaneously between GCDE and full-orbit equations and to focus numerical resources only where the GCDE are inadequate. The procedures presented in this section are directly applicable to single particle orbit tracing, e.g. for comparing or switching from a guiding-centre to full-lorentz formulation, but are also relevant for simulating fast particle populations, starting from an analytic distribution in terms of constants of the guiding-centre motion and generating distributions of full-orbits with matching properties; in the case of strongly varying electromagnetic fields, for which the guiding-centre approximation may break down, both distributions are expected to evolve differently.

Figure 3.9 shows an example of a 10 KeV D^+ ion undergoing a banana orbit in an axisymmetric equilibrium of MAST. When its guiding-centre enters an area of the magnetic configuration where the field variation criterion (3.37) is above the arbitrary threshold choice of 6%, the algorithm switches between GCDE and full-orbit equations and vice-versa when (3.37) is below 6%.

The mapping between particle and guiding-centre variables is defined at the same order as the guiding-centre equations of motion because the guiding-centre phase-space is basically a contraction (average) of the particle’s (Littlejohn, 1982). The techniques described hereafter are strictly speaking valid up to first order in a ρ_L expansion. They are however found to minimise the divergence between guiding-centre trajectories and full-orbits. Indeed, a small discrepancy is induced when switching from guiding-centre to particle variables, as observed on the bottom right plot of figure 3.9 showing the relative increase of energy and relative

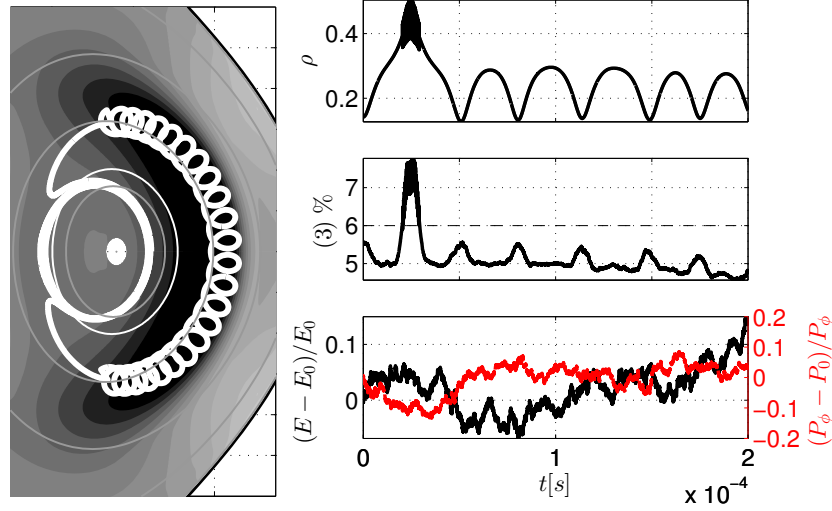


Figure 3.10 – *De-trapping of the same particle as in figure 3.9 due to the action of Monte-Carlo operators simulating Coulomb collisions with the background plasma Albergante et al. (2012). The particle receives random kicks in energy \mathcal{H} and pitch-variable v_{\parallel}/v which perturb its orbit and its collisionless constants of motion to greater extent than the switching between guiding-centre and particle phase-space.*

increase of toroidal momentum (both constants of motion). The guiding-centre trajectory follows the average particle motion with an error that scales proportionally to $|(\boldsymbol{\rho}_L \cdot \nabla)\mathbf{B}|/B$ as explained in section 3.5. Divergences are minimised by making sure that constants of motion match in the two phase-spaces and the switching process is triggered in an area of the magnetic field where its variation is small. A second order expansion as in the work by Belova et al. (2003) would help improve the transition between guiding-centre and full-orbit variables, including for example the Baños drift term (see equation 3.32). The algorithm is especially appropriate in conjunction with various Monte-Carlo operators (for e.g. Coulomb collisions with the background, charge exchange, anomalous transport, etc.), where the random kicks perturb the particle’s motion to greater extent than the switching process, as observed in figure 3.10.

Figure 3.11 illustrates how a collection of particle orbits (in green), each initialised with a different gyro-phase around the same guiding-centre position (in red) using formulae (3.53-3.50), tend to deviate after a few gyro-periods in MAST axisymmetric equilibrium. The dark green dots on figure 3.11 mark the position of those particles at consecutive times. The initial ring of particles (on the left-hand side of figure 3.11) is progressively stretched and deformed. The initial parallel velocity slightly differs for each particle around that ring such that particles stream down the guiding-centre line at different speeds. This behaviour is aggravated at larger gyro-radius and higher energy, due to the neglect of the Baños drift term (3.32). It is noticed however that the guiding-centre trajectory passes exactly through the tube formed by the ring of particles, which indicates that the guiding-centre approximation in the plane perpendicular to \mathbf{B} agrees better than in the parallel direction. Small deviation in particle trajectories with respect to their guiding-centre is an issue for barely trapped or passing particles, for which those changes can equate to a totally different orbit topology. For this family of orbits, it seems

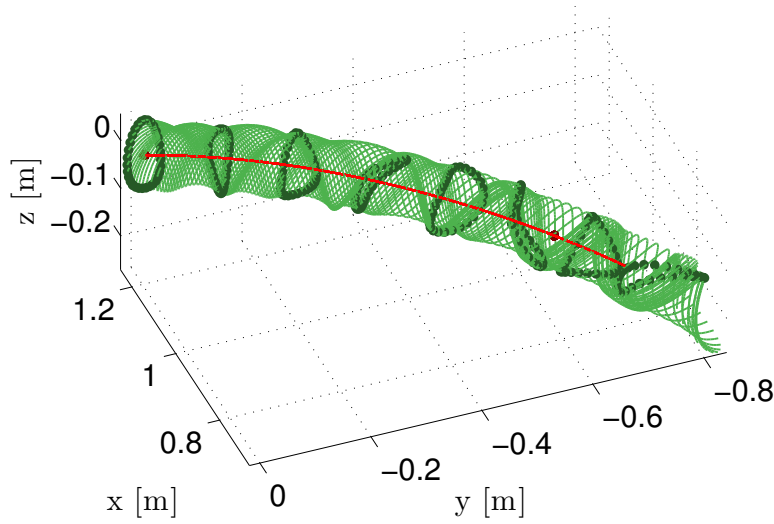


Figure 3.11 – Collection of particle orbits (in green), each initialised with a different gyro-phase around the same guiding-centre position (in red). Dark green dots represent the position of these particles at consecutive times (beginning on the left-hand side). H^+ ions at $\mathcal{H} = 20\text{KeV}$, $v_{0\parallel}/v = 0.43$, $\rho_0 = 0.4$ with Larmor radius $\rho_{\perp} \approx 5.8\text{cm}$ evolved for $t_f = 5 \cdot 10^{-5}\text{s}$.

that even the notion of trapped or passing guiding-centre is somewhat indistinct.

3.6.1 From particle to guiding-centre variables

The mapping from the particle coordinates (\mathbf{x}, \mathbf{v}) to the guiding-centre coordinates $(\mathbf{X}, v_{\parallel}, \mu)$ is a surjection in the sense that an infinite number of particles share the same guiding-centre. At first order, the guiding-centre position is calculated from the particle variables as

$$\mathbf{X} = \mathbf{x} - \boldsymbol{\rho}_L(\mathbf{x}) = \mathbf{x} + \frac{m}{qB(\mathbf{x})} \mathbf{v} \times \mathbf{b}(\mathbf{x}). \quad (3.45)$$

After setting the guiding-centre position, it is important to ensure that the guiding-centre energy and the particle energy are equal, since they are identical constants of motion in the presence of static electromagnetic fields, i.e.

$$\mathcal{H} = \frac{1}{2} m v^2 + q\Phi_E(\mathbf{x}) = \frac{1}{2} m g_{ij}(\mathbf{x}) v^i v^j + q\Phi_E(\mathbf{x}) = \frac{1}{2} m v_{\parallel}^2 + \mu B(\mathbf{X}) + q\Phi_E(\mathbf{X}) = \mathcal{H}_{GC}.$$

The particle toroidal momentum and the guiding-centre toroidal momentum in axisymmetric systems are also supposed to match, i.e.

$$P_{\phi} = qA_{\phi} + m v_{\phi} = qA_{\phi}(\mathbf{x}) + m g_{i\phi}(\mathbf{x}) v^i = qA_{\phi}(\mathbf{X}) + m v_{\parallel} b_{\phi}(\mathbf{X}).$$

From the two previous equations, even for non-axisymmetric or time-varying fields, it is reasonable to express the guiding-centre velocity variables as a function of the particle phase-

space coordinates in the following way

$$v_{\parallel} = \frac{B(\mathbf{X})}{B_{\phi}(\mathbf{X})} \left\{ g_{i\phi}(\mathbf{x}) v^i + \frac{q}{m} [A_{\phi}(\mathbf{x}) - A_{\phi}(\mathbf{X})] \right\} \quad (3.46a)$$

$$\mu = \frac{1}{2} \frac{m}{B(\mathbf{X})} [g_{ij}(\mathbf{x}) v^i v^j - v_{\parallel}^2] + \frac{q}{B(\mathbf{X})} [\Phi_E(\mathbf{x}) - \Phi_E(\mathbf{X})]. \quad (3.46b)$$

In magnetic fields relevant for tokamak and stellarator equilibria, the toroidal component of the vector potential is, up to a gauge choice, equal to the poloidal magnetic flux $A_{\phi} = -\Psi(\rho)$. Equations (3.46) are simplified by linearly expanding in gyro-radius, for example $A_{\phi}(\mathbf{x}) - A_{\phi}(\mathbf{X}) \approx -\boldsymbol{\rho}_L \cdot \nabla \Psi$ and $\Phi_E(\mathbf{x}) - \Phi_E(\mathbf{X}) \approx \boldsymbol{\rho}_L \cdot \nabla \Phi_E = -\boldsymbol{\rho}_L \cdot \mathbf{E}$.

Neither the energy nor the toroidal momentum of the particle can be seen to change on figure 3.9, as steps in \mathcal{H} and P_{ϕ} are instead due to switching from guiding-centre to particle coordinates.

3.6.2 From guiding-centre to particle variables

Changing from the guiding-centre to the particle phase-space is not as straight-forward, in the sense that the direction of $\boldsymbol{\rho}_L$ in the perpendicular plane to \mathbf{b} can be chosen arbitrarily. The motion of the guiding-centre does not depend on the initial angle around the guiding-centre, namely the gyro-angle, property known as *phase anholonomy* (Littlejohn, 1988). The question is then what is the simplest and most correct displacement to impose from the guiding-centre to the particle position and in what proportion v_{\parallel} and v_{\perp} must be set knowing that the magnetic field (and thus the projection of the particle's velocity) slightly differs from one position to the other. Rigorously, one would make sure that the average over a gyro-period recovers exactly the guiding-centre position but this is understandably very tedious.

Clearly, it is important that the energy of the guiding-centre and the energy of the particle match, thus fixing the modulus of \mathbf{v} , $v^2 = v_{\parallel}^2 + v_{\perp}^2$ is one step. It is then reasonable to assume that the ratio between parallel and perpendicular velocity, v_{\parallel} and v_{\perp} , is defined at the position of the guiding-centre \mathbf{X} via the guiding-centre velocity variables (μ and ρ_{\parallel}). The parallel velocity is then supported by the magnetic field at that position as

$$\mathbf{v}_{\parallel} = v_{\parallel} \frac{\mathbf{B}(\mathbf{X})}{B(\mathbf{X})} \iff v_{\parallel}^i = v_{\parallel} \frac{\mathbf{B}}{B} \cdot \nabla u^i = v_{\parallel} \frac{B^i}{B} \quad (3.47)$$

The perpendicular velocity can be seen as a combination of two orthogonal vectors perpendicular to $\mathbf{B}(\mathbf{X})$. Let s be the radial flux label of a generic flux coordinate system (s, u, v) , such that $\mathbf{B} \cdot \nabla s = 0$. Let the first vector be perpendicular to flux surfaces, namely

$$\mathbf{v}_{\perp\perp} = v_{\perp} \frac{\nabla s}{|\nabla s|} \iff v_{\perp\perp}^i = v_{\perp} \frac{g^{si}}{\sqrt{g^{ss}}}.$$

The second perpendicular velocity vector lies therefore within (tangent to) a flux surface, but

Chapter 3. Particle motion and guiding-centre drift

still perpendicular to the magnetic field,

$$\mathbf{v}_{\perp\parallel} = v_{\perp} \frac{\mathbf{B}}{B} \times \frac{\nabla s}{|\nabla s|} \iff \begin{cases} v_{\perp\parallel}^s = 0 \\ v_{\perp\parallel}^u = \frac{v_{\perp}}{\sqrt{g^{ss}}\sqrt{g}} \frac{B_v}{B} \\ v_{\perp\parallel}^v = -\frac{v_{\perp}}{\sqrt{g^{ss}}\sqrt{g}} \frac{B_u}{B} \end{cases} .$$

Combining $\mathbf{v}_{\perp\perp}$ and $\mathbf{v}_{\perp\parallel}$, the total perpendicular velocity is written generically as

$$\mathbf{v}_{\perp} = \mathbf{v}_{\perp\perp} \cos \alpha + \mathbf{v}_{\perp\parallel} \sin \alpha \quad (3.48)$$

where α is the gyro-angle extended to curvilinear coordinates. It is important to note that the velocity vector $\mathbf{v} = \mathbf{v}_{\parallel} + \mathbf{v}_{\perp}$, and therefore its components v^i , are constructed at the position of the guiding-centre \mathbf{X} . This is valid in the plasma rest frame where the gyro-averaged component of the electric field is zero.

The particle is shifted from the guiding-centre position using a vector proportional to the Larmor radius, $\mathbf{x} = \mathbf{X} + \boldsymbol{\rho}_L$, as

$$\boldsymbol{\rho}_L = \frac{m}{qB} \frac{\mathbf{B}}{B} \times \mathbf{v} = \frac{mv_{\perp}}{qB} \frac{\mathbf{B}}{B} \times \left(\frac{\nabla s}{|\nabla s|} \cos \alpha + \frac{\mathbf{B}}{B} \times \frac{\nabla s}{|\nabla s|} \sin \alpha \right) = \rho_L \left(-\frac{\nabla s}{|\nabla s|} \sin \alpha + \frac{\mathbf{B}}{B} \times \frac{\nabla s}{|\nabla s|} \cos \alpha \right). \quad (3.49)$$

Similarly to the transformation of particle to guiding-centre, it is recommended to do this displacement in Cartesian coordinates if the transformation from Cartesian to curvilinear coordinates is known (or if an inverse mapping or fast root finding algorithm is available). Otherwise, it helps to perform this operation in a pseudo-Cartesian coordinate system where the basis vectors are nearly unit vectors, and then invert back to curvilinear coordinates (see section 3.6.3). After this translation, the components of the velocity must be re-evaluated at the particle's position, thus respecting *parallel transport* of this vector

$$v^i(\mathbf{x}) = \mathbf{v} \cdot \nabla u^i(\mathbf{x}) = v^j(\mathbf{X}) \mathbf{e}_j(\mathbf{X}) \cdot \nabla u^i(\mathbf{x}) = \frac{\partial u^i}{\partial x^k} \bigg|_{\mathbf{x}} \frac{\partial x^k}{\partial u^j} \bigg|_{\mathbf{X}} v^j = [\Lambda^{-T}(\mathbf{x})\Lambda(\mathbf{X})]^i_j v^j(\mathbf{X}). \quad (3.50)$$

Process (3.50) guarantees that the particle's energy remains equal to that of the guiding-centre. Unfortunately, the translation slightly modifies the parallel and perpendicular projection of the particle's velocity due to the variations of the field (direction and amplitude). This is why the choice of gyro-angle in equation (3.48) can create a small discrepancy between full-orbit and guiding-centre trajectories.

For most toroidal MHD equilibrium plasmas, the dominant source of field variation appears from the gradient of the field strength. The gyro-angle can be automatically chosen such that the modulus of the magnetic field varies the least from the particle position to the guiding-centre position. The norm of the perpendicular velocity at both positions is nearly the same

$$v_{\perp}^2(\mathbf{X}) = \frac{2\mu}{m} B(\mathbf{X}) \approx \frac{2\mu}{m} B(\mathbf{x}) = v_{\perp}^2(\mathbf{x})$$

The same argument applied to $\mathcal{H}_{GC} = \frac{1}{2}mv_{\parallel}^2 + \mu B + q\Phi_E$ shows that the parallel velocity $v_{\parallel}^2(\mathbf{X}) \approx v_{\parallel}^2(\mathbf{x}) + q[\Phi_E(\mathbf{x}) - \Phi_E(\mathbf{X})]/2m$. To set the particle position, the Larmor radius vector $\boldsymbol{\rho}_L$ is thus chosen perpendicularly to ∇B

$$\mathbf{x} = \mathbf{X} + \boldsymbol{\rho}_L(\mathbf{X}) = \mathbf{X} \pm \rho_L \frac{\mathbf{B} \times \nabla B}{|\mathbf{B} \times \nabla B|} \Big|_{\mathbf{X}} \quad (3.51)$$

where $\rho_L = \sqrt{\frac{2}{B(\mathbf{X})} \frac{m}{q} \frac{\mu}{q}} \approx \sqrt{\frac{2}{B(\mathbf{x})} \frac{m}{q} \frac{\mu}{q}}$. With this prescription, the perpendicular velocity vector at the guiding-centre position is determined as

$$\mathbf{v}_{\perp}(\mathbf{X}) = \frac{q}{m} \boldsymbol{\rho}_L \times \mathbf{B}(\mathbf{X}) = v_{\perp} \frac{\nabla B - \mathbf{b}(\mathbf{b} \cdot \nabla B)}{|\mathbf{B} \times \nabla B|} \Big|_{\mathbf{X}}$$

The total velocity vector of the particle at the guiding-centre position is

$$\mathbf{v}(\mathbf{X}) = v_{\parallel}(\mathbf{X}) \mathbf{b}(\mathbf{X}) + \mathbf{v}_{\perp}(\mathbf{X}) \stackrel{!}{=} \mathbf{v}(\mathbf{x})$$

and is assumed to be the same at the particle position. In Cartesian coordinates, this means that the components of the velocity vector are equal at both locations. In curvilinear coordinates, these components must be re-evaluated by parallel transport because the basis vectors change as in equation (3.50). Notice that this procedure could be exploited to implement a general curvilinear Boris-Buneman integrator.

Ideally, this operation preserves the modulus of the velocity vector, $v^2 = g_{ij}(\mathbf{x})v^i(\mathbf{x})v^j(\mathbf{x}) = g_{ij}(\mathbf{X})v^i(\mathbf{X})v^j(\mathbf{X})$, and ensures that the particle's energy is defined equally to the guiding-centre's. Applying several coordinate transformations (matrix multiplications) is however sensitive to truncation error, as observed from the relative increase in energy in the bottom plot of figure 3.9.

Matching P_{ϕ} from the guiding-centre to the particle position is not enforced in this method. Depending on the field variation, the small induced discrepancy (see red dashed curve in bottom right plot of 3.9 and the top right plot showing secular motion in ρ) will accumulate over successive switches causing an artificial drift (minuscule change in the bounce tips position). This mismatch is much smaller than the action of Monte-Carlo operators in slowing-down simulations, as observed on figure 3.10, and is controlled by adjusting the switching threshold.

3.6.3 Small vector displacements in curvilinear coordinates

In Cartesian coordinates, $\mathbf{x} = \mathbf{X} + \boldsymbol{\rho}_L$ is simply written $x^i = X^i + \hat{\rho}_L^i$, where $\hat{\rho}_L^i$ are the Cartesian components of the Larmor radius vector. In curvilinear coordinates, the coordinates are formally written $u^i(\mathbf{x}) = u^i(\mathbf{X} + \boldsymbol{\rho}_L)$. This non-linear equation is solvable if the mapping from Cartesian to curvilinear coordinates is known. This mapping is not often provided and only the transformation from curvilinear to Cartesian is available. Then, one relies on root finding algorithms (slow) or linearisation (fast). For current applications, it is sufficient to expand at

lowest order in gyro-radius, i.e.

$$u^i(\mathbf{x}) = u^i(\mathbf{X}) + \boldsymbol{\rho}_L(\mathbf{X}) \cdot \nabla u^i + O(\rho_L^2) = u^i(\mathbf{X}) + \rho_L^i(\mathbf{X}) + O(\rho_L^2) \quad (3.52)$$

where $\rho_L^j = \boldsymbol{\rho}_L \cdot \nabla u^j$ are the components of the Larmor radius in curvilinear coordinates. From the general definition of gyro-angle (3.49), the coordinates of the position in the curvilinear system are expanded at first order as

$$\rho_L^i = \rho_L \left(-\frac{\nabla s}{|\nabla s|} \sin \alpha + \frac{\mathbf{B}}{B} \times \frac{\nabla s}{|\nabla s|} \cos \alpha \right) = \rho_L \left(-\frac{g^{si}}{\sqrt{g^{ss}}} \sin \alpha + \frac{\epsilon^{ijs}}{\sqrt{g}} \frac{B_j}{B} \frac{1}{\sqrt{g^{ss}}} \cos \alpha \right) \quad (3.53)$$

where right-hand side terms are evaluated at the guiding-centre position.

From prescription (3.51), those components are

$$\rho_L^i = \rho_L \frac{\mathbf{B} \times \nabla B}{|\mathbf{B} \times \nabla B|} \cdot \nabla u^i = \rho_L \frac{\epsilon^{ijk}}{\sqrt{g}} \frac{B_j}{B} \frac{\partial_k B}{N}$$

where

$$N = \sqrt{|\nabla B|^2 - (\mathbf{b} \cdot \nabla B)^2} = \sqrt{(\partial_m B) g^{mn} (\partial_n B) - (B^l \partial_l B)^2} / B^2$$

Flux coordinates are however singular near the magnetic axis and this expansion can lead to sensitive results when the norm of the basis vectors diverge. For this reason, it is preferable to linearise in a pseudo-Cartesian system. For example, if $u^1 = \rho$ is a radial flux label, $u^2 = u$ is a poloidal angle and $u^3 = v$ is a toroidal angle, the pseudo-Cartesian coordinates are defined

$$\begin{cases} \mathcal{X} = (R_0 + a\rho \cos u) \cos v \\ \mathcal{Y} = (R_0 + a\rho \cos u) \sin v \\ \mathcal{Z} = a\rho \sin u \end{cases} \quad (3.54)$$

where R_0 is the major radius and a the minor. Then, the small displacement is written in the pseudo-Cartesian system as

$$\mathcal{X}^i(\mathbf{x}) \approx \mathcal{X}^i(\mathbf{X}) + \boldsymbol{\rho}_L \cdot \nabla \mathcal{X}^i = \mathcal{X}^i(\mathbf{X}) + \rho_L^j(\mathbf{X}) \frac{\partial \mathcal{X}^i}{\partial u^j}$$

where the jacobian matrix $\frac{\partial \mathcal{X}^i}{\partial u^j}$ is easily obtained from (3.54) and $\rho_L^j = \boldsymbol{\rho}_L \cdot \nabla u^j$ are again the components of the Larmor radius in curvilinear coordinates (3.52). After this operation, the \mathcal{X}^i coordinates are easily inverted back to the original curvilinear coordinates.

3.7 Conclusions

This chapter mainly focuses on the equations of motion of charged particles in general magnetic fields. The strong relation between the topology of field-lines and particle orbits is illustrated with the use of curvilinear coordinates in both the full-orbit formulation and the

guiding-centre approach. Several choices of variables are proposed for deriving first-order GCDE. The resulting equations are proven to be algebraically identical. The parallel velocity is used as a pivot variable in the non-canonical guiding-centre Lagrangian, in which anisotropy and parallel perturbations can be (trivially) included. By studying analytic full-orbits in a simple example of purely sheared magnetic field, it was realised that the Baños drift term is missing in the first-order Lagrangian treatment of GCDE. This term appears to be important in low-aspect ratio devices, where the parallel current and shearing of field-lines can significantly contribute to the variation of the magnetic field at the scale of energetic ion Larmor radii. A criterion is proposed to map the regions with strong field variation. The importance of gradients, curvature and curl of \mathbf{B} is analysed for a few fusion devices, including JET, Wendelstein-7X (W7X) and MAST. A $0.27/B_0 R_0 \ll 1$ estimation is proposed for fusion alpha particles in large aspect ratio machines. The field variation criterion is used in VENUS-LEVIS to switch from guiding-centre to a full-orbit treatment of the particle motion. The difficulty of mapping a 4-dimensional to a 6-dimensional phase-space is addressed and the source of discrepancy is discussed.

4 VENUS-LEVIS and numerical methods

Numerical methods are indispensable to provide quantitative as well as realistic predictions of fast ion transport in fusion plasmas. Various orbit solving codes exist, each having advantages and limitations. Diversity is important in order to cover various aspects of fast ion dynamics.

One of the earliest guiding-centre codes is ORBIT (White and Chance, 1984). It pioneered guiding-centre theory and is still used to investigate fast ion motion in various devices as well as their interaction with MagnetoHydroDynamics (MHD) instabilities, especially Alfvén waves. The guiding-centre equations are expressed in canonical variables in order to benefit from the convenient representation of the magnetic equilibrium in Boozer coordinates (see section 2.3.3). Such formulation of the drift equations is intrinsically Hamiltonian, but only applies to nested flux-surface equilibria and small electromagnetic perturbations, which are constrained to the form $\delta\mathbf{A} = \alpha\mathbf{B}$, i.e. $\delta\mathbf{B} = \nabla \times (\alpha\mathbf{B})$, where \mathbf{B} is the magnetic field at equilibrium (for which $\alpha = 0$).

The drift orbit solver of the HAGIS code (Pinches et al., 1998) is similarly formulated in terms of Hamiltonian guiding-centre equations based on toroidally symmetric magnetic equilibria and Boozer coordinates. It additionally calculates the evolution of α via δf feedback of the particle distribution into a set of wave equations. It is extensively used for the study of fast ion interaction with Toroidal Alfvén Eigenmode (TAE).

Over the years, codes have been designed in order to keep up with research developments that consider non-axisymmetric magnetic configurations in tokamaks. The OFMC code (Tani et al., 2012) is a pioneer in the investigation of fast ion losses due to magnetic ripple, the error field from the test blanket modules (TBMs) and edge-localised mode (ELM) mitigation coils. The non-Hamiltonian formulation of its guiding-centre equations may be suitable for the study of supra-thermal populations (neutral beam injection) in conjunction with Monte-Carlo collision operators but potentially problematic in the case of highly energetic ions with large Larmor radii (α -particles).

The ASCOT code (Hirvijoki et al., 2012), which primarily focuses on fast particle losses and heat deposition on the wall of the vacuum vessel, reproduces the results of previously mentioned codes using non-canonical Lagrangian guiding-centre equations, derived for axisymmetric magnetic equilibria in straight field-line (Boozer) coordinates. In this case, the approach is identical to ORBIT or HAGIS. Time-dependent magnetic and electric perturbations are implemented here again via the parallel vector potential and electrostatic potential. Static Resonant Magnetic Perturbations (RMPs) have been studied by adding to the equilibrium the vacuum field generated by the external RMP current coils. Full-orbit equations are provided. Field quantities are interpolated and transformed to Cartesian coordinates using PSLINE techniques, originally suited for data smoothing. ASCOT's primary aim appears to be the

realistic modelling plasma facing components to calculate heat-loads from fast particles but, with a plasma model limited to axisymmetry, losses are only the result of external perturbations or ad-hoc MHD activity, which somewhat limits the realism of the approach.

Some codes just focus on solving full-Lorentz equations (exact solver, 6D phase-space), bypassing the issues related to guiding-centre formulations and the adiabatic expansion of magnetic moment. The major drawback of such codes is computational efficiency; their range of applicability is limited to specific problems, where the number of particles to track is not too high. CUEBIT (McKay et al., 2008) is an example of a full-orbit code that has been applied to heavy impurity transport in rotating plasmas using ad-hoc axisymmetric circular or Solov'ev analytic equilibria (Solov'ev, 1968) in cylindrical coordinates. The full-orbit code SPIRAL (Kramer et al., 2013) is used to quantitatively study a variety of fast ion phenomena in tokamaks. The axisymmetric equilibrium and vacuum fields are based on experimental measurements of the poloidal flux, reconstructed with EFIT (Lao et al., 1985). MHD activity is added via an interface with the linear resistive two-fluid code M3D-C1 (Jardin et al., 2008). Fast ion distribution profiles are imported from TRANSP/NUBEAM simulations (Pankin et al., 2004) and the effects of high harmonic fast wave heating is addressed. The pragmatic approach of SPIRAL depends on the precise evaluation of the electromagnetic fields and robust time-integration schemes via the NAG numerical libraries. It delivers quantitative results of fast ion losses and heat-loads on the plasma-facing components.

In this chapter, the development of the orbit code VENUS-LEVIS is detailed. VENUS-LEVIS was inspired by the VENUS code (Fischer et al., 2002), but has been redesigned and rewritten from scratch in FORTRAN 2003 in order to match modern performance, modularity and clarity criteria. Capable of addressing various phenomena related to fast particles, one of the main goals of the VENUS-LEVIS project is to reconcile methods from guiding-centre theory with full-orbit equations in general three-dimensional magnetic geometry, thus providing a versatile and flexible orbit solver. It is suited for the study of fast particles in tokamaks as well as in stellarator devices. The outcome of VENUS-LEVIS's runs is a self-consistent (Particle-In-Cell (PIC)) estimation of the saturated fast ion distribution, power deposition, losses and flux-averaged moments (fast ion density, pressure, current, etc.). It is typically used to study the impact of 3D global magnetic field configurations on fast ion losses, fast ion transport, power deposition from heating devices such as Neutral Beam Injection (NBI) or Ion Cyclotron Resonance Heating (ICRH).

4.1 Code description

VENUS-LEVIS excels at solving the trajectories of an ensemble of Klimontovich markers (Aydemir, 1994). The evolution of supra-thermal distributions is assessed by calculating moments of the distribution at regular intervals called diagnostic times, as depicted on figure 4.1. Between diagnostic times, particles are pushed in phase-space using general curvilinear coordinates Guiding-centre Drift Equations (GCDE) (3.12) or full-orbit equations (3.7). Although lower order schemes can be loaded, a fourth-order Runge-Kutta integrating scheme is generally used in both cases. An adaptative time-step is employed for simulations over long times (several slowing-down times), in order to focus numerical effort around the delicate regions of

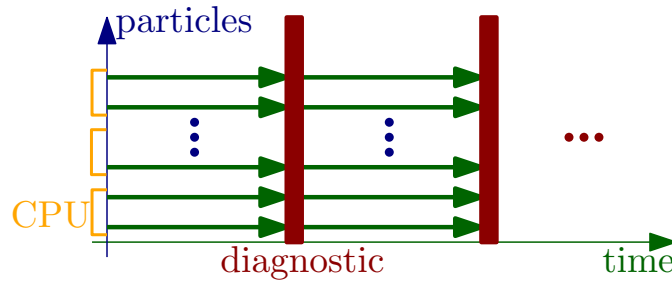


Figure 4.1 – Sketch of the steps carried out by VENUS-LEVIS. The code is trivially parallelised by letting each processor solve the dynamics of only a subgroup of markers.

the equilibrium, like near the magnetic axis, the internal boundary of a 3D kink displacement (see section 5.2) or near the last closed flux-surfaces of a confined plasma. For finer precision around those areas, the time-step dt is set inversely proportionally to the particle's velocity v (Kovanen and Core, 1993), proportionally to the guiding-centre phase-space Jacobian (denominator of equations of motion) $B_l W^{*l}$ as well as to the radial flux label s . The adaptive RK4 time-step is thus set as

$$dt = C \frac{s^\alpha}{v} B_l W^l = C \frac{s^\alpha}{v} \sqrt{g} B_l B^{*l}$$

where C is a control parameter and α some arbitrary power relaxing the dependency on s away from the magnetic axis (typically $\alpha = 1/4$). The varying time-step for full-orbit equations is usually set as a fraction of the gyro-period, $dt \propto qB/m$.

VENUS-LEVIS handles full 3D magnetic fields in arbitrary coordinate systems. This is a key advantage making it possible to import magnetic configurations from various MHD equilibrium codes, such as VMEC or ANIMEC or stability codes, such as TERPSICHORE (Anderson et al., 1990) or MINERVA (Aiba et al., 2009), or to represent analytic magnetic fields, such as Solov'ev equilibria, or arbitrary fields in plain Cartesian coordinates. The components of the electromagnetic field and the metric elements are controlled in separate modules such that the coordinate system is replaceable at compile time and the formulation stays general. The magnetic components and field representation used in VENUS-LEVIS are derived in section 2.3.3 and B.1.

The magnetic fields and properties of the background plasma remain fixed throughout a simulation. The influence of the background plasma over energetic particles is emulated via Monte-Carlo collision operators which account for both slowing down and pitch angle scattering phenomena, as described in section 4.5. At each time step, a series of kicks increment the particles energy and pitch-angle to reproduce Coulomb interaction with the background plasma.

The challenging task of following particles over long (slowing-down) timescales, while resolving the frequent crossing of particles through the magnetic axis and other difficult regions of the 3D equilibrium, has required the development of a robust interpolation scheme that produces a continuous representation of the fields. This unconventional scheme is based on cubic splines in the radial direction and Fourier reconstruction in the poloidal and toroidal di-

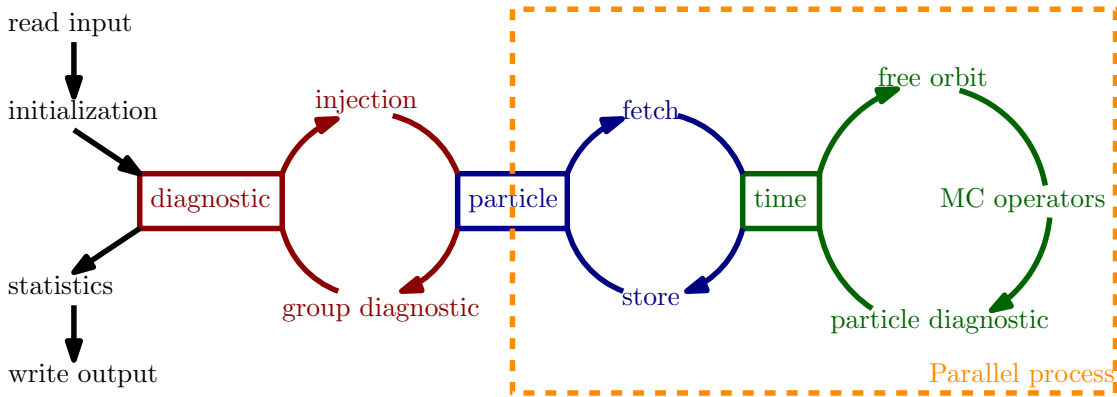


Figure 4.2 – VENUS-LEVIS flow chart

rection, most suited for equilibria generated by codes that minimise the poloidal and toroidal mode spectrum, such as VMEC (Hirshman and Whitson, 1983) or ANIMEC (Cooper et al., 2009). Proper boundary conditions must be imposed on the cubic splines in order to deal with the singular nature of the magnetic axis. This is especially important for non-axisymmetric configurations, where orbits naturally and periodically come close to the magnetic axis. The spline-Fourier method for computing derivatives makes the implementation in general curvilinear coordinates of both guiding-centre and full-orbit equations of motion convenient. The gain in accuracy is claimed to be worth the additional computer resources compared to faster algorithms, noting that the technique requires low amounts of memory.

The various steps carried out within a VENUS-LEVIS run are summarised on the flow-chart of figure 4.2.

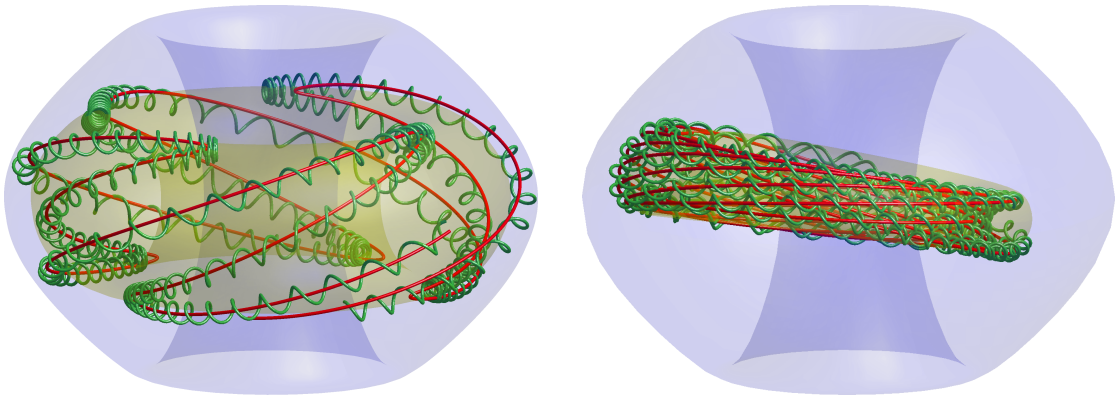
Figure 4.3(a) illustrates a full-orbit and guiding-centre motion computed with VENUS-LEVIS in the case of a trapped ion (banana orbit) in a typical axisymmetric equilibrium from VMEC. The equilibrium is based on MAST hybrid-like plasmas where the reversed q -profile has its minimum q_{min} close to unity¹. This setup is also the host of a 3D MHD equilibrium code solution known as the helical core (Cooper et al., 2011b) which has the characteristics of a saturated ideal internal kink. Figure 4.3(b) shows the orbit (full and guiding-centre) of a passing ion in this particular configuration, confined in the inner kinked region (depicted by the tilted flux surface in transparent yellow). To further illustrate the versatility of the formulation and its application to 3D magnetic configurations, figure 4.4 displays the orbit of a deeply trapped ${}^3\text{He}^{2+}$ ion heated by ICRH up to $\mathcal{H} = 1\text{MeV}$ in W7X stellarator².

In all these examples, VMEC native coordinates were used to represent the fields and to evolve the equations of motion.

In addition to the application to fast ion transport described in this thesis, it is mentioned that phenomena like runaway electrons can be investigated, thanks to the implementation of

¹Characteristic values of the toroidal magnetic field on the magnetic axis are $B_0 = 0.4\text{T}$, major radius $R_0 = 0.95\text{m}$, minor radius $a = 0.54\text{m}$ and $q_{min} \sim 1$ at $\rho_{min} \sim r/a = 0.435$.

²Characteristic values of the toroidal magnetic field on the magnetic axis are $B_0 = 2\text{T}$, major radius $R_0 = 10.9\text{m}$, minor radius $a = 0.6\text{m}$.



(a) Trapped (banana) D^+ ion at $\mathcal{H} = 10\text{KeV}$, $v_{0\parallel}/v = 0.55$, $\rho_0 = 0.7$ with a Larmor radius $\rho_{\perp} \approx 5.6\text{cm}$ in axisymmetric equilibrium.

(b) Passing D^+ ion at $\mathcal{H} = 10\text{KeV}$, $v_{0\parallel}/v = 0.6$, $\rho_0 = 0.22$ with a Larmor radius $\rho_{\perp} \approx 4.1\text{cm}$ in helically kinked core equilibrium.

Figure 4.3 – Orbits computed by VENUS-LEVIS in Mega-Ampère Spherical Tokamak (MAST) equilibria using the guiding-centre equations (red) and full-orbit equations (green). Blue transparent surface represents the axisymmetric last closed flux-surface of the considered MAST equilibrium. Yellow transparent surface is the 3D flux-surface at the average radial position of the particle.

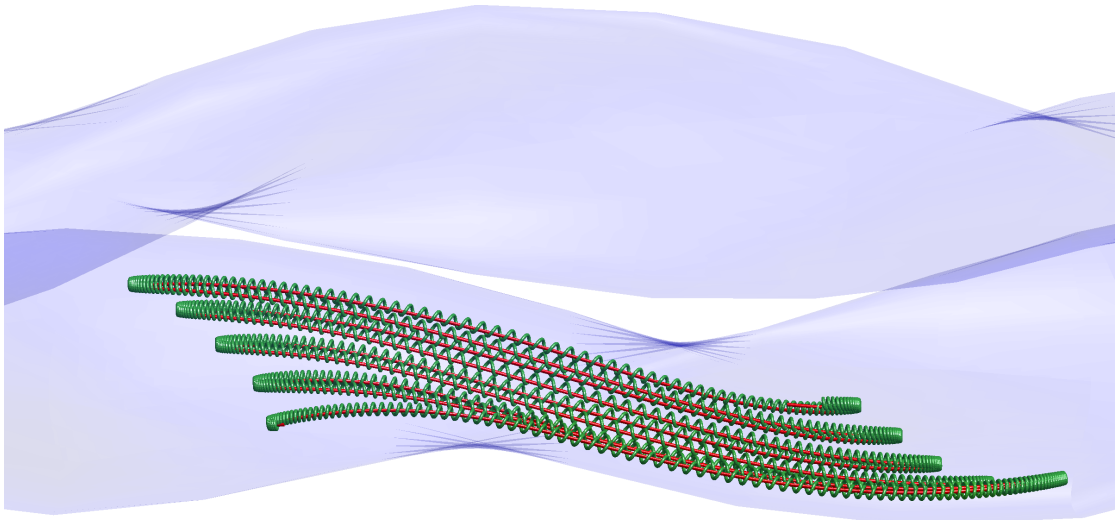


Figure 4.4 – Deeply-trapped ${}^3\text{He}^{2+}$ at $\mathcal{H} = 1\text{MeV}$, $v_{0\parallel}/v = 0.05$, $\rho_0 = 0.6$ with a Larmor radius $\rho_{\perp} \approx 6.2\text{cm}$. Guiding-centre calculation in red and full-orbit in green. Blue transparent surface represents the last closed flux-surface of W7X stellarator equilibrium.

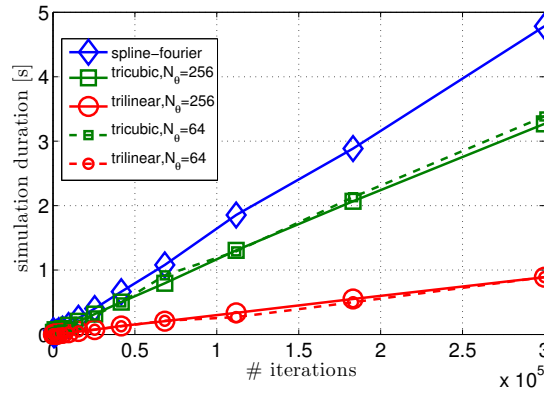


Figure 4.5 – Duration of a given particle simulation based on an axisymmetric equilibrium from ANIMEC (11 poloidal modes) using different interpolation techniques as a function of the number of time steps.

relativistic guiding-centre equations (C.16-C.17). Anomalous transport is also modelled with another set of Monte-Carlo operators built in VENUS-LEVIS (Albergante et al., 2012).

4.2 Spline-Fourier interpolation

Solving the motion of charged particles requires the precise evaluation of the electromagnetic field and derivatives along its trajectory. For realistic and experimentally relevant simulations, the magnetic structure is provided by an MHD equilibrium code, in our case VMEC/ANIMEC, TERPSICHOE (Boozer representation) or MINERVA, as a series of scalars on a finite number of grid points. In most codes, fast and simple schemes are deployed over large 3D meshes (tri-linear, tri-cubic, p-splines, etc. . .) but the accuracy of those finite element techniques is rather limited. Smoothness of the equations of motion is crucial, especially in 3D equilibria, for simulations over long timescales with the intention of obtaining saturated NBI or alpha populations (typically $\sim 10^7$ bounce periods or half a million gyro-turns), or else numerical error rapidly accumulates and ruins the convergence properties of the time-integration. Hereafter, a convenient scheme is proposed, automatically guaranteeing continuity and analyticity of the fields as well as their derivatives, regardless of the number of grid points. It is a combination of cubic splines in the radial direction and Fourier modes in the poloidal and toroidal directions. A reason for this choice is that most equilibrium codes readily deliver a decomposition in sine and cosine functions for the toroidal and poloidal angles of the equilibrium flux surfaces, as well as all components (covariant and contravariant) of the magnetic field. VMEC/ANIMEC, in particular, yields a minimum Fourier spectrum representing the MHD magnetic equilibrium studied (typically ~ 12 modes for axisymmetric cases, ~ 130 modes for 3D cases). Recomposing the field quantities at every time-step - an a priori computationally expensive task - actually protects the order of the integration scheme. In conjunction with a high-order integrator (RK4 or better), the spline-Fourier technique competes well against faster and more economical solutions in terms of precision versus Computer Processing Unit (CPU)-time. Figure 4.5 shows that it is half the speed of tri-linear interpolation and takes just 20% more time than tri-cubic interpolation in the case of an axisymmetric equilibrium.

The spline-Fourier technique occupies far less computer memory than other mesh-based techniques, for which the poloidal and toroidal directions are discretised using a massive amount of grid points only to obtain comparable precision. Derivatives represent additional fields to store in memory when using mesh-based techniques, while they are automatically produced with a single spline-Fourier field. A low memory imprint is useful on super-computing machines where many processors communally share the memory of a single node. The spline-Fourier technique might even be appealing for Graphics Processing Unit (GPU) implementations. On the down side, the number of operations per iteration grows proportionally to the number of modes used, such that, in the case of 3D magnetic fields, it effectively becomes 10 to 15 times slower than tri-linear interpolation. Nevertheless, the precision acquired of the computed trajectories is worth the extra CPU time. Conservation properties, e.g. equations (3.19-3.20) and (3.8-3.9), are degraded by the imprecision involved in numerical time-integration, by data interpolation and ultimately by floating-point errors. Unlike mesh-based techniques, the accuracy of the spline-Fourier interpolation technique is independent of the number of grid points or the number of modes, as seen on figure 4.6. By virtue of the fourth order Runge-Kutta scheme, orbits satisfy conservation of energy and toroidal momentum at a convergence rate equal to the fourth power of the fixed time-step. While tri-linear and tri-cubic methods saturate (horizontal lines in figure 4.6) because the number of available grid points is fixed, the spline-Fourier technique reaches machine precision, limited by floating-point errors. By reducing the number of poloidal grid points by a factor four, the saturation point of tri-linear or tri-cubic methods rises by at least an order of magnitude. A similar loss of precision is observed when reducing the number of radial grid points. To reach the convergence properties of the spline-Fourier technique with finite-difference methods in the case of 3D fields, the mesh has to be so fine that the limiting factor is the available amount of CPU memory. The trend on super-computing machines is to increase the number of processors per node but not necessarily providing more memory. These mesh-based techniques appear less suited for those newer architectures.

4.2.1 Fourier recomposition

In a more detailed description of the spline-Fourier scheme, let the variables (s, u, v) define the coordinate system where $s = \Phi/\Phi_{\text{edge}} \approx r^2/a^2$ is the radial variable proportional to the toroidal magnetic flux, u is a poloidal angle and v is the geometric toroidal angle. Any quantity $Y(s, u, v)$ from VMEC/ANIMEC, TERPSICHORE or MINERVA is expressed either as³

$$Y = \sum_{m,n} Y_{mn}(s) \cos(mu - nv) \quad \text{or} \quad Y = \sum_{m,n} Y_{mn}(s) \sin(mu - nv).$$

To speed up the Fourier reconstruction, instead of calling the implicit cosine or sine functions for each m, n couple (computationally expensive), the list of $\cos(mu - nv)$ and $\sin(mu - nv)$ is generated by consecutive multiplication of unity in the complex plane by e^{iu} and e^{-iv} , then

³For simplicity, stellarator symmetry is considered here such that quantities are either purely cosine or purely sine functions. It is straightforward to relax this condition.

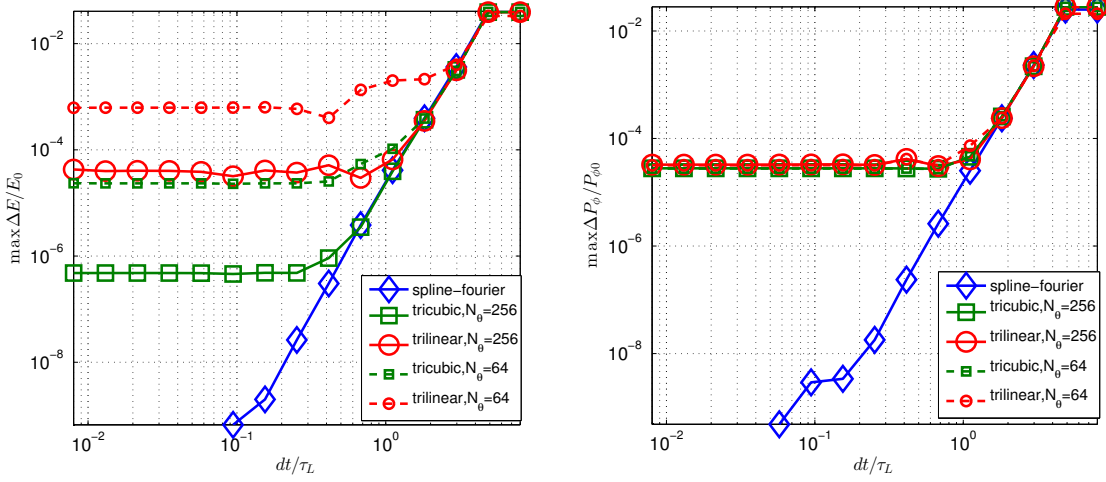


Figure 4.6 – Convergence study of a trapped ion at $\mathcal{H} = 30$ KeV, $v_{\parallel}/v = 0.7$, $\rho_0 = 0.74$ with Larmor radius $\rho_{\perp} \approx 5.4$ cm evolved for $t = 3 \cdot 10^{-4}$ s, using different interpolation routines. The time-step dt is normalised to the gyro-period τ_L . (left) maximum relative energy variation $\Delta E/E_0 = |1 - E/E_0|$. (right) maximum relative toroidal momentum variation $\Delta P_{\phi}/P_{\phi 0} = |1 - P_{\phi}/P_{\phi 0}|$. The tri-linear and tri-cubic mesh involved 288 radial times 256/64 poloidal grid points multiplied by 3 to include derivatives, whereas spline-Fourier required 288×4 radial coefficients times 11 modes.

taking the real part for cosine, respectively the imaginary part for sine. For example,

$$\cos(mu - nv) = \text{Re} \left[\underbrace{e^{iu} \dots e^{iu}}_{m \times} \underbrace{e^{-iv} \dots e^{-iv}}_{n \times} \right] \quad (4.1)$$

Since multiplication comes with a small floating-point error, the cumulative error increases proportionally to the mode number, as depicted on figure 4.7(a). Therefore, this fast multiplication technique is used if the number of modes to reconstruct is low (< 100). The obtained speed-up is between 1.5 and 2 as shown on figure 4.7(b).

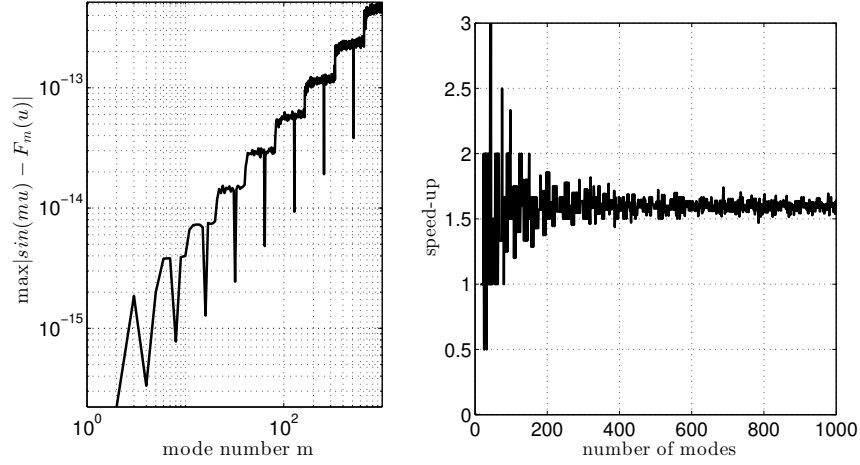
Thanks to Fourier reconstruction, derivatives along u or v are analytic operations. For example, if Y is a cosine based function, its first derivative along the poloidal direction is reconstructed as

$$\frac{\partial Y}{\partial u} = - \sum_{m,n} m Y_{mn} \sin(mu - nv).$$

Derivatives along the toroidal direction and higher-order derivatives have similar expressions. These expressions are crucial to yield smooth and continuous guiding-centre or full-orbit equations, where derivatives appear in the calculation of metric elements or field curvature and gradients.

4.2.2 Radial cubic splines

The radial direction in ANIMEC is discretised on a linear grid in flux label $\{s_i\}_{i=1, N_s}$ and only a finite number of Fourier coefficients $\{Y_{mn,i}\}$ are known. Cubic splines are used to ensure



(a) Error appearing after consecutive multiplication of a root cosine function instead of direct evaluation on a 16 digit machine precision. Maximum error is taken over evaluation of 10^4 random numbers between 0 and 2π .

(b) Speed-up factor (ratio between CPU time) using fast multiplication method instead of hard-coded cosine function as a function of the number of modes in the Fourier series.

Figure 4.7 – Properties of the fast multiplication scheme.

analyticity and continuity of functions $Y_{mn}(s)$. This choice over higher or lower order interpolation methods is justified by the fact that the equations of motion contain, at worst, second derivatives; cubic splines happen to be *globally* continuous functions up to second derivatives. Other methods of interpolation using a reduced number of grid-points (linear, quadratic, cubic, Bézier, polynomial, etc...) are continuous only on portions of the mesh, such that moving from one segment to the next triggers spurious discontinuities in first and second derivatives.

In defining cubic splines, each discretised Fourier coefficient is represented by a collection of $N_s - 1$ third-degree polynomials. For interval $s \in [s_i, s_{i+1}]$,

$$Y_{mn}(s) = P_{mn,i}(s) = A_{mn,i} + B_{mn,i}(s - s_i) + C_{mn,i}(s - s_i)^2 + D_{mn,i}(s - s_i)^3. \quad (4.2)$$

By virtue of this formulation, derivatives in s are exact, i.e. they are provided by (mn indices are dropped for simplicity hereafter):

$$\frac{dY}{ds}(s) = P'_i(s) = B_i + 2C_i(s - s_i) + 3D_i(s - s_i)^2 \quad \frac{d^2Y}{ds^2}(s) = P''_i(s) = 2C_i + 6D_i(s - s_i).$$

Coefficients A_i , B_i , C_i and D_i are uniquely defined via the following linear system of equations

$$P_i(s_i) = Y_i \quad P_i(s_{i+1}) = Y_{i+1} \quad P'_i(s_{i+1}) = P'_{i+1}(s_{i+1}) \quad P''_i(s_i) = P''_{i-1}(s_i) \quad (4.3)$$

This requirement essentially means that those splines, as well as their first and second derivatives, are continuous functions from one interval to the next, ensuring that the equations of motion are continuous and smooth throughout the radial direction. The spreading of

numerical error is thus minimised and longer orbit simulations are made possible.

In order to solve the linear system above, it is practical to define $t = \frac{s-s_i}{s_{i+1}-s_i}$ and express the cubic polynomial in its symmetric form, i.e.

$$P_i(s) = Q_i(t) = (1-t)Y_i + tY_{i+1} + t(1-t)[(1-t)a_i + tb_i]$$

which trivially satisfies the first and second conditions of (4.3), $Q_i(0) = P_i(s_i) = Y_i$ and $Q_i(1) = P_i(s_{i+1}) = Y_{i+1}$. The third condition of (4.3) is automatically respected if, for $k_i \equiv P'_i(s_i)$,

$$\begin{cases} k_i = \frac{Y_{i+1}-Y_i+a_i}{s_{i+1}-s_i} \\ k_{i+1} = \frac{Y_{i+1}-Y_i-b_i}{s_{i+1}-s_i} \end{cases} \iff \begin{cases} a_i = k_i\Delta_{i+\frac{1}{2}} - \delta_{i+\frac{1}{2}} \\ b_i = -k_{i+1}\Delta_{i+\frac{1}{2}} + \delta_{i+\frac{1}{2}} \end{cases}$$

where $\Delta_{i+\frac{1}{2}} = s_{i+1} - s_i$ and $\delta_{i+\frac{1}{2}} = Y_{i+1} - Y_i$ were defined⁴. Finally, the condition of second derivative continuity, last of (4.3), yields a linear system of equations for coefficients $\{k_i\}_{i=1, N_s}$

$$\frac{k_{i-1}}{\Delta_{i-\frac{1}{2}}} + 2\left(\frac{1}{\Delta_{i-\frac{1}{2}}} + \frac{1}{\Delta_{i+\frac{1}{2}}}\right)k_i + \frac{k_{i+1}}{\Delta_{i+\frac{1}{2}}} = 3\left(\frac{\delta_{i-\frac{1}{2}}}{\Delta_{i-\frac{1}{2}}^2} + \frac{\delta_{i+\frac{1}{2}}}{\Delta_{i+\frac{1}{2}}^2}\right). \quad (4.4)$$

This system is self-consistent (closed) when boundary conditions are prescribed, of which various choices are discussed in the next section 4.2.3. The linear system (4.4) is visualised as a matrix multiplication, $M\vec{k} = \vec{v}$, where M is a tri-diagonal symmetric matrix, with diagonal elements $\{d_i\}_{i=1, N_s}$ and upper-diagonal and lower-diagonal elements $\{u_i\}_{i=1, N_s-1}$,

$$d_i = 2\left(\Delta_{i-\frac{1}{2}}^{-1} + \Delta_{i+\frac{1}{2}}^{-1}\right) \quad u_i = \Delta_{i+\frac{1}{2}}^{-1} \quad v_i = 3\left(\delta_{i-\frac{1}{2}}\Delta_{i-\frac{1}{2}}^{-2} + \delta_{i+\frac{1}{2}}\Delta_{i+\frac{1}{2}}^{-2}\right)$$

The desired coefficients are obtained by inverting M , i.e. $\vec{k} = M^{-1}\vec{v}$. This task is performed in $O(N_s)$ steps with the so-called Thomas algorithm (see Thomas, 1949). The original polynomial coefficients of equation (4.2) are finally recovered using the following relations

$$A_i = Y_i \quad B_i = k_i \quad C_i = \frac{3\delta_{i+\frac{1}{2}} - (k_{i+1} + 2k_i)\Delta_{i+\frac{1}{2}}}{\Delta_{i+\frac{1}{2}}^2} \quad D_i = \frac{(k_{i+1} + k_i)\Delta_{i+\frac{1}{2}} - 2\delta_{i+\frac{1}{2}}}{\Delta_{i+\frac{1}{2}}^3}.$$

Notice that, for equally-spaced grid points, $\Delta_{i+\frac{1}{2}} = \Delta$, the matrix elements, as well as the Thomas algorithm, are somewhat simpler.

4.2.3 Spline boundary conditions

Various boundary conditions can be imposed on the linear system (4.4), thus providing distinct physical constraints.

⁴The $\frac{1}{2}$ notation highlights the direction of the difference, which is convenient when it comes to applying parity transformations.

Plasma boundary: The so-called *natural* or *free-end* condition is applied at the last-closed flux-surface ($s_{N_s} = 1$), for which the second derivative is set to zero $P''_{N_s-1}(s_{N_s} = 1) = 0$, yielding

$$d_{N_s} = 2\Delta_{N_s-\frac{1}{2}}^{-1} \qquad v_{N_s} = 3\delta_{N_s-\frac{1}{2}}\Delta_{N_s-\frac{1}{2}}^{-2}$$

Magnetic axis: The choice of boundary conditions for the magnetic axis is critical because it is a singular point in toroidal coordinates. Also, in 3D configurations, particle orbits can often cross its path. The boundary condition must respect the fact that, at $s = 0$, no fields depend on the poloidal angle. Therefore modes with $m \neq 0$ are set to zero on the axis. Additionally, imagining that the radial direction continues to negative values as if the poloidal angle was flipped by 180 degrees, modes with $m = 0$ are even functions of s , and modes with $m \neq 0$ odd. Boundary conditions for even/odd functions must reflect the fact that, if the positive grid points were duplicated onto the negative side (yielding double the amount of grid points $\{s_i\}_{i=-N_s, \dots, N_s}$ with $s_{-i} = -s_i$), the spline would pass through $Y_{-i} = \pm Y_i$. It is seen hereafter that there is no need to double the number of points; oddness or evenness can be ensured with a specific set of boundary conditions.

Under the so-called parity transformation ($i \rightarrow -i$), coefficients are altered as

$$\Delta_{-i+\frac{1}{2}} = s_{-i+1} - s_{-i} = -s_{i-1} + s_i = \Delta_{i-\frac{1}{2}} \qquad \delta_{-i+\frac{1}{2}} = Y_{-i+1} - Y_{-i} = \pm(Y_{i-1} - Y_i) = \mp\delta_{i-\frac{1}{2}}$$

which, in matrix language, means that the parity operator P , acting on M and \vec{v} , possesses the properties that $PM = MP$ and $P\vec{v} = \mp\vec{v}$. It is therefore concluded that \vec{k} transforms under parity as⁵

$$P\vec{k} = PM^{-1}\vec{v} = M^{-1}P\vec{v} = \mp M^{-1}\vec{v} = \mp\vec{k}.$$

Since $k_{-i} = \mp k_i$, the negative axis is redundant and the system can be solved on the positive axis only.

In the case where the first grid point $s_0 = 0$ ($\Delta_{\frac{1}{2}} = s_1$), odd boundary conditions are similar to the *natural* condition in that the second derivative is zero (inflection point), whereas even boundary conditions imply that the first derivative is zero and the function has an extremum on the magnetic axis. This statement is summarised in the following table:

even ($s_0 = 0$)	odd ($s_0 = 0$)
$k_0 = 0, u_0 = 0$	$Y_0 = 0$
$d_1 = 2(s_1^{-1} + \Delta_{\frac{3}{2}}^{-1})$	$d_0 = \frac{2}{s_1}$
$v_1 = 3\left(\delta_{\frac{1}{2}}s_1^{-2} + \delta_{\frac{3}{2}}\Delta_{\frac{3}{2}}^{-2}\right)$	$v_0 = 3\frac{Y_1}{s_1^2}$

These conditions are referred to as *full-mesh* axis boundary conditions.

If the first positive grid point s_1 is not on the magnetic axis, then $s_0 = -s_1$, $\Delta_{\frac{1}{2}} = 2s_1$, $\delta_{\frac{1}{2}} = Y_1 \mp Y_1$ and the table of axis boundary conditions becomes:

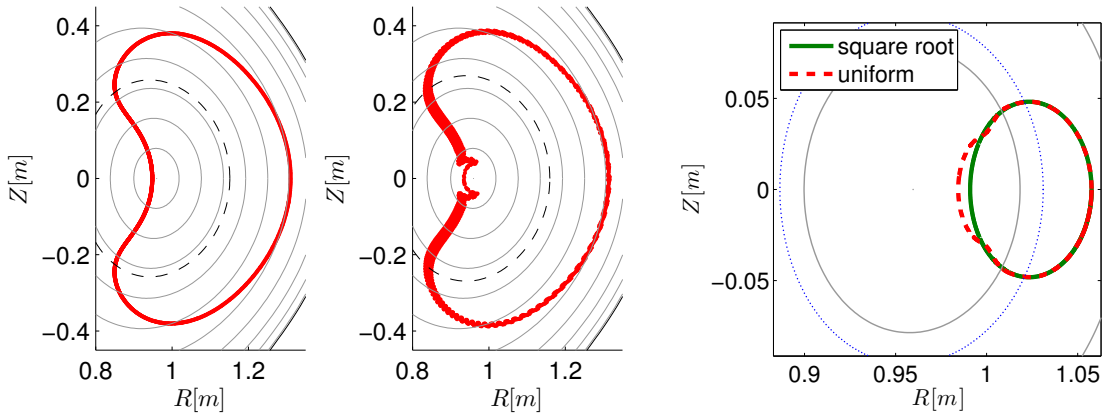
⁵This could have been deduced from the fact that the derivative of an even/odd function is odd/even.

even ($s_1 \neq 0$)	odd ($s_1 \neq 0$)
$d_1 = \frac{1}{2} s_1^{-1} + 2\Delta_{\frac{3}{2}}^{-1}$	$d_1 = \frac{3}{2} s_1^{-1} + 2\Delta_{\frac{3}{2}}^{-1}$
$v_1 = 3\delta_{\frac{3}{2}} \Delta_{\frac{3}{2}}^{-2}$	$v_1 = 3 \left(\frac{Y_1}{2s_1^2} + \delta_{\frac{3}{2}} \Delta_{\frac{3}{2}}^{-2} \right)$

These conditions are referred to as *half-mesh* axis boundary conditions. In practice, with half-mesh splines, one extra negative grid point is included, so that interpolation in the interval between $-s_1$ and s_1 is made possible. This extra segment satisfies $k_0 = \mp k_1$ and its spline coefficients are given by

even ($s_0 = -s_1$)	odd ($s_0 = -s_1$)
$A_0 = A_1$	$A_0 = -A_1$
$B_0 = -B_1$	$B_0 = B_1$
$C_0 = \frac{B_1}{2s_1}$	$C_0 = \frac{3}{2s_1} \left(\frac{A_1}{s_1} - B_1 \right)$
$D_0 = 0$	$D_0 = \frac{1}{2s_1^2} \left(B_1 - \frac{A_1}{s_1} \right) = -\frac{C_0}{3s_1}$

Figure 4.8(a) illustrates the relevance of boundary conditions for particles skirting the magnetic axis, where the correct half-mesh boundary conditions (left-hand side of figure 4.8(a)) were exchanged with full-mesh ones (right-hand side of figure 4.8(a)). With the wrong boundary conditions, the motion of this H^+ ion describing a potato orbit looks rather unphysical in the vicinity of the magnetic axis. Such a particle would end up on vastly incorrect orbit if it were deflected by a collision during its passage near the magnetic axis.



(a) Boundary conditions impacting the potato orbit of an H^+ ion at $\mathcal{H} = 50$ KeV, $v_{||}/v = 0.6$, $\rho_0 = 0.59$ with Larmor radius $\rho_{\perp} = 7.7$ cm. On the left, the correct half-mesh boundary conditions are being used and on the right, erroneous full-mesh boundary conditions.

(b) Effect of basing cubic splines on different grids for potato trajectories close to the magnetic axis. In the case of uniform grid in flux (in dashed red), a spurious wobble appears because the singular terms of the equations of motion are poorly represented by cubic functions.

Figure 4.8 – Effect of boundary conditions and grid substitution on particle orbits skirting the singular magnetic axis

4.2.4 Grid substitution

As mentioned previously, the radial variable is proportional to the magnetic flux, i.e. proportional to the square of minor radius $s \sim r^2/a^2$. Consequently, when approaching the magnetic axis, the coordinate system becomes singular and induces divergent terms, for example in $R(s, u) \approx R_{\text{major}} + R_{\text{minor}}\sqrt{s}\cos u$, $\partial_s R \propto 1/\sqrt{s}$. Cubic splines based on a uniform grid in s will poorly represent these divergences. It is advised to make $1/\sqrt{s}$ terms appear explicitly. This is done by constructing the splines over an alternate grid defined by some function $w(s)$, such that

$$P_i(s) = A_i + B_i [w(s) - w(s_i)] + C_i [w(s) - w(s_i)]^2 + D_i [w(s) - w(s_i)]^3 = Q_i(w)$$

and derivatives become

$$P'_i(s) = \frac{dQ_i}{dw} \frac{dw}{ds} = [B_i + 2C_i(w - w_i) + 3D_i(w - w_i)^2] w'(s).$$

Choosing an equidistant grid on an axis scaled by $w(s) = \sqrt{s}$ is convenient because derivatives of $Q_i(w)$ splines are now regular functions in s as the singular part is supplemented by $w'(s) = 1/(2\sqrt{s})$. By virtue of this trick, inertial forces in the equations of motion due to the polar-like coordinate system have the correct behaviour when particles come close to the magnetic axis, as seen on figure 4.8(b).

4.2.5 Interpolated integrals

The integral of flux quantities is often required, e.g. for computing the vector potential \mathbf{A} , entering in the definition of toroidal momentum $P_\phi \sim A_\phi = -\Psi$, as in equations (3.20) or (3.9). Compared to other finite element techniques, integrating cubic splines is a straightforward analytic operation, which preserves continuity and smoothness throughout the radial direction. Without continuous integrals, implicit conservation properties (energy and toroidal momentum conservation in time-independent axisymmetric cases) of the equations of motion are concealed.

Spline integrals are split into two parts,

$$\int_{s_1}^s Y(s') ds' = \int_{s_1}^{s_i} Y(s') ds' + \int_{s_i}^s P_i(s') ds' = \sum_{j < i} I_j + \int_{s_i}^s P_i(s') ds'$$

The first part is progressively recorded at the construction of the spline as an extra coefficient

I_i for each interval⁶. The second integral is expressed as

$$\begin{aligned} \int_{s_i}^s P_i(s') ds' &= (A_i - B_i w_i + C_i w_i^2 - D_i w_i^3) (s - s_i) \\ &+ (B_i - 2C_i w_i + 3D_i w_i^2) \int_{s_i}^s w(s') ds' \\ &+ (C_i - 3D_i w_i) \int_{s_i}^s w^2(s') ds' \\ &+ D_i \int_{s_i}^s w^3(s') ds' \end{aligned}$$

where the various integrals involving powers of $w(s)$ are prescribed functions.

4.3 External fields (vacuum fields)

In addition to equilibrium fields, arbitrary perturbations can be included in the total magnetic field of VENUS-LEVIS. The external magnetic field $\delta \mathbf{B}$ is algebraically added to the equilibrium \mathbf{B}_{eq} such that the total magnetic field is $\mathbf{B} = \mathbf{B}_{eq} + \delta \mathbf{B}$. The perturbed field is handled in an independent module and can be provided in a different coordinate system, e.g. cylindrical coordinates. The components are then transformed to curvilinear coordinates and added to the equations of motion (3.12), which entails computing the covariant and contravariant components of $\delta \mathbf{B}$, i.e. δB^i and δB_i , as well as derivatives like $\partial_j(\delta B_i)$ and $\partial_j(\delta B^i)$. In both curvilinear representations, the total magnetic field becomes the sum of the equilibrium and external field as

$$B^i = B_{eq}^i + \delta B^i \quad B_i = B_{eq,i} + \delta B_i \quad B = \sqrt{B^i B_i} \quad (4.5a)$$

$$\partial_j B = \frac{1}{2B} \partial_j B^2 = \frac{1}{2B} (B_i \partial_j B^i + B^i \partial_j B_i) \quad [\nabla \times \delta \mathbf{B}]^k = \frac{\epsilon^{ijk}}{\sqrt{g}} \partial_i (\delta B_j) \quad (4.5b)$$

The modulus of the magnetic field B in equation (4.5a) involves the quadratic contraction of the equilibrium plus external field, so do ∇B terms in equation (4.5b). This way of making the external field appear in B as well as in ∇B ensures that the equations of motion are exact, even for arbitrarily large perturbations. This is more rigorous than other methods, where those quantities are assumed to emanate only from the equilibrium magnetic field.

An application of the external field module is the study of fast particle losses due to resonant magnetic perturbations (RMPs). The latter are purposely induced magnetic fields, produced by external current coils, in order to mitigate instabilities near the edge of the plasma known as edge-localised modes (Edge Localised Mode (ELM)s). Although RMPs have been proven to be beneficial (Evans et al., 2006), they could also be responsible for deteriorating fast particle confinement and enhancing hot ion losses (Garcia-Munoz et al., 2013b). By forcing a 3D magnetic structure upon the plasma, RMPs spoil tokamak axisymmetry at the boundary, producing magnetic islands and stochastic regions. However, the plasma responds by partially

⁶It is assumed that the integral is zero on the first grid point, i.e. $I_1 = 0$

absorbing the RMP field (screening). Consistent modelling of the interaction between RMP and plasma involving screening, edge turbulence, magnetic reconnection and other physics has been attempted and compared in various codes (Turnbull, 2012). In VENUS-LEVIS, the external field module is used to include the vacuum RMPs. The complete discussion of RMPs is left to the later chapter 6.

The vacuum magnetic field created by the RMP coils is computed in a program called `Coil.Spell` (Cooper et al., 2004). This code solves the Biot-Savart law on a mesh, integrating the contribution of each filament with current I_C for every coil C (Miyamoto, 1989, section 2.3d)

$$\delta \mathbf{B}(\mathbf{r}) = \frac{\mu_0}{4\pi} \sum_C I_C \int_C \frac{d\mathbf{l} \times (\mathbf{r} - \mathbf{r}')}{|\mathbf{r} - \mathbf{r}'|^3} = \sum_C \sum_{i=1}^{N_C} \Delta \mathbf{B}_{Ci}(\mathbf{r}) \quad (4.6)$$

where $d\mathbf{l}$ is an infinitesimal displacement along the filament at position \mathbf{r}' and $\Delta \mathbf{B}_{Ci}$ is the magnetic field produced by the straight segment i (delimited by points \mathbf{x}_i and \mathbf{x}_{i+1}) of the closed current loop C

$$\Delta \mathbf{B}_{Ci} = \frac{\mu_0 I_C}{4\pi} \frac{\mathbf{s}_i \times \mathbf{r}_i}{|\mathbf{s}_i \times \mathbf{r}_i|} \int \frac{\sin \theta}{R^2} dl = \frac{\mu_0 I_C}{4\pi r_i \sin \theta_i} (\cos \theta_i - \cos \theta'_i) \frac{\mathbf{s}_i \times \mathbf{r}_i}{|\mathbf{s}_i \times \mathbf{r}_i|} \quad (4.7)$$

where $\mathbf{r}_i = \mathbf{r} - \mathbf{x}_i$ and $\mathbf{s}_i = \mathbf{x}_{i+1} - \mathbf{x}_i$, $\cos \theta_i = \mathbf{s}_i \cdot \mathbf{r}_i / (|\mathbf{s}_i| |\mathbf{r}_i|)$ and $\cos \theta'_i = \mathbf{s}_i \cdot \mathbf{r}_{i+1} / (|\mathbf{s}_i| |\mathbf{r}_{i+1}|)$.

The raw RMP magnetic field $\delta \mathbf{B}$ is provided on a 3D cylindrical mesh in orthonormal cylindrical coordinates. Tri-cubic interpolation (Lekien and Marsden, 2005) is applied to the data in order to yield a smooth and continuous representation of the components of the RMP field as well as its derivatives at any given R , Z and ϕ position

$$\delta \mathbf{B} = \widehat{\delta B}^R \hat{\mathbf{e}}_R + \widehat{\delta B}^Z \hat{\mathbf{e}}_Z + \widehat{\delta B}^\phi \hat{\mathbf{e}}_\phi \quad (4.8)$$

where $\hat{\mathbf{e}}_M$ are the orthonormal vectors forming the cylindrical basis. The components of each field are ultimately expressed in VMEC's flux coordinate system (s, u, v) , where $s = \Phi / \Phi_e$ is the radial variable proportional to the toroidal magnetic flux Φ (Φ_e is its value on the last closed flux-surface), u the poloidal angle and $v = \phi$ the geometric toroidal angle. Converting the components of $\delta \mathbf{B}$ from orthonormal cylindrical to flux coordinates relies on the knowledge of $R(s, u, v)$ and $Z(s, u, v)$, which are extracted from VMEC's output and interpolated in VENUS-LEVIS using the dedicated spline-Fourier scheme. The method to transform the vacuum fields into flux coordinates is

$$\delta B^i = [\Lambda^{-1}]^i_j \widehat{\delta B}^j \quad \delta B_i = \Lambda^j_i \widehat{\delta B}_j \quad \Lambda = \begin{pmatrix} \frac{\partial R}{\partial s} & \frac{\partial R}{\partial u} & \frac{\partial R}{\partial v} \\ \frac{\partial Z}{\partial s} & \frac{\partial Z}{\partial u} & \frac{\partial Z}{\partial v} \\ 0 & 0 & R \end{pmatrix} \quad (4.9)$$

It is straight-forward to find analytic expressions for the derivatives of the matrix Λ , as well as the derivatives of $\widehat{\delta B}^{(R,Z,\phi)}$ such that it is possible to represent all quantities listed in equations (4.5b) avoiding the use of finite differences thus preserving precision and smoothness. The divergence-free condition for the vacuum RMP field is respected in cylindrical coordinates with a maximum discrepancy of $\nabla \cdot \mathbf{B} \sim 10^{-5}$ [T/m] on the last closed flux-surface, closest to

the coils. This error is barely affected by the component transformation and is small compared to the effect of Monte-Carlo collision operators on particle transport. The evaluation of these metric elements would not have been tractable without the spline-Fourier interpolation routine described in section 4.2.

4.4 Neutral Beam Injection module

The source of markers for NBI simulations is calculated externally to VENUS-LEVIS with the help of a pre-existing set of Matlab routines (Albergante, 2011). Code development was required to make them compatible with 3D fields. It was also necessary to implement a fast and robust algorithm to map Cartesian coordinates to flux coordinates. The methods behind the NBI module are fairly straight-forward and are briefly mentioned in this section.

First, the user prescribes the characteristics of the NBI Positive Ion Neutral Injectors (PINIs) or uses preset values for the following list of fusion devices: International Thermonuclear Experimental Reactor (ITER), DEMO, ASDEX, Tokamak à Configuration Variable (TCV), MAST, Joint European Torus (JET), TFTR, DIII-D, Textor. The information required is: number of PINIs, starting and end points of the NBI beam, energies and fractions of the injected neutrals, charge and mass ratios, surface of the PINIs (surface of emission) and angle for the beam spread. One beam-line per PINI is traced across the magnetic equilibrium and subdivided in many small segments that are verified to remain within the plasma boundaries. The position of these segments are mapped from Cartesian coordinates into flux-coordinates using a dedicated C++ subcode called `inverse2Dmap` (Pfefferlé and Albergante, 2015). The value of the background density and temperature are interpolated from experimental profiles (flux functions). The profiles are used in the following ionisation equation to estimate the number of neutrals still in the beam

$$N_b(l) = N_b(0) e^{-\int_0^l n_e \sigma_{\text{eff}} dl'}$$

where l is the length along the beam-line from the entry point of the plasma, n_e the electron density, σ_{eff} the ionisation/stopping cross-section. Markers are then evenly distributed along the beam-line and assigned a weight proportional to the ionisation rate dN_b/dl . Finally, a random perpendicular deviation is set for each marker in order to account for beam spread. The velocity is projected on the magnetic field so that only the energy E and the pitch-variable $\lambda = v_{\parallel}/v$ are recorded for each marker.

4.5 Monte-Carlo collision operators

To settle a factor 2 problem in previous work (Albergante, 2011, section 4.3 and references therein), the Monte-Carlo collision operators of VENUS-LEVIS is rederived in detail from Fokker-Planck equations. The variation in time of the hot particle distribution function f_α due to Coulomb collisions against multiple species f_β is generically expressed as the divergence of

a collisional current as

$$\frac{df_\alpha}{dt} = \frac{\delta f_\alpha}{\delta t} \Big|_{coll} = \sum_\beta C[f_\alpha, f_\beta] = - \sum_\beta \frac{\partial}{\partial \mathbf{v}} \cdot \mathbf{J}^{\alpha/\beta}.$$

In the rest frame of the plasma, the distribution functions of the background species are assumed Maxwellian

$$f_\beta = n_\beta \left(\frac{m_\beta}{2\pi T_\beta} \right)^{3/2} e^{-\frac{m_\beta v^2}{2T_\beta}} = \frac{n_\beta}{\sqrt{\pi^3} v_\beta^3} e^{-\frac{v^2}{v_\beta^2}} \quad T_\beta = \frac{1}{2} m_\beta v_\beta^2.$$

In this case, the collisional current can be shown to reduce to (NRL Plasma Formulary, 2009, p.35)

$$\mathbf{J}^{\alpha/\beta} = -\frac{\mu_{\alpha\beta}}{m_\beta} v_s^{\alpha/\beta} \mathbf{v} f_\alpha - \frac{1}{2} v_{\parallel}^{\alpha/\beta} \mathbf{v} \left(\mathbf{v} \cdot \frac{\partial f_\alpha}{\partial \mathbf{v}} \right) - \frac{1}{4} v_{\perp}^{\alpha/\beta} (v^2 \mathbf{I} - \mathbf{v}\mathbf{v}) \cdot \frac{\partial f_\alpha}{\partial \mathbf{v}} \quad (4.10)$$

where $\mu_{\alpha\beta} = m_\alpha m_\beta / (m_\alpha + m_\beta)$ is the reduced mass and the collision frequencies are given by (NRL Plasma Formulary, 2009, p.31)

$$v_0^{\alpha/\beta} = \frac{Z_\alpha^2 Z_\beta^2 e^4 \ln \Lambda}{4\pi \epsilon_0^2} \frac{n_\beta}{m_\alpha^2 v^3} = c_{\alpha\beta} \frac{n_\beta}{m_\alpha^2 v^3} \quad (4.11a)$$

$$v_s^{\alpha/\beta} = \frac{m_\alpha}{\mu_{\alpha\beta}} \psi(x^{\alpha/\beta}) v_0^{\alpha/\beta} \quad (4.11b)$$

$$v_{\perp}^{\alpha/\beta} = 2 \left(\psi + \psi' - \frac{\psi}{2x^{\alpha/\beta}} \right) v_0^{\alpha/\beta} \quad (4.11c)$$

$$v_{\parallel}^{\alpha/\beta} = \frac{\psi}{x^{\alpha/\beta}} v_0^{\alpha/\beta} \quad (4.11d)$$

and $x^{\alpha/\beta} = \frac{v^2}{v_\beta^2} = \frac{m_\beta v^2}{2T_\beta}$, $Z_{\alpha,\beta}$ is the number of charges, e the electric charge, $\ln \Lambda$ the Coulomb logarithm, ϵ_0 the vacuum permittivity and

$$\psi(x) = \frac{2}{\sqrt{\pi}} \int_0^x dt \sqrt{t} e^{-t} \quad \psi' = \frac{d\psi}{dx} = \frac{2\sqrt{x}}{\sqrt{\pi}} e^{-x}. \quad (4.12)$$

The ψ function is determined in terms of the error function Φ as

$$\psi(x) + \psi'(x) = \frac{2}{\pi} \int_0^x \frac{dt}{\sqrt{t}} e^{-t} = \frac{2}{\sqrt{\pi}} \int_0^{\sqrt{x}} e^{-y^2} dy = \Phi(\sqrt{x}), \quad \sqrt{x} \frac{d\Phi}{d\sqrt{x}} = \frac{d\psi}{dx} \quad (4.13a)$$

$$\Psi(\sqrt{x}) = \frac{\psi(x)}{2x}, \quad \Psi(z) = \frac{\Phi - z\Phi'}{2z^2} \quad (4.13b)$$

where the special function Ψ was defined in anticipation of its later appearance in the final collision operator.

By using spherical velocity coordinates $\mathbf{v} = v \hat{\mathbf{e}}_v$, the collision operator simplifies after pursuing

the following intermediate steps,

$$\begin{aligned}\frac{\partial}{\partial \mathbf{v}} v(v) &= \frac{\partial v}{\partial v} \frac{\partial v}{\partial \mathbf{v}} = \frac{\partial v}{\partial \mathbf{v}} \mathbf{v} \\ \frac{\partial}{\partial \mathbf{v}} \cdot (v_s \mathbf{v} f_\alpha) &= \frac{1}{v^2} \frac{\partial}{\partial v} (v^3 v_s f_\alpha) \\ \frac{\partial}{\partial \mathbf{v}} \cdot \left[v_{\parallel} \mathbf{v} \left(\mathbf{v} \cdot \frac{\partial f_\alpha}{\partial \mathbf{v}} \right) \right] &= \frac{\partial}{\partial v} \cdot \left(v_{\parallel} v \mathbf{v} \frac{\partial f_\alpha}{\partial v} \right) = \frac{1}{v^2} \frac{\partial}{\partial v} \left(v^4 v_{\parallel} \frac{\partial f_\alpha}{\partial v} \right) \\ \frac{\partial}{\partial \mathbf{v}} \cdot \left[v_{\perp} (v^2 \mathbf{I} - \mathbf{v} \mathbf{v}) \cdot \frac{\partial f_\alpha}{\partial \mathbf{v}} \right] &= \frac{\partial v_{\perp}}{\partial v} \mathbf{v} \cdot (v^2 \mathbf{I} - \mathbf{v} \mathbf{v}) \cdot \frac{\partial f_\alpha}{\partial \mathbf{v}} + v_{\perp} \frac{\partial}{\partial v} \cdot \left[(v^2 \mathbf{I} - \mathbf{v} \mathbf{v}) \cdot \frac{\partial f_\alpha}{\partial \mathbf{v}} \right].\end{aligned}$$

The right term of the last equation is identified as the Lorentz collision operator \mathcal{L}_C , conveniently expressed as a function of the pitch-variable $\lambda = v_{\parallel}/v$ and the gyro-phase ξ as

$$\mathcal{L}_C = \frac{1}{2} \frac{\partial}{\partial \mathbf{v}} \cdot \left[(v^2 \mathbf{I} - \mathbf{v} \mathbf{v}) \cdot \frac{\partial}{\partial \mathbf{v}} \right] = \frac{1}{2} \left[\frac{\partial}{\partial \lambda} (1 - \lambda^2) \frac{\partial}{\partial \lambda} + \frac{1}{1 - \lambda^2} \frac{\partial^2}{\partial \xi^2} \right]. \quad (4.14)$$

The second term of (4.14) is dropped invoking gyro-phase invariance of the distribution functions. Collecting all the pieces, the collision operator against Maxwellian species becomes

$$C[f_\alpha, f_\beta] = \frac{1}{2} v_{\perp}^{\alpha/\beta} \mathcal{L}_C f_\alpha + \frac{1}{v^2} \frac{\partial}{\partial v} \left[v^3 \left(\frac{\mu_{\alpha\beta}}{m_\beta} v_s^{\alpha/\beta} f_\alpha + \frac{1}{2} v_{\parallel}^{\alpha/\beta} v \frac{\partial f_\alpha}{\partial v} \right) \right] \quad (4.15a)$$

$$= v_{\lambda}^{\alpha/\beta} \mathcal{L}_C f_\alpha + \frac{1}{v^2} \frac{\partial}{\partial v} \left[v^2 v_E^{\alpha/\beta} \left(v f_\alpha + \frac{T_\beta}{m_\alpha} \frac{\partial f_\alpha}{\partial v} \right) \right] \quad (4.15b)$$

where the pitch-variable and energy frequencies are defined as

$$v_{\lambda}^{\alpha/\beta} = \frac{c_{\alpha\beta} n_\beta}{m_\alpha^2 v^3} \left(\psi + \psi' - \frac{\psi}{2x^{\alpha/\beta}} \right) = \frac{c_{\alpha\beta} n_\beta}{m_\alpha^2 v^3} \left[\Phi \left(\frac{v}{v_\beta} \right) - \Psi \left(\frac{v}{v_\beta} \right) \right] \quad (4.16a)$$

$$v_E^{\alpha/\beta} = \frac{c_{\alpha\beta} n_\beta}{m_\alpha m_\beta v^3} \psi = \frac{c_{\alpha\beta} n_\beta}{m_\alpha T_\beta v} \Psi \left(\frac{v}{v_\beta} \right). \quad (4.16b)$$

The form of equation (4.15b) and the frequencies of equation (4.16) are consistent with the derivation by Boozer and Kuo-Petravic (1981).

The two terms in (4.15b) can be considered separately to construct the Monte-Carlo pitch-angle scattering and slowing-down scheme. We first focus on the random kicks on the pitch-variable. The moments of a generic function $g(\lambda)$ are expressed as

$$\langle g \rangle = \int_{-1}^1 g(\lambda) f_\alpha d\lambda.$$

By rewriting the Lorentz collision operator ($v_{\lambda}^{\alpha/\beta}$ is independent of λ) as

$$\frac{\delta f_\alpha}{\delta t} \Big|_{\lambda} = \sum_{\beta} v_{\lambda}^{\alpha/\beta} \mathcal{L}_C f_\alpha = \sum_{\beta} \left\{ \frac{\partial}{\partial \lambda} \left(v_{\lambda}^{\alpha/\beta} \lambda f_\alpha \right) + \frac{1}{2} \frac{\partial^2}{\partial \lambda^2} \left[v_{\lambda}^{\alpha/\beta} (1 - \lambda^2) f_\alpha \right] \right\},$$

the full time-derivative of $\langle g \rangle$ is easily expressed after integrating by parts as

$$\frac{d}{dt} \langle g \rangle = \sum_{\beta} v_{\lambda}^{\alpha/\beta} \left[- \langle \frac{dg}{d\lambda} \lambda \rangle + \frac{1}{2} \langle \frac{d^2g}{d\lambda^2} (1 - \lambda^2) \rangle \right].$$

The average effect of collisions on $g(\lambda) = \lambda$ is thus found to be

$$\frac{d \langle \lambda \rangle}{dt} = - \sum_{\beta} v_{\lambda}^{\alpha/\beta} \langle \lambda \rangle$$

and on the standard deviation $g(\lambda) = \lambda^2$

$$\frac{d \langle \lambda^2 \rangle}{dt} = \sum_{\beta} v_{\lambda}^{\alpha/\beta} (1 - 3 \langle \lambda^2 \rangle) \quad \frac{d\sigma^2}{dt} = \frac{d}{dt} (\langle \lambda^2 \rangle - \langle \lambda \rangle^2) = \sum_{\beta} v_{\lambda}^{\alpha/\beta} (1 - \langle \lambda^2 \rangle).$$

As in the work by Boozer and Kuo-Petravic (1981), this knowledge is used to construct the random pitch-angle scattering and slowing-down increments of λ (final result below).

Focusing now on the energy term of the collision operator, the moments from a generic function $k(v) = K(E)$, where $E = \frac{1}{2} m_{\alpha} v^2$, are

$$\langle K \rangle = \int_0^{\infty} k(v) f_{\alpha} 4\pi v^2 dv.$$

Noticing that $dE/dv = m_{\alpha} v$, the energy collision operator is written in the following convenient form in order to compute various moments

$$\left. \frac{\delta f_{\alpha}}{\delta t} \right|_{\beta, E} = \frac{1}{v^2} \frac{\partial}{\partial v} \left\{ v^2 f_{\alpha} \left[v_E^{\alpha/\beta} v \left(1 - \frac{T_{\beta}}{v_E^{\alpha/\beta}} \frac{dv_E^{\alpha/\beta}}{dE} \right) - 2 \frac{v_E^{\alpha/\beta} T_{\beta}}{m_{\alpha} v} \right] \right\} + \frac{1}{v^2} \frac{\partial^2}{\partial v^2} \left[v^2 f_{\alpha} \frac{T_{\beta}}{m_{\alpha}} v_E^{\alpha/\beta} \right]$$

so that the full time-derivative of $\langle K \rangle$ becomes

$$\frac{d}{dt} \langle K \rangle = \sum_{\beta} \left[- \langle \frac{dk}{dv} v_E v \left(1 - T_{\beta} \frac{d \ln v_E^{\alpha/\beta}}{dE} \right) \rangle + 2 \langle \frac{dk}{dv} \frac{v_E^{\alpha/\beta} T_{\beta}}{m_{\alpha} v} \rangle + \langle \frac{d^2 k}{dv^2} \frac{v_E^{\alpha/\beta} T_{\beta}}{m_{\alpha}} \rangle \right].$$

Concerning the effect of collisions on $K(E) = E$,

$$\begin{aligned} \frac{d \langle E \rangle}{dt} &= \sum_{\beta} \left[- \langle m v^2 v_E^{\alpha/\beta} \left(1 - T_{\beta} \frac{d \ln v_E^{\alpha/\beta}}{dE} \right) \rangle + 2 T_{\beta} \langle v_E^{\alpha/\beta} \rangle + T_{\beta} \langle v_E^{\alpha/\beta} \rangle \right] \\ &= - \langle \sum_{\beta} 2 v_E^{\alpha/\beta} \left[E - \left(\frac{3}{2} + \frac{E}{v_E^{\alpha/\beta}} \frac{dv_E^{\alpha/\beta}}{dE} \right) T_{\beta} \right] \rangle. \end{aligned}$$

Assuming that $f_{\alpha} \propto \delta(E - E_0)$ is a delta-function for each marker, the time-variation of the mean energy simplifies to

$$\frac{\delta E_0}{\delta t} = - \sum_{\beta} 2 v_E^{\alpha/\beta} \left[E_0 - \left(\frac{3}{2} + \frac{E_0}{v_E^{\alpha/\beta}} \frac{dv_E^{\alpha/\beta}}{dE} \right) T_{\beta} \right].$$

where $v_E^{\alpha/\beta}$ and $dv_E^{\alpha/\beta}/dE$ are evaluated at E_0 .

Noticing that $dE^2/dv = m^2 v^3$ and $d^2E^2/dv^2 = 3m^2 v^2$, the variation of $K(E) = E^2$ is

$$\frac{d\langle E^2 \rangle}{dt} = \sum_{\beta} \left[-\langle 4E^2 v_E^{\alpha/\beta} \left(1 - T_{\beta} \frac{d \ln v_E^{\alpha/\beta}}{dE} \right) \rangle + 10 T_{\beta} \langle E v_E^{\alpha/\beta} \rangle \right].$$

The standard deviation thus becomes

$$\frac{d\sigma^2}{dt} = \frac{d}{dt} (\langle E^2 \rangle - \langle E \rangle^2) = 4 \sum_{\beta} v_E^{\alpha/\beta} T_{\beta} E_0$$

Finally, the effective Monte-Carlo kicks on numerical marker α are constructed as

$$\Delta\lambda = - \sum_{\beta} v_{\lambda}^{\alpha/\beta} \lambda \Delta t + \mathcal{R}_{\lambda} \sqrt{(1 - \lambda^2) \sum_{\beta} v_{\lambda}^{\alpha/\beta} \Delta t} \quad (4.17)$$

$$\Delta E = - \sum_{\beta} 2v_E^{\alpha/\beta} \Delta t \left[E - \left(\frac{3}{2} + \frac{E}{v_E^{\alpha/\beta}} \frac{dv_E^{\alpha/\beta}}{dE} \right) T_{\beta} \right] + 2\mathcal{R}_E \sqrt{\sum_{\beta} v_E^{\alpha/\beta} T_{\beta} E \Delta t} \quad (4.18)$$

where $\mathcal{R}_{\lambda,E} = \pm 1$ are random plus or minus signs and Δt is the minimum time-step among characteristic collisional times $\tau = 1/\nu$ and the RK4 time-step.

The resulting Monte-Carlo scheme is the same as in the ASCOT code (Hirvijoki et al., 2012). Hirvijoki et al. (2013) have recently found a more consistent formulation of the guiding-centre collision operators. Future work will include these new results in VENUS-LEVIS.

4.6 MAST neutron camera synthetic diagnostic

A virtual diagnostic of MAST neutron camera is implemented in VENUS-LEVIS in order to compare simulations of fast ions with experimental measurements. This virtual diagnostic is detailed in this section because it plays a role in section 5.3.1 where simulated fast ion redistribution patterns in MAST Long-Lived Modes (LLMs) are compared against neutron camera signals.

The neutron camera system collects neutrons emitted from the plasma due to fusion reactions. The advantage of this experimental diagnostic is that it captures processes only triggered by fast particles, thus yielding a representative measure of the fast particle density. A lead collimator makes its field of view comparable to a narrow cone, pointing through the plasma at mid-plane (see figure 4.9). At every point in space, there is a small probability that fast particles undergo fusion processes and produce neutrons. This probability is estimated via well tabulated fusion cross-sections, as explained hereafter. Assuming that neutrons are emitted isotropically from fusion processes (valid in the centre of mass of the colliding ions, but assumed in the lab frame), the number of neutrons pointing towards the detector is proportional to the neutron production rate $dR/dV(\mathbf{x})$, i.e. the number of neutrons produced per seconds in volume dV . The signal of the detector ε is the sum over the field of view of

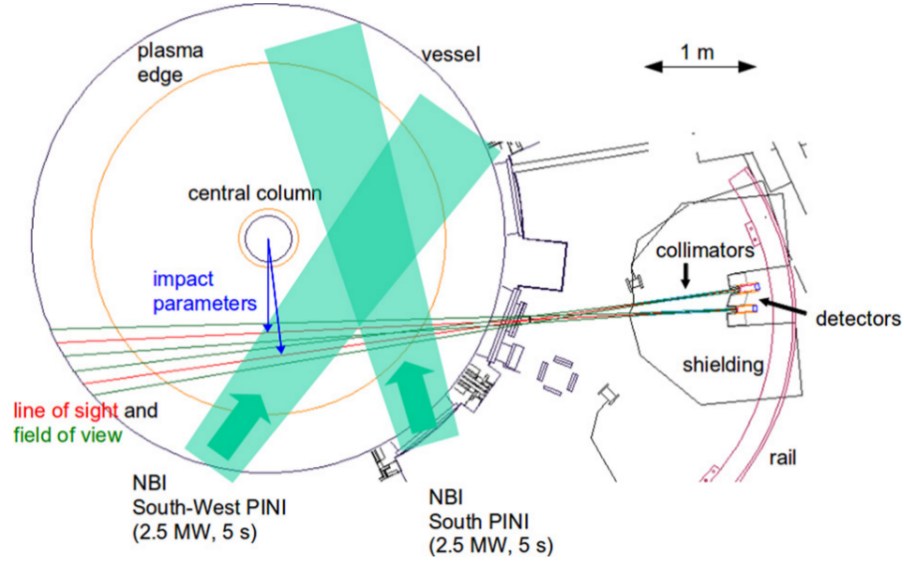


Figure 4.9 – Mid-plane cut of MAST showing the geometry of the lines-of-sight (red lines) and the field of view (green limiting lines) of the neutron camera diagnostic. Courtesy of Cecconello et al. (2012).

the produced neutrons. Because of the small opening, the signal is approximated as the line integral of the neutron production rate times the detector's surface. This quantity depends on the impact parameter b which represents the minimal distance between the line-of-sight and cylindrical axis (blue arrows on figure 4.9). For an arbitrary choice of axis where the line of sight is along the y direction, the signal is roughly proportional to

$$\varepsilon(b) \propto \int_{\text{FoV}} G(\mathbf{x}) \frac{dR}{dV} dV \approx S_{\text{NC}} \int dy \frac{dR}{dV}(b, y, 0) = 2S_{\text{NC}} \int_b^{R_{\text{max}}} \frac{dR}{dV}(b, \sqrt{r^2 - b^2}, 0) \frac{r dr}{\sqrt{r^2 - b^2}}$$

where $G(\mathbf{x})$ is the solid angle of the neutron detector seen at \mathbf{x} , S_{NC} the surface of the detector and R_{max} the maximum radius of the plasma.

In fact, the precise evaluation of the neutron camera signal based on the production rate is performed with the LINE2 code (Cecconello et al., 2010). This code takes into account the exact geometry of the field of view and sensitivity of the detector and produces better results than the coarse estimation of $\varepsilon(b)$ above.

4.6.1 Neutron production rate or emissivity in VENUS-LEVIS

Neutron emissivity is computed at diagnostic time for each marker of the fast ion distribution, for which fusion reactions between fast particles and the background plasma are taken into account. Assuming a beam-on-target process, the fusion rate per unit volume is equal to the reactants' densities times the process's reactivity (Miley and Towner, 1975)

$$\frac{dR}{dV}(\mathbf{x}) = \sum_{t,b} n_t(\mathbf{x}) n_b(\mathbf{x}) \langle \sigma v \rangle_{bt} \quad (4.19)$$

where the reactivity between beam species b and target species t is the sum over all configurations at a given position \mathbf{x}

$$\langle \sigma v \rangle_{bt}(\mathbf{x}) = \iint d\mathbf{v}_b^3 d\mathbf{v}_t^3 f_t(\mathbf{x}, \mathbf{v}_t) f_b(\mathbf{x}, \mathbf{v}_b) |\mathbf{v}_t - \mathbf{v}_b| \sigma_{bt}(|\mathbf{v}_t - \mathbf{v}_b|). \quad (4.20)$$

In equation (4.20), f_b is the beam distribution function, f_t the target distribution function and σ_{bt} the fusion cross-section between reactants b and t . The background plasma constitutes the target reactants and the fast ion population the beam reactants. The fusion cross-sections are experimentally tabulated functions, for which various parametrisations exist. In the range of energies from keVs to a few MeVs, an accurate parametrisation is given by Bosch and Hale (1992) as

$$\sigma_{bt}(|\mathbf{v}_t - \mathbf{v}_b|) = \frac{S(E_{cm})}{E_{cm}} e^{-\frac{B_G}{\sqrt{E_{cm}}}} \quad (4.21)$$

where $E_{cm} = \frac{\mu}{2} v^2$ is the energy in the centre of mass, $v = |\mathbf{v}_t - \mathbf{v}_b|$ the norm of the relative velocity, $\mu = \left(\frac{1}{m_b} + \frac{1}{m_t}\right)^{-1} = \frac{m_b m_t}{m_b + m_t}$ the reduced mass, $B_G = \pi \alpha Z_b Z_t \sqrt{2\mu c^2}$ the so-called Gamov constant, $\alpha \approx 1/137$ the fine-structure constant, c the speed of light, Z the reactants' charge and

$$S(E) = \frac{A_1 + E(A_2 + E(A_3 + E(A_4 + EA_5)))}{1 + E(B_1 + E(B_2 + E(B_3 + EB_4)))} \quad (4.22)$$

the astrophysical factor expressed as a Pade fraction of polynomials. The Pade coefficients A_i and B_i of relevant fusion reactions are gathered in table 4.1. It was not possible to find the exact parametrisation of the reaction $T + T \rightarrow {}^4\text{He} + 2n$ in the literature but only linear approximations (Mikkelsen, 1989) or a logarithmic polynomial (Slaughter, 1983), valid for a smaller range of energies. For the study of deuterium NBI, this reaction is irrelevant and none of the presented results depend on its use. The astrophysical factor $S(E)$ for various

	$D + T \rightarrow \alpha + n$	$D + D \rightarrow T + p$	$D + D \rightarrow {}^3\text{He} + n$	${}^3\text{He} + D \rightarrow \alpha + p$
B_G [$\sqrt{\text{keV}}$]	34.3827	31.397	31.397	68.7508
A_1	$6.927 \cdot 10^4$	$5.557 \cdot 10^4$	$5.3701 \cdot 10^4$	$5.7501 \cdot 10^6$
A_2	$7.454 \cdot 10^8$	$2.1054 \cdot 10^2$	$3.3027 \cdot 10^2$	$2.5266 \cdot 10^3$
A_3	$2.05 \cdot 10^6$	$-3.2638 \cdot 10^{-2}$	$-1.2706 \cdot 10^{-1}$	$4.5566 \cdot 10^1$
A_4	$5.2002 \cdot 10^4$	$1.4987 \cdot 10^{-6}$	$2.9327 \cdot 10^{-5}$	0
A_5	0	$1.8181 \cdot 10^{-10}$	$-2.5151 \cdot 10^{-9}$	0
B_1	$6.38 \cdot 10^1$	0	0	$-3.1995 \cdot 10^{-3}$
B_2	$-9.95 \cdot 10^{-1}$	0	0	$-8.553 \cdot 10^{-6}$
B_3	$6.981 \cdot 10^{-5}$	0	0	$5.9014 \cdot 10^{-8}$
B_4	$1.728 \cdot 10^{-4}$	0	0	0

Table 4.1 – Gamov constant B_G and Pade coefficients A_i , B_i parametrising the astrophysical factor of equation (4.22) for E in keV of various fusion reactions so that the cross-section of equation (4.21) is in units of millibarn (10^{-31}m^2). Courtesy of Bosch and Hale (1992).

fusion processes is displayed on figure 4.10(a) and the resulting cross sections (probability) on figure 4.10(b). Among those fusion reactions, those that produce neutrons are of interest for

4.6. MAST neutron camera synthetic diagnostic

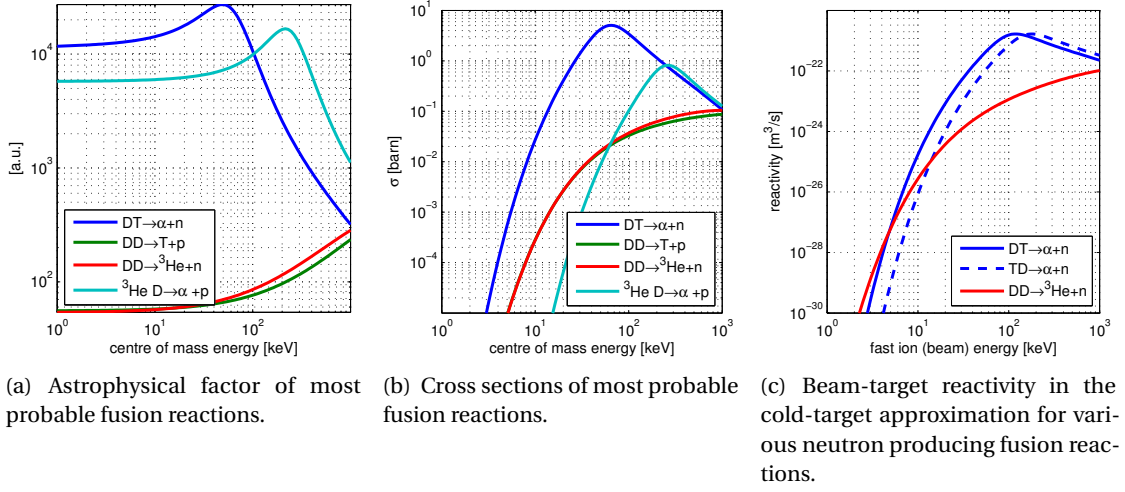


Figure 4.10 – Astrophysical factor, cross-section and beam-target reactivity as a function of the energy of the centre of mass.

the virtual diagnostic, i.e.



In our PIC simulations, the background target is considered as a Maxwellian distribution with temperature $T_{th}(\mathbf{x})$, and the beam distribution is represented by the discretised klimontovich distribution of numerical markers

$$f_t(\mathbf{x}, \mathbf{v}) = \frac{n_t(\mathbf{x})}{\sqrt{\pi^3} v_{th}^3} e^{-\frac{v^2}{v_{th}^2}} \quad f_b(\mathbf{x}, \mathbf{v}) = \sum_k w_k \delta(\mathbf{x} - \mathbf{x}_k) \delta(\mathbf{v} - \mathbf{v}_k)$$

such that the fusion rate is expressed as

$$\frac{dR}{dV}(\mathbf{x}) = \sum_{t,k} w_k \delta(\mathbf{x} - \mathbf{x}_k) n_t(\mathbf{x}) \langle \sigma v \rangle_{kt} \quad (4.23)$$

where

$$\langle \sigma v \rangle_{kt}(\mathbf{x}) = \frac{1}{\sqrt{\pi^3} v_{th}^3} \int d^3v_t |\mathbf{v}_t - \mathbf{v}_k| \sigma(|\mathbf{v}_t - \mathbf{v}_k|) e^{-\frac{v_t^2}{v_{th}^2}}$$

The integral over all velocity space is performed in spherical coordinates after the change of variable $\mathbf{v} = \mathbf{v}_t - \mathbf{v}_k$ and redefinition of the exponents

$$v_t^2 = v^2 + 2\mathbf{v} \cdot \mathbf{v}_k + v_k^2 = v^2 + 2vv_k \cos\theta + v_k^2 \quad dv_t^3 = dv^3 = v^2 \sin\theta dv d\theta d\phi$$

where (θ, ϕ) are the spherical angles between \mathbf{v}_k and \mathbf{v} and $v = |\mathbf{v}| = |\mathbf{v}_t - \mathbf{v}_k|$ is the modulus of the relative velocity. The integral is easily performed over both angles such that only the

integral over the modulus v remains

$$\begin{aligned} \langle \sigma v \rangle_{kt} &= \frac{2\pi}{\sqrt{\pi^3} v_{th}^3} \int_0^\infty dv v^3 \sigma(v) e^{-\frac{v^2+v_k^2}{v_{th}^2}} \int_0^\pi d\theta \sin\theta e^{-\frac{2vv_k \cos\theta}{v_{th}^2}} \\ &= \frac{1}{\sqrt{\pi} v_{th} v_k} \int_0^\infty dv v^2 \sigma(v) \left[e^{-\frac{(v-v_k)^2}{v_{th}^2}} - e^{-\frac{(v+v_k)^2}{v_{th}^2}} \right]. \end{aligned}$$

The cross-section is redefined for convenience with respect to the relative velocity as

$$\sigma(v) = \frac{2S(\frac{\mu}{2}v^2)}{\mu v^2} e^{-\frac{b}{v}} \quad \text{where} \quad b = 2\pi\alpha Z_b Z_t c$$

Finally, the beam-target reactivity of a given fusion process is calculated at each point in space as a function of the beam velocity as

$$\langle \sigma v \rangle_{kt} = \frac{2}{\mu\sqrt{\pi} v_{th} v_k} \int_0^\infty dv S(\frac{\mu}{2}v^2) e^{-\frac{b}{v}} \left[e^{-\frac{(v-v_k)^2}{v_{th}^2}} - e^{-\frac{(v+v_k)^2}{v_{th}^2}} \right] \quad (4.24)$$

The contribution of the second term being always smaller than $e^{-v_k^2/v_{th}^2}$, it is reasonable to neglect it. To further simplify, the beam-target reactivity is computed in the limit where the background temperature is low, i.e. $v_{th} \rightarrow 0$ (cold target approximation). With this assumption, the exponential becomes a Dirac function and the integral is easily resolved as

$$\frac{1}{\sqrt{\pi} v_{th}} e^{-\frac{(v-v_k)^2}{v_{th}^2}} \xrightarrow{v_{th} \rightarrow 0} \delta(v - v_k) \quad \iff \quad \langle \sigma v \rangle_k \xrightarrow{v_{th} \rightarrow 0} \frac{2S(\frac{\mu}{2}v_k^2)}{\mu v_k} e^{-\frac{b}{v_k}} = \sigma v_k \quad (4.25)$$

Figure 4.10(c) displays the beam-target reactivity calculated in the cold-target approximation for neutron producing DD and DT reactions. The curve for a tritium beam and a deuterium target differs from that of a deuterium beam and tritium target because the beam velocity as well as the centre-of-mass energy are different at equal beam energy (due to the mass difference).

4.7 Hybrid kinetic-MHD model

The formulation of an interface between the MHD stability code MINERVA (Aiba et al., 2009) and VENUS-LEVIS is described in this section. Concluding results have not yet been obtained because theoretical and code development is still in progress. It seems however important to present the modelling approach as well as the current status of the implementation in order to help future progress. This section thus focuses on laying-out the key ingredients of the interface as well as the theoretical background.

MINERVA is an advanced code developed by the Japan Atomic Energy Agency for realistic modelling of MHD modes, such as internal kink modes, ELMs and Resistive Wall Mode (RWM), in the presence of plasma rotation. It is one of the few codes that treat linear MHD stability in toroidally rotating systems self-consistently. In particular, it is employed to analyse high

pressure experimental plasma results in JT-60U, the Japanese tokamak experiment. It has for example clarified when plasma rotation can stabilise or destabilise RWM (Aiba et al., 2013). So far, however, kinetic effects from supra-thermal particles are neglected. Energetic particles play an important role on the stability of slowly growing MHD modes like the internal kink mode and the RWM. Quantitative results are needed to understand the interaction of energetic particles with toroidal rotation. At the present time, few numerical codes can handle consistently and quantitatively both fast particles and rotation. We therefore propose to combine the MINERVA MHD code and the PIC code VENUS-LEVIS with the long-term goal to simulate the interplay between plasma rotation, energetic particles and linear MHD modes such as ELMs, internal kink modes and RWM. The MHD model is extended by adding non-ideal (kinetic) components to the existing MHD equations, thereby applying an alternate kinetic closure. The interface between MINERVA and VENUS-LEVIS permits many physical effects to be explored. The novelty and strength of the model reside in the self-consistent treatment of plasma rotation and the accurate tracking of fast particle orbits in the equilibrium fields.

The interface works as follows. MINERVA provides the equilibrium fields and solves the evolution of a spectrum of MHD perturbations. The most unstable is transferred to the orbit solver, which, using a delta-f PIC method, evaluates the perturbed hot pressure tensor by integrating the unperturbed particle trajectories and calculating deviations from a given equilibrium distribution function via a dedicated weight equation, before returning the perturbed hot pressure tensor to MINERVA for the next iteration of the process. Growth rates and frequencies of the modes studied are assessed and compared with known results in limiting cases. The interface is basically a numerical representation of analytic work by Porcelli et al. (1994) and Helander et al. (1997), extending the results by exactly solving the dynamics of fast particles and retaining all perturbed components.

4.7.1 MINERVA fields and perturbations with toroidal rotation

Unless specified otherwise, equilibrium quantities are denoted in the remaining of this section with a subscript 0 as in B_0 and perturbed quantities with a δ prefix as in δA .

Equilibrium quantities

MINERVA establishes a standard axisymmetric MHD equilibrium in the presence of toroidal rotation $\mathbf{v}_0 = R^2 \Omega(\Psi) \nabla \zeta = \Omega(\Psi) \mathbf{e}_\zeta$, by solving the isothermal Grad-Shafranov equation (2.3.1). The fields are represented within VENUS-LEVIS using a straight field-line coordinates $(\bar{\Psi}, \theta, \zeta)$ where $\zeta = -\phi$ the geometric toroidal angle⁷, $\bar{\Psi} = \sqrt{\Psi/\Psi_e}$ the radial variable proportional to the poloidal magnetic flux and θ the poloidal angle such that the coordinate system is field-aligned. The equilibrium magnetic field is written as in equation (2.5)

$$\mathbf{B}_0 = F(\bar{\Psi}) \nabla \zeta + \nabla \zeta \times \nabla \psi$$

⁷The ζ angle is opposite to the geometrical angle ϕ such that the coordinate system is right-handed.

where the poloidal magnetic flux Ψ , current profile F , coordinate jacobian $\sqrt{g_\Psi}$ and q-profile are related, by virtue of the straight field-line coordinate system, by

$$\frac{\mathbf{B}_0 \cdot \nabla \zeta}{\mathbf{B}_0 \cdot \nabla \theta} = \frac{F |\nabla \zeta|^2}{\psi_e \nabla \theta \cdot (\nabla \zeta \times \nabla \psi)} = \frac{F \sqrt{g_\Psi}}{\psi_e R^2} = q(s) \Rightarrow \sqrt{g_\Psi} = \frac{q \psi_e R^2}{F}$$

By virtue of ideal Ohm's law, the toroidal flow implies a radial electric field in the non-rotating frame of reference (lab frame)

$$\mathbf{E}_0 = -\mathbf{v}_0 \times \mathbf{B}_0 = \Omega \nabla \Psi \qquad \Phi_{E0} = - \int_0^\Psi \Omega(\Psi') d\Psi'$$

The details of the representation are given in appendix B.1.2 without rotation⁸. MINERVA actually uses the radial variable $s = \sqrt{\Psi}$ instead of Ψ which requires precaution when converting radial components and radial derivatives.

Linear perturbations

The linear MHD stability problem is assessed by computing the evolution of the perturbed fluid displacement ξ according to the Frieman-Rosenbluth equation (Frieman and Rosenbluth, 1960). The fluid displacement induces a perpendicular electromagnetic perturbation $\delta \mathbf{A}$ corresponding to

$$\delta \mathbf{A} = \xi \times \mathbf{B}_0 \qquad \delta \Phi_E = \xi \cdot \mathbf{E}_0 = (\xi \cdot \nabla \Psi) \Omega.$$

MINERVA extracts the most unstable toroidal mode and generates the perturbed vector potential $\delta \mathbf{A}$ (complex field) as

$$\delta \mathbf{A}(s, \theta, \zeta, t) = \sum_m \delta A_m(s) e^{im\theta} e^{-in\zeta} e^{(\gamma+i\omega)t} \quad (4.26)$$

where γ is the growth rate and ω the mode frequency⁹. The covariant components of the vector potential in coordinates $u^i = (s, \theta, \zeta)$ as

$$\delta \mathbf{A} = \delta A_s \nabla s + \delta A_\theta \nabla \theta + \delta A_\zeta \nabla \zeta = \delta A_i \nabla u^i$$

So, $\delta A_s = \delta \mathbf{A} \cdot \mathbf{e}_s$, $\delta A_\theta = \delta \mathbf{A} \cdot \mathbf{e}_\theta$ and $\delta A_\zeta = \delta \mathbf{A} \cdot \mathbf{e}_\zeta$ where $\mathbf{e}_i = \partial \mathbf{x} / \partial u^i$. Each mode component δA_{im} (complex number) is treated as a cubic spline over a non-equidistant grid in s (see cubic spline techniques section 4.2.2). Radial derivatives of the splines are taken with respect to s as $\delta A' \equiv d\delta A/ds$. VENUS-LEVIS then evaluates the magnetic field using the usual relation

$$\delta \mathbf{B} = \nabla \times \delta \mathbf{A} = \nabla \delta A_j \times \nabla u^j = \partial_i \delta A_j \nabla u^i \times \nabla u^j = \partial_i \delta A_j \frac{\mathbf{e}^{ijk}}{\sqrt{g_s}} \mathbf{e}_k$$

⁸The expressions in that section stay valid for the components of the magnetic field when rotation is included, but the current components have to be slightly modified. This is easily performed by using the results of section 2.3.1.

⁹Frequency and growth rate are normalised to the Alfvén frequency $\tilde{\gamma} = \gamma/\Omega_A$ and $\tilde{\omega} = \omega/\Omega_A$

where $\sqrt{g_s}$ is the jacobian of the flux-coordinates (s, θ, ζ) . Hence,

$$\begin{aligned}\delta B^s &= (\partial_\theta \delta A_\zeta - \partial_\zeta \delta A_\theta) / \sqrt{g_s} \leftarrow (im\delta A_\zeta + in\delta A_\theta) / \sqrt{g_s} \\ \delta B^\theta &= (\partial_\zeta \delta A_s - \partial_s \delta A_\zeta) / \sqrt{g_s} \leftarrow (-in\delta A_s - \delta A'_\zeta) / \sqrt{g_s} \\ \delta B^\zeta &= (\partial_s \delta A_\theta - \partial_\theta \delta A_s) / \sqrt{g_s} \leftarrow (\delta A'_\theta - im\delta A_s) / \sqrt{g_s}\end{aligned}$$

A few adjustments are necessary to plug these components in the GCDE since they are written with respect to the radial variable $\bar{\Psi} = \Psi / \Psi_e = s^2$

$$\nabla s = \nabla \bar{\Psi} \frac{ds}{d\bar{\Psi}} = \frac{\nabla \bar{\Psi}}{2s} \quad \mathbf{e}_s = \frac{\partial \mathbf{x}}{\partial s} = \frac{\partial \mathbf{x}}{\partial \bar{\Psi}} \frac{d\bar{\Psi}}{ds} = 2s \mathbf{e}_{\bar{\Psi}} \quad \sqrt{g_s} = \mathbf{e}_s \cdot \mathbf{e}_\theta \times \mathbf{e}_\zeta = 2s \sqrt{g_{\bar{\Psi}}}$$

The components to be converted from s to $\bar{\Psi}$ are thus

$$\begin{aligned}\delta A_{\bar{\Psi}} &= \delta \mathbf{A} \cdot \mathbf{e}_{\bar{\Psi}} = \delta \mathbf{A} \cdot \frac{\mathbf{e}_s}{2s} = \frac{\delta A_s}{2s} \\ \delta B^{\bar{\Psi}} &= (\partial_\theta \delta A_\zeta - \partial_\zeta \delta A_\theta) \frac{\mathbf{e}_s}{\sqrt{g_s}} \cdot \nabla \bar{\Psi} = (\partial_\theta \delta A_\zeta - \partial_\zeta \delta A_\theta) / \sqrt{g_{\bar{\Psi}}} \\ \delta B^{\theta, \zeta} &= (\partial_{\zeta, \theta} \delta A_s - \partial_s \delta A_{\zeta, \theta}) / 2s \sqrt{g_{\bar{\Psi}}}\end{aligned}$$

4.7.2 Fast ion contribution via δf PIC scheme without rotation (preliminary)

Vlasov equation in non-canonical coordinates

Starting from the non-canonical phase-space Lagrangian,

$$\mathcal{L}(z^\mu, t) = \Lambda_\alpha \dot{z}^\alpha - H(z^\mu, t) = \Lambda_M \dot{z}^M$$

where Greek letters run from 1 to $2N$ and capitalised Latin letters from 0 to $2N$ with $z^0 \equiv t$, the motion in non-canonical phase-space $z^M(q, p, t)$ is formally governed by

$$\begin{aligned}\dot{z}^\alpha &= \Gamma^\alpha(z^\mu, t) = \Pi^{\alpha\beta} (\partial_\beta H + \partial_t \Lambda_\beta) \\ \dot{z}^0 &= \dot{t} = 1\end{aligned}$$

where the last equation for $z^0 = t$ is the closure to the otherwise under-determined system of equations. Let $f(q, p, t) = f(z^\mu, t)$ be a fast ion distribution function, i.e. a physical measure of the number of particles in volume $dqdp = \sqrt{\Omega} dz^\mu$

$$f(z^\mu, t) dqdp = f(z^\mu, t) \sqrt{\Omega} dz^\mu,$$

where $\sqrt{\Omega} = \mathcal{J}$ is the Jacobian of the transformation from canonical to non-canonical coordinates (see equation C.11). Without collisions nor particle sources, the total number of particles is constant such that the following continuity equation is stated

$$\frac{1}{\sqrt{\Omega}} \frac{\partial}{\partial z^M} \left(\dot{z}^M \sqrt{\Omega} f \right) = \frac{1}{\sqrt{\Omega}} \frac{\partial}{\partial t} \left(\sqrt{\Omega} f \right) + \frac{1}{\sqrt{\Omega}} \frac{\partial}{\partial z^\alpha} \left(\dot{z}^\alpha \sqrt{\Omega} f \right) = 0.$$

By virtue of the Hamiltonian treatment of the equations of motion, the Jacobian satisfies Liouville equation implying that phase-space volume is conserved (see equation A.63),

$$\frac{\partial \sqrt{\Omega}}{\partial t} + \frac{\partial}{\partial z^\alpha} (\sqrt{\Omega} \dot{z}^\alpha) = 0$$

Thus, despite working with non-canonical coordinates, the distribution function evolves according to the well-known Vlasov equation

$$\frac{df}{dt} = \frac{\partial f}{\partial t} + \dot{z}^\alpha \frac{\partial f}{\partial z^\alpha} = \frac{\partial f}{\partial t} + \Gamma^\alpha \frac{\partial f}{\partial z^\alpha} = \Gamma^M \partial_M f = 0. \quad (4.27)$$

Linear Vlasov equation and δf method

MINERVA perturbations result from a linear treatment of the MHD equations and are considered small. This suggests the use of the so-called δf method, for which the fast particle distribution function is split in an equilibrium part f_{eq} and a δf term as explained hereafter.

Without electromagnetic perturbations, the guiding-centre Lagrangian is axisymmetric and independent of time as well as gyro-angle Θ (see equation 3.10)

$$\mathcal{L}_0(t, \mathbf{X}, \rho_{||}, \mu, \Theta) = (\mathbf{A}_0 + \rho_{||} \mathbf{B}_0) \cdot \dot{\mathbf{X}} + \frac{m}{q} \mu \dot{\Theta} - \left(\frac{1}{2} \frac{q}{m} \rho_{||}^2 B_0^2 + \frac{\mu}{q} B_0 \right) \dot{t}. \quad (4.28)$$

This Lagrangian gives rise to a set of GCDE (see equation 3.12), which are put in the form of $\dot{z}^M = \Gamma_0^M(z^M)$. The motion is characterised by conservation of three constants $(C_t, C_\phi, C_\Theta) = (-E, P_\phi, m\mu/q)$, namely energy, adiabatic magnetic moment and toroidal momentum. By the Noether theorem, these constants of motion correspond to the conjugate momentum of the symmetry variable (Cary and Littlejohn, 1983)

$$C_i = \frac{\partial \mathcal{L}_0}{\partial \dot{z}^i} \Rightarrow \frac{d_0 C_i}{dt} = \frac{\partial \mathcal{L}_0}{\partial z^i} = 0 \quad (4.29)$$

where d_0 is a notation to mention differentiation with respect to the unperturbed trajectories. The unperturbed constants of motion are explicitly identified as

$$E = \frac{\mu}{q} B_0 + \frac{1}{2} \frac{m}{q} v_{||}^2 \quad \mu = \frac{m v_{\perp}^2}{2 B_0} \quad P_\phi = A_{0,\phi} + \frac{m}{q} v_{||} b_{0,\phi} = -\Psi + \frac{m v_{||} F}{q B_0}.$$

A distribution $f_{eq}(C_i)$ that is written as a function of the constants of motion automatically respects the unperturbed Vlasov equation

$$\frac{d_0}{dt} f_{eq} = \Gamma_0^M \partial_M f_{eq} = \frac{\partial f_{eq}}{\partial t} + \Gamma_0^\alpha \frac{\partial f_{eq}}{\partial z^\alpha} = \frac{d_0 C_i}{dt} \frac{\partial f_{eq}}{\partial C_i} \stackrel{(4.29)}{=} 0$$

In the presence of MINERVA electromagnetic perturbations, the equations of motion originate

from the total Lagrangian \mathcal{L}

$$\mathcal{L}(t, \mathbf{X}, \rho_{\parallel}, \mu, \Theta) = (\mathbf{A} + \rho_{\parallel} \mathbf{B}) \cdot \dot{\mathbf{X}} + \frac{m}{q} \mu \dot{\Theta} - \left(\frac{1}{2} \frac{q}{m} \rho_{\parallel}^2 B^2 + \frac{\mu}{q} B + \delta \Phi_E \right) t$$

where $\mathbf{A} = \mathbf{A}_0 + \delta \mathbf{A}$ and $\mathbf{B} = \mathbf{B}_0 + \delta \mathbf{B}$.

Perturbed and unperturbed terms are distinguished in the equations of motion and in the distribution function as

$$\dot{z}^{\alpha} = \Gamma^{\alpha} = \Gamma_0^{\alpha} + \delta \Gamma^{\alpha} \qquad f = f_{eq} + \delta f$$

Given the linear treatment of MHD stability and the small amplitude of $\delta \mathbf{A}$ in MINERVA, the Vlasov equation is expanded at first order¹⁰

$$0 = \frac{d}{dt} f = (\Gamma_0^M + \delta \Gamma^M) \partial_M (f_{eq} + \delta f) = \Gamma_0^M \partial_M f_{eq} + \delta \Gamma^M \partial_M f_{eq} + \Gamma_0^M \partial_M \delta f + O(\delta^2) = 0$$

The equilibrium distribution function being a function of the unperturbed constants of motion, the first phase-space gradient term is equal to $\delta \Gamma^M \partial_M \equiv \dot{C}_i \frac{\partial}{\partial C_i}$. The second term describes the evolution of δf under the unperturbed motion. The linear Vlasov equation is rearranged as

$$\frac{d_0}{dt} \delta f = -\dot{C}_i \frac{\partial f_{eq}}{\partial C_i} = -\frac{\partial \mathcal{L}}{\partial z^i} \frac{\partial f_{eq}}{\partial C_i} \qquad (4.30)$$

where z^i is the symmetry variable leading to conservation of C_i without perturbations. The δf distribution is thus solved by integrating the right-hand side along unperturbed trajectories. Similarly to δf , the total Lagrangian \mathcal{L} is evaluated along unperturbed orbits. It is possible to isolate the symmetry-breaking components of the Lagrangian at first order

$$\mathcal{L} - \mathcal{L}_0 = \delta \mathcal{L} + O(\delta^2) \qquad \delta L = \delta \mathcal{L}|_0 = (\delta A_i + \rho_{\parallel}^0 \delta B_i) \Gamma_0^i - \left(\frac{\mu}{q} + v_{\parallel}^0 \rho_{\parallel}^0 \right) \delta B_{\parallel} - \delta \Phi_E$$

where δL represents the evaluation of the perturbed Lagrangian along unperturbed trajectories and the magnetic strength was expanded at first order as

$$B^2 = (\mathbf{B}_0 + \delta \mathbf{B}) \cdot (\mathbf{B}_0 + \delta \mathbf{B}) = B_0^2 + 2\delta \mathbf{B} \cdot \mathbf{B}_0 + O(\delta^2) = B_0^2 + 2\delta B_{\parallel} B_0 + O(\delta^2)$$

$$B = \sqrt{B^2} = B_0 + \delta B_{\parallel} + O(\delta^2).$$

Without plasma flow (no electric drift), the unperturbed guiding-centre motion is written in terms of parallel motion and perpendicular drift due to curvature and gradients (see equations 3.13 and 3.14) as,

$$\dot{\mathbf{X}} = \mathbf{\Gamma}_0 = v_{\parallel}^0 \mathbf{b}_0 + \mathbf{V}_B^0 \qquad \mathbf{V}_B^0 = \mathbf{b}_0 \times \left(\frac{\mu}{q} \nabla B_0 + v_{\parallel}^0 \rho_{\parallel}^0 \boldsymbol{\kappa}_0 \right) / B_{\parallel}^{*0}$$

where $\boldsymbol{\kappa}_0$ is the curvature of the equilibrium magnetic field and $B_{\parallel}^{*0} = \mathbf{b}_0 \cdot (\mathbf{B}_0 + \rho_{\parallel}^0 \nabla \times \mathbf{B}_0)$.

¹⁰The approach can be extended to a non-linear treatment. In this case, the evolution of δf would have to be solved in VENUS-LEVIS along perturbed trajectories.

Noticing that $\delta \mathbf{A} \cdot \mathbf{B}_0 = 0$ in this gauge, the perturbed Lagrangian term δL conveniently reduces to

$$\delta L = (\delta \mathbf{A} + \rho_{\parallel}^0 \delta \mathbf{B}) \cdot \mathbf{V}_B^0 - \frac{\mu}{q} \delta B_{\parallel} - \delta \Phi_E. \quad (4.31)$$

Recalling equation (4.26), the electromagnetic perturbations are described with a unique toroidal mode number, frequency and growth rate. Thus,

$$\partial_t \mathcal{L}|_0 = (\gamma + i\omega) \delta L \quad \partial_{\phi} \mathcal{L}|_0 = -in \delta L \quad \partial_{\Theta} \mathcal{L}|_0 = 0$$

so that the δf equation finally becomes

$$\frac{d_0}{dt} \delta f = \left[(\gamma + i\omega) \frac{\partial f_{eq}}{\partial E} + in \frac{\partial f_{eq}}{\partial P_{\phi}} \right] \delta L \quad (4.32)$$

This expression is consistent with the kinetic response of the work by Porcelli et al. (1994) and Helander et al. (1997). It is however remarked that the guiding-centre Lagrangian is a truncation of the particle Lagrangian. Treating the perturbations as an extra term $\delta \mathcal{L}$ modifies the definition of the guiding-centre variables and constants of motion. The correct approach (future work) consists of yielding the total guiding-centre Lagrangian from the particle Lagrangian with the use of Hamiltonian truncation schemes such as Lie perturbation theory (Brizard, 2000; Brizard and Hahm, 2007; Krommes, 2010). We realised that this subtlety was not properly resolved in the current manuscript and acknowledge the fact that only the kinetic contribution to the δf is obtained (missing adiabatic terms).

Weight equation and PIC scheme

The benefit of solving the linear δf equation (4.32) is to obtain various moments, in particular the perturbed pressure from hot particles. This is performed analytically in some simple cases, but for more general applications, we employ VENUS-LEVIS to solve the fast particle dynamics and compute δf numerically via a Monte-Carlo PIC scheme. The idea is to sample the fast particle distribution with a finite number of Klimontovich markers and evolve their weights along their unperturbed trajectories (Aydemir, 1994). Let $P(q, p, t) = P(z, t)$ govern the Monte-Carlo sampling, i.e. the marker probability density function. Moments of the physical distribution f are formally calculated as

$$\begin{aligned} I[A] &= \int A(z) f_{eq}(z, t) \sqrt{\Omega} dz + \int A(z) \delta f(z, t) \sqrt{\Omega} dz \\ &= I_0[A] + \underbrace{\int \left(\frac{A \delta f}{P} \right) P \sqrt{\Omega} dz}_g = I_0[A] + \langle g \rangle \end{aligned}$$

In the situation where $|f - f_{eq}| = |\delta f| \ll |f|$, the expected value $\langle g \rangle$ is estimated with N markers on unperturbed trajectories $z_j(t)$ as

$$\langle g \rangle \xrightarrow{N \rightarrow \infty} \frac{1}{N} \sum_{j=1}^N g_j = \frac{1}{N} \sum_{j=1}^N \frac{A(z_j(t)) \delta f(z_j(t), t)}{P(z_j(t), t)} = \sum_{j=1}^N w_j(t) A_j(t)$$

where the weight $w_j(t) \equiv \delta f(z_j(t), t) / NP(z_j(t), t)$ becomes an attribute of the marker, to be evaluated along its unperturbed trajectory. Since the probability density function P satisfies its own Vlasov equation $d_0 P / dt = 0$, the weight evolves according to

$$\frac{d_0}{dt} w_j = \frac{1}{N} \frac{d_0}{dt} \left(\frac{\delta f}{P} \right) \Big|_j = \underbrace{\frac{1}{NP_j}}_{\Delta_j(t)} \frac{d_0}{dt} \delta f \Big|_j \stackrel{(4.32)}{=} \Delta_j(0) \left[(\gamma + i\omega) \frac{\partial f_{eq}}{\partial E} + in \frac{\partial f_{eq}}{\partial P_\phi} \right] \delta L_j(t)$$

where $\Delta_j(t) = \Delta_j(0) = \Delta_j$ actually represents the phase-space volume sampled by marker j . This coefficient has to be calculated for each marker at initialisation. The linear Vlasov equation is integrated in VENUS-LEVIS with a RK4 scheme alongside the GCDE.

Phase-space loading

Proper sampling of phase-space is important to reduce the noise from the Monte-Carlo scheme. There are various choices to initialise the position of markers in phase-space, the most effective being $P \equiv f_{eq}$, called importance sampling in the work by Aydemir (1994). When the physical distribution is not a simple product of phase-space variables but an intricate 5D-function, importance sampling numerically requires a loading technique such as the acceptance-rejection method (Saucier, 2000, section 3.4). This technique is computationally slow and under-performing. A hybrid technique is discussed hereafter.

Markers are loaded uniformly using a Hammersley sequence (Hammersley and Handscomb, 1964) in a set of coordinates $\mathcal{U} = (E, \lambda, s, \theta, \zeta)$, where $\lambda = v_{||} / v$. Let $\mathcal{X} = (\mu, \rho_{||}, s, \theta, \zeta)$ be the guiding-centre phase-space and \mathcal{C} the canonical particle phase-space. Δ_j is the volume represented by marker j in \mathcal{C} , i.e.

$$\Delta_j \propto dpdq = mq\sqrt{\Omega} dz = J_{\mathcal{C} \rightarrow \mathcal{U}} dU = mq\sqrt{\Omega} J_{\mathcal{X} \rightarrow \mathcal{U}} dU$$

where

$$mq\sqrt{\Omega} = J_{\mathcal{C} \rightarrow \mathcal{X}} \stackrel{(C.11)}{=} mqBB_{||}^* \sqrt{g} \qquad J_{\mathcal{X} \rightarrow \mathcal{U}} = \frac{\sqrt{2mE}}{qB^2}$$

Instead of loading uniformly in (E, s) , it may be useful to replicate some features of the equilibrium distribution, for example an exponential behaviour in energy or a bunching at a specific radial position. For this, the *inverse transformation technique* is applied to populate phase-space (Saucier, 2000, section 3.1) according to one-dimensional distribution functions $p_{E,s}(X)$. First, the cumulative distribution $P(X)$ is constructed (either analytically or numerically interpolated), such that $P'(X) = p(X)$. Then, the inverse function is used to generate X from the uniformly distributed number $Y \in (0, 1)$ of the Hammersley sequence, i.e.

$X = P^{-1}(Y)$. The inversion is performed via simple root finding algorithm (Newton's method). Knowing that $dY = P' dX = p dX$, additional Jacobians appear in the phase-space volume coefficient, such that we obtain

$$\Delta_j \propto \frac{B_{||}^*}{B} \frac{\sqrt{g}}{p_s} \frac{\sqrt{E}}{p_E}$$

To settle the overall normalisation of Δ_j , the markers are temporarily borrowed to sample the properties of the equilibrium distribution function f_{eq} . The physical number of hot particles, approximated by Monte-Carlo scheme, can be used to set the normalisation of Δ_j as

$$N_{hot} = \int f_{eq} dp dq = \int \left(\frac{f_{eq}}{P} \right) P dp dq \approx \frac{1}{N} \sum_{j=1}^N \frac{f_{eq}(z_j)}{P(z_j)} = \sum_{j=1}^N \Delta_j f_{eq,j}$$

Evaluation of the perturbed hot pressure

At every diagnostic time, the position, velocity, energy and weight of each marker are recorded. At the end of a simulation, an independent post-processing routine is launched to calculate the hot perturbed pressure. The perturbed pressure is evaluated as a moment of the δf distribution

$$\begin{aligned} \delta P_{\perp}(\mathbf{x}, t) &= m \int dv^3 \frac{v_{\perp}^2}{2} \delta f(x, v, t) \approx \frac{m}{2V} \sum_{j \in V} w_j v_{j,\perp}^2 \\ \delta P_{||}(\mathbf{x}, t) &= m \int dv^3 v_{||}^2 \delta f(x, v, t) \approx \frac{m}{V} \sum_{j \in V} w_j v_{j,||}^2 \end{aligned}$$

where $V = \sqrt{g} \Delta s \Delta \theta \Delta \zeta$ is a small volume around \mathbf{x} . Then, it is Fourier decomposed in the poloidal and toroidal direction using the basis $e^{im\theta - in\zeta}$. Each mode is found as

$$\delta P_{mn}(s, t) = \int \frac{d\theta d\zeta}{2\pi} \delta P e^{-im\theta + in\zeta} \approx \frac{m}{\sigma} \sum_{j \in \sigma} w_j v_j^2 e^{-im\theta_j + in\zeta_j}$$

where $\sigma = \langle \sqrt{g} \rangle \Delta s$ is the volume of a flux shell.

Since the perturbations have the form $e^{(\gamma+i\omega)t}$, a Laplace transform is performed to retrieve the kinetic response of hot particles as

$$\delta \hat{P}_{mn}(s, \Gamma) = \int_0^T dt \delta P_{mn}(s, t) e^{-\Gamma t}$$

where Γ is chosen equal to $(\gamma + i\omega)$.

The idea of the interface is to return quantities $\delta P_{||}$ and δP_{\perp} to MINERVA for the next iteration, solving MHD equations as an initial value problem. The contribution from hot particles to the pressure tensor will either provide external drive or will damp the MHD mode studied. Ultimately, the stability problem is addressed in the presence of toroidal plasma rotation. Before this, the guiding-centre equations have to be extended with the correct centrifugal

force terms and the linear Vlasov equation modified with the appropriate perturbations. This is the subject of an ongoing collaboration with our colleagues in Japan working on MINERVA.

4.8 Conclusions

This chapter highlights the main features of the VENUS-LEVIS code, replacing the VENUS guiding-centre code with a modern design. Flexibility is obtained by separating different sub-parts into independent and interchangeable modules. For example, one module takes care of pushing particles via the RK4 stepper, another deals with interpolation of the fields via the spline-Fourier technique, another includes external vacuum fields, another handles Coulomb collisions via Monte-Carlo kicks, another captures moments of the distribution using a full- f or δf approach, another controls the virtual neutron camera diagnostic, etc...

The spline-Fourier technique is capable of computing metric elements with high accuracy anywhere inside the magnetic equilibrium, thus yielding a globally continuous and smooth representation of the fields. Convergence and conservation properties (energy and toroidal momentum) of energetic particle trajectories are obtained with the spline-Fourier technique, where other finite difference methods persistently fail. Even if the amount of operations using spline-Fourier interpolation grows proportionally to the number of employed modes, thus being slower than mesh-based methods, its accuracy and low memory imprint makes it remarkably advantageous for deploying on super-computing facilities or GPU architectures. The fine-tuning of boundary conditions, as well as the possibility to scale the radial grid arbitrarily (for example, linear versus square root) considerably improves the computation of the orbits approaching the singular magnetic axis.

A method to include in curvilinear coordinates arbitrary external fields on top of equilibrium is briefly discussed. The NBI module is upgraded to 3D flux geometries, providing realistic fast ion sources in saturated MHD equilibria. The Monte-Carlo collision operator for slowing-down and pitch-angle scattering is revised. A virtual neutron camera diagnostic is implemented so that comparisons between numerical simulations and experimental data can be made. The formulation of a hybrid kinetic-MHD interface between VENUS-LEVIS and MINERVA is presented. This project is the basis of a numerical tool to assess the interaction between MHD modes and fast particles in rotating plasmas with great consistency.

The clean architecture of VENUS-LEVIS is suitable for code extensions and long-term development. This numerical tool thus provides a robust platform for the study of fast particle motion in 3D magnetic fields which will hopefully continue to evolve. Beyond the applications of this thesis, VENUS-LEVIS is pertinent for addressing confinement of energetic ions in stellarator MHD equilibrium, leaning on a guiding-centre and/or full-orbit treatment of the equations of motion. An example of ongoing applications is the consistent establishment of ICRH populations in Wendelstein-7X (W7X) via the SCENIC platform (Jucker et al., 2011).

5 NBI fast ion redistribution in saturated ideal internal kink

VENUS-LEVIS and techniques described in previous chapters are applied to the investigation of fast ion redistribution in saturated ideal internal kinks. Our analysis focuses on the Mega-Ampère Spherical Tokamak (MAST) experiment, for which numerical results are conveniently compared against experimental measurements. This work was performed in collaboration with people at Culham Centre for Fusion Energy (CCFE) in the UK who gathered fast ion data in MAST and people at Uppsala university in Sweden who processed data concerning the neutron camera. Obtained results are the object of two publications (Pfefferlé et al., 2014, 2015a).

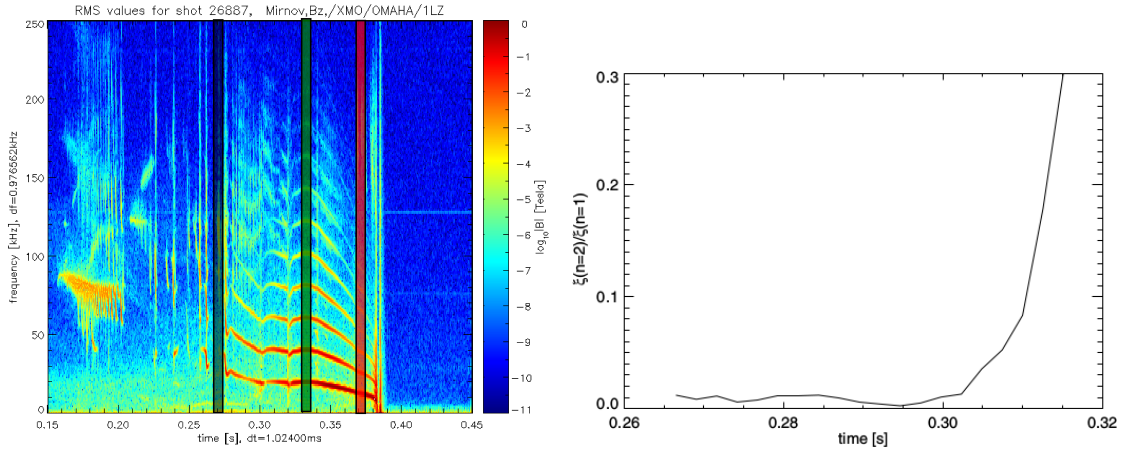
In this chapter, we discuss the representation of saturated ideal internal kinks with the helical core equilibrium from VMEC. This solution is described in detail, in particular applying the field variation criterion (3.37). The use of Guiding-centre Drift Equations (GCDE) (3.12) is verified to describe the motion of hot particles in the kinked core as faithfully as full-orbit equations (3.7). The Neutral Beam Injection (NBI) external module, described in section 4.4, is employed to produce initial sources of markers respecting the characteristics of MAST Positive Ion Neutral Injector (PINI) and the kinked geometry of flux-surfaces. Applying the slowing-down algorithm discussed in section 4.5, the hot distribution function is evolved in the guiding-centre approximation over slowing-down timescales until saturation occurs between constant injection, losses and thermalisation due to Monte-Carlo collisions.

5.1 Phenomenology and modelling

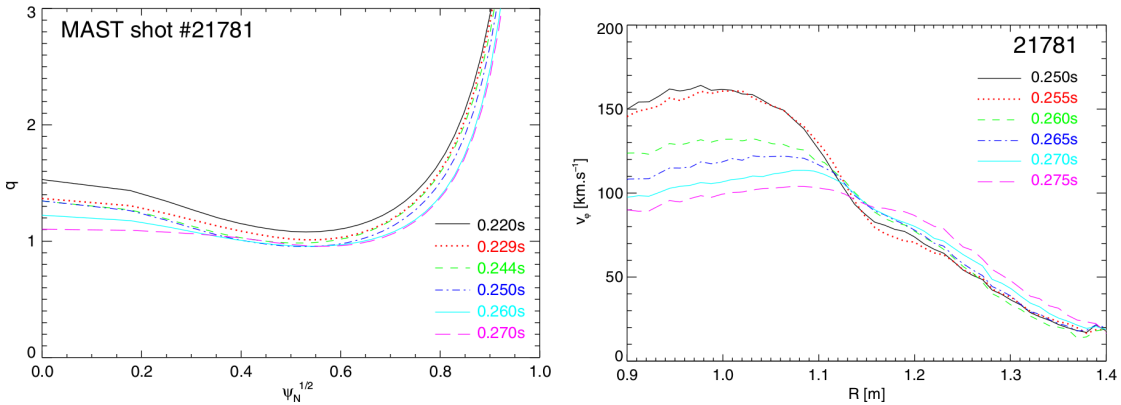
Due to the high- β and low aspect ratio of the MAST machine, the drift excursion of collisionless fast ions is relatively large. Because of the low confining magnetic field, between 0.3 and 0.6 T, energetic particles that may arise from fusion reactions between beam ions and the bulk plasma (beam-thermal contribution) or between injected nucleons (beam-beam contribution) or, to negligible extent, among thermal particles, have such large Larmor radii that they are immediately lost. Hence, the confined fast ion population in MAST originates in majority from NBI, which produces deuterium ions at 3 different energies 60keV, 30keV and 20keV. These populations constitute a minority compared to thermal species such that the plasma evolution and geometry are essentially determined by bulk ions and electrons. The magnetic configuration as well as large-scale plasma instabilities are well described within the MagnetoHydroDynamics (MHD) model. Fast particles are viewed as an additional population that can provide external drive for energetic particle modes such as fishbones, which arise from resonance between trapped fast ion motion and the internal kink mode. Experimentally, the interaction between hot particles and the bulk plasma is revealed by burst-like behaviour with rapid chirping down of the mode frequency, as seen for example on figure 5.1 (a) between $t = 0.15\text{s}$ and $t = 0.27\text{s}$. In hybrid scenario plasmas, the fishbones eventually evolve into

Chapter 5. NBI fast ion redistribution in saturated ideal internal kink

Long-Lived Modes (LLMs) (Chapman et al., 2010). The confinement of fast particles seems to be degraded (Ceconello et al., 2012) in those steady-state saturated modes. Transports codes are not capable of reproducing the fast particle transport patterns seen for instance in neutron camera traces. Instead, the dynamics of fast ions in 3D magnetic configurations are studied here using VMEC and VENUS-LEVIS. The important aspects of LLMs are briefly summarised to support our modelling approach. The phenomenology of LLMs is described for MAST by Chapman et al. (2010), for Tokamak à Configuration Variable (TCV) by Reimerdes et al. (2006) and for National Spherical Tokamak eXperiment (NSTX) by (Menard et al., 2005).



(a) frequency spectrogram of the MHD activity measured by Mirnov coils during hybrid pulse #26887 showing the appearance at $t = 0.27$ s of a LLM lasting for $t \approx 0.1$ s before soft disrupt of the plasma at $t = 0.37$ s. (b) amplitude of the $n = 2$ mode with respect to the $n = 1$ mode as a function of time, deduced from the soft x-ray emission.



(c) q -profile at various moments during the LLM phase of pulse #21781, determined by the EFIT code and MSE measurements. (d) rotation profile at various moments during the LLM phase for pulse #21781 determined by charge exchange recombination spectroscopy.

Figure 5.1 – Phenomenology of the MAST LLM. Courtesy of Chapman et al. (2010).

MAST advanced tokamak scenario profiles are obtained in the experiments with a low plasma density and early NBI heating. The frequency sweeping $n = 1$ mode evolves into a saturated mode with the structure of an ideal internal kink, as seen by the dominant $n = 1$ amplitude on figure 5.1(a) after $t = 0.27$ s as well as figure 5.1(b) showing the ratio between the $n = 2$ and $n = 1$ amplitude. During the LLM phase, NBI heating prevents q_{min} of the reversed q -profile

from crossing unity, avoiding an $n = 1$ reconnecting mode until the plasma locks and ends abruptly. As seen on figure 5.1(c), the reconstructed q -profile flattens in the core region but stays at around unity¹. In both MAST (Hua et al., 2010) and TCV (Graves et al., 2013) the long lived helical modes, occurring when the minimum value of q is just above unity, appear to be absent of magnetic islands near $q = 1$. Small islands on neighbouring surfaces are often seen and are to be expected (Brunetti et al., 2015).

Fast ion transport from the core, as is evident from bolometer measurements but also from neutron camera signals (black circles vs red squares on figure 5.2), explains the absence of fishbone activity during LLMs. Reduction in heating efficiency due to fast ion loss from the core, would explain in part the large drop in beta (e.g. figure 3 of Chapman et al. (2011)), and consequent reduction in non-inductive current which ordinarily helps to sustain the hybrid configuration. While a reduction in bootstrap current normally follows from the reduced beta, the change in NBI current drive efficiency is best assessed with dedicated simulations that correctly account for fast ion confinement in helical equilibria. The effects of a helical core on calculations of fast ion confinement has received little attention thus far, at least compared to the effects of toroidal ripple (Goldston et al., 1981) and Resonant Magnetic Perturbations (RMPs) (Kim et al., 2012). In contrast to ripple and RMPs, the 3D distortion associated with a helical core during hybrid scenario operation probably reaches 10% of the minor radius as observed from soft X-ray reconstruction of the mode geometry (Hua et al., 2010). The large amplitude of the ideal saturated kink is also deduced from the complete flattening of the strong NBI induced toroidal flow in the core region (see figure 5.1(d)) and the rigid rotation of the helical deformation, $\hat{V}_\phi = \Omega R$. From the failed attempt by transport models, e.g. TRANSP, to reproduce the fast ion redistribution patterns observed in the presence of LLMs (see figure 5.2), it is clear that the 3D distortions of the magnetic field are too large to be treated with a linear model from originally axisymmetric plasmas. Calculations of fast ion confinement during LLMs require the inclusion of realistic 3D magnetic field geometry.

Fast particle transport in the presence of 3D fields has been addressed by various authors, notably interested in confinement of energetic ions in stellarators (Dettrick et al., 1998). Boozer representations (Boozer, 1982) often prevail, with the advantage of making flux quantities appear explicitly but with the drawback of a complex coordinate system. If the numerical treatment of stellarator equilibrium is recommended in Boozer coordinates, helical kinks in tokamaks requires an undesirably large Boozer spectrum, as will be seen hereafter. Some effects of 3D magnetic perturbations have been carried through $\delta A_{||}$ terms and the redefinition of $v_{||}$ (White and Chance, 1984). Corrections to toroidal precession rate have been derived and particle loss, e.g. in the fishbone oscillation, have been investigated. However, these models are valid for small deviations from axisymmetry and obviously neglect parallel magnetic perturbations that become large in the case of large kink deformation. Orbits in high n helical systems have also been categorised using expansions of the second adiabatic moment for particles only slightly departing from field-lines (Cary et al., 1988). That approach does not apply to the special case of $n = 1$ helical core, for which orbits are more exotic, radial drift is

¹It is noted that the q -profile is calculated with the EFIT code; a 2D equilibrium is reconstructed according to the experimental constraints from the motional stark effect (MSE) diagnostic. Given the 3D nature of the LLM, it is not clear if the measured flattening of the q -profile is a geometric effect or the true evolution of the field-line pitch on the flux-surfaces (if existent).

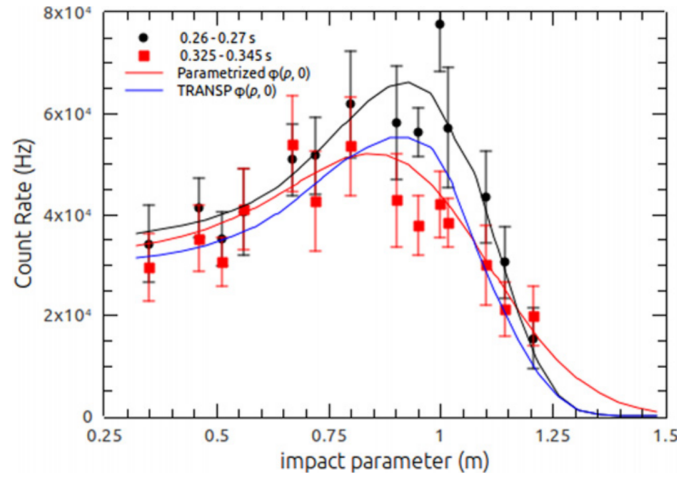


Figure 5.2 – Neutron camera signal before the onset of the LLM (black circles) and during LLM activity (red squares). Agreement with TRANSP simulations before the LLM (black curve), but largely unsuccessful fit during the LLM phase despite the fine-tuning of diffusion coefficients (blue curve). Improved fit of data with ad-hoc parametric model (red curve). Courtesy of Cecconello et al. (2012).

larger and the full magnetic field must be taken into account.

Numerically reproducing internal kink states is usually performed with MHD stability codes like XTOR (Lütjens et al., 2009), for which the linear evolution and non-linear saturation of MHD modes is addressed as an initial value problem. The resulting fields are accurate for MHD stability analysis, but are not always sufficiently smooth for solving energetic particle orbits, even less so if orbits are followed over slowing-down timescales. For reversed shear q -profile with q_{min} slightly above unity, equilibrium codes like VMEC (Hirshman and Whitson, 1983) or ANIMEC (Cooper et al., 2009) conveniently bifurcates into two *sister* solutions although an axisymmetric boundary is prescribed (Cooper et al., 2010); a standard axisymmetric solution and another with an $n = 1$ helical displacement of the magnetic axis and a kinked core. These 3D helical configurations qualitatively and quantitatively resemble saturated states modelled by XTOR in the ideal MHD limit (Brunetti et al., 2014). The smoothness and simplicity of VMEC output, which is Fourier decomposed in toroidal and poloidal angles, is better suited for orbit solving, where the precision and continuity of the field components is crucial for computing fast particle full-orbits and guiding-centre trajectories. The core plasma is largely unaffected by non ideal MHD effects providing $q_{min} > 1$; VMEC is valid for non-resonant surfaces avoiding the formation of an infinite current sheet. Another advantage of VMEC is that, with one helical and one otherwise identical axisymmetric solution for the same boundary and plasma profiles, the direct effect of the helical field on particle transport can be assessed. Therefore, fast ion redistribution is determined by solving with VENUS-LEVIS the motion of NBI fast ions in the helical core produced with VMEC.

5.1.1 Helical core equilibrium solution from VMEC

The coordinate system, field representation and vector components are derived in appendix B.2.1. The geometry of the flux-surfaces is obtained from VMEC under the condition of stellarator

symmetry (see section 2.4) as a Fourier series. The metric is reconstructed in VENUS-LEVIS with the spline-Fourier interpolation scheme (see section 4.2) as

$$R(s, u, v) = \sum_{mn} R_{mn}(s) \cos(mu - nv) \quad Z(s, u, v) = \sum_{mn} Z_{mn}(s) \sin(mu - nv) \quad (5.1)$$

where $s = \sqrt{\Phi/\Phi_e}$ is the radial variable proportional to the normalised toroidal magnetic flux, Ψ_e is the value at q_{95} , u the poloidal angle on each flux surface² and $v = \phi$ the geometric toroidal angle. VMEC flux-coordinate system is neither orthogonal nor straight field-line, which required a general and flexible treatment of the equations of motion. Section 3.3.1 explains the used GCDE and section 3.2 the full-orbit equations.

The parameter δ_h , which measures the distance between the helical and axisymmetric magnetic axis normalised to the minor radius a , is used to characterise the various helical equilibria. The minor radius a is extracted from the Fourier components of the $m = 1, n = 0$ mode on the edge ($s = 1$) and δ_h from the $m = 0, n = 1$ mode on the magnetic axis ($s = 0$),

$$\delta_h = \frac{\sqrt{R_{01}(0)^2 + Z_{01}(0)^2}}{a} \quad a = \sqrt{R_{10}(1)^2 + Z_{10}(1)^2}. \quad (5.2)$$

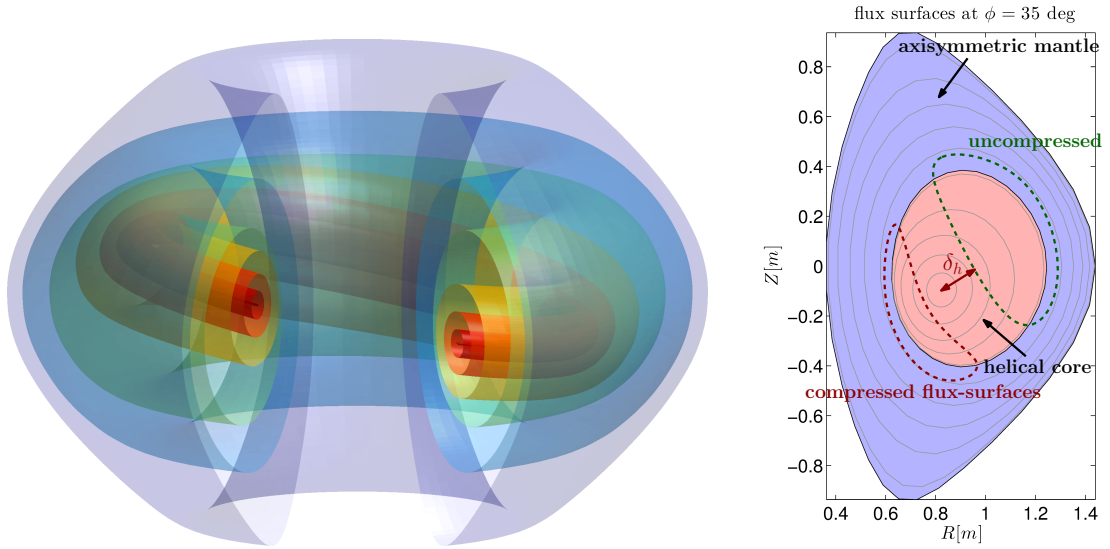


Figure 5.3 – (left) 3D representation of the helically kinked flux surfaces of the VMEC bifurcated equilibrium. (right) poloidal cross-section isolating the helical core and axisymmetric mantle. The helical displacement δ_h measures the shift of the magnetic axis with respect to the axisymmetric centre.

As shown on figure 5.3, the flux-surfaces of the bifurcated equilibrium are kinked in the core region but return to axisymmetry beyond a certain radial position, approximately coinciding with the location of q_{min} . The rapid transition from helical to axisymmetric flux-surfaces leads to their compression on one side of the core at $u - v = \pi$, where gradients become sharp. The other side at $u - v = 0$ is a wide area where the surface are uncompressed and the value of the flux is slowly varying with respect to a radial coordinate perpendicular to the flux-surfaces.

²Notice that $u = \text{const}$ correspond to non-planar surfaces

Chapter 5. NBI fast ion redistribution in saturated ideal internal kink

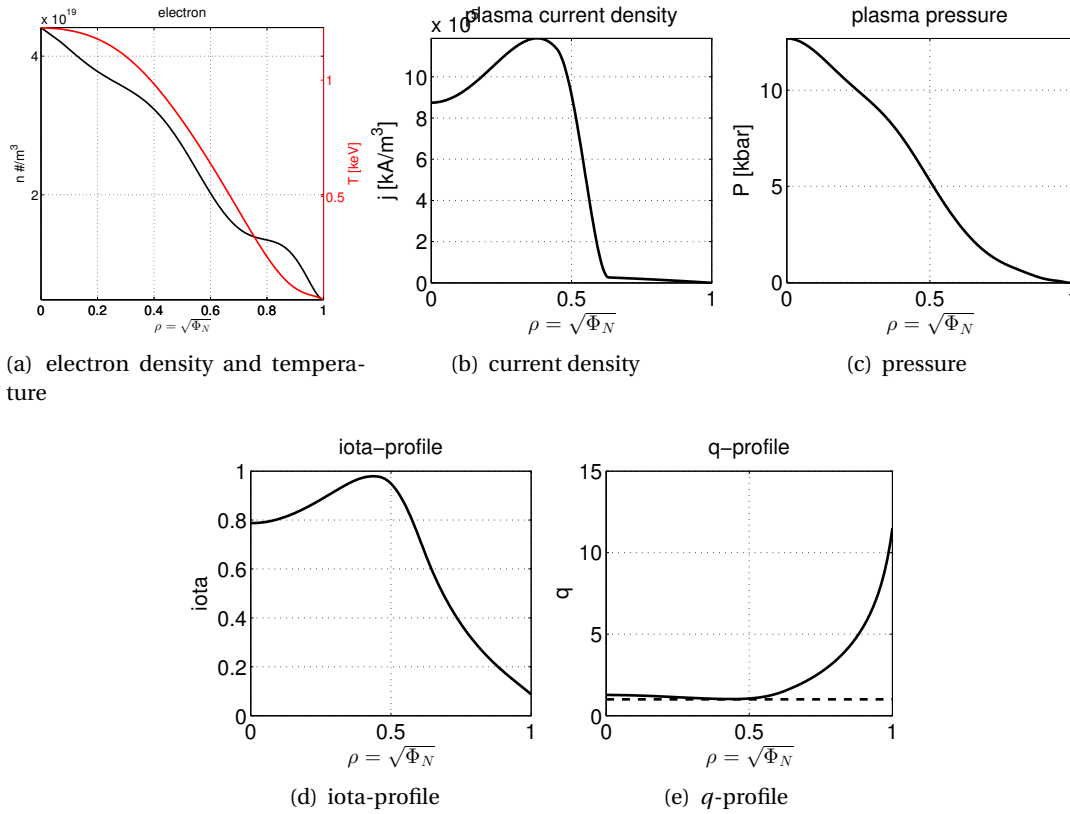


Figure 5.4 – Profiles based on experimental data from MAST (shot #26887) and resulting q -profile for the helical state in VMEC.

The input profiles of the modelled MAST equilibrium are shown on figure 5.4. The bulk electron density and temperature profile (figure 5.4(a)) are taken from actual experimental data measured as a function of the major radius and fitted to the radial variable $\rho = \sqrt{s}$ of the axisymmetric branch. The bulk ion density is considered to be equal to the electron's, invoking quasi-neutrality and neglecting impurities. The bulk ion temperature is set identical to the electron temperature, relying on steady-state thermal equilibrium of both species. The pressure profile (figure 5.4(c)) corresponds to the summed product of density and temperature over ion and electron species. The current density (figure 5.4(b)) is a best fit of the experimental profile using quadratic/cubic/linear polynomials (Cooper et al., 2011c). The bootstrap current is disregarded for the reason that neoclassical contributions are difficult to model for such large deviations from axisymmetry. Neoclassical transport coefficients could be calculated numerically with, for example, the DKES code (Hirshman et al., 1986b). Feeding back the resulting bootstrap current within VMEC until obtaining a stable helical core solution is tedious and the impact on the kinked deformation will be marginal. Plasma rotation is also neglected because of its inconsistent representation in non-toroidally symmetric flows (issue with magnetic pumping). The toroidal velocity of passing NBI ions at 10 – 75keV is at least an order of magnitude faster, so dropping out rotation seems a reasonable momentary assumption.

The bifurcation between axisymmetric and helical state is very sensitive to the iota-profile

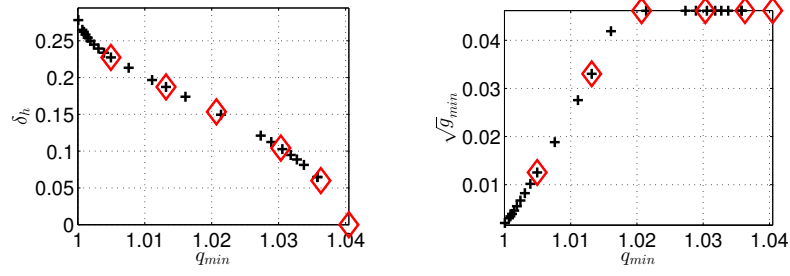


Figure 5.5 – Resulting helical displacement as a function of q_{min} and corresponding reduction of VMEC Jacobian. Red diamonds denote the equilibria used in VENUS-LEVIS for NBI redistribution simulations discussed later on.

(figure 5.4(d)) or q -profile (figure 5.4(e)), which is shaped by the current density profile. A series of helical cores were obtained by varying the normalisation of the total current between 333kA and 340kA, effectively bringing q_{min} closer to unity (see black crosses on figure 5.5). As seen on that figure, the helical displacement grows up to a maximum of $\delta_h \sim 0.27$ while q_{min} flirts with unity. Because flux surfaces become strongly compressed in the region between the helical core and the axisymmetric mantle, namely the *transition region*, the Jacobian of the VMEC coordinate system can approach zero (see right plot of figure 5.5 and figure 5.9(d)). This indicates that a current sheet is forming in the limit $q_{min} = 1$. In reality, if q_{min} reached unity, finite resistivity would lead to the formation of magnetic islands (tearing and reconnection) which would eventually smooth the abrupt transition out. To be consistent with the ideal MHD treatment, a choice of 6 equilibria with $q_{min} > 1$ depicted with red diamonds on figure 5.5 are used in later fast ion simulations.

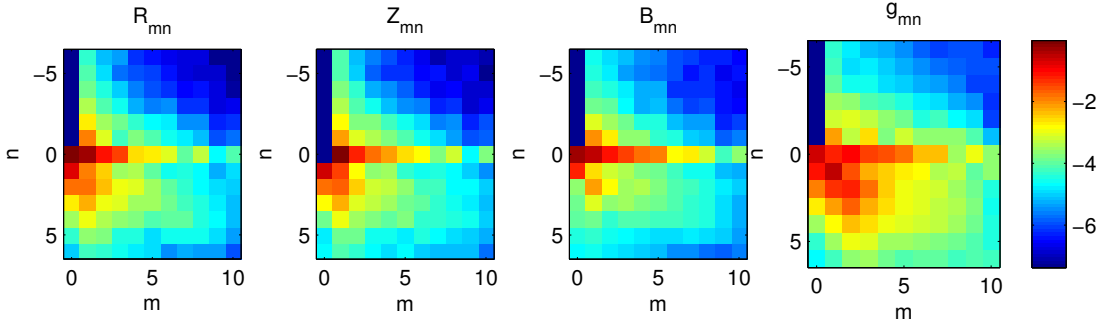


Figure 5.6 – Maximum amplitude of poloidal m and toroidal n modes for the largest helical displacement of $\delta_h = 0.23$. Colour scale is logarithmic, i.e. amplitude is $X_{mn} = 10^C$ where C is the colour.

VMEC converges, with a minimal set of poloidal and toroidal modes, to an equilibrium state that respects the MHD force balance to machine precision. We have chosen a spectrum of poloidal modes $m = 0, 1, \dots, 11$ and toroidal modes $n = -6, -5, \dots, 5, 6$ over a radial grid of 288 points (equidistant in Φ/Φ_e). Although a rigorous convergence study of VMEC's solutions has not been carried out, it is agreed that additional mode content as well as a larger number of radial points does not significantly improve the precision of their representation. As illustrated on figure 5.6, the amplitude of modes with higher mode number decays to the extent where extra precision unnecessarily impedes the spline-Fourier interpolation (see figure 4.5 and

comments of section 4.2).

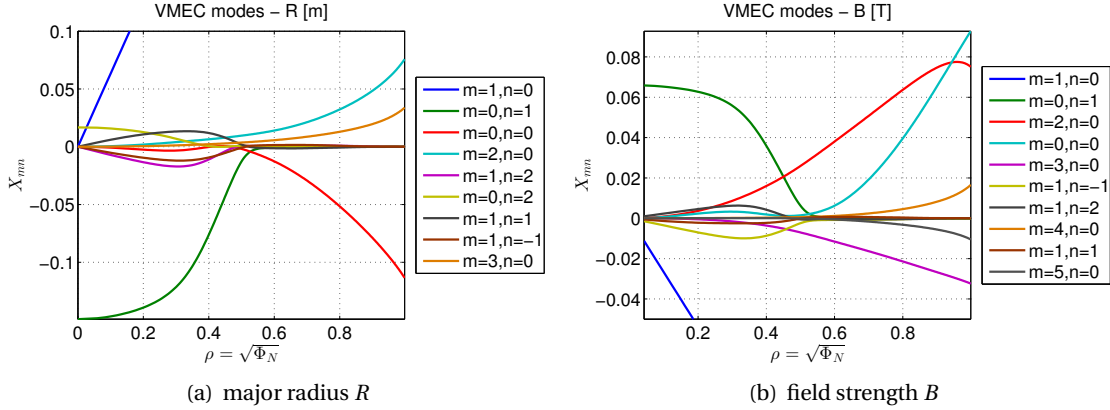


Figure 5.7 – Largest poloidal and toroidal core modes from VMEC bifurcated helical solution with $\delta_h = 0.23$. The value on axis of the $m = n = 0$ mode has been subtracted. The dominant $m = 1, n = 0$ mode exceeds the limits of the plots and grows to a maximum of $R_{10} = 0.5m$ and $B_{10} = -0.3T$ at the edge.

As seen on figure 5.7 displaying the largest modes in the spectrum, the helical core equilibrium is characterised by a dominant $m = 0, n = 1$ helical mode (kink) and various $n \neq 0$ side-bands that spoil axisymmetry in the core. These modes fade to zero just beyond the q_{min} surface. A large $m = 1, n = 0$ mode (blue cropped curve on figure 5.7) linearly increases with the radial label. Although it is expected in the axisymmetric case, its interpretation is different in the kinked case because the reference for the poloidal angle is now the helical magnetic axis. The coordinate system near the magnetic axis is approximated as

$$R \approx R_0 - \delta_h \cos v + \rho \cos u \qquad Z \approx -\delta_h \sin v + \rho \sin u \qquad (5.3)$$

such that the poloidal angle u is pictured as the angle formed with a horizontal plane crossing the helical axis. Because of this helical viewpoint, the 3D equilibrium spectrum should not be confused with that an ideal internal kink, which is usually considered as small deviations from axisymmetry.

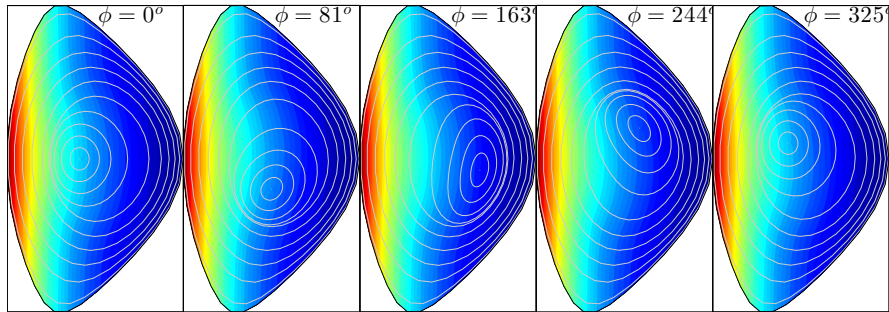


Figure 5.8 – Field strength of the helical core solution with $\delta_h = 0.23$ at various toroidal angles. The behaviour of B is largely axisymmetric, corresponding to the standard tokamak $1/R$ dependency.

In fact, the field strength B is mostly axisymmetric even though the geometry of the flux-

surfaces in the core is helical, as observed on figure 5.8 showing B on a poloidal cross-section at various toroidal angles. This tokamak-like behaviour spoils helical symmetry and, in addition to the induced toroidal current, makes such magnetic configurations different from classical stellarator equilibria. It seems that the helical core solution actually resembles the state of quasi-axisymmetric stellarators.

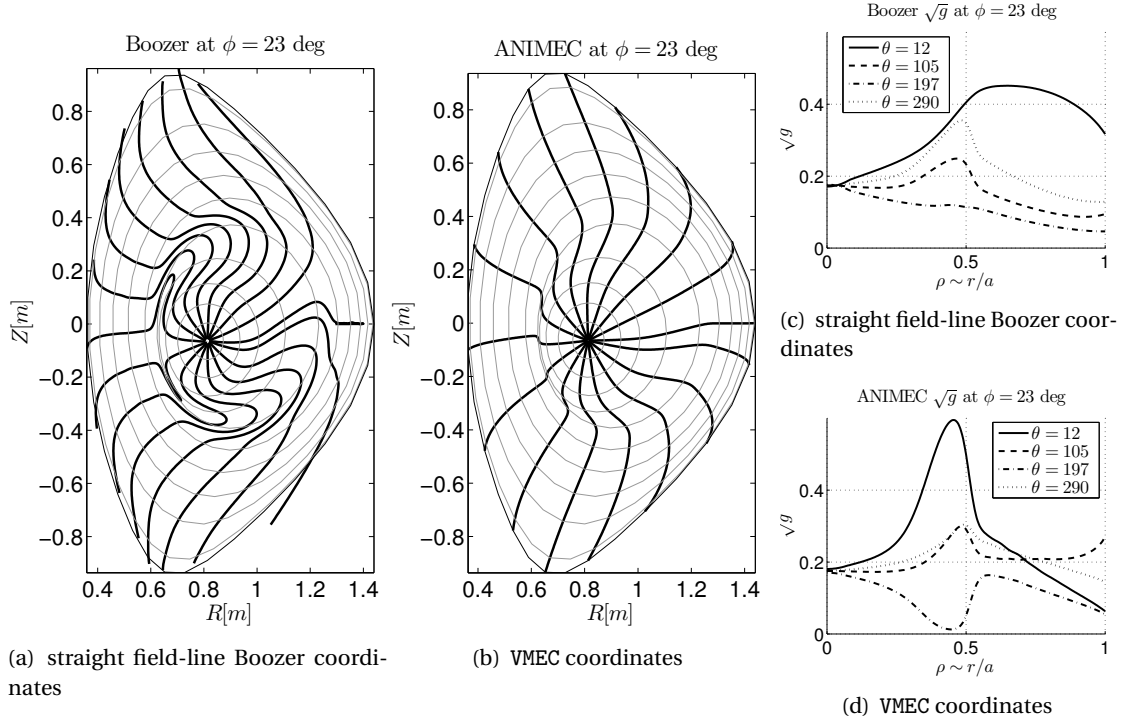


Figure 5.9 – (left) Constant poloidal angle lines in different coordinate systems at a fixed toroidal angle $\phi = 23$ degrees in the largest helical displacement of $\delta_h = 0.23$. (right) Jacobian of the coordinate transformation at a fixed toroidal angle $\phi = 23$ degrees as a function of radial label ρ for different poloidal angles in the largest helical displacement of $\delta_h = 0.23$.

The transition between the helical core and the axisymmetric mantle is smoother than the analytic picture of the ideal internal kink mode modelled as a top-hat function. The representation of the transition region is numerically challenging but crucial for solving fast particle orbits. The implemented guiding-centre equations (3.12) are inversely proportional to the coordinate Jacobian \sqrt{g} such that, in VMEC coordinates, small inaccuracies in the field values lead to greatly varying force terms. In the straight field-line Boozer coordinates, for which the Jacobian is proportional to $B^2 \sim 1/R^2$ and apparently far from zero (see figure 5.9(c)), the transition region exhibits extreme bending of constant poloidal angle curves (see figure 5.9(a)). This leads to strong variations of the metric elements, implying that terms like $\partial_\theta B$ and $B_s = \mathbf{B} \cdot \mathbf{e}_s$ have rapidly varying dependencies in the Boozer angles so that the GCDE will also contain large force terms (see equations C.25 derived in the appendix). In practice, Boozer coordinates are numerically disadvantageous to represent this particular equilibrium because more than 1000 Fourier modes must be kept to calculate the straight field-line metric. In contrast, using VMEC coordinates, the constant poloidal angle curves are more regular (see figure 5.9(b)), with the advantage that fewer modes are required (about 2 orders of magnitude less). The numeri-

cal difficulties with Boozer coordinates has led to the abandon of a canonical formulation of GCDE in favour of a more general treatment with non-canonical coordinates, as derived in section 3.3.1. The issues with the transition region also initiated the implementation of the spline-Fourier interpolation scheme described in section 4.2, which is essentially designed to ensure continuity in poloidal and toroidal angles, and continuity up to second derivative in the radial direction. The spline-Fourier technique guarantees the smoothness of the orbits even when the Jacobian is close to zero and does not allow flux-surfaces to artificially cross each other, which can happen with mesh-based and finite element interpolation techniques.

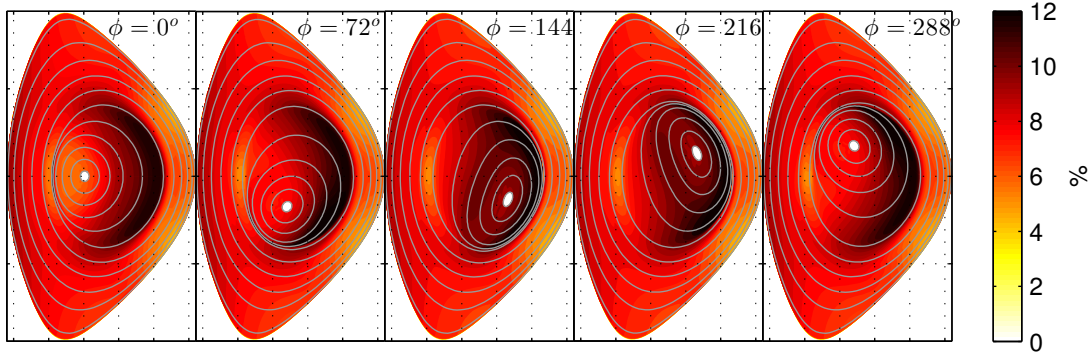


Figure 5.10 – Field variation criterion $|(\boldsymbol{\rho}_\perp \cdot \nabla)\mathbf{B}|/B$ (equation 3.37) represented on $R - Z$ planes at successive toroidal angles and applied to MAST helical core of $\delta_h = 0.23$ and a D^+ ion with $E_\perp = 10$ KeV, $\rho_L \sim 5.5$ cm. Gray dashed lines depict flux-surfaces; at $\phi = 0$, the compressed region is around $u = \pi$ and uncompressed around $u = 0$.

Due to the low-aspect ratio of MAST and its relatively high beta value, the perpendicular variation of the magnetic field $|(\boldsymbol{\rho}_\perp \cdot \nabla)\mathbf{B}|/B$, whose evaluation is derived in section 3.5, is sizeable even in the axisymmetric case (see related analysis of MAST field variation in section 3.5.3). The widest problematic region for first-order GCDE is located on the low field side of the core where the field variation can rise up to 12% for deuterium ions with $E_\perp = 10$ KeV ($\rho_L \sim 5$ cm), as seen on figure 5.10 showing a map of the field variation at various toroidal angles in an equilibrium with a helical core of amplitude $\delta_h = 0.23$. Figure 5.11(a) plots the maximum eigenvalue of $|\nabla\mathbf{B}|_{\max}/B$ at mid-plane (bold red curve). It also shows various constituents such as perpendicular gradients $|\nabla_\perp B|/B$, curvature $|\mathbf{B} \times (\nabla \times \mathbf{B})|/B^2$ and parallel currents $|\mathbf{B} \cdot (\nabla \times \mathbf{B})|/B^2$. The dominant contribution is due to the perpendicular gradient of $|B|$ (exact contribution) as in the axisymmetric case (see section 3.5.3). This is deduced from the fact that the green curve falls right under the bold red curve on figure 5.11(a) in the high-field side between 0.4m and 0.6m and in the low-field side between 1.25m and 1.4m. In the region between 0.6m and 1.2m, the gap formed between the maximum field variation and the gradient is due to parallel currents and field-line shearing, as observed from the rising purple curve (partial contribution³). The core region is characterised by low shear close to the resonant layer, which explains the formation of parallel currents. The latter spike in the region where the flux-surfaces are tightly compressed ($R = 0.6$ m on figure 5.11(a)). The discrepancies between

³Only a fraction of the parallel current enters in the maximum field variation which is why the purple curve exceeds the red curve in the core region. The correct fraction is determined by projecting in the perpendicular direction to the magnetic field.

5.2. Particle orbits in helical cores, drift surfaces and drift islands

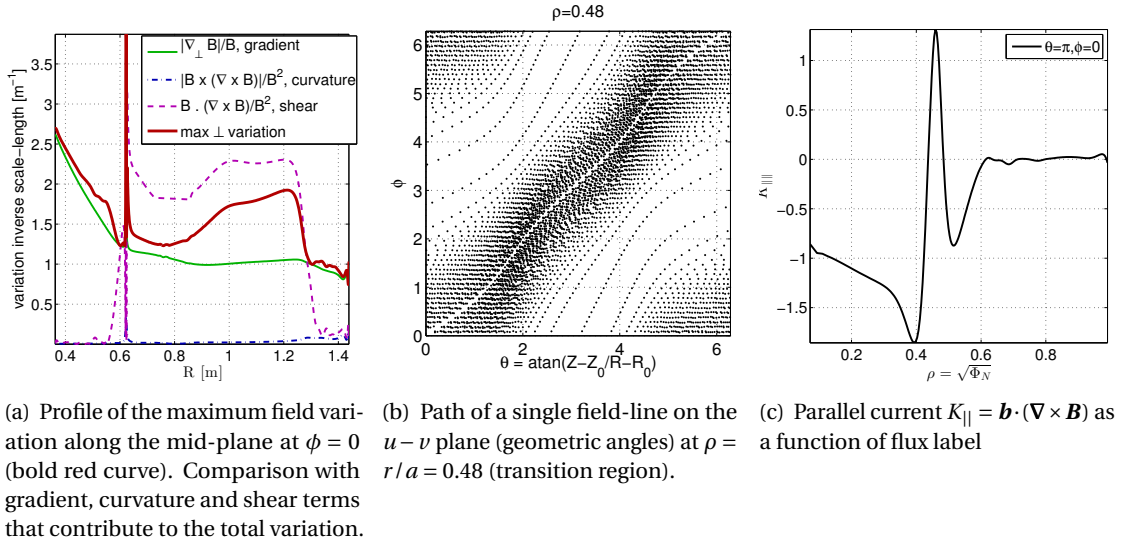


Figure 5.11 – Characteristics of the transition region between the helical core and the axisymmetric mantle of the MAST $\delta_h = 0.23$ distorted equilibrium.

guiding-centre and full-orbit calculations are expected to be magnified in this region, mostly affecting the interpretation of the parallel velocity, as discussed in section 3.5 and in analogy with particle orbits in the purely-sheared magnetic field example of section 3.4. In principle, second-order terms such as the Baños correction $\frac{1}{2} \frac{m}{q} \mu v_{\parallel} \mathbf{b} \cdot (\nabla \times \mathbf{b})$ (see equation 3.31) should be included in the definition of the guiding-centre Lagrangian in order to account for strong parallel currents. The implementation of these corrections is not straight-forward and is the subject of on-going work.

Figure 5.11(b) traces the path of a single field-line at a given flux label in the transition region on the periodic plane (θ, ϕ) (geometric poloidal and toroidal angles). The field-lines are observed to avoid the compressed flux-surface zone; the $\phi - \theta = 0$ uncompressed region is more densely visited by field-lines than the $\phi - \theta = \pi$ compressed region such that their bending (S-shape) is more pronounced in the latter region. Even though the flux-surface average shear of the q -profile is weak (zero at q_{min}), the local pitch of the field varies extensively at different poloidal and toroidal angle on a flux-surface but also from one surface to the next. Field-lines are locally strongly sheared, analogously to the example of section 3.4. In the limit where the q -profile reaches unity and in the framework of ideal MHD, an infinite current sheet will form. As previously argued, resistive effects would however soften the sharp transition in generating magnetic islands and a different approach for generating the equilibrium should be considered for the resonant q case.

5.2 Particle orbits in helical cores, drift surfaces and drift islands

Without providing an exhaustive classification of orbits in helical cores, the following general statements are made. Two properties of the helical core equilibrium guarantee the confinement of fast particles. First, the outer region effectively acts as a pinch, in which confinement

is preserved by virtue of axisymmetry. Particles that stay in the axisymmetric mantle will exhibit usual bounce or banana motion. Second, as argued in section 3.3.1, the topology of guiding-centre trajectories is analogous to perturbed field-lines, at least for passing particles. The assumption of nested flux-surfaces in VMEC automatically implies the integrability of field-line equations (see section 2.2 and 2.3.2). As a consequence of the KAM theorem and the first-order expansion of GCDE, the guiding-centre motion (especially that of passing particles) will mostly remain quasi-periodic (Lichtenberg and Lieberman, 2010) and the trajectories will align on smooth drift-surfaces. Orbits near rational surfaces will be subject to resonance (in the Hamiltonian sense), thus forming drift-islands. Orbit losses will consequently not increase in the presence of the internal kink structure and super-banana transport should not be observed. The helical distortion of the core provokes exotic drift orbits similar to those found in stellarators but different in that the field strength is not helically symmetric but mostly axisymmetric.

Guiding-centre calculations

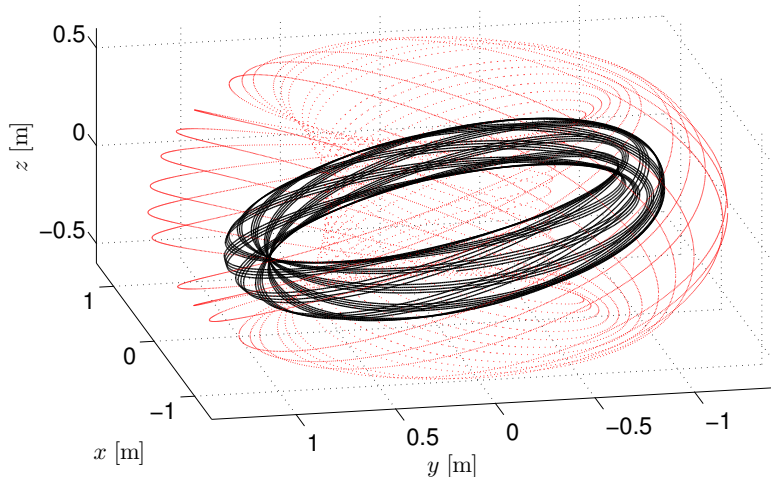


Figure 5.12 – 3D trajectories of typical 10 KeV co-passing ($v_{\parallel}/v = 1$) deuterium guiding-centre in the helical core equilibrium with displacement $\delta_h = 0.23$: in the helical core (black curve) and in the axisymmetric mantle (red dotted curve). Orbits are here calculated in VENUS-LEVIS with first-order GCDE (3.12).

Two examples of deeply-passing guiding-centre trajectories (computed in VENUS-LEVIS using first-order GCDE) are shown on figure 5.12, one in the helical core (black) and the other in the axisymmetric mantle (red). Because of the small deviation of drift surfaces from the flux-surfaces, passing particles in the helical region have, on top of the bounce motion, a slower bounded radial excursion with respect to the helical axis, as shown on figures 5.13(a). Figure 5.13(c) displays two orbits of trapped-particles on the $R - Z$ plane (again using GCDE to solve their motion). Trapped particles are typically able to wander in and out of the kinked region causing perturbed banana orbits.

A significant fraction of particles regularly skirt the magnetic axis (see figure 5.13(b) but also 5.14(b)) because drift surfaces naturally intersect it. This is a major difference with

5.2. Particle orbits in helical cores, drift surfaces and drift islands

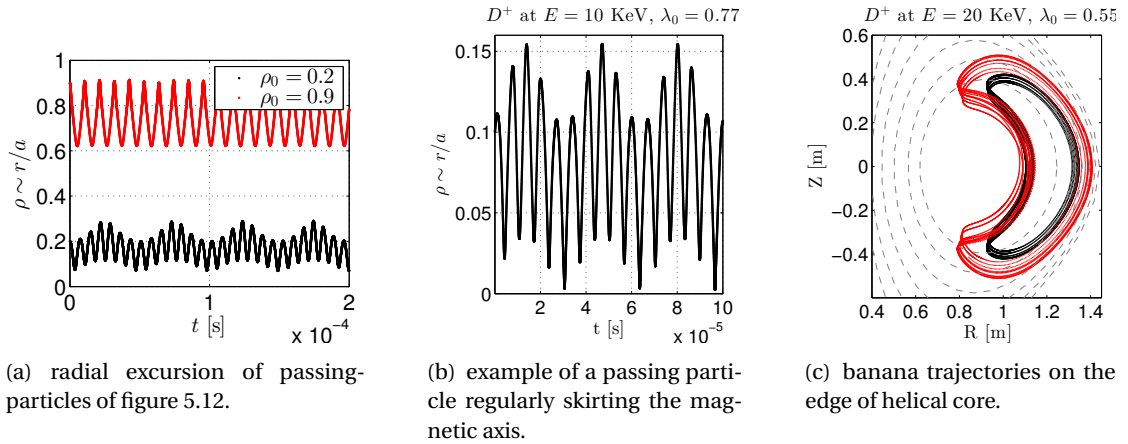


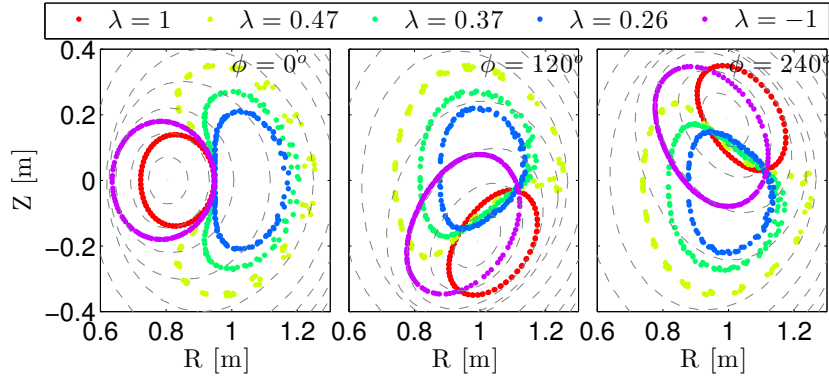
Figure 5.13 – Typical fast deuterium orbits in the helical core equilibrium; (left) two perturbed bananas initialized at different minor radii, (right) particle frequently passing close to the magnetic axis.

axisymmetric cases where difficulties with the magnetic axis only occur through collisional processes. Due to the singular nature of flux coordinate systems, trajectories close to the axis require finer computational effort, which makes helical core simulations heavier. The region where flux surfaces are compressed is also numerically challenging and remains the main source of error in the simulation. It covers a limited region in real space such that particles spend little time there. Spurious particle motion is damped thanks to the robust spline-Fourier representation of the equilibrium and convergence of energy conservation is numerically achieved.

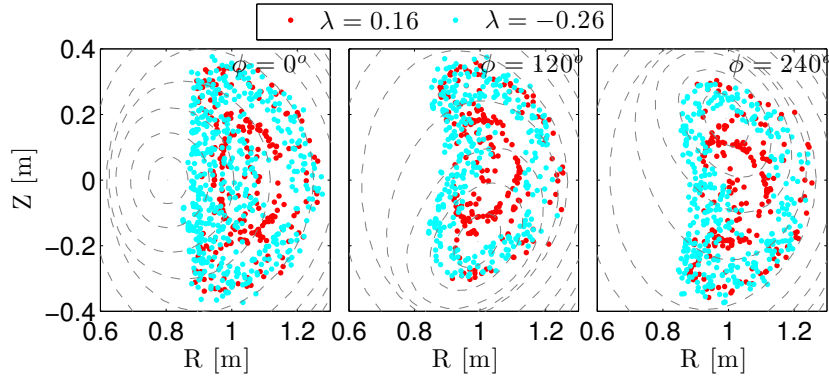
Full-orbit calculations

As discussed earlier in this chapter but also in section 3.3.1, the existence of drift surfaces is a consequence of the guiding-centre formulation. It is not obvious that full-orbits will follow such smooth structures in the presence of the helical core. In axisymmetric magnetic fields, drift surfaces are a direct consequence of the conservation of toroidal momentum and the adiabatic invariance of the magnetic moment. In helical states, the fact that drift surfaces exist indicates that there is a non-trivial constant of motion, possibly a combination of toroidal and poloidal momentum, related to the symmetry behind the (forced) existence of nested flux-surfaces. On a poloidal cut at a fixed toroidal angle, drift surfaces are reduced to closed contours, progressively drawn by the punctures of the guiding-centre trajectory across that same vertical plane. Figure 5.14(a) shows such guiding-centre trajectories, computed from full particle orbits⁴. As long as particles do not transit from the helical region to the axisymmetric outer mantle, helical drift surfaces are clearly present despite using full-orbit equations (see equation 3.7). If particles transit out of the core, their motion is randomised by successively following helical and axisymmetric drift surfaces (see figure 5.14(b)). These Poincaré plots prove that particle confinement is not necessarily degraded by the presence of the helical

⁴To locate the guiding-centre position in curvilinear coordinates, the switching algorithm of section 3.6.1 is employed.



(a) Particles staying in the helical region draw out drift surfaces, projected as closed contours on poloidal planes.



(b) Particles transitioning between helical core and axisymmetric mantle display chaotic motion.

Figure 5.14 – Poincaré section of the guiding-centre trajectories of a set of 10 KeV D^+ ions initialised at $\rho = \sqrt{\Phi/\Phi_e} = 0.22$ and $\phi = \theta = 0$ but with different pitch-variable $\lambda = v_{||}/v$. The guiding-centre position are traced from the particles' full-orbit in this MAST $\delta_h = 0.23$ helical core.

kink. The existence of drift-surfaces in a full-orbit computation allows us to conclude that the dynamics of fast ions are correctly portrayed by GCDE. Finally, it demonstrates the robustness of VENUS-LEVIS to solve the motion of charged particles in extremely distorted curvilinear coordinates.

In anticipation to the next section on NBI deposition, it is mentioned that MAST PINIs emit neutrals at the energy of 60 KeV. Larmor radii of trapped particles at these energies are a few centimetres large, but since injection is tangential, the kind of fast particles produced are almost exclusively passing, especially in the core region close to the helical magnetic axis. It is instructive to focus on single particle orbits with initial pitch-variable $\lambda = v_{||}/v$ close to unity (small magnetic moment). For particles with a pitch-variable equal to unity (zero magnetic moment), the guiding-centre equations trivially reduce to $v_{||} = v = \text{const}$. For maximum value of the pitch-variable $\lambda = v_{||}/v = \pm 1$, drift surfaces are closest to flux-surfaces (see red and purple curves on figure 5.14(a)). On Poincaré sections of figure 5.15, it is observed that, while all deeply counter-passing particles travel around the plasma magnetic axis (figure 5.15(b)), some deeply co-passing particles circulate on drift surfaces that do not enclose the helical

5.2. Particle orbits in helical cores, drift surfaces and drift islands

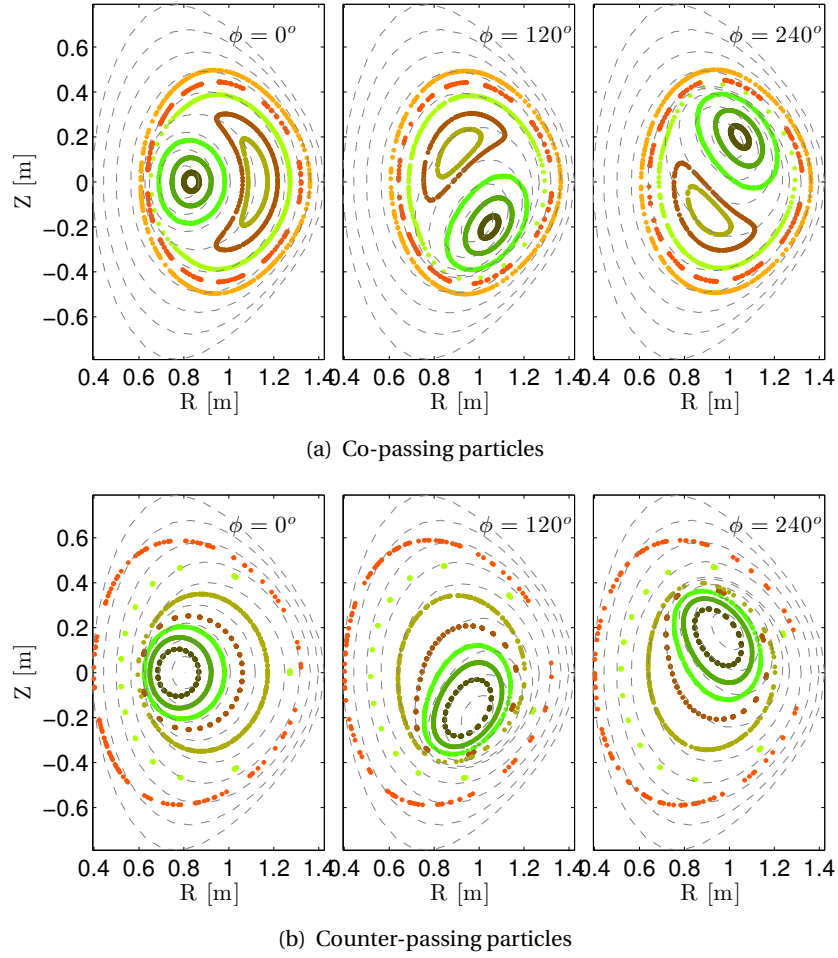


Figure 5.15 – Poincaré cut of drift surfaces created by 10 KeV D^+ ions initially with $v_{\parallel}/v = \pm 1$ as computed using full-orbit equations in MAST helical core with $\delta_h = 0.23$ displacement.

magnetic axis in the region of uncompressed flux-surfaces (figure 5.15(a)). Those co-passing particles move around a *helical drift axis*, positioned on the opposite side of the magnetic axis inside the kinked core. Consecutive punctures through the poloidal plane circle around what appears to be a new helical axis. The q -profile being close yet always above unity, the expected behaviour without drift effects would be that of field-lines, wrapping around each flux-surface in the same poloidal direction (clockwise). Instead, starting at a specific radial position, these co-passing particles are able to complete more than a poloidal turn after one toroidal turn, boosted by the drift correction $\rho_{\parallel} \mathbf{B}$ appearing in the guiding-centre Lagrangian. Although the orbit definitely qualifies as passing, because $v_{\parallel}/v = 1$ is constant (no magnetic mirror), the result is that successive punctures seem to reverse, effectively creating the structure of a *drift-island*. This pattern is not observed for deeply counter-passing particles with identical initial conditions except $v_{\parallel}/v = -1$, because the drift term is odd in v_{\parallel} with respect to the motion along the field lines. It is mentioned that the size of the drift island scales with the energy, consistent with a drift effect. The important consequence of this exotic motion is a reduction of fast ion density and pressure in the core, as well as particle bunching in the area of uncompressed flux surfaces. That behaviour is in part responsible for off-axis redistribution

of NBI fast particles, evidenced by MAST neutron camera traces and illustrated numerically in the slowing-down simulations presented in the next section.

In full-orbit calculations, particles develop non-zero gyro-motion even though their pitch-variable is initially equal to unity (zero Larmor radius). The magnetic moment $\mu = mv_{\perp}^2/2B$, the lowest-order adiabatic invariant, is indeed not constant as the particle gyrates around the variations of the magnetic field. Instead, the magnetic moment oscillates around an average value. Second-order corrections to the drift equations like Baños terms are proportional to the magnetic moment. Deviations are expected to be minimal for deeply-passing particles where $\mu \sim 0$. The troublesome region of compressed flux-surface is geometrically very small such that few NBI particles are deposited in it. A low fraction of guiding-centres cross through this area, similarly to the field-lines avoiding the compressed region (see figure 5.11(b)).

The investigation of fast particles with larger Larmor radii, e.g. resulting from Ion Cyclotron Resonance Heating (ICRH) or fusion processes, in similar MAST magnetic configurations will however require the use of higher-order GCDE or a full-orbit approach. The switching techniques described in section 3.6 in conjunction with the field variation criteria of section 3.5 should greatly help completing fast ion confinement simulations on moderate computational resources.

5.3 Slowing-down simulations of NBI distributions

With the knowledge gathered in previous sections, the redistribution of NBI hot particles due to saturated ideal internal kink modes is now addressed. VENUS-LEVIS is employed to follow the guiding-centre motion of several hundred thousand markers over slowing-down timescales, including the action Monte-Carlo kicks (see section 4.5). The sampled spawning of markers constitutes the source term of the slowing-down approach. The random Monte-Carlo kicks act on the energy (slowing-down) and pitch-angle (scattering) of the markers in order to emulate Coulomb collisions with the background plasma. Each marker is followed until it reaches a multiple of the thermal energy (an arbitrary factor of 3 was chosen for the simulations presented here), after which it is no longer considered part of the hot particle distribution. This mechanism represents the sink of the slowing-down model. Eventually the source and sink term balance out such that the distribution saturates. The saturated distribution is considered to model the deposition of fast particles due to NBI. Moments of the saturated distribution, such as density, current and pressure, are compared for various equilibria increasing the helical displacement. MAST NBI ions enter the plasma at around 60 KeV, an energy at which collisions are rare. It takes about $\sim 0.05s$ for the whole distribution to slow-down, which is why a precise and robust orbit solver is necessary. The combination of long marker following time, and the radial drift excursions of particles in the core region due to the three-dimensional geometry, means that many markers will pass close to the magnetic axis and the transition region.

The initial position, velocity and weight of all markers are pre-computed according to the characteristics of MAST PINIs and the temperature and density profiles used to generate the equilibrium (see figure 5.4). The details of the external NBI routines in charge of marker

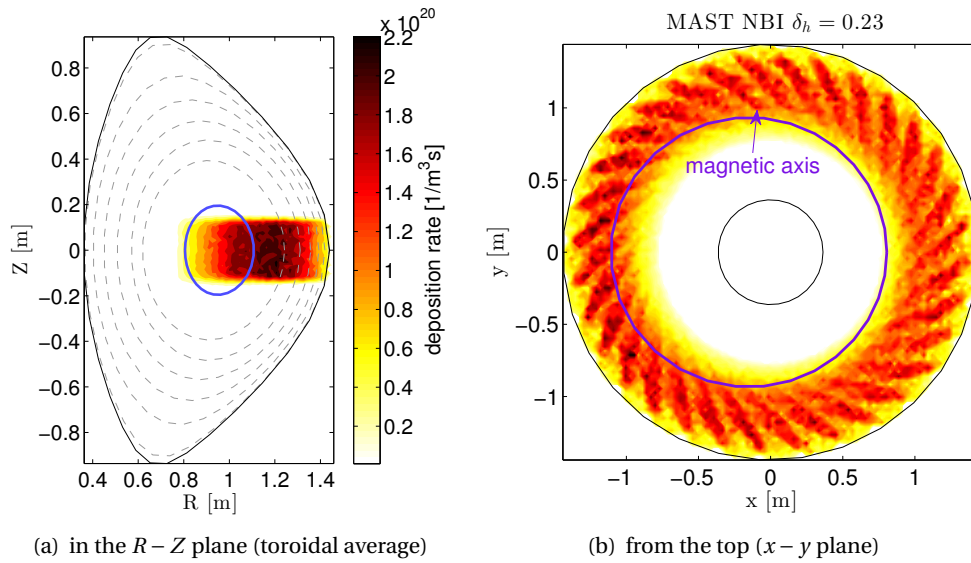


Figure 5.16 – Deposition rate of NBI markers. The purple line depicts the path of the helically displaced magnetic axis.

deposition are described in section 4.4. The particularity here is that 32 virtual PINIs are placed every $1/32^{nd}$ of a turn to account for the rotation of the plasma relative to the neutral beam. In this way, particles are evenly deposited around the kinked equilibrium instead of at a preferential angle with respect to the helical core. The birth position of NBI markers is not perfectly axisymmetric, as seen on figure 5.16(b) where the 32 beam-lines are clearly identified. This toroidal pattern is washed out during slowing-down simulations such that increasing the number of duplicated PINIs does not significantly improve the final saturated results. In the presence of the kink, the ionisation rate has an additional and important toroidal dependency, as noticed on figure 5.16(b) by the weak colour imbalance between the left side (where the magnetic axis passes through the hot-spot) and the right side (where the magnetic axis is too far inside the device). This asymmetry is caused by the helical geometry of flux-surfaces and the fact that temperature and density profiles are 3D flux functions. Consequently, the

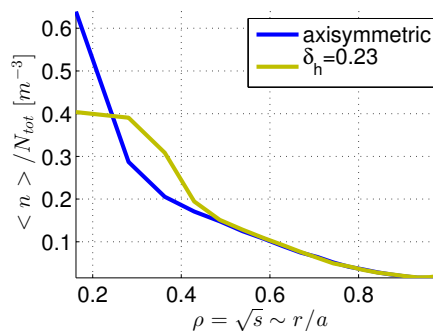


Figure 5.17 – Comparison of flux-surface average deposition rate (NBI birth profile) between axisymmetric equilibrium and helical core.

flux-surface average of the deposition rate is flatter in the helical core than in the axisymmetric

case, as depicted on figure 5.17.

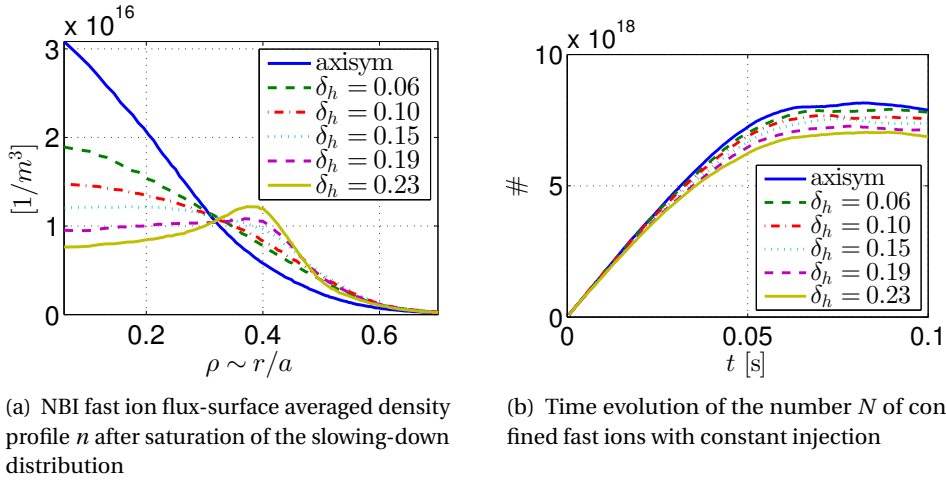


Figure 5.18 – Saturated flux-surface averaged density profile of MAST NBI fast particles and its evolution in time for an increasing helical displacement δ_h .

The (helical) flux-surface averaged density profiles of the saturated NBI distributions are shown on figure 5.18(a). They are observed to progressively hollow out near the magnetic axis as the helical displacement δ_h increases, which is a combination of two effects. First, the fast ion birth profile starts flatter than in the axisymmetric case. Secondly, as evidenced in the previous section, particles undergo large radial drifts due to the 3D geometry of the kink, which also contributes to erase gradients in the density profile. For the most extreme

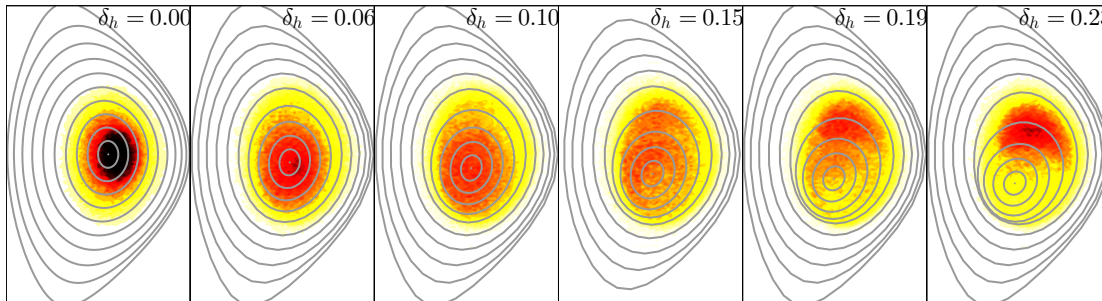


Figure 5.19 – Hot particle density shifting from the magnetic axis to the uncompressed region as the helical displacement expands ($\phi = 23.2$ degrees)

helical core, the density profile peaks off-axis, resulting from the bunching of co-passing particles in the uncompressed flux-surface region. The poloidal cut of the fast ion density at a fixed toroidal angle on figure 5.19 confirms that the hot particle density gradually shifts from the core (magnetic axis) to the uncompressed flux-surface region of the equilibrium as the helical displacement becomes large. These simulations show that, in the presence of very large helical kinks, NBI particles, supposed to heat the plasma around the magnetic axis, are in fact deposited at an off-axis location. Such off-axis heating will have a degrading effect on the plasma, not least on the driven current.

Similar flattening and off-axis peaking appears in the fast ion pressure and current profiles,

5.3. Slowing-down simulations of NBI distributions

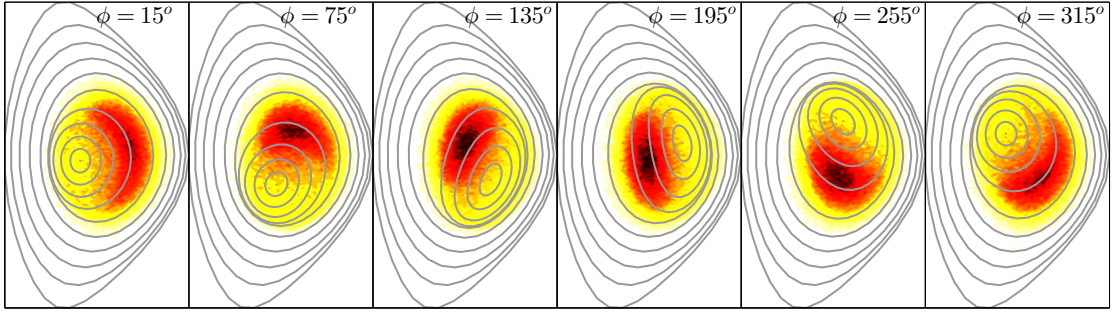
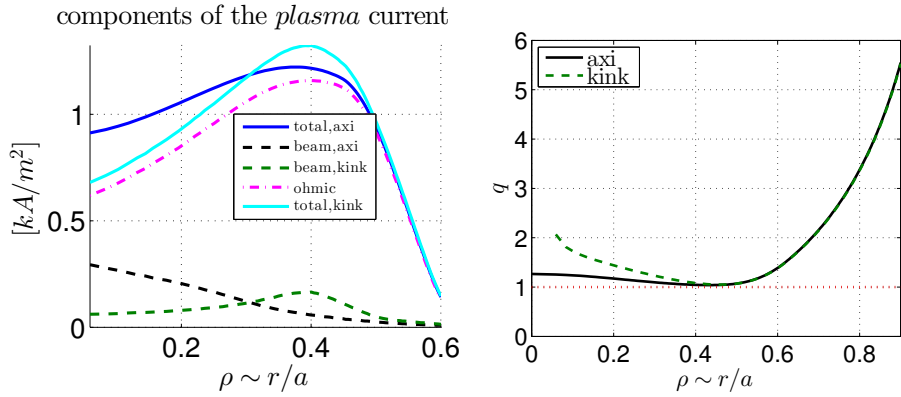


Figure 5.20 – The NBI fast ion density follows the helical geometry forming a hot spot in the uncompressed flux-surface region of the most extreme helical displacement $\delta_h = 0.23$.

which could partially explain why fishbones disappear during LLM activity, i.e. the LLM efficiently removes the fast ion pressure gradient drive for fishbones. Additionally, the resonance between fishbones and toroidal drift precession is modified in 3D such that there are many (weaker) characteristic frequencies.



(a) Estimation of the beam current drive from NBI fast particles (b) Effect of hollow beam current profile on the q -profile.

Figure 5.21 – Estimation of the effect of a hollow beam current profile on the q -profile.

The beam current drive (see figure 5.21(a)) is coarsely estimated by multiplying the saturated hot ion current by the following drag factor $j_d = 1 - (1 - 1.46\sqrt{\epsilon}A_Z)/Z_{eff}$, where $\epsilon = r/R_0 = \rho a/R_0$, $Z_{eff} \approx 1.66$ and $A_Z \approx 1.5$ (Connor and Cordey, 1974; Start et al., 1980)⁵. The values in figure 5.21(a) are compared with an axial ohmic current density of $1.2 kA/m^2$. The predicted off-axis current drive will tend to accentuate the q -profile reversal, as quickly deduced from the approximate relation for perturbation to the safety factor $q_{kink} \approx qI/I_{kink}$. Figure 5.21(b) shows a recalculation of the total q -profile, given the beam driven current of figure 5.21(a). It is noted that the LLM redistribution of NBI current drive goes against the flattening of the q -profile and will tend to delay the time at which q becomes rational, and in this sense it is seen that the LLM is beneficial, as pointed out by Menard et al. (2006). Notice that the modification of the bootstrap current due to 3D and the change in the bulk pressure has not

⁵Note that the derivation of the drag factor assumes axisymmetry. A more elaborate neoclassical treatment should be used to adjust for the helical geometry.

been calculated. This effect may be more important than the change in current density just described. On-going work is addressing the topic of bootstrap in 3D equilibrium.

5.3.1 Comparison with experimental neutron camera data

Experiments have reported that helical kinks affect fast particle confinement. The effect is evidenced in particular by neutron camera data (Ceconello et al., 2010), a reliable diagnostic that has the advantage of being directly proportional to fusion processes between fast ions and background deuterium, thus providing a clean measure of hot particle densities.

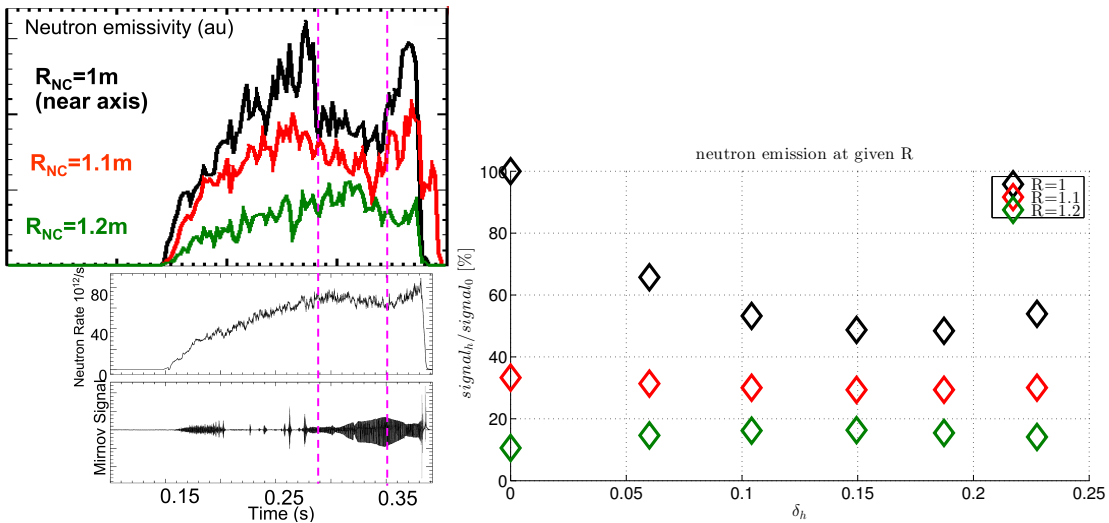


Figure 5.22 – Comparison between experimental time traces of neutron emission and simulated signals in increasing helical amplitude. (left) Time evolution of the neutron emissivity during growing and shrinking phase of LLM at different major radii; (right) Virtual neutron emissivity as a function of helical displacement. Black, red and green data match the corresponding curves in both plots.

Considering a series of MAST discharges around pulse #26887, Ceconello et al. (2012) observe that, before the onset of the LLM, the neutron emissivity is maximal in the area around the magnetic axis represented by the black time-trace on the upper left plot of figure 5.22. The neutron emissivity drops in the core region as soon as the LLM appears (see Mirnov time-trace on the lower left plot of figure 5.22), to the benefit of the outer region (small increase of the green curve $R = 1.2\text{m}$ on the top left plot of figure 5.22). The total neutron rate however remains constant during the LLM activity (central left plot of figure 5.22), which suggests that global confinement is not lost but fast particles are mostly redistributed. During the LLM phase at $t = 0.33\text{s}$, the neutron signal as a function of the impact parameter (green squares on figure 5.23(a)) is flatter and broader than the signal at $t = 0.25$ (black data points of figure 5.23(a)) and reaches its maximum on the high-field side of the machine. This is a counter-intuitive result in the context of 2D equilibrium and is partly why transport models fail to replicate experimental time-traces. As the mode fades away (Mirnov coils on figure 5.22), the neutron production in the central region nearly returns to its initial intensity, suggesting that fast ions move back into the core.

These experimental facts are qualitatively recovered by VENUS-LEVIS simulations. We com-

5.3. Slowing-down simulations of NBI distributions

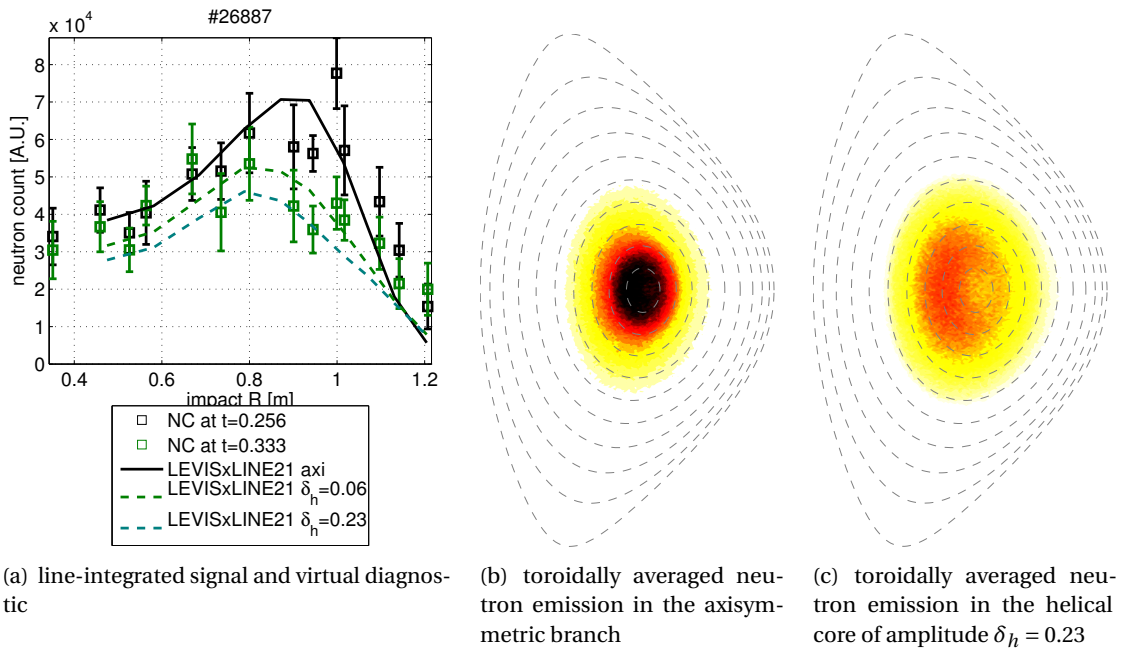


Figure 5.23 – Comparison between MAST experimental neutron camera traces around pulse #26887 (Ceconello et al., 2012) (top) and virtual diagnostic from saturated NBI distributions (bottom). The black (red) signal on the top plot represents the neutron emission before (after) LLM activity. It compares with the black curve on the bottom plot from numerical simulations based on an axisymmetric equilibrium. The top green data during LLM is put in relation with the bottom green dashed curve from neutron emission in helical core.

pare them via a synthetic diagnostic of the neutron camera, whose details are presented in section 4.6.1. The virtual diagnostic computes the probability for each marker to participate in fusion reactions with the deuterium background according to beam-on-target rates of DD reactions (Bosch and Hale, 1992; Miley and Towner, 1975). The toroidally averaged fusion rate, obtained at the end of each slowing-down simulation, is considered to model the instantaneous neutron emission. In the axisymmetric equilibrium, shown on figure 5.23(b), the emission is focused around the magnetic axis in the core plasma. In the largest helical core (figure 5.23(c)), the neutron rate is broader both vertically and horizontally forming a bean shape that is more intense on the high-field side. This pattern is the geometric consequence of toroidally averaging the fast ion hot-spot in the uncompressed region pictured on figure 5.20.

The final step to compare against neutron camera traces is to integrate the simulated fusion rate along the line of sight of the detector as a function of the detectors tangent radius. For more realistic results, this integration is performed by the LINE2 code (Ceconello et al., 2010), which accounts for the detailed geometry, field of view and sensitivity of MAST neutron camera. In accordance with experimental traces as a function of the impact radius, there is a drop in the central region and a peaking on the high-field side of the neutron emissivity. This already occurs in our NBI simulations for a relatively small helical core of $\delta_h = 0.06$. The drop is slightly more pronounced in the largest kink with $\delta_h = 0.23$ (in turquoise on figure 5.23(a)) but the progression is not as severe as from the axisymmetric case (black curve on the same graph).

The right plot of figure 5.22 is an estimate at a fixed tangent radius of the varying neutron emission with the helical displacement. This graph is put in relation with the time evolution of the neutron camera signal on the top plot of figure 5.22. In both cases, the signal drops significantly in the direction of the (axisymmetric) magnetic axis at impact radius $R = 1$ [m] (black diamonds), stays constant at radius $R = 1.1$ [m] (red diamonds) and slightly increases at $R = 1.2$ [m] (green diamonds). These numerical results indicate that the 3D geometry of helical cores strongly and rapidly affects NBI redistribution, although preserving global confinement of fast particles. If the camera were positioned higher (line-of-sight above the mid-plane), neutron counts would be expected to actually increase during a LLM phase due to the off-axis bunching of NBI ions broadening the hot ion density in the z -direction.

5.4 Conclusions

NBI fast ion redistribution observed in MAST hybrid experiments is accurately modelled by tracking the particle motion in 3D magnetic fields. The saturated state of ideal internal kink modes are conveniently reproduced with stationary helical core equilibria in VMEC. The accurate representation of the kinked geometry of flux-surfaces is important, especially in the region where they are compressed against the axisymmetric outer layers where parallel currents can develop. The spline-Fourier interpolation scheme is vital to yield smooth guiding-centre and full-orbit equations of motion in the curvilinear flux coordinate system. The presence of drift-surfaces and drift islands, resulting from the perturbation of field-lines on nested tori, suggests confinement of passing particles. The quasi-axisymmetric behaviour of the field strength in the core and the outer axisymmetric mantle guarantees good confinement of trapped particles. In addition to asymmetric ionisation, the helical drift pattern created by particles bunching in the uncompressed region causes off-axis NBI heating, off-axis current drive and off-axis neutron emission. The toroidal average of the hot density produces a bean shape neutron production rate that is stronger on the high-field side, exactly like the ones found on neutron camera traces.

In this simple but realistic model, redistribution is a direct consequence of axisymmetry breaking and flux-surface kinking. Fine-tuning of diffusion coefficients or the inclusion of anomalous transport was not necessary to explain redistribution mechanisms. Results would be further improved by taking into account the effect of plasma rotation and the correction to bootstrap current in generating three-dimensional equilibria. Plasma rotation is expected to have an important effect on the motion of particles, giving rise to centrifugal forces in the rotating frame (radial electric field and $\mathbf{E} \times \mathbf{B}$ flows in the laboratory frame) that shift the orbit topology outwards and change the fraction of passing/trapped particles. Work is on-going to include the effect rotation in the GCDE and full-orbit equations. Bootstrap current is expected to affect the equilibrium calculation and to lesser extent the amplitude and geometry of core helical deformations.

The assumption of nested flux-surfaces and stationary equilibrium, which is considered as an important limitation of our model, should be relaxed to allow for the formation of tearing islands as well as regions of stochastic field-lines. In this paradigm, fast ion transport will be enhanced by diffusion across the stochastic layers. However, this requires more sophisti-

cated representations of the magnetic layout, for example using equilibrium codes like HINT2 (Suzuki et al., 2006), PIES (Krommes and Reiman, 2009), SIESTA (Hirshman et al., 2011) or SPEC (Hudson et al., 2012) or non-linear fluid codes such as XTOR. The first class of codes are however incompatible with plasma rotation. Fluid codes like XTOR require heavy computational resources and produce fields that are less smooth than equilibrium codes. Drift-surfaces and conservation properties may not be recovered due to numerical imprecision.

6 Effect of Resonant Magnetic Perturbation on NBI fast ion confinement

In this chapter, VENUS-LEVIS is employed to investigate fast particle losses due to Resonant Magnetic Perturbations (RMPs) with the goal of comparing two contrasting models. Either the RMP field is added to the axisymmetric equilibrium as an external vacuum field (magnetic islands but no plasma response), or an ideal 3D magnetic equilibrium is established including the RMPs (nested flux-surfaces assumed). Accurate slowing-down simulations show different transport properties between the two RMP field models. The approach and results obtained has led to a short publication (Pfefferlé et al., 2015b).

Coils to generate RMPs have been identified as a means to influence deleterious edge magneto-hydrodynamic instabilities known as Edge Localised Modes (ELMs). The prospect of using these coils in normal tokamak operation has led to a very active field of research. First used extensively in the DIII-D tokamak, RMPs were observed to completely eliminate ELMs while maintaining a steady-state high-confinement (H-mode) plasma (Evans et al., 2004). This success is theoretically interpreted by a reduction of edge pressure gradients due to stochastic field-lines induced by the RMPs. Convinced by the beneficial effect, other machines have implemented RMP coils and achieved varying levels of ELM mitigation. In Joint European Torus (JET), type-I ELMs were actively controlled with $n = 1$ perturbation fields (Liang et al., 2007) and mitigated with $n = 2$ fields (Liang et al., 2013). In the Axially Symmetric Divertor Experiment (ASDEX) Upgrade (AUG), significant reduction of plasma energy loss associated with type-I ELMs was observed (Suttrop et al., 2011b). In Mega-Ampère Spherical Tokamak (MAST) however, RMPs actually triggered ELMs in ELM free H-mode periods with $n = 3$ and increased their frequency (Kirk et al., 2010). A similar destabilising effect was found in National Spherical Tokamak eXperiment (NSTX) (Canik et al., 2010). These experimental results are not well understood theoretically, in particular the plasma response to the applied magnetic perturbations and the effective level of stochasticity. This aspect is studied both experimentally (Chapman et al., 2013; Moyer et al., 2012; Schmitz et al., 2008; Suttrop et al., 2011a) and via numerical modelling (Bird and Hegna, 2013; Canik et al., 2012; Chu et al., 2011; Ferraro, 2012; Huysmans et al., 2009; Liu et al., 2012). An overview comparing various theoretical and numerical approaches is reported by Turnbull et al. (2013).

Another important aspect related to RMPs is the induced loss of fast particles on the plasma facing components. Fast ion transport and loss has indeed been observed to increase in the presence of RMPs, in particular causing heat-loads at specific toroidal angles on the wall (Garcia-Munoz et al., 2013a,b) and enhancing prompt losses (Zeeland et al., 2014). The strong effect of RMPs on hot populations is evidenced by various numerical simulations. Most approaches use the so-called “vacuum-RMP” model, where the magnetic field due to the RMP current coils is summed perturbatively on top of a 2D axisymmetric tokamak equilibrium (Asunta et al., 2012; Shinohara et al., 2012; Tani et al., 2012). This approximation, in line with the study of transport due to magnetic ripple, ferritic inserts and Test Blanket Module (TBM)

(Kurki-Suonio et al., 2009; Oyama et al., 2012; Tani et al., 1981), allows for stochastic field-lines but neglects altogether the plasma response. Asunta et al. (2012) claim that fast particle losses simulated with the vacuum-RMP model would represent a “worst-case” scenario, arguing that the plasma would in reality damp or screen the effect of RMPs. Kramer et al. (2013), Garcia-Munoz et al. (2013b) and Zeeland et al. (2014) have investigated fast ion transport in the perturbed fields from the linear resistive runs of the M3D-C1 code and have found opposing results. In this case, RMPs appear to have been amplified locally in the plasma, thus living up to the same resonant perturbations.

The aim of this chapter is to contrast the vacuum-RMP model with the so-called “equilibrium-RMP” model, where a 3D magnetic equilibrium is established in the presence of RMP coil currents using the free-boundary VMEC code (Hirshman et al., 1986a). Retrospectively, this idea has been considered by Spong (2011) in combining VMEC and the DELTA5D (Spong, 2006) codes and to lesser extent by Garcia-Munoz et al. (2013b) by using VMEC and the GOURDON codes. The equilibrium-RMP model, in assuming nested flux-surfaces with a single magnetic axis, does not allow for the formation of magnetic islands nor the appearance of stochastic field-lines inside the last closed magnetic flux-surface. This somewhat goes against the intuitive interpretation of the effect of RMPs. However, it properly accounts for the plasma response in the sense that a saturated ideal equilibrium state is produced, satisfying ideal MagnetoHydroDynamics (MHD) force balance. The simulations presented here, in contrast to previous assertions on fast particle transport related to RMPs, show that the large 3D structures induced by the RMPs can cause important drifts, in effect increasing fast ion losses, which disproves that the vacuum-RMP approach overestimates particle losses. Self-consistent 3D equilibrium states, which allow internal island structures and stochastic domains, would provide the basis for a more elaborate and precise evaluation of fast particle orbits (for example with HINT2 (Suzuki et al., 2006), PIES (Krommes and Reiman, 2009), SIESTA (Hirshman et al., 2011) or SPEC (Hudson et al., 2012)).

According to the Chirikov criterion (Chirikov, 1979), measuring the overlap of magnetic islands, MAST plasmas with RMPs, in line with many other machines, should be characterised by broad stochastic regions. However, the expected mitigating effect has not been seen on type I ELMs (Nardon et al., 2009), pointing to an important plasma response. To compare the two RMP models, the effect of MAST $n = 3$ coil configuration is studied on fast ion populations from neutral beam injection (Neutral Beam Injection (NBI)). Realistic ion sources are produced according to the characteristics of MAST positive ion neutral injectors (Positive Ion Neutral Injector (PINI)s) as described in section 4.4, with a tangential radius of 0.9m, an opening of 21.8cm×8.25cm and a beam spread of 0.6°. The NBI distributions are evolved within the VENUS-LEVIS code using the set of phase-space Lagrangian derived Guiding-centre Drift Equations (GCDE) (see equation 3.12). Fast ion losses resulting from the two different RMP models are assessed.

6.1 Coil configuration and compatibility with stellarator symmetry

VMEC calculations are purposely launched with the constraint of stellarator symmetry. In this context, an axisymmetric equilibrium is automatically up-down symmetric, corresponding

6.1. Coil configuration and compatibility with stellarator symmetry

to Double Null Diverted (DND) discharges. To generate consistent stellarator symmetric 3D fields, a compatible RMP coil configuration must be carefully chosen¹.

MAST is equipped with a set of internal RMP coils consisting of six upper coils spaced toroidally, every 60° above the mid-plane, and 12 bottom coils, every 30° below. The first top and bottom coils are aligned. Each of them is composed of 4 turns of an aluminium alloy filament that can carry up to 1.4kA of current (total of 5.6kAt). Different current patterns can produce a range of perturbations with toroidal mode numbers from $n = 1$ to 6. In order to respect stellarator symmetry, a matching number of upper and lower coils must be activated so that the maximum mode number in our model is limited to $n = 3$. In the case of $n = 3$ perturbations, the current pattern in the the upper coils is a repeated (+, -), where the positive sign means a counter-clockwise current loop, i.e. a right-hand rule vector pointing out of the torus, and a negative sign means a clockwise current loop, i.e. a right-hand rule vector pointing inside the torus. With the 12 lower coils, 4 different phases (90° increments) can be imposed to strengthen the $n = 3$ perturbation. The 4 phases are obtained by cyclically permuting and repeating the current pattern (+, 0, -, 0) in the lower coils. In what follows, 0°-phase corresponds to the current pattern with an "even" parity (figure 6.1(a) and 6.2(a)) and 180°-phase to "odd" parity (figure 6.1(b) and 6.2(c)), where the top and bottom activated coils are aligned and the bottom coils repeat the sequence $\pm(+, 0, -, 0)$. The 90° and 270° phases refer to an alternating activation where the bottom coils repeat $\pm(0, +, 0, -)$ (figure 6.1(c), 6.2(b) and 6.2(d)).

For each current phase, the entire coil setup (including TF coils) must be given a toroidal offset (angle with respect to $\phi = 0$) to enforce stellarator symmetry; the current \mathbf{J} has to become a SS axial-vector (see equation B.11), i.e. $J_R(R, -\phi, -Z) = -J_R(R, \phi, Z)$, $J_\phi(R, -\phi, -Z) = J_\phi(R, \phi, Z)$ and $J_Z(R, -\phi, -Z) = J_Z(R, \phi, Z)$. The offset ϕ_1 indicates the toroidal position of the centre of the first top coil. Figures 6.1(a), 6.1(b) and 6.1(c) justify the various combinations². For 0°-phase (even parity, figure 6.1(a)), the first and last coils (top and bottom) are symmetrically disposed at $\phi_1 = 30^\circ$ and $\phi_6 = -30^\circ$. The direction of the current in the lower horizontal segment (red vector J_ϕ) of the first top coil is then the same as the direction of the current in the upper horizontal segment of the last bottom coil. The direction of the current in the right vertical segment (blue vector J_Z) of the first top coil is the same as the direction of the current in the left vertical segment of the bottom coil. For 180°-phase (odd parity, figure 6.1(b)), the first top and bottom coils are centred at $\phi_1 = 0$ so that the direction of the current in the lower horizontal segment (red vector J_ϕ) of the top coil is the same as the direction of the current in the upper horizontal segment of the bottom coil. The direction of the current in the right vertical segment of the top coil (blue vector J_Z) is the same as the direction of the current in the left vertical segment of the bottom coil. A similar reasoning applies to $\pm 90^\circ$ -phases to yield a toroidal offset of $\phi_1 = \pm 15^\circ$ (figure 6.1(c)).

The vacuum field $\delta \mathbf{B}_{RMP}$, calculated with Coil.Spell (Cooper et al., 2004) (see section 4.3), is either directly sent to VENUS-LEVIS for the vacuum-RMP model or to VMEC that will include

¹After some confusing results, it appeared that the coil configuration used initially in this study was incompatible with stellarator symmetry.

²If the bottom coils are mirrored from the top coils, the paths are defined in the opposite direction such that an additional change of sign must be considered in the coil file.

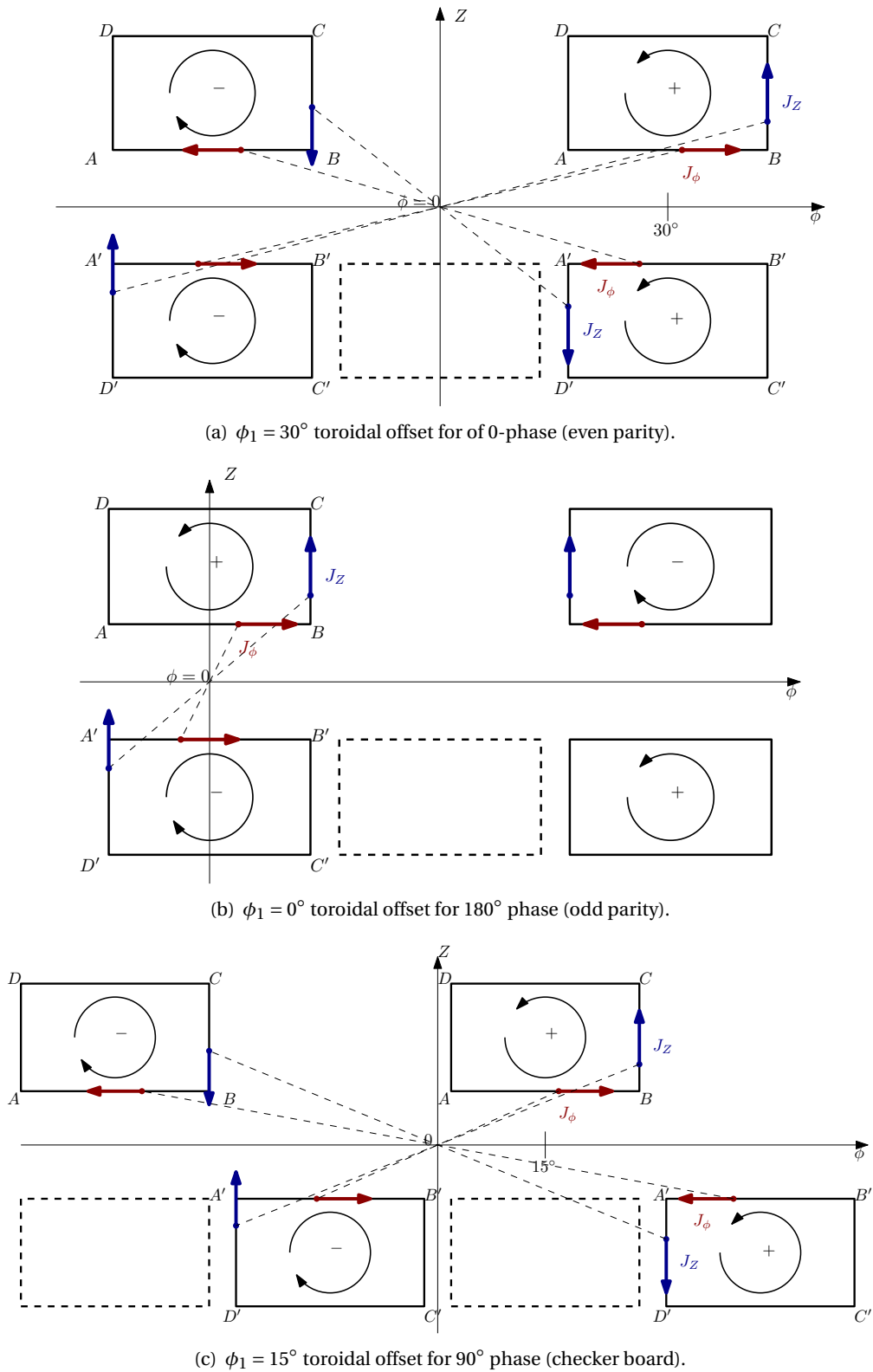


Figure 6.1 – Schematic justification of the toroidal offset of the centre of the first coil in order to satisfy stellarator symmetry of the $n = 3$ RMPs.

6.1. Coil configuration and compatibility with stellarator symmetry

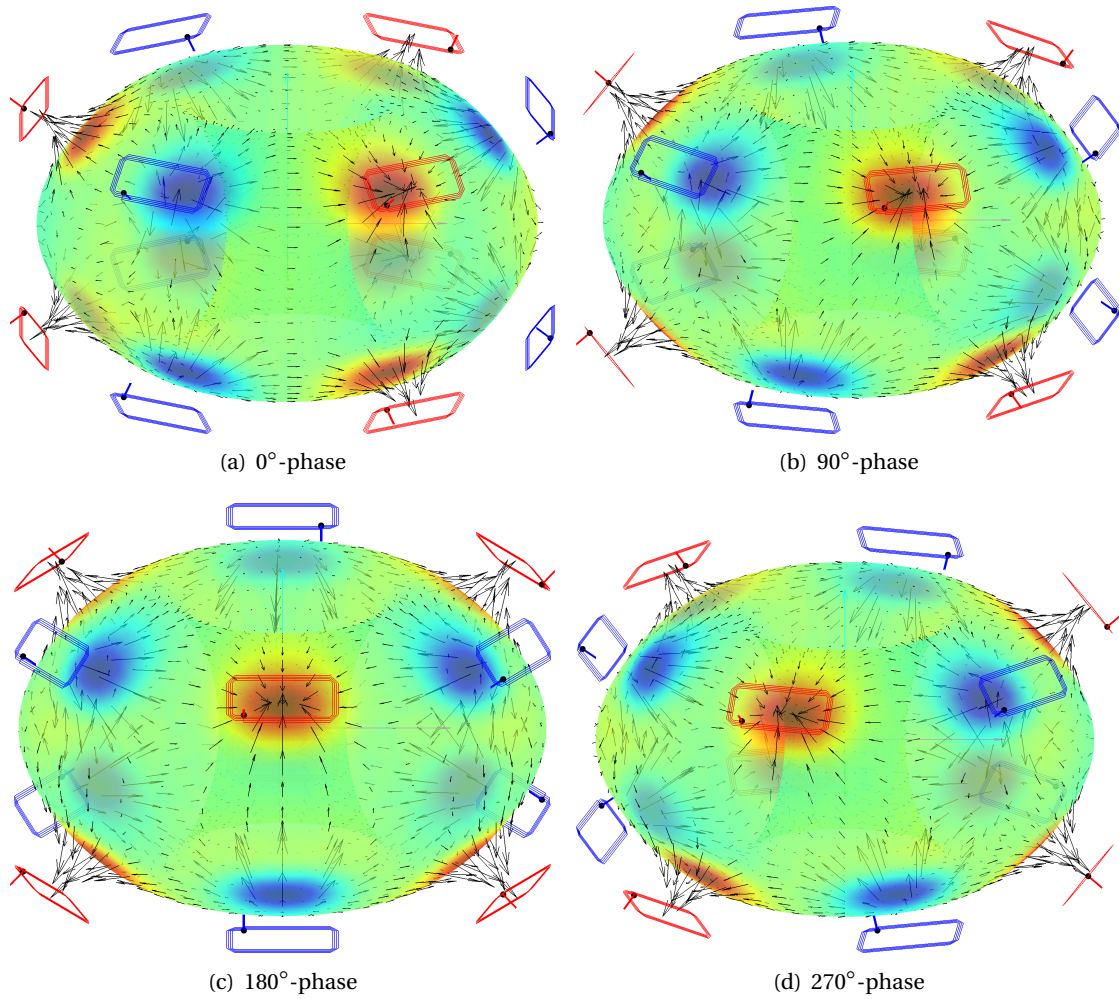


Figure 6.2 – Stellarator symmetric RMP coil configuration and magnetic field generated in the vacuum for different current patterns.

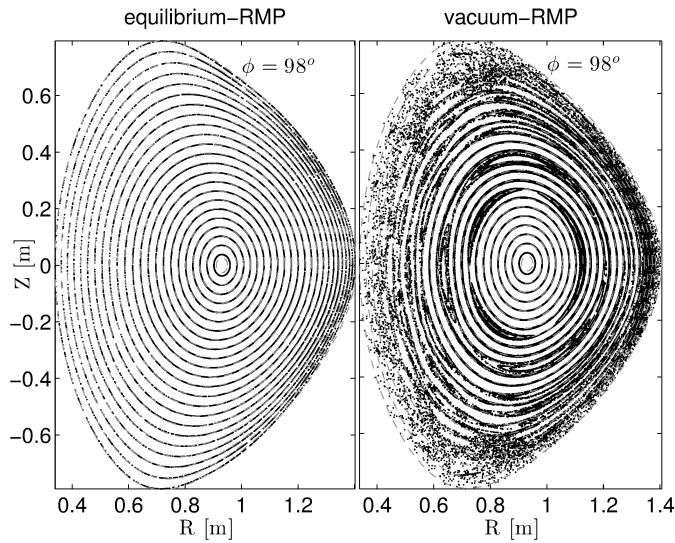


Figure 6.3 – Comparison of the field-line structure in response to 0° -phase current pattern for the equilibrium-RMP (left) and vacuum-RMP (right) model.

this additional vacuum field in a free-boundary calculation thus yielding the equilibrium-RMP model. VENUS-LEVIS is readily capable of handling 3D equilibrium fields and solving the equations of motion in VMEC's native coordinate system. Code development was required to include the RMP field as an external vacuum field, a rather challenging task that is described in section 4.3. The RMP field is algebraically added to the equilibrium prior to calling the GCDE (3.12), yielding exact equations for arbitrary large perturbations (respecting the guiding-centre approximation). Since Coil.Spell calculates the vacuum fields on a cylindrical mesh, the metric is used to convert each component into curvilinear flux-coordinates. This task is greatly facilitated by the spline-Fourier interpolation scheme (see section 4.2), especially to compute covariant derivatives.

6.2 Plasma response and magnetic field structure of the contrasting RMP models

With regards to the magnetic structure induced by RMPs, the main difference between the two approaches is presented on figure 6.3. The latter shows the points where the magnetic field-lines cross the R-Z plane at a given toroidal angle (Poincaré section of the field-line tracing) for the case of MAST $n = 3$ RMP coil configuration with a current of 1400A per turn for a total of 5600A per coil (4 turns). In the equilibrium-RMP model (left plot of figure 6.3), the magnetic field-lines lie on 3D nested flux-surfaces that are slightly deformed with respect to the nearly axisymmetric unperturbed equilibrium (dashed lines), whereas in the vacuum-RMP model (right plot of figure 6.3), the magnetic field-lines draw out a series of magnetic islands (with $n = 3$ periodicity half-way between the axis and the edge) and large stochastic regions.

Figure 6.4 shows the difference between the total magnetic field and the nearly axisymmetric unperturbed equilibrium for the two models. In the vacuum-RMP approach, $\delta \mathbf{B}$ only depends

6.2. Plasma response and magnetic field structure of the contrasting RMP models

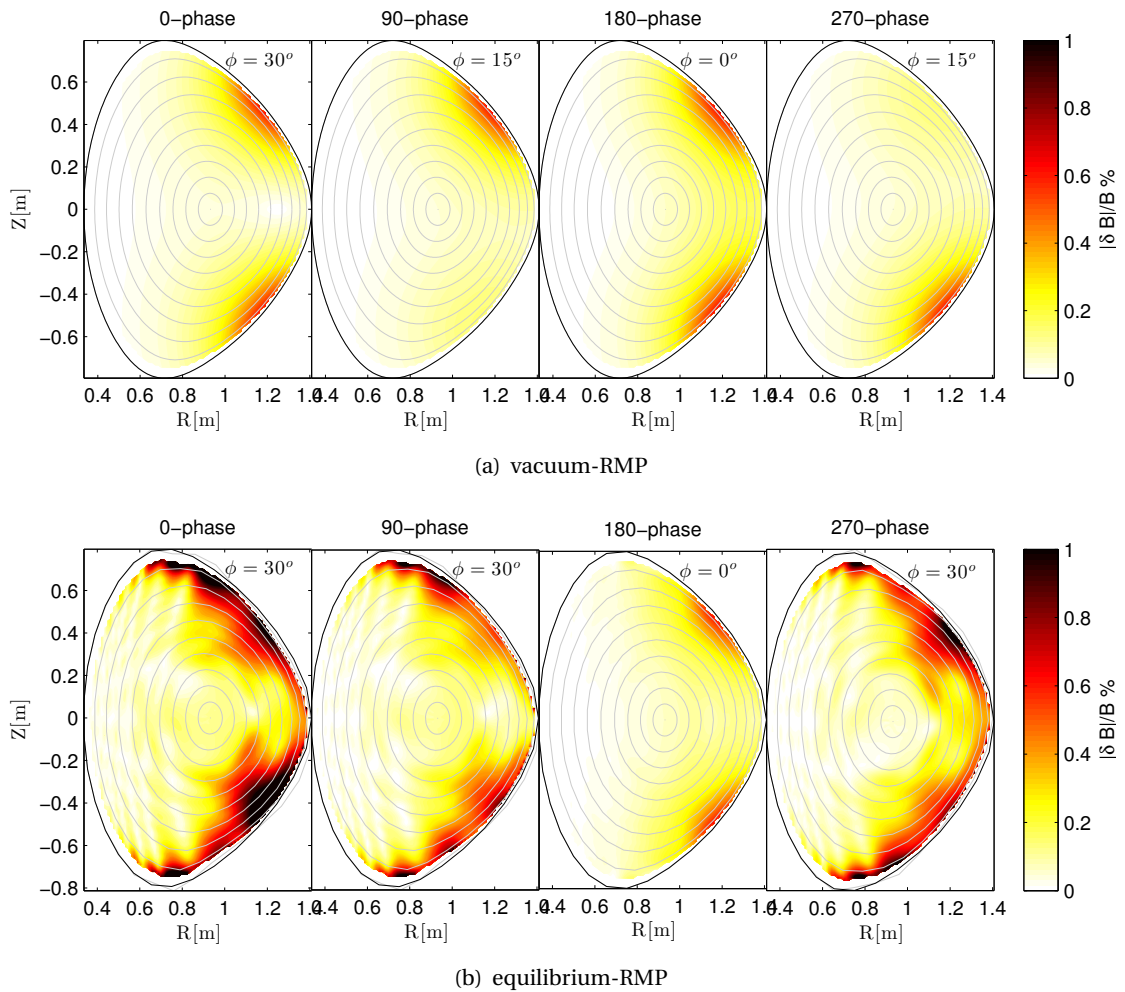


Figure 6.4 – Modulus of the perturbed magnetic field $|\delta\mathbf{B}| = |\mathbf{B}_{tot} - \mathbf{B}_{no\ RMP}|$ at a toroidal angle where the amplitude is maximum. Colour bar indicates the percentage with respect to the unperturbed field. Flux surfaces of the unperturbed equilibrium are indicated by dashed lines and the last-closed flux-surface at q_{95} in solid black. In the vacuum-RMP model (top), this map corresponds to the vacuum field. In the equilibrium-RMP model (bottom), the plot informs on the penetration of RMPs and the plasma response.

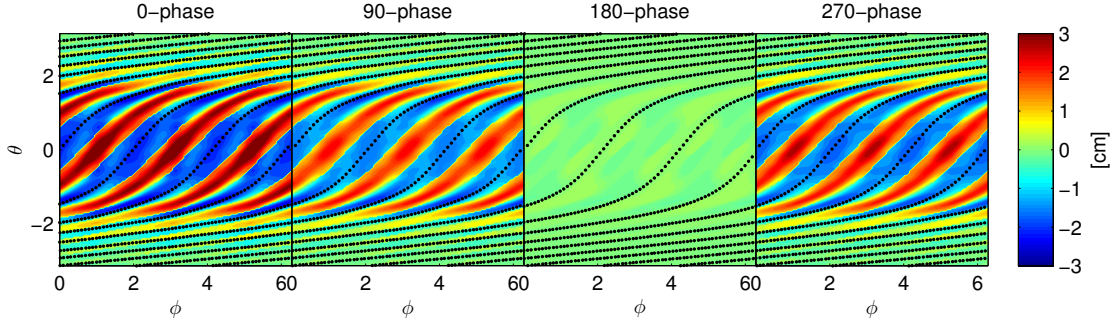


Figure 6.5 – Normal displacement of the last closed flux-surface $\delta_b(u, v) = \sqrt{(R - R_{noRMP})^2 + (Z - Z_{noRMP})^2}$ between the RMP-perturbed 3D equilibrium and the 3D equilibrium without RMPs for varying current patterns. δ_b is evaluated at $s = 0.98$ and equal (u, v) coordinates. Field-line trajectories are represented with black dots in order to highlight that the dominant $m = n = 3$ perturbation aligns with the field-line pitch. The q -value at $s = 0.98$ is approximately 5.

on the geometry of the coils, as it portrays the vacuum field without plasma, which explains why plots in figure 6.4(a) are smooth. In the vacuum-RMP model, the maximum amplitude of the field due to RMPs is approximately 0.6% of the unperturbed field. In the equilibrium-RMP model, $\delta\mathbf{B}$ results from the combined effect of flux-surface deformations and adjustments of the magnetic field to the MHD force balance. A more complex pattern is thus observed in the plots of figure 6.4(b), with the strongest response for the current pattern of 0° -phase coil activation (even parity). The RMP field is observed to propagate within the plasma, actually enhancing (resonantly) the amplitude of the perturbations. Similar enhancement has been reported in linear MHD studies (Liu et al., 2011, 2012), especially the component that is resonant to the external kink mode (Haskey et al., 2014). The amplitude of $\delta\mathbf{B}$ exceeds 1% of the unperturbed field with the 0° -phase current pattern and decreases to a moderate value in the $\pm 90^\circ$ -phases. In the 180° -phase case, $\delta\mathbf{B}$ is slightly weaker than the vacuum RMP field, which suggests that the plasma is actually screening the perturbations.

Looking at the normal displacement of the last-closed flux-surface in the equilibrium-RMP model (figure 6.5), the boundary is seen to be most distorted for the 0° -phase current pattern (even parity), with a maximum displacement of 3cm. The edge is practically unperturbed for the 180° -phase case (odd parity) as if the flux-surfaces were insensitive to the application of RMPs in this particular current pattern³. In all situations of figure 6.5, the distorted boundary has a dominant $m = n = 3$ mode structure whose iso-contours align with the magnetic field, as highlighted by the displayed field-line trajectory (black dots in figure 6.5). This corresponds to a perpendicular edge displacement, expected from the external kink-like response.

The spectrum of the equilibrium-RMP configuration, where unperturbed modes are removed, is displayed on figure 6.6 for even and odd coil parities (0° and 180° phases). Although there is an order of magnitude difference in the spectrum between even and odd coil parities, a dominant $m = n = 3$ component is identified in both cases. It is observed in figure 6.6(b) that only odd multiples of 3, i.e. $n = \pm 1 \times 3, \pm 3 \times 3, \dots$ are resonant with the applied perturbation.

³It may also be possible that odd parity RMPs cause deformations that are incompatible with stellarator symmetry. A stability analysis (full 3D) should be carried out to verify this interpretation.

6.3. Slowing-down simulations, saturated loss rates and energy dependency of even parity coil configuration

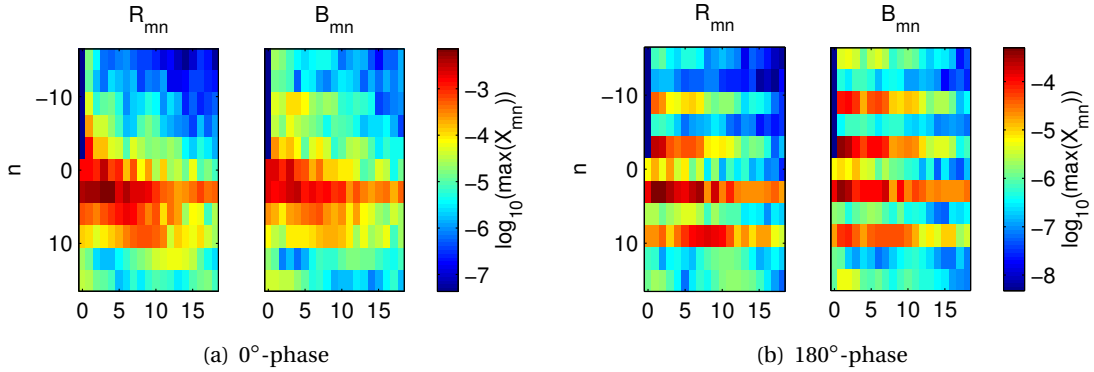


Figure 6.6 – Maximum amplitude of the modes present in the equilibrium-RMP which are not in the unperturbed equilibrium.

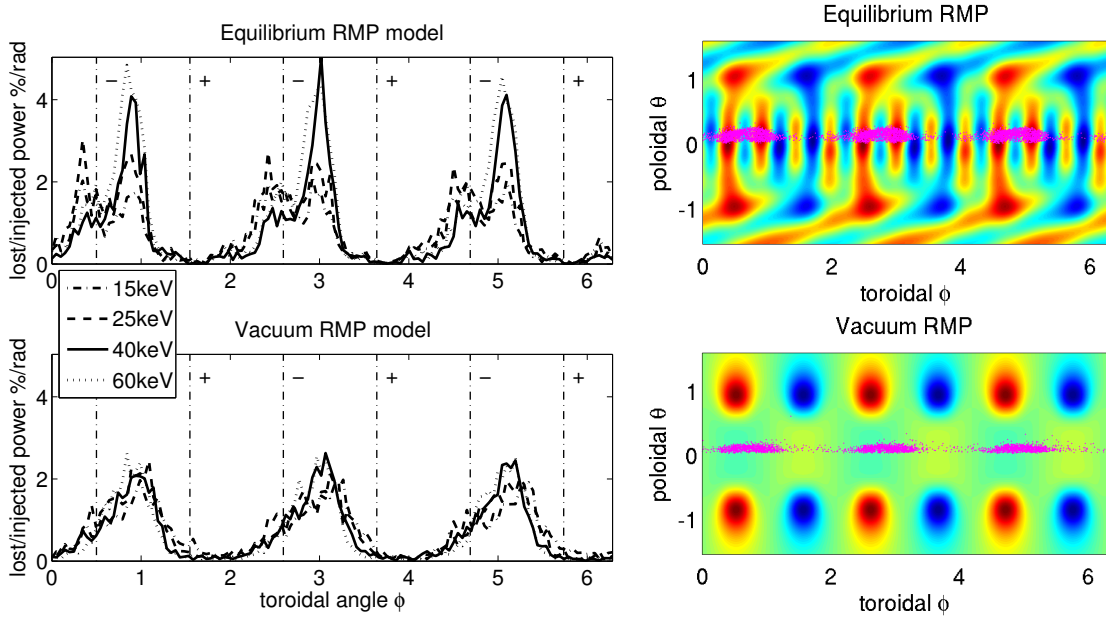
The spectrum is broader and smoother for even parity (figure 6.6(a)).

6.3 Slowing-down simulations, saturated loss rates and energy dependency of even parity coil configuration

With the goal of comparing the effect of vacuum-RMP and equilibrium-RMP approaches on fast ion losses, a series of three slowing-down NBI simulations were performed in the even parity coil configuration. From the plasma response analysis above, this coil activation is expected to yield clear differences. Populations of fast ions from NBI with varying beam energies were evolved, first in an axisymmetric MAST equilibrium, then in the presence of vacuum-RMP fields and finally in the equilibrium RMP configuration. Collisionality with the background plasma was included via the set of Monte-Carlo operators of section 4.5 based on experimental temperature and density profiles to model slowing-down and pitch-angle scattering (self-collisions among energetic particles are neglected). Loss rates are compared in the three cases after obtaining saturated fast ion distributions, when continuous particle injection is balanced by particle loss and thermalisation. Such distributions are evolved over slowing-down time-scales of $100ms$.

Figure 6.7(a) shows the steady-state energy flux across the last closed flux-surface normalised to the total injected power as a function of the toroidal angle ϕ . On figure 6.7(b), purple dots depict where on the $\theta - \phi$ plane particles have left the plasma, to be compared with the patterns of $|\delta\mathbf{B}|$ on the last closed flux-surface. In both RMP models, fast ion losses clearly follow the $n = 3$ periodicity of the coil configuration, as the three maxima are situated on the mid-plane at the same toroidal location where the RMP perturbation points outwards (red colour, matching the situation of figure 6.2(a) in the vacuum-RMP case).

In the equilibrium-RMP case (top plot of figure 6.7(a)), the maxima gradually increase with the beam energy, whereas losses seem to stay relatively constant in the vacuum-RMP model (bottom plot of figure 6.7(a)). This fact is better illustrated in figure 6.8, which shows the percentage of total injected power lost through the last closed flux surface as a function of



(a) lost particle flux (energy) normalised with the injection power as a function of the toroidal angle ϕ . The different curves correspond to simulations with different NBI energy (maximum fast ion birth energy). Vertical dash-dotted lines indicate the toroidal position of the centre of the RMP coils.

(b) amplitude $|\delta \mathbf{B}|$ on the last-closed flux-surface (colour-map) and location of lost particles in the $\theta - \phi$ plane (purple dots).

Figure 6.7 – Steady-state Deuterium ion losses across the last closed flux-surface for the even parity RMP current pattern.

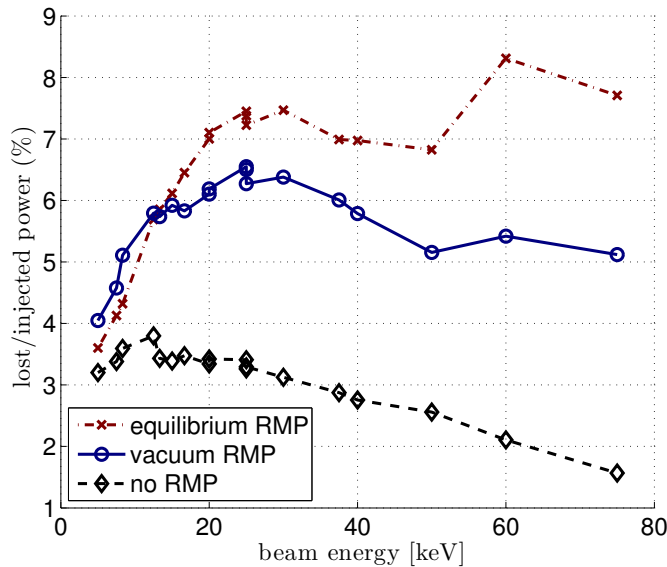


Figure 6.8 – Percentage of total injected power lost through the last closed flux surface in the steady-state regime where particle injection is balanced by losses and thermalisation (slowing-down due to Coulomb collisions with the background) as a function of the beam energy. Per slowing-down run, three families of particles are evolved with initial energy E_0 , $E_0/2$ and $E_0/3$ at the fractions of 89%, 8% and 3% as is the case with MAST PINIs. Data points nearly overlap between consecutive runs for groups of particles with matching initial energy.

6.3. Slowing-down simulations, saturated loss rates and energy dependency of even parity coil configuration

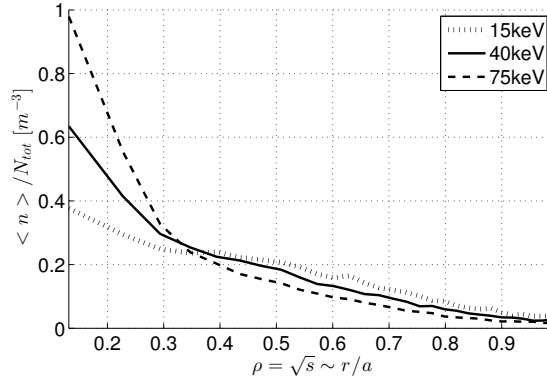


Figure 6.9 – Deposited particle density (initial particle source) normalised by the total number of ionised particles as a function of radial label $\sqrt{s} \sim r/a$ (results of figure 6.8 are based on these initial distributions). This corresponds to the ionisation probability density at a given s .

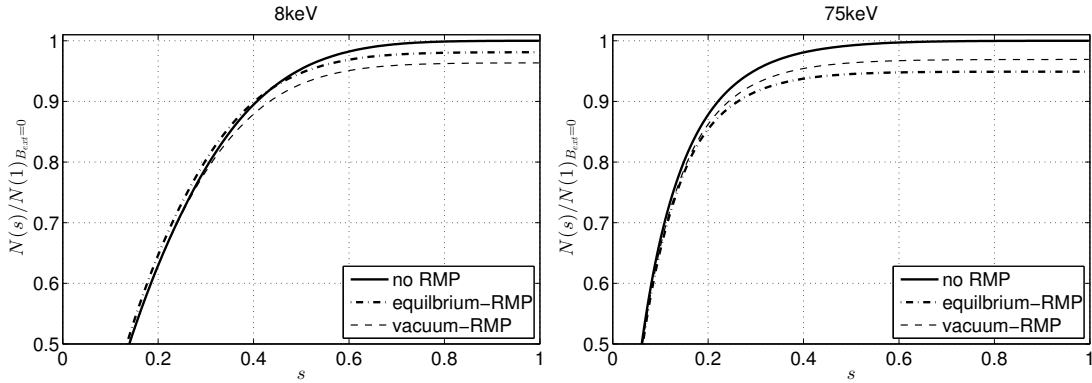


Figure 6.10 – Volume integrated saturated density profiles, normalised to the total number of confined particles in the absence of RMPs.

the beam energy. Although increased losses are expected at higher beam energies because particles have larger drift orbits, two extra mechanisms are at play here: diffusion losses due to parallel transport in the stochastic field-lines (relevant in the vacuum-RMP model) and losses through 3D drifts (relevant in the equilibrium-RMP model). At low energies (< 30 keV), losses are most significant in the vacuum-RMP model, whereas at high energies, the equilibrium-RMP model presents the largest amount. Typical injection energy of the MAST NBI system is around 56keV, and thus, perhaps surprisingly, the equilibrium-RMP model yields a higher estimation of the loss rate than the vacuum-RMP model at realistic injection energy.

Losses end up decreasing with energy from around 20keV in the vacuum-RMP model and in the situation without RMPs. This is because more energetic neutrals are ionised closer to the magnetic axis of the plasma (see figure 6.9 showing the deposition flux-averaged density as a function of minor radius) and are less affected by the action of RMP, thus better confined in the plasma. In the equilibrium-RMP model, losses do not stop rising, indicating that the 3D deformation of flux-surfaces influences the trajectories of a larger fraction of particles, also near the core (see penetration maps in figure 6.4).

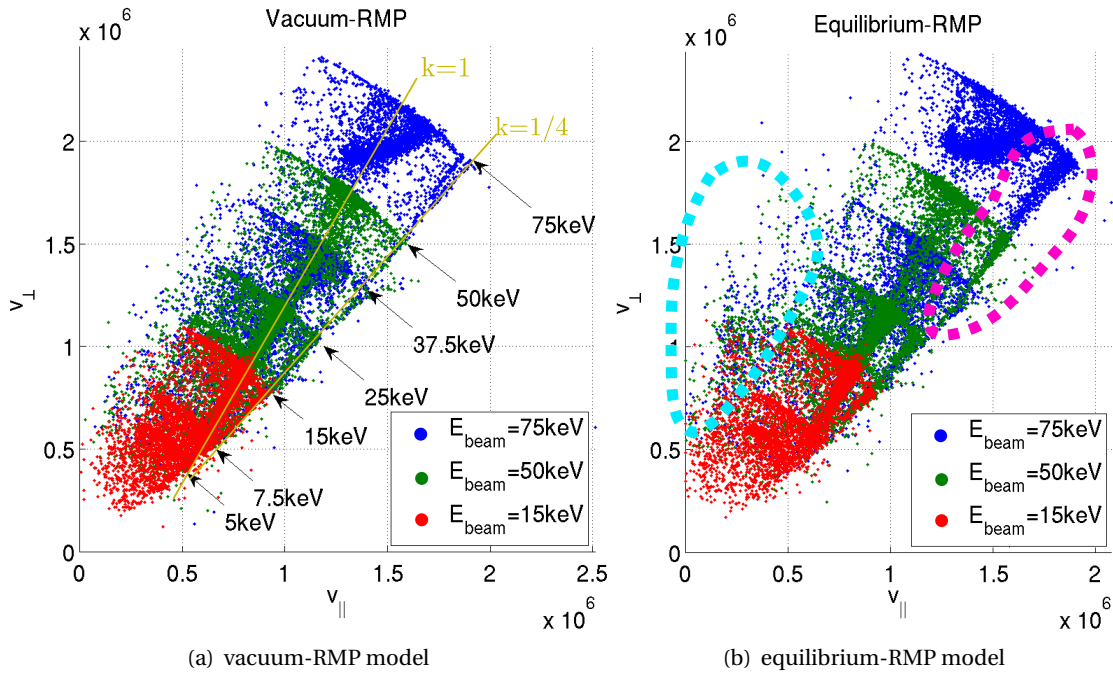


Figure 6.11 – Phase-space coordinates of lost particles due to RMPs, characterised by prompt losses at injection energy (pronounced arcs), diffusive losses (sparse clouds of point) and kinetic resonances (straight lines)

Figure 6.10 shows the saturated cumulative particle density normalised to the total number of confined particles in the absence of RMPs. These curves represent the fraction of particles enclosed by a given flux-surface s . Comparing the left graph of figure 6.10 where particles are injected at 8keV with the right graph of figure 6.10 where the beam energy is 75keV, the fraction of particles near the core is larger at higher injection energy. At 8keV injection, in the vacuum-RMP model (fine dashed curve on the top plot of figure 6.10), it is seen that the RMP field spoils the confinement of fast particles starting from around $s = 0.3$. This is expected from the presence of magnetic islands and stochastic regions, as shown on the Poincaré plots of figure 6.3. In the equilibrium-RMP model (dash-dotted line on the left plot of figure 6.10), only particles beyond $s = 0.45$ are lost because the drift motion away from field-lines is small at 8keV. At the injection energy of 75keV (right plot of figure 6.10), losses are now more significant in the equilibrium-RMP model than in the vacuum-RMP model, consistent with the crossing of the lines in figure 6.8. It is seen that particles are affected closer to the core starting from $s = 0.1$, because drift orbits are considerably larger and, in the equilibrium-RMP case, because the 3D perturbation propagates all around the plasma (see figure 6.4).

6.4 Prompt losses, diffusion and resonances

To give a clearer interpretation of the loss mechanisms, lost particles are plotted in velocity space in figure 6.11. Various patterns are identified. For each family of NBI beam energies, prompt losses are identified on arcs of constant velocity $v^2 = v_{\parallel}^2 + v_{\perp}^2$ at their initial injection

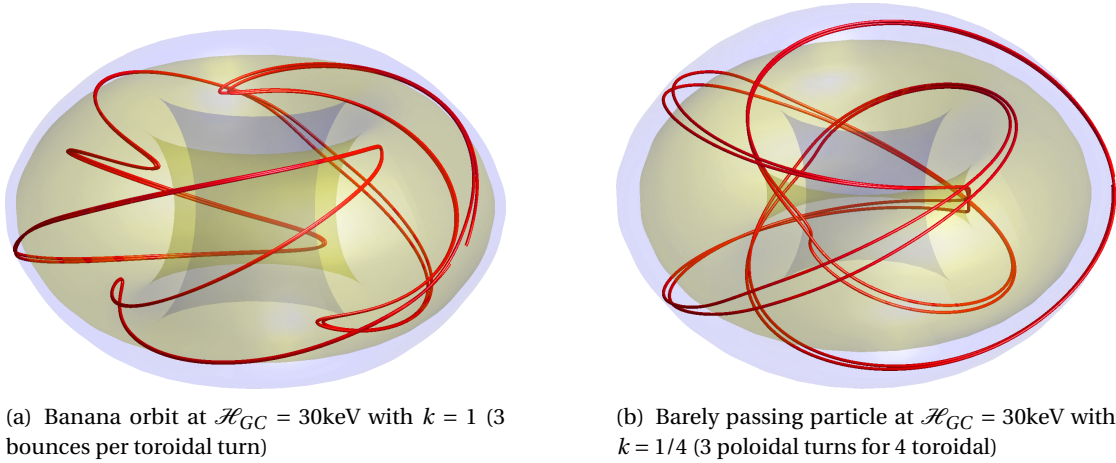


Figure 6.12 – Selection of resonant guiding-centre orbits (lost) for which the bounce/transit motion and precession drift divide into rational numbers matching the RMP periodicity.

energy (arrows in figure 6.11(a)). RMPs are observed to enhance prompt losses by perturbing the axisymmetric equilibrium, in effect preventing conservation of toroidal momentum. Particles subject to prompt losses are mostly located near the plasma edge where the perturbations are strongest. Prompt losses are reduced at higher NBI beam energy, because ionisation takes place deeper in the core. The arcs of prompt losses are somewhat thicker in the equilibrium-RMP model.

The velocity space of figure 6.11 is also filled with lost particles that have entered, via Coulomb scattering or stochastic field-line diffusion, a portion of unconfined phase-space. This mechanism is obviously slower than prompt losses but can affect a larger fraction of NBI populations. The equilibrium-RMP model is observed to broaden this fraction, in particular enhancing losses of deeply-trapped particles (see cyan circle near the $v_{\parallel} = 0$ on the left of figure 6.11(b)). For NBI, the portion of deeply-trapped particles is very low, especially at higher beam energies for which ionisation takes place closer to the magnetic axis. RMPs might provoke higher loss rates in the case of Ion Cyclotron Resonance Heating (ICRH) or fusion alpha fast particles. Modelling of the effect of RMPs on those populations in a DEMO reactor configuration design with VENUS-LEVIS is planned for future work.

Two diagonal lines (in gold-yellow) are noticed on both plots of figure 6.11, one through the bulk of the losses and one at the edge of the lost distribution, beyond the passing/trapped limit. These losses correspond to resonances between the bounce/transit motion and the precession drift. In analogy with swinging a child in a playground, a particle that successively passes through the maximum RMP field will be forced out of the plasma after a few turns. This resonance condition is expected to be

$$\frac{\omega_{\text{poloidal}}}{\omega_{\text{toroidal}}} = nk = \frac{p}{q} \quad (6.1)$$

where $n = 3$ is the RMP periodicity, $k \in \mathbb{Q}$ is a rational number, ω_{poloidal} is the bounce frequency for trapped and poloidal transit frequency for passing particles, ω_{toroidal} is the average toroidal

drift (precession). For passing particles, $p \in \mathbb{N}$ corresponds to the number of poloidal turns within $q \in \mathbb{N}$ toroidal rotations. Figure 6.12 highlights two possible resonances among other. Figure 6.12(a) is a banana orbit where the bounce frequency precisely matches the precession drift such that after one full toroidal rotation, the particle returns close to its initial position. But, because of this, the RMPs pull the particle out after 3 full turns. The first distinct line through the bulk of the lost distribution in figure 6.11 is composed of such kind of trapped particle resonances with $k = 1$. Figure 6.12(b) shows a passing particle that undergoes 4 toroidal turns while completing 3 poloidal transits. The edge of the lost distribution in figure 6.12(b) is the consequence of the resonant behaviour of passing particles with $k = 1/4$. The condition evidently depends on the initial pitch angle and the particle energy. It is conjectured that the coil phase has an incidence on the fraction of lost particles by modifying the resonance condition, especially for passing particles, but this has yet to be verified. Compared to the vacuum-RMP model, the equilibrium-RMP model gives rise to a higher number of resonance possibilities. It especially affects a larger fraction of passing particles, yielding a thicker resonance line (purple dashed circle) on the right plot of figure 6.11(b).

6.5 Conclusions

In conclusion, numerical simulations indicate that fast ions are sensitive to the application of RMPs. There is however a significant difference between modelling their effect via the addition of a vacuum field to a 2D unperturbed equilibrium and establishing a 3D MHD equilibrium embodying the perturbation. The spline-Fourier interpolation scheme offered the opportunity for accurate comparison. In the equilibrium-RMP model, the assumption that the RMP field is embedded in a 3D equilibrium is convenient because the solution, rapidly found in VMEC, corresponds to a saturated plasma state (satisfying the minimal energy principle applied to ideal MHD).

The RMP field in the equilibrium-RMP model is seen to propagate throughout the plasma and become enhanced in some cases. The strongest response occurs for a 0° -phase of the current pattern where the deformation of the last closed flux-surface reaches 3cm. With a 180° -phase activation, flux-surfaces are hardly perturbed and the field inside the plasma is similar to the vacuum-RMP field. More elaborate studies should however include resistive effects for a more realistic description of plasma screening.

In slowing-down simulations, it is observed that fast ion losses are dominated by 3D drifts rather than magnetic field stochasticity at the typical beam energies of the MAST NBI setup, a somewhat counter-intuitive result given the stochasticity of the field and the unaltered penetration of the vacuum-RMP case. The RMPs affect particles close to the last-closed flux-surface by causing prompt losses. Via Coulomb collisions and parallel field-line diffusion, ions can randomly be ejected out of the plasma. This mechanism is slower but affects a larger fraction of the NBI population. Losses occur through drift resonances, when the poloidal and toroidal average motion have a rational ratio. In this case, particles get dragged out after many turns. The equilibrium-RMP model is seen to increase all loss channels due to a deeper penetration of the RMPs and a more complex RMP pattern (flux-surface deformation and magnetic field enhancement).

The two models (vacuum-RMP and equilibrium-RMP) may provide an upper and lower approximation of the real situation: the vacuum-RMP model does not take into account the plasma response, the equilibrium model neglects the formation of internal stochastic field lines and island structures. Each model comes with a specific loss mechanism, that scales differently with energy. By weighting both contributions, it may be possible to provide a more accurate estimate of RMP losses.

The singular current sheets that form at rational surfaces are not determinant for the study of fast ion transport, at least not at the level of guiding-centre theory. Additional gyro-orbit effects are low for tangential NBI because most particles are deeply passing and have a small gyro-motion. Such effects will however play an important role for energetic populations with larger gyro-radii, for example in the case of ICRH or fusion alphas. Future work will investigate the transport of hot particles due to RMPs switching between guiding-centre and full-orbits equations (see section 3.6). Ongoing work is devoted to extending the coordinate system beyond the last-closed flux-surface, such that VENUS-LEVIS will be able to follow particles up to the wall.

7 Final remarks and perspectives

As findings were summarised in the conclusions of each chapter, the following chapter is more of a synthesis and a discussion of perspectives for future research.

This thesis addressed the challenging problem of solving fast particle motion in a category of 3D magnetic fields occurring in fusion devices. The main outcome of the work is an orbit solving code, VENUS-LEVIS, that allows a flexible investigation of fast ion transport in 3D saturated MagnetoHydroDynamics (MHD) configurations. The use of curvilinear flux coordinates, highlighting the intricate relation between magnetic field-line geometry and particle orbits, is at the centre of the code's design. In this context, the spline-Fourier interpolation scheme of section 4.2 significantly helps the numerical implementation of the curvilinear coordinate framework, avoiding issues faced with finite-difference techniques altogether. The benefits of the spline-Fourier technique as well as the Lagrangian approach to full-orbit (section 3.2) and Guiding-centre Drift Equations (GCDE) (section 3.3.1) are reflected in the computed trajectories and the underlying Hamiltonian properties are faithfully recovered. In axisymmetric systems, such expected properties are conveniently used as validation criteria. In 3D equilibrium fields with nested flux-surfaces, in particular in the helical core solution of VMEC (section 5.1.1), the presence of drift-surfaces is a non-trivial outcome of particle simulations (section 5.2).

First-order guiding-centre theory is extensively used in orbit codes, although a quantitative justification is not generally given. The criterion derived in section 3.5 proposes a straightforward evaluation of the field variation at linear order in Larmor radius around the guiding-centre. It is reported that parallel currents lead to a parallel drift identified as the Baños drift, which appears at second-order in the guiding-centre expansion of the Lagrangian. This term has a small incidence on the orbits of Neutral Beam Injection (NBI) fast ions, but is of concern in the case of fusion alphas or energetic particles from Ion Cyclotron Resonance Heating (ICRH) in tokamaks like Mega-Ampère Spherical Tokamak (MAST), Joint European Torus (JET) or the International Thermonuclear Experimental Reactor (ITER). Deviations occurring between guiding-centre and full-orbit trajectories in a purely-sheared magnetic field (section 3.4) justifies the need for the switching algorithm of section 3.6. This technique will both improve the quality of fast ion simulations and reduce CPU consumption in future simulations.

MAST Long-Lived Modes (LLMs) are considered in this work as ideally saturated MHD states, conveniently modelled with the 3D helical core solution of VMEC. The existence of nested flux-surfaces is a strong assumption, but provides a suitable viewpoint for interpreting fast ion redistribution in internal plasma deformations. Helical drift-surfaces and helical drift-islands are an expected consequence of field-line integrability on magnetic flux-surfaces. From the KAM theorem, these helical orbit topologies are expected to be preserved in more general

treatments of saturated ideal internal kinks. The methods proposed can be used to predict the level of off-axis NBI fast ion deposition and potentially help optimise various heating scenarios in tokamaks like ITER or DEMO. The robust numerical techniques devised are immediately transferable to the study of fast ion confinement in stellarator equilibria.

The side-by-side comparison of Resonant Magnetic Perturbation (RMP) implementations highlights the conceptual difference in modelling approaches. The application of external non-axisymmetric perturbations triggers field-line stochasticity. The idea that breaking flux-surfaces would yield more losses appears to be correct only for low energy drift orbits and, by extension, for thermal particles. However, allowing 3D deformations of nested flux-surfaces, which is topologically equivalent for field-line tracing to the situation without RMPs, has a more significant impact on drift orbits at realistic NBI beam energies. These conclusions illustrate the importance of the plasma response to RMPs in fast ion simulations and encourages further investigation.

More generally, the work carried out in this thesis reminds how challenging and sensitive numerical modelling can be. It conveys the message that, to some extent, it is more important (and exciting) to understand the underlying physics than provide untenable quantitative predictions. Testing the range of applicability of a model usually provides an opportunity for improvements and further discoveries.

7.1 Perspectives and future expansions

The VENUS-LEVIS code can certainly be improved and applied to the study of other fast ion related phenomena. There is room for numerical optimisation and plenty of benchmarking opportunities.

7.1.1 Code development

A fourth-order Runge-Kutta is usually used to solve the equations of motion. A selection of lower-order schemes is implemented. More evolved techniques, such as implicit schemes have not been attempted. For full-orbit solving, it would make sense to use an energy conserving Boris-Buneman integrator. The latter would have to be adjusted to the curvilinear formulation, which is not straight-forward. This scheme might be prone to high truncation error due to multiple coordinate transformations and might not perform better than RK4.

The NBI module is sufficient for qualitative results but should be improved for quantitative and systematic studies. The beam attenuation, and hence the weights of the markers, is only determined from a single beam-line shone in the plasma. The approach is valid when the beam spread is narrow and the profiles do not vary too rapidly. A more realistic injection method should consider multiple beam-lines with a random orientation within the parameters of beam spread. Furthermore, the linear sampling along the beam-line is not optimal for an exponential beam attenuation. The marker population is composed of a large group of tracers with small weights and a fraction with large weights. If the weight assignment was better balanced, statistics from the Particle-In-Cell (PIC) sampling would be improved and

simulations would require fewer markers.

Recent work by Hirvijoki et al. (2013) shows that the Monte-Carlo Coulomb collision operator is valid for a full-orbit approach, but only at zeroth-order for guiding-centres. VENUS-LEVIS could easily be corrected to include their resulting guiding-centre collision operator. The effect on saturated distributions, which is expected to be small, should be reassessed in a series of benchmarks against ASCOT.

The switching algorithm should be systematically exploited in slowing-down simulations. Full-orbit trajectories could be followed until the Larmor radius causes a field variation below a given threshold, then, GCDE would be solved until thermalisation, reducing Computer Processing Unit (CPU) consumption. The transition from particle to guiding-centre coordinates has a minimal impact on the trajectories. The technique however requires more fine-tuning to pass from guiding-centre to particle variables where a small discrepancy in the toroidal momentum causes the orbit to gently drift out of shape. Second-order guiding-centre expansion will help perform this switching in a more consistent way.

Instead of switching directly to full-orbit equations, it may be more efficient to use a higher-order guiding-centre formulation of the GCDE. This entails expanding the guiding-centre Lagrangian at second (or third) order in the Larmor radius and apply the gyro-averaging techniques from Littlejohn (1983). The Baños drift would become a correction to the parallel velocity, and other terms will also appear in the perpendicular drift. Guiding-centre and full-orbits would compare better and the adiabatic conservation of the magnetic moment would be more accurate.

The representation of magnetic fields should be extended beyond the last-closed flux-surface in order to follow particles up to the wall. This will soon be done by extrapolating the flux-surface coordinate system in order to preserve the advantages of the spline-Fourier technique and avoid swapping coordinate systems. In doing so, estimates of heat-loads on plasma facing components from fast particles can be predicted.

7.1.2 Physics applications

With the formulation of curvilinear full-orbit equations, accurate simulations are possible in various 3D magnetic equilibria. VENUS-LEVIS can be applied to the study of highly energetic ions in stellarators. An ongoing project to upgrade the SCENIC package (Jucker et al., 2011) is exploiting this feature to simulate ICRH heating in Wendelstein-7X (W7X). First, a saturated ICRH distribution is obtained from guiding-centre calculations in the presence of ICRH Monte-Carlo kicks. Then, only the tail of the marker distribution is evolved with full-orbit equations in the full electric field produced by the ICRH waves. The goal is to capture higher-harmonic resonances.

The study of RMPs will be continued, first by taking a closer look at the plasma response to the external perturbations and yielding a clearer understanding of the magnetic equilibrium solutions found with VMEC. These stellarator symmetric states correspond to minimum MHD energy configurations but they may be unstable if the stellarator symmetry condition is relaxed.

Chapter 7. Final remarks and perspectives

Without this constraint, the coil configuration can be arbitrarily rotated to see if similar RMP patterns are obtained. VENUS-LEVIS is extended to include asymmetric equilibria from VMEC and fast ion losses will be addressed in Single Null Diverted (SND) configurations, for which a stronger impact on losses due to RMPs is expected. A similar approach will be applied to the investigation of ITER Test Blanket Module (TBM), magnetic ripple and ferritic inserts.

VENUS-LEVIS can assist experiments in the analysis of fast ion transport in the presence of 3D MHD structures. The comparison with neutron camera signals could be used to estimate the size of internal kinked structures. More virtual diagnostics can be implemented to compare fast ion simulations with other experimental traces, for example, from the FILD detectors or FIDA signals.

A Mathematical complements

A.1 Curvilinear coordinates

Curvilinear coordinates are convenient when dealing with magnetic fields and the motion of charged particles. Scale separations and simple dependencies appear from a smart choice of coordinates. The fundamental theorems of Hamiltonian/Lagrangian mechanics are in fact based on the existence of *canonical* coordinates which explicitly display the system's underlying symmetries. The connections between various domains of physics that explicitly use curvilinear coordinates, for example general relativity, gauge theories in quantum field theory, result from profound theorems of differential geometry. The algebra of curvilinear equations possesses generality and unfolds elegantly. The drawback of using curvilinear coordinates is that the complexity of the algebra sometimes overrides physical intuition.

In this section, a short review of curvilinear coordinates is given in order to familiarise the reader with the notations and properties that are used throughout the thesis as well as in the implementation of magnetic equilibrium and equations of motion in the VENUS-LEVIS code. The objective is not to present curvilinear coordinates with great rigour, because it would imply presenting an unnecessary amount of mathematical definitions and theorems just to define what is a vector, a scalar product, etc. but remind at least how they should be manipulated. For more details and further reading, the reader may refer to D'Haeseleer (1991); Grøn and Hervik (2007, chapter 2).

A.1.1 General definitions and properties

Let us start with a Cartesian coordinate system in \mathbb{R}^n equipped with the Euclidean norm and assume that the implied properties are well understood.

A vector is represented with its Cartesian components as $\boldsymbol{v} = v^1 \hat{\boldsymbol{e}}_1 + \dots + v^n \hat{\boldsymbol{e}}_n = v^i \hat{\boldsymbol{e}}_i$, where Einstein summation convention is used, and will be used hereafter. $(\hat{\boldsymbol{e}}_1, \dots, \hat{\boldsymbol{e}}_n)$ is a Cartesian orthonormal basis¹ with the property that $\hat{\boldsymbol{e}}_i \cdot \hat{\boldsymbol{e}}_j = \delta_{ij}$. As known from linear algebra, we could have chosen a non-orthonormal basis $(\boldsymbol{e}_1, \dots, \boldsymbol{e}_n)$ to represent the vector as $\boldsymbol{v} = v^i \boldsymbol{e}_i$. The components v^i (upper indices) are called contravariant components. The non-orthonormal basis vectors are expressed in terms of the Cartesian basis vectors by a linear transformation

$$\boldsymbol{e}_i = \Lambda_i^j \hat{\boldsymbol{e}}_j \qquad [\Lambda^{-1}]_k^i \boldsymbol{e}_i = \hat{\boldsymbol{e}}_k. \qquad (\text{A.1})$$

The matrix Λ corresponds to the projection of the non-orthonormal vectors on the Cartesian

¹Unless specified otherwise, the hat notation will refer to the Cartesian coordinate system.

Appendix A. Mathematical complements

basis

$$\Lambda_i^j = \mathbf{e}_i \cdot \hat{\mathbf{e}}_k \delta^{jk} \equiv \mathbf{e}_i \cdot \hat{\mathbf{e}}^j. \quad (\text{A.2})$$

The transformation must satisfy $\det \Lambda \neq 0$, otherwise the non-orthonormal basis vectors is not linearly independent and does not form a complete basis. The contravariant components of the vector $\mathbf{v} = v^i \mathbf{e}_i = v^i \Lambda_i^j \hat{\mathbf{e}}_j = \hat{v}^j \hat{\mathbf{e}}_j$ are seen to transform as

$$\hat{v}^j = v^i \Lambda_i^j \quad \hat{v}^j [\Lambda^{-1}]_j^k = v^k, \quad (\text{A.3})$$

in the opposite way than the basis vectors (A.1), contra-variant (row-vector).

For every basis, there exists a unique list of vectors, called the dual basis $(\mathbf{e}^1, \dots, \mathbf{e}^n)$, such that

$$\mathbf{e}^i \cdot \mathbf{e}_j = \delta_j^i. \quad (\text{A.4})$$

Figure A.1 pictures a non-orthonormal basis and its dual in \mathbb{R}^2 . Notice that, by orthonormality, the Cartesian basis and its dual is the same list of vectors, i.e. $\hat{\mathbf{e}}^i \equiv \hat{\mathbf{e}}_i$. From (A.2) and (A.4), the relation between the dual basis and the Cartesian basis is contravariant as in (A.3)

$$\hat{\mathbf{e}}^j = \mathbf{e}^i \Lambda_i^j \quad \hat{\mathbf{e}}^j [\Lambda^{-1}]_j^k = \mathbf{e}^k. \quad (\text{A.5})$$

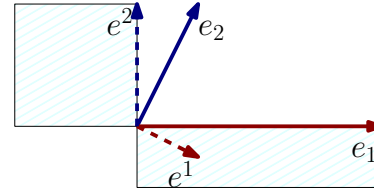


Figure A.1 – Non-orthonormal basis vectors (in black) and dual basis vectors (in grey). The blue boxes have unit area representing the scalar product between basis vectors and their dual.

In the dual basis, a vector is expressed with covariant components as $\mathbf{v} = \hat{v}_j \hat{\mathbf{e}}^j = \Lambda_i^j \hat{v}_j \mathbf{e}^i = v_i \mathbf{e}^i$, transforming as

$$v_i = \Lambda_i^j \hat{v}_j \quad [\Lambda^{-1}]_k^i v_i = \hat{v}_k \quad (\text{A.6})$$

just like the basis vectors (A.1), co-variant (a column vector).

The scalar product between non-orthonormal basis vectors yields

$$\mathbf{e}_i \cdot \mathbf{e}_j = \Lambda_i^k \delta_{kl} \Lambda_j^l = [\Lambda \Lambda^T]_{ij} \equiv g_{ij} \quad (\text{A.7})$$

what is called the metric tensor. Notice that $\det g = \det[\Lambda \Lambda^T] = \det \Lambda^2 \neq 0$. The scalar product between dual basis vectors defines its inverse

$$\mathbf{e}^i \cdot \mathbf{e}^j \stackrel{(\text{A.5})}{=} [\Lambda^{-1}]_k^i \delta^{kl} [\Lambda^{-1}]_l^j = [\Lambda^{-T} \Lambda^{-1}]^{ij} = [(\Lambda \Lambda^T)^{-1}]^{ij} = g^{ij} \quad \text{i.e.} \quad g^{ij} g_{jk} = \delta_k^i \quad (\text{A.8})$$

The metric tensor is used to change representations (go from lower to upper indices and vice-versa)

$$v^i = \mathbf{e}^i \cdot \mathbf{v} = \mathbf{e}^i \cdot \mathbf{e}^j v_j = g^{ij} v_j \quad v_i = \mathbf{e}_i \cdot \mathbf{v} = \mathbf{e}_i \cdot \mathbf{e}_j v^j = g_{ij} v^j \quad (\text{A.9})$$

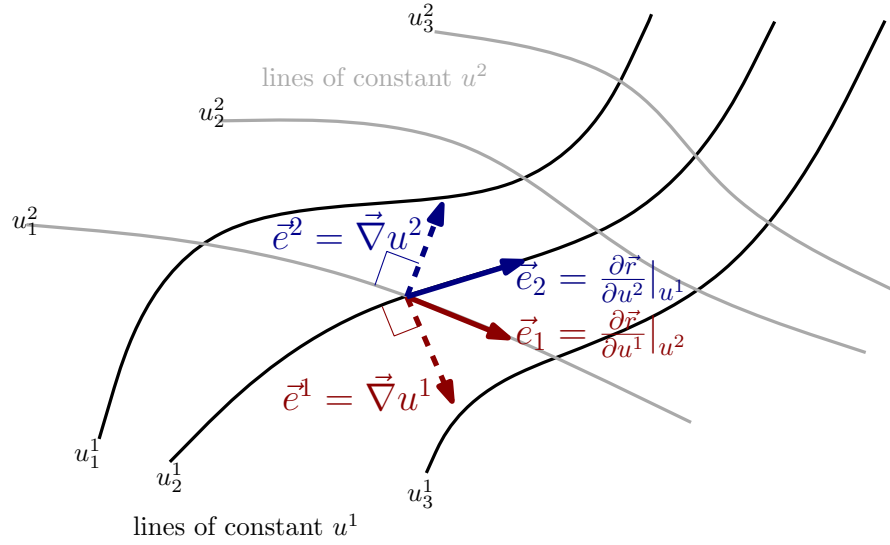


Figure A.2 – Basis vectors and dual vectors naturally arising from curvilinear coordinates. Lines of constant $u^1(\mathbf{r})$ are in black, lines of constant $u^2(\mathbf{r})$ in grey. Moving along one of these grey curves means varying u^1 only; the tangent red vector to this curve $\partial\mathbf{r}/\partial u^1$ forms a covariant basis vector. Moving along one of the black curves means varying u^2 only; the tangent blue vector $\partial\mathbf{r}/\partial u^2$ forms the other covariant basis vector. Moving perpendicularly away from the black curve (perpendicular to the blue tangent vector) means following the gradient of u^1 ; ∇u^1 (dashed red) forms a dual contravariant basis vector. Moving perpendicularly away from the grey curve (perpendicular to the red tangent vector) means following the gradient of u^2 ; ∇u^2 (dashed blue) forms the other dual contravariant basis vector. Because of the bending of the constant u^i lines, basis vectors of same kind are not necessarily orthogonal.

Scalar products and contractions are thus expressed in multiple ways. If $\mathbf{w} = w^j \mathbf{e}_j = w_j \mathbf{e}^j$,

$$\mathbf{v} \cdot \mathbf{w} = v^i \mathbf{e}_i \cdot \mathbf{e}_j w^j = g_{ij} v^i w^j \quad \text{or} \quad \mathbf{v} \cdot \mathbf{w} = v_i \mathbf{e}^i \cdot \mathbf{e}^j w_j = g^{ij} v_i w_j \quad (\text{A.10})$$

and even simpler

$$\mathbf{v} \cdot \mathbf{w} = v^i \mathbf{e}_i \cdot \mathbf{e}^j w_j = v^i w_i = v_i w^i. \quad (\text{A.11})$$

In Cartesian coordinates, the metric tensor is the unity matrix δ_{ij} and without surprise, the scalar product is Euclidian $\mathbf{v} \cdot \mathbf{w} = \delta_{ij} \hat{v}^i \hat{w}^j = \hat{v}^1 \hat{w}^1 + \dots + \hat{v}^n \hat{w}^n$.

The Cartesian basis $(\hat{\mathbf{e}}_1, \dots, \hat{\mathbf{e}}_n)$ is fixed everywhere in \mathbb{R}^n as a global basis, but imagine that the non-orthonormal basis varies (smoothly) from one point in space to the other, such that the basis vectors (and thus the metric) depends on the position² \mathbf{r} . Locally, the previous properties would still hold true, only that we now expect the basis to vary with \mathbf{r} as $\mathbf{e}_i(\mathbf{r})$ and $\mathbf{e}^i(\mathbf{r})$.

Consider a list of (scalar) functions $(u^1(\mathbf{r}), \dots, u^n(\mathbf{r}))$ such that the $u^i = \text{const}$ hyper-surfaces uniquely intersect at the point \mathbf{r} . This defines a new coordinate system, that is related to the

²In Cartesian coordinates, the position vector is $\mathbf{r} = \hat{x}^1 \mathbf{e}_1 + \dots + \hat{x}^n \mathbf{e}_n$, where the components are equal to the coordinates $\hat{x}^i = \mathbf{x} \cdot \hat{\mathbf{e}}^i$. In general however, it must be remembered that the components of \mathbf{r} , $x^i = \mathbf{r} \cdot \nabla u^i$, do not match the coordinates u^i .

Appendix A. Mathematical complements

Cartesian coordinate system via the invertible (non-linear) mapping, or diffeomorphism³, $u^i(\mathbf{r})$ and $\mathbf{r}(u^i)$. It turns out that the list of $\frac{\partial \mathbf{r}}{\partial u^i} \equiv \mathbf{e}_i$ forms a covariant basis and the list of $\frac{\partial u^i}{\partial \mathbf{r}} = \nabla u^i \equiv \mathbf{e}^i$ the dual contravariant basis. Indeed, as pictured on figure A.2,

$$\frac{\partial \mathbf{r}}{\partial u^i} \cdot \nabla u^j = \frac{\partial \hat{x}^k}{\partial u^i} \frac{\partial u^j}{\partial \hat{x}^k} = \frac{\partial u^j}{\partial u^i} = \delta_i^j \quad \Lambda_i^j = \frac{\partial \hat{x}^j}{\partial u^i} \quad g_{ij} = \frac{\partial \mathbf{r}}{\partial u^i} \cdot \frac{\partial \mathbf{r}}{\partial u^j} \quad (\text{A.12})$$

where the basis transformation Λ_i^j is identical to the Jacobian matrix of the coordinate mapping. In relation to the Cartesian basis, notice that

$$\mathbf{e}_i = \frac{\partial \hat{x}^j}{\partial u^i} \hat{\mathbf{e}}_j \quad \text{and} \quad \mathbf{e}^i = \nabla u^i = \frac{\partial u^i}{\partial \hat{x}^j} \hat{\mathbf{e}}^j \quad (\text{A.13})$$

In the basis formed by the curvilinear coordinates, vectors are expressed in terms of covariant (lower indices) and contravariant (upper indices) as

$$\mathbf{v} = v^i \frac{\partial \mathbf{r}}{\partial u^i} = v_j \nabla u^j \quad \text{i.e.} \quad v^i(\mathbf{r}) = \mathbf{v} \cdot \nabla u^i \quad v_j(\mathbf{r}) = \mathbf{v} \cdot \frac{\partial \mathbf{r}}{\partial u^j}. \quad (\text{A.14})$$

In curvilinear coordinates, the components generally depend on the position even if the vector \mathbf{v} is constant everywhere, because the basis vectors and the projection now vary in space. Conversely, a vector whose components are fixed in space is not necessarily constant, since it is supported by basis vectors that are changing in space. This is where curvilinear coordinates actually become powerful; if one finds a coordinate system in which physical quantities (components) have simple dependencies, part of the dynamics is transferred to the problem of solving the geometry (topology). In most cases, evaluating the precise geometry of the physical system (field-lines, orbits, etc. . .) comes after finding the underlying physical properties, such as constants of motion, average motion, limiting cases, etc.

Christoffel symbols

Since the basis vectors vary in space, it is difficult to compare components at different positions. This fact affects the definition of derivatives, which are essentially a mathematical way of comparing the values of a function at infinitesimally close positions. Derivatives involving vector components will have to be compensated by the variation of the basis vector. The variation of the covariant basis vectors with respect to the contravariant basis is recorded in a coefficient $\Gamma_{k,ij}$ called the Christoffel symbol of first kind

$$\Gamma_{k,ij} \equiv \mathbf{e}_k \cdot \partial_i \mathbf{e}_j = \frac{\partial \mathbf{r}}{\partial u^k} \cdot \frac{\partial^2 \mathbf{r}}{\partial u^i \partial u^j} \quad \Longleftrightarrow \quad \partial_i \mathbf{e}_j = \Gamma_{l,ij} \nabla u^l. \quad (\text{A.15})$$

³An invertible function that maps one differentiable manifold to another, such that both the function and its inverse are smooth.

The same variation with respect to the covariant basis defines the Christoffel symbol of second kind

$$\Gamma_{ij}^k \equiv \nabla u^k \cdot \partial_i \mathbf{e}_j = \nabla u^k \cdot \frac{\partial^2 \mathbf{r}}{\partial u^i \partial u^j} = g^{kl} \Gamma_{l,ij} \iff \partial_i \mathbf{e}_j = \Gamma_{ij}^l \mathbf{e}_l \quad (\text{A.16})$$

Notice from these definitions that the Christoffel symbol is symmetric in the lower indices $\Gamma_{ij}^k = \Gamma_{ji}^k$. The variation of the contravariant basis is indirectly found by differentiating the orthonormality condition

$$0 = \partial_i (\nabla u^k \cdot \mathbf{e}_j) = \partial_i \nabla u^k \cdot \mathbf{e}_j + \nabla u^k \cdot \partial_i \mathbf{e}_j \iff \partial_i \nabla u^k = -\Gamma_{ij}^k \nabla u^j \quad (\text{A.17})$$

The most convenient way of computing the Christoffel symbol is usually by equation (A.15). Alternatively, a relation between the Christoffel symbol and the derivatives of the metric tensor can be established as

$$\partial_i g_{jk} = \partial_i (\mathbf{e}_j \cdot \mathbf{e}_k) = \mathbf{e}_k \cdot \partial_i \mathbf{e}_j + \mathbf{e}_j \cdot \partial_i \mathbf{e}_k = \Gamma_{k,ij} + \Gamma_{j,ik}$$

and by using the symmetry properties of the metric tensor and the Christoffel symbol, it is not hard to show that

$$\Gamma_{k,ij} = \frac{1}{2} (\partial_i g_{kj} + \partial_j g_{ki} - \partial_k g_{ij}) \quad \Gamma_{ij}^l = \frac{1}{2} g^{lk} (\partial_i g_{kj} + \partial_j g_{ki} - \partial_k g_{ij}). \quad (\text{A.18})$$

An interesting property of the Christoffel symbol of second kind is

$$\Gamma_{il}^l = \frac{1}{2} (g^{lk} \partial_i g_{kl} + \cancel{g^{lk} \partial_l g_{ki}} - \cancel{g^{lk} \partial_k g_{il}}) = \frac{1}{2} g^{kl} \partial_i g_{kl} = \frac{1}{2} \partial_i \ln g = \partial_i \ln \sqrt{g} \quad (\text{A.19})$$

where the relation between the determinant and the trace of a matrix $\ln \det G = \text{tr} \ln G$ was used as well as the fact that $d \ln G = G^{-1} dG$.

Covariant derivatives

Now, consider a trajectory in \mathbb{R}^n parametrised by t (not necessarily representing time) as $\mathbf{r}(t) = (\hat{x}^1(t), \dots, \hat{x}^n(t)) = (u^1(t), \dots, u^n(t))$. The tangent vector to the curve is automatically obtained via

$$\frac{d\mathbf{r}}{dt} = \frac{d\hat{x}^j}{dt} \hat{\mathbf{e}}_j = \frac{du^i}{dt} \frac{\partial \hat{x}^j}{\partial u^i} \hat{\mathbf{e}}_j \stackrel{(\text{A.13})}{=} \frac{du^i}{dt} \mathbf{e}_i$$

where the contravariant components of the tangent vector is identified in Cartesian coordinates as $d\hat{x}^i/dt$ and in curvilinear coordinates as du^i/dt .

Imagine that there is a scalar field (i.e. a function depending on space) $\Phi(\mathbf{r})$ evaluating a physical quantity like density, electrostatic potential, etc., and we are interested in measuring the rate of change of this quantity along the trajectory. We would write

$$\frac{d\Phi}{dt} = \frac{d\mathbf{r}}{dt} \cdot \nabla \Phi = \frac{du^j}{dt} \frac{\partial \mathbf{r}}{\partial u^j} \cdot \nabla u^i \frac{\partial \Phi}{\partial u^i} \stackrel{(\text{A.12})}{=} \dot{u}^j \delta_j^i \frac{\partial \Phi}{\partial u^i} = \dot{u}^i \partial_i \Phi$$

Appendix A. Mathematical complements

where the compact notation $\frac{\partial}{\partial u^i} = \partial_i$ and $du^i/dt = \dot{u}^i$ is introduced for convenience. From the first equality, the rate of change is shown to be the projection of the gradient of the field on the tangent vector to the curve $d\mathbf{r}/dt$. The scalar product yields a quantity that is independent on the choice of coordinates. The rate of change of a scalar function along a given curve is thus universally represented by the contraction of the contravariant components \dot{u}^i of the tangent vector $d\mathbf{r}/dt$ and the covariant components $\partial_i\Phi$ of the gradient $\nabla\Phi$.

Now imagine a vector field $\mathbf{B}(\mathbf{r}) = \hat{B}^i(\mathbf{r})\hat{\mathbf{e}}_i = B^i(\mathbf{r})\mathbf{e}_i(\mathbf{r}) = B_i(\mathbf{r})\nabla u^i(\mathbf{r})$ like the magnetic field, the electric field, the fluid flow, etc. We expect the rate of change of this vector along the curve to be a vector. In Cartesian coordinates, it would be expressed as

$$\frac{d\mathbf{B}}{dt} = \left(\frac{d\mathbf{r}}{dt} \cdot \nabla\right)\mathbf{B} = \dot{x}^i \partial_i \hat{B}^j \hat{\mathbf{e}}_j$$

but in curvilinear coordinates, the components of the derivative are corrected by the Christoffel symbol

$$\frac{d\mathbf{B}}{dt} = \frac{d}{dt} [B^i \mathbf{e}_i] = \frac{dB^l}{dt} \mathbf{e}_l + B^j \frac{d\mathbf{e}_j}{dt} = \dot{u}^i \left(\partial_i B^l \mathbf{e}_l + B^j \partial_i \mathbf{e}_j \right) \stackrel{(A.16)}{=} \dot{u}^i \underbrace{\left(\partial_i B^l + B^j \Gamma_{ij}^l \right)}_{B_{;i}^l} \mathbf{e}_l$$

or

$$\frac{d\mathbf{B}}{dt} = \frac{d}{dt} [B_i \nabla u^i] = \dot{u}^i \left(\partial_i B_j \nabla u^j + B_k \partial_i \nabla u^k \right) \stackrel{(A.17)}{=} \dot{u}^i \underbrace{\left(\partial_i B_j - B_k \Gamma_{ij}^k \right)}_{B_{;i}^j} \nabla u^j$$

The derivative of a vector along a curve precisely defines the covariant derivative $\nabla\mathbf{B}$, whose contravariant and covariant are

$$B_{;j}^i = \mathbf{e}_j \cdot (\nabla\mathbf{B}) \cdot \nabla u^i = \partial_j B^i + B^k \Gamma_{kj}^i \quad B_{i;j} = \partial_j B_i - B_k \Gamma_{ij}^k \quad B_{i;j} = g_{ik} B_{;j}^k \quad (A.20)$$

The individual components of the covariant derivatives represent the variation of the vector components along the curves traced by each curvilinear coordinate. With this definition, the covariant derivative can be verified to transform as a tensor when changing coordinates, for example, from the Cartesian coordinates

$$\begin{aligned} B_{;j}^i &= [\Lambda^{-1}]_k^i \Lambda_j^l \hat{B}_{;l}^k = \frac{\partial u^i}{\partial \hat{x}^k} \frac{\partial \hat{x}^l}{\partial u^j} \frac{\partial \hat{B}^k}{\partial \hat{x}^l} = \frac{\partial u^i}{\partial \hat{x}^k} \frac{\partial \hat{B}^k}{\partial u^j} \stackrel{(A.3, A.12)}{=} \frac{\partial u^i}{\partial \hat{x}^k} \frac{\partial}{\partial u^j} \left(\frac{\partial \hat{x}^k}{\partial u^l} B^l \right) \\ &= \frac{\partial u^i}{\partial \hat{x}^k} \frac{\partial \hat{x}^k}{\partial u^l} \frac{\partial B^l}{\partial u^j} + B^l \frac{\partial u^i}{\partial \hat{x}^k} \frac{\partial^2 \hat{x}^k}{\partial u^l \partial u^j} = \partial_j B^i + B^l \Gamma_{jl}^i \end{aligned}$$

A.1.2 Special case of \mathbb{R}^3

In plasma physics, we usually deal with three-dimensional space. Curvilinear coordinates in \mathbb{R}^3 have a repertoire of properties that are useful to highlight.

Vector product

The vector product provides a direct relation between covariant and contravariant basis⁴. In Cartesian coordinates, the vector product (or cross product) is defined by

$$\hat{\mathbf{e}}_1 = \hat{\mathbf{e}}_2 \times \hat{\mathbf{e}}_3 \quad \hat{\mathbf{e}}_2 = \hat{\mathbf{e}}_3 \times \hat{\mathbf{e}}_1 \quad \hat{\mathbf{e}}_3 = \hat{\mathbf{e}}_1 \times \hat{\mathbf{e}}_2 \quad (\text{A.21})$$

Introducing the purely anti-symmetric Levi-Civita symbol

$$\epsilon_{ijk} \equiv \hat{\mathbf{e}}_i \cdot (\hat{\mathbf{e}}_j \times \hat{\mathbf{e}}_k), \quad \epsilon^{ijk} \equiv \hat{\mathbf{e}}^i \cdot (\hat{\mathbf{e}}^j \times \hat{\mathbf{e}}^k) \Rightarrow \epsilon_{ijk} \hat{\mathbf{e}}^i = \hat{\mathbf{e}}_j \times \hat{\mathbf{e}}_k, \quad \epsilon^{ijk} \hat{\mathbf{e}}_i = \hat{\mathbf{e}}^j \times \hat{\mathbf{e}}^k, \quad (\text{A.22})$$

the vector product of any given vectors is conveniently expressed in Cartesian coordinates as

$$\mathbf{v} \times \mathbf{w} = \hat{v}^i \hat{w}^j \hat{\mathbf{e}}_i \times \hat{\mathbf{e}}_j = \epsilon_{ijk} \hat{v}^i \hat{w}^j \hat{\mathbf{e}}^k \quad (\text{A.23})$$

In curvilinear coordinates, the cross product between covariant basis vectors is in fact along the direction of the third contravariant vector

$$\mathbf{e}_i \times \mathbf{e}_j \stackrel{(\text{A.1})}{=} \Lambda_i^l \Lambda_j^m \hat{\mathbf{e}}_l \times \hat{\mathbf{e}}_m = \epsilon_{lmn} \Lambda_i^l \Lambda_j^m \hat{\mathbf{e}}^n \stackrel{(\text{A.5})}{=} \epsilon_{lmn} \Lambda_i^l \Lambda_j^m \Lambda_k^n \mathbf{e}^k = \det \Lambda \epsilon_{ijk} \mathbf{e}^k \quad (\text{A.24})$$

where $\det \Lambda \equiv \epsilon_{lmn} \Lambda_1^l \Lambda_2^m \Lambda_3^n = -\epsilon_{lmn} \Lambda_2^l \Lambda_1^m \Lambda_3^n = \text{sign}(\sigma) \epsilon_{lmn} \Lambda_{\sigma_1}^l \Lambda_{\sigma_2}^m \Lambda_{\sigma_3}^n$. Therefore, the vector product provides a means of exchanging covariant to contravariant basis vectors (rather than using the metric tensor)

$$\nabla u^1 = \frac{\mathbf{e}_2 \times \mathbf{e}_3}{\sqrt{g}} \quad \nabla u^2 = \frac{\mathbf{e}_3 \times \mathbf{e}_1}{\sqrt{g}} \quad \nabla u^3 = \frac{\mathbf{e}_1 \times \mathbf{e}_2}{\sqrt{g}} \quad (\text{A.25})$$

where $\mathbf{e}_1 \cdot (\mathbf{e}_2 \times \mathbf{e}_3) = \det \Lambda \equiv \sqrt{g}$. Conversely, one finds

$$\frac{\partial \mathbf{r}}{\partial u^1} = \sqrt{g} \nabla u^2 \times \nabla u^3 \quad \frac{\partial \mathbf{r}}{\partial u^2} = \sqrt{g} \nabla u^3 \times \nabla u^1 \quad \frac{\partial \mathbf{r}}{\partial u^3} = \sqrt{g} \nabla u^1 \times \nabla u^2 \quad (\text{A.26})$$

and $\nabla u^1 \cdot (\nabla u^2 \times \nabla u^3) = 1/\det \Lambda = 1/\sqrt{g}$. The vector product between any vector in curvilinear coordinates is thus expressed as

$$\mathbf{v} \times \mathbf{w} = v^i w^j \mathbf{e}_i \times \mathbf{e}_j = \underbrace{\sqrt{g} \epsilon_{ijk} v^i w^j}_{[\mathbf{v} \times \mathbf{w}]_k} \nabla u^k \quad \text{and} \quad \mathbf{v} \times \mathbf{w} = v_i w_j \nabla u^i \times \nabla u^j = \underbrace{\frac{\epsilon^{ijk}}{\sqrt{g}} v_i w_j}_{[\mathbf{v} \times \mathbf{w}]^k} \mathbf{e}_k \quad (\text{A.27})$$

It is useful to define the following object in order to simplify the notation and write "covariant" expressions (that look identical in every coordinate system)

$$\epsilon_{ijk} = \sqrt{g} \epsilon_{ijk} = \mathbf{e}_i \cdot (\mathbf{e}_j \times \mathbf{e}_k) \quad \epsilon^{ijk} = \frac{\epsilon^{ijk}}{\sqrt{g}} = \nabla u^i \cdot (\nabla u^j \times \nabla u^k) \quad (\text{A.28})$$

ϵ can be shown to be a tensor.

⁴More generally, this statement would hold true in the framework of differential forms with the use of the exterior product.

Appendix A. Mathematical complements

Divergence and curl operators

Assuming that the vector calculus identities are well known in Cartesian coordinates, the curl operator is very simply written in curvilinear coordinates with the covariant components. Reminding that $\nabla \times \nabla f = 0$ for any given function f , the curl of the vector $\mathbf{A} = A_i \nabla u^i$ is written as

$$\nabla \times \mathbf{A} \equiv \nabla A_j \times \nabla u^j = \partial_i A_j \nabla u^i \times \nabla u^j \stackrel{(A.27-A.28)}{=} \partial_i A_j \varepsilon^{ijk} \mathbf{e}_k \quad (\text{A.29})$$

By the symmetric properties of the Christoffel symbol, the curl is represented with the components of the covariant derivative as $[\nabla \times \mathbf{A}]^k = A_{j;i} \varepsilon^{ijk}$.

The divergence operator is best expressed with the contravariant components $\mathbf{A} = A^i \mathbf{e}_i = \frac{1}{2} A^i \sqrt{g} \varepsilon_{ijk} \nabla u^j \times \nabla u^k$. Reminding that $\nabla \cdot (\nabla f \times \nabla g) = (\nabla \times \nabla f) \times \nabla g - \nabla f \times (\nabla \times \nabla g) = 0$, the divergence is written as

$$\begin{aligned} \nabla \cdot \mathbf{A} &= \frac{1}{2} \varepsilon_{ijk} \nabla (\sqrt{g} A^i) \cdot (\nabla u^j \times \nabla u^k) = \frac{1}{2} \partial_l (\sqrt{g} A^i) \varepsilon_{ijk} \nabla u^l \cdot (\nabla u^j \times \nabla u^k) \\ &= \frac{1}{\sqrt{g}} \partial_l (\sqrt{g} A^i) \frac{1}{2} \varepsilon_{ijk} \varepsilon^{ljk} = \frac{1}{\sqrt{g}} \partial_l (\sqrt{g} A^l) \\ &= \partial_l A^l + A^l \partial_l \ln \sqrt{g} \stackrel{(A.19)}{=} \partial_l A^l + A^k \Gamma_{kl}^l = A_{;l}^l \end{aligned} \quad (\text{A.30})$$

A.1.3 Examples

Cylindrical coordinates

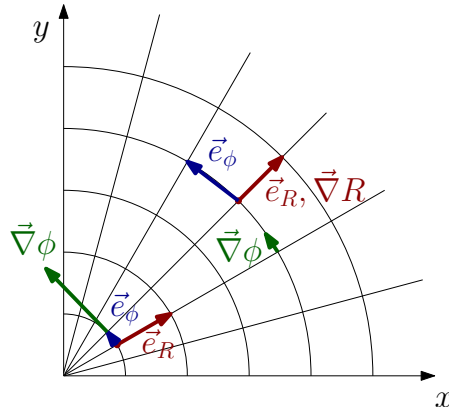


Figure A.3 – Basis vectors of the cylindrical coordinate system

Fusion relevant devices are usually toroidal, therefore cylindrical coordinates are often used as an intermediate step to calculate the metric elements in a more sophisticated curvilinear

system. Considering coordinates $(r^1, r^2, r^3) = (R, \phi, Z)$, it follows that

$$\begin{cases} x = R \cos \phi \\ y = R \sin \phi \\ z = Z \end{cases} \quad \frac{\partial \hat{x}^i}{\partial r^j} = \begin{pmatrix} \cos \phi & -R \sin \phi & 0 \\ \sin \phi & R \cos \phi & 0 \\ 0 & 0 & 1 \end{pmatrix} \quad (\text{A.31})$$

$$\sqrt{\hat{g}} = \det \left[\frac{\partial \hat{x}^i}{\partial r^j} \right] = R \quad \hat{g}^{ij} = \frac{\partial \hat{x}^k}{\partial r^i} \frac{\partial \hat{x}^l}{\partial r^j} = \begin{pmatrix} 1 & 0 & 0 \\ 0 & R^2 & 0 \\ 0 & 0 & 1 \end{pmatrix}. \quad (\text{A.32})$$

As deduced from the diagonal form of metric tensor \hat{g}_{ij} , the vectors of the contravariant basis $\left(\frac{\partial \mathbf{x}}{\partial R}, \frac{\partial \mathbf{x}}{\partial \phi}, \frac{\partial \mathbf{x}}{\partial Z} \right) = (\mathbf{e}_R, \mathbf{e}_\phi, \mathbf{e}_Z)$ are mutually orthogonal, and only the norm of $|\mathbf{e}_\phi| = R$ is different from unity. The covariant basis is formed by $(\nabla R, \nabla \phi, \nabla Z) = (\mathbf{e}_R, \mathbf{e}_\phi / R, \mathbf{e}_Z)$. The orthonormal cylindrical basis is $(\hat{\mathbf{e}}_R, \hat{\mathbf{e}}_\phi, \hat{\mathbf{e}}_Z) = (\mathbf{e}_R, \mathbf{e}_\phi / R, \mathbf{e}_Z) = (\nabla R, R \nabla \phi, \nabla Z)$. Thus, the components of the vector field \mathbf{B} in cylindrical coordinates are

$$B^{R,Z} = \mathbf{B} \cdot \nabla R, Z = \mathbf{B} \cdot \mathbf{e}_{R,Z} = B_{R,Z} \quad B^\phi = \mathbf{B} \cdot \nabla \phi = \frac{\hat{B}_\phi}{R} \quad B_\phi = \mathbf{B} \cdot \mathbf{e}_\phi = R \hat{B}_\phi$$

The components of the Christoffel symbol of first type $\Gamma_{i,jk} = \frac{\partial \mathbf{x}}{\partial r^i} \cdot \frac{\partial^2 \mathbf{x}}{\partial r^j \partial r^k}$ are mostly zero except for

$$\Gamma_{R,\phi\phi} = -R \quad \Gamma_{\phi,R\phi} = \Gamma_{\phi,\phi R} = R \quad \Longrightarrow \quad \Gamma_{\phi\phi}^R = -R \quad \Gamma_{R\phi}^\phi = \Gamma_{\phi R}^\phi = \frac{1}{R} \quad (\text{A.33})$$

Therefore the covariant derivative is written as

$$B_{;j}^i = \begin{pmatrix} \partial_R B^R & \partial_\phi B^R & \partial_Z B^R \\ \partial_R B^\phi & \partial_\phi B^\phi & \partial_Z B^\phi \\ \partial_R B^Z & \partial_\phi B^Z & \partial_Z B^Z \end{pmatrix} + \begin{pmatrix} 0 & -R B^\phi & 0 \\ \frac{B^\phi}{R} & \frac{B^R}{R} & 0 \\ 0 & 0 & 0 \end{pmatrix}$$

or alternatively

$$B_{i;j} = \begin{pmatrix} \partial_R B_R & \partial_\phi B_R & \partial_Z B_R \\ \partial_R B_\phi & \partial_\phi B_\phi & \partial_Z B_\phi \\ \partial_R B_Z & \partial_\phi B_Z & \partial_Z B_Z \end{pmatrix} + \begin{pmatrix} 0 & -R B^\phi & 0 \\ -R B^\phi & R B^R & 0 \\ 0 & 0 & 0 \end{pmatrix}.$$

The divergence in cylindrical coordinates is found either via

$$\nabla \cdot \mathbf{B} = B_{;i}^i = \partial_R B^R + \frac{B^R}{R} + \partial_\phi B^\phi + \partial_Z B^Z = \partial_R B_R + \frac{B_R}{R} + \frac{1}{R} \partial_\phi \hat{B}_\phi + \partial_Z B_Z$$

or via

$$\nabla \cdot \mathbf{B} = \frac{1}{\sqrt{g}} \partial_l (\sqrt{g} B^l) = \frac{1}{R} \partial_R (R B^R) + \partial_\phi B^\phi + \partial_Z B^Z = \frac{1}{R} \partial_R (R B_R) + \frac{1}{R} \partial_\phi \hat{B}_\phi + \partial_Z B_Z.$$

Appendix A. Mathematical complements

The curl is

$$\begin{aligned}
 \nabla \times \mathbf{B} &= (\partial_\phi B_Z - \partial_Z B_\phi) \nabla \phi \times \nabla Z + (\partial_Z B_R - \partial_R B_Z) \nabla Z \times \nabla R + (\partial_R B_\phi - \partial_\phi B_R) \nabla R \times \nabla \phi \\
 &= (\partial_\phi B_Z - R \partial_Z \hat{B}_\phi) \frac{\mathbf{e}_R}{R} + (\partial_Z B_R - \partial_R B_Z) \frac{\mathbf{e}_\phi}{R} + [\partial_R (R \hat{B}_\phi) - \partial_\phi B_R] \frac{\mathbf{e}_Z}{R} \\
 &= \left(\frac{1}{R} \partial_\phi B_Z - \partial_Z \hat{B}_\phi \right) \hat{\mathbf{e}}_R + (\partial_Z B_R - \partial_R B_Z) \hat{\mathbf{e}}_\phi + \frac{1}{R} [\partial_R (R \hat{B}_\phi) - \partial_\phi B_R] \hat{\mathbf{e}}_Z
 \end{aligned}$$

In the case where only the mapping from curvilinear to cylindrical coordinates is available, the transformation from curvilinear to Cartesian coordinates is facilitated by using the chain rule $\frac{\partial \hat{x}^i}{\partial u^j} = \frac{\partial \hat{x}^i}{\partial r^k} \frac{\partial r^k}{\partial u^j}$. Metric elements of the curvilinear system are then expressed with respect to the cylindrical variables as

$$g_{mn} = \frac{\partial \hat{x}^i}{\partial u^m} \frac{\partial \hat{x}_i}{\partial u^n} = \frac{\partial r^j}{\partial u^m} \frac{\partial \hat{x}^i}{\partial r^j} \frac{\partial \hat{x}_i}{\partial r^k} \frac{\partial r^k}{\partial u^n} = \frac{\partial r^j}{\partial u^m} \hat{g}_{jk} \frac{\partial r^k}{\partial u^n} = \frac{\partial R}{\partial u^m} \frac{\partial R}{\partial u^n} + \frac{\partial Z}{\partial u^m} \frac{\partial Z}{\partial u^n} + R^2 \frac{\partial \phi}{\partial u^m} \frac{\partial \phi}{\partial u^n} \quad (\text{A.34})$$

and the Jacobian of the coordinate transformation as

$$\sqrt{g} = \det \left[\frac{\partial \hat{x}^i}{\partial r^k} \right] \det \left[\frac{\partial r^k}{\partial u^j} \right] = R \det \left[\frac{\partial r^k}{\partial u^j} \right] = R \epsilon^{ijk} \frac{\partial R}{\partial u^i} \frac{\partial \phi}{\partial u^j} \frac{\partial Z}{\partial u^k}. \quad (\text{A.35})$$

If one of the coordinates is the geometrical toroidal angle, say $u^3 = \phi$, the Jacobian conveniently reduces to

$$\sqrt{g} = -R \left(\frac{\partial R}{\partial u^1} \frac{\partial Z}{\partial u^2} - \frac{\partial R}{\partial u^2} \frac{\partial Z}{\partial u^1} \right). \quad (\text{A.36})$$

Toroidal coordinates

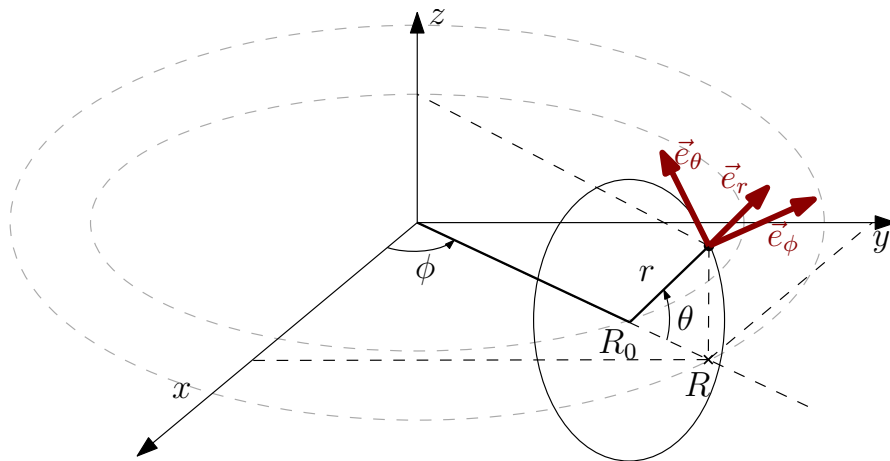


Figure A.4 – Toroidal coordinate system.

In tokamaks, the basic coordinate system is made of toroidal coordinates. Considering coordi-

nates $(t^1, t^2, t^3) = (r, \theta, \phi)$, it follows

$$\begin{cases} x = (R_0 + r \cos \theta) \cos \phi = R \cos \phi \\ y = (R_0 + r \sin \theta) \sin \phi = R \sin \phi \\ z = r \sin \theta \end{cases} \quad \frac{\partial \hat{x}^i}{\partial t^j} = \begin{pmatrix} \cos \theta \cos \phi & -r \sin \theta \cos \phi & -R \sin \phi \\ \cos \theta \sin \phi & -r \sin \theta \sin \phi & R \cos \phi \\ \sin \theta & r \cos \theta & 0 \end{pmatrix} \quad (\text{A.37})$$

$$\sqrt{\hat{g}} = \det \left[\frac{\partial \hat{x}^i}{\partial t^j} \right] = -r(R_0 + r \cos \theta) \quad \hat{g}_{ij} = \frac{\partial \hat{x}^k}{\partial t^i} \frac{\partial \hat{x}^l}{\partial t^j} = \begin{pmatrix} 1 & 0 & 0 \\ 0 & r^2 & 0 \\ 0 & 0 & (R_0 + r \cos \theta)^2 \end{pmatrix}. \quad (\text{A.38})$$

Notice that the Jacobian is negative because it forms a left-handed coordinate system. As deduced from the diagonal form of metric tensor \hat{g}_{ij} , the vectors of the contravariant basis $\left(\frac{\partial \mathbf{x}}{\partial r}, \frac{\partial \mathbf{x}}{\partial \theta}, \frac{\partial \mathbf{x}}{\partial \phi} \right) = (\mathbf{e}_r, \mathbf{e}_\theta, \mathbf{e}_\phi)$ are mutually orthogonal. The norms of $|\mathbf{e}_\theta| = r$ and $|\mathbf{e}_\phi| = R$ are different from unity. The covariant basis is formed by $(\nabla r, \nabla \theta, \nabla \phi) = (\mathbf{e}_r, \mathbf{e}_\theta / r^2, \mathbf{e}_\phi / R^2)$. The orthonormal cylindrical basis is $(\hat{\mathbf{e}}_r, \hat{\mathbf{e}}_\theta, \hat{\mathbf{e}}_\phi) = (\mathbf{e}_r, \mathbf{e}_\theta / r, \mathbf{e}_\phi / R) = (\nabla r, r \nabla \theta, R \nabla \phi)$.

A.2 Lagrangian and Hamiltonian formalism

Lagrangian and Hamiltonian mechanics are a mathematical treatment of dynamical systems that applies not only to various realms of physics, from basic mechanics to quantum physics, but also more generally to a large category of problems in economy, statistics, biology, etc. The point of view is rigorously anchored in mathematics and the connections with fundamental theorems of differential geometry are profound. Using Lagrange or Hamiltonian methods sometimes seems superfluous, a little bit like cracking a nut open with a bulldozer, but often the solutions unroll with an enjoyable level of elegance and consistency and reveals much more about the physical properties of the studied system than when more direct methods are employed.

In this section, some useful aspects of Lagrangian mechanics are highlighted, in particular the extension to phase-space variables and the underlying symplectic algebra relating the Lagrangian to the Hamiltonian formalism. The reader may refer to Goldstein et al. (2001) for more introductory and physical explanations and Arnol'd (1989) for more mathematical and rigorous proofs.

The Lagrangian \mathcal{L} is a scalar function of independent coordinates $q^i(t)$, their derivatives $\dot{q}^i(t)$ and time. The coordinates $q^i(t)$ represent all the possible "evolutions" or trajectories that lead the system from one state A to another state B . The following functional, called the *action integral*, measures the likely-hood or "cost" for each trajectory

$$S[q] = \int_A^B \mathcal{L}(q^i, \dot{q}^i, t) dt \quad (\text{A.39})$$

In classical mechanics, the system evolves according to the *minimum action principle* or *D'Alembert principle*, i.e. the system always chooses a path for which the action is minimal. It is interesting to mention that quantum mechanics can be interpreted in terms of a minimum

Appendix A. Mathematical complements

action principle by realising that all paths are possible only that their probability exponentially decays away from classical evolution. Applying the minimum action principle to S yields a set of differential equations of motion, called the *Euler-Lagrange equations*

$$\delta S = 0 \iff \int_A^B dt \left[\frac{\partial \mathcal{L}}{\partial q^i} \delta q^i + \frac{\partial \mathcal{L}}{\partial \dot{q}^i} \delta \dot{q}^i \right] = 0 \iff \int_A^B dt \left[\frac{\partial \mathcal{L}}{\partial q^i} - \frac{d}{dt} \left(\frac{\partial \mathcal{L}}{\partial \dot{q}^i} \right) \right] \delta q^i = 0$$

where, in the last step, an integration by parts was performed assuming that $\delta \dot{q}^i = d\delta q^i/dt$ and that the perturbations vanish at the end-points, i.e. $\delta q^i(A) = \delta q^i(B) = 0$. This equation being valid for arbitrary perturbations, it is equivalent to solving

$$\frac{d}{dt} \left(\frac{\partial \mathcal{L}}{\partial \dot{q}^i} \right) = \frac{\partial \mathcal{L}}{\partial q^i} \quad (\text{A.40})$$

Notice that these equations are unchanged if the Lagrangian is altered by a full time-derivative

$$\mathcal{L} \equiv \mathcal{L} + \frac{df}{dt}, \quad (\text{A.41})$$

a property closely related to gauge invariance in electrodynamics.

The structure of the Euler-Lagrange equations reminds of Newton equations $dp_i/dt = \partial_i L$ after identifying the *canonical momenta*

$$p_i(q^i, \dot{q}^i, t) = \frac{\partial \mathcal{L}}{\partial \dot{q}^i} \longrightarrow \dot{q}^i(q^i, p_i, t) \quad (\text{A.42})$$

The canonical momenta enter in the Legendre transform of the Lagrangian with respect to \dot{q}^i , namely the *Hamiltonian*

$$\mathcal{H}(q^i, p_i, t) = p_i \dot{q}^i - \mathcal{L} \quad (\text{A.43})$$

where summation over repeated indices is assumed. The Hamiltonian of the system often represents its energy. The equations of motion, known as *Hamilton equations* are written

$$\dot{q}^i = \frac{\partial \mathcal{H}}{\partial p_i} \qquad \dot{p}_i = -\frac{\partial \mathcal{H}}{\partial q^i} \qquad \frac{\partial \mathcal{L}}{\partial t} = -\frac{d\mathcal{H}}{dt} \quad (\text{A.44})$$

Euler-Lagrange and Hamilton equations (A.40 and A.44) are qualified as dual; there is no difference in treating mechanical systems with either formalism, except for the sake of simplicity. Hamiltonian method is arguably more powerful and elegant when there is underlying symmetry but Lagrangian methods should not be considered as *less correct*.

Hamilton equations can be derived from a variational principle by introducing the *phase-space Lagrangian* (Goldstein et al., 2001, chapter 8.5)

$$L(q^i, \dot{q}^i, p_i, \dot{p}_i, t) = p_i \dot{q}^i - \mathcal{H}(q^i, p_i, t) \longrightarrow S = \int L dt \quad (\text{A.45})$$

This Lagrangian is formally different from the usual Lagrangian in the sense that \dot{q}^i as well as \dot{p}_i have been promoted to independent quantities. The minimal action principle now holds for the two sets of canonical coordinates q^i and p_i , yielding

$$\frac{d}{dt} \left(\frac{\partial L}{\partial \dot{q}^i} \right) - \frac{\partial L}{\partial q^i} = 0 \quad \Rightarrow \quad \dot{p}_i + \frac{\partial \mathcal{H}}{\partial q^i} = 0 \quad (\text{A.46})$$

$$\frac{d}{dt} \left(\frac{\partial L}{\partial \dot{p}_i} \right) - \frac{\partial L}{\partial p_i} = 0 \quad \Rightarrow \quad \frac{\partial \mathcal{H}}{\partial p_i} - \dot{q}^i = 0 \quad (\text{A.47})$$

the usual Hamilton equations.

A.2.1 Phase-space Lagrangian and non-canonical Hamilton equations of motion

Phase-space Lagrangian is useful when the problem is formulated in terms of non-canonical coordinates⁵ (Cary and Brizard, 2009). Let us consider a change of coordinates $z^\alpha = z^\alpha(q^i, p_i, t)$ and its inverse $[q^i, p_i](z^\alpha, t)$. Then

$$\dot{q}^i = \partial_t q^i + \dot{z}^\alpha \partial_\alpha q^i \quad (\text{A.48})$$

where the notation $\partial_t \equiv \frac{\partial}{\partial t}$ and $\partial_\alpha \equiv \frac{\partial}{\partial z^\alpha}$. The phase-space Lagrangian becomes

$$L(z^\alpha, \dot{z}^\alpha, t) = p_i \partial_\alpha q^i \dot{z}^\alpha + p_i \partial_t q^i - \mathcal{H}(z^\alpha, t) = \Lambda_\alpha \dot{z}^\alpha - H \quad (\text{A.49})$$

where $\Lambda_\alpha = p_i \partial_\alpha q^i$ and $H = \mathcal{H} - p_i \partial_t q^i$.

The Euler-Lagrange equations read

$$0 = \frac{d}{dt} \left(\frac{\partial L}{\partial \dot{z}^\alpha} \right) - \frac{\partial L}{\partial z^\alpha} = \partial_t \Lambda_\alpha - (\partial_\alpha \Lambda_\beta - \partial_\beta \Lambda_\alpha) \dot{z}^\beta + \partial_\alpha H \iff \Omega_{\alpha\beta} \dot{z}^\beta = \partial_\alpha H + \partial_t \Lambda_\alpha \quad (\text{A.50})$$

where the tensor Ω is defined as

$$\Omega_{\alpha\beta} = \partial_\alpha \Lambda_\beta - \partial_\beta \Lambda_\alpha = - \left\{ z^\alpha, z^\beta \right\} = - \left(\frac{\partial q^i}{\partial z^\alpha} \frac{\partial p_i}{\partial z^\beta} - \frac{\partial q^i}{\partial z^\beta} \frac{\partial p_i}{\partial z^\alpha} \right) \quad (\text{A.51})$$

The components of Ω are equal to the so-called *Lagrange brackets* of the non-canonical coordinates. Finding the inverse of Ω , namely Π , such that $\Pi^{\alpha\beta} \Omega_{\beta\gamma} = \delta_\gamma^\alpha$, allows us to write the equations of motion as

$$\dot{z}^\alpha = \Pi^{\alpha\beta} (\partial_\beta H + \partial_t \Lambda_\beta) \quad (\text{A.52})$$

Equations (A.52) are a form of Hamilton equations of motion for non-canonical coordinates. They have the combined advantage of having an underlying Hamilton structure and being flexible in the use of meaningful coordinates.

⁵Coordinates in which the equations of motion do not have the symplectic structure of equations (A.44).

Appendix A. Mathematical complements

A.2.2 Lagrange and Poisson brackets

To understand what is hidden behind the non-canonical equations of motion, let us write Ω as

$$\Omega_{\alpha\beta} = \frac{\partial Z^\mu}{\partial z^\alpha} \omega_{\mu\nu} \frac{\partial Z^\nu}{\partial z^\beta} \quad \text{or} \quad \Omega = D^T \omega D \quad (\text{A.53})$$

where $Z = (q, p)$ is the $2N$ vector of canonical coordinates, $D^\alpha_\beta = \frac{\partial Z^\alpha}{\partial z^\beta} = (D^T)_\beta^\alpha$ the Jacobian matrix of the transformation from canonical to non-canonical coordinates and

$$\omega = \begin{pmatrix} 0 & -I_{N \times N} \\ I_{N \times N} & 0 \end{pmatrix}$$

is the symplectic matrix. We recognize (A.53) as the transformation of a 2-covariant tensor. A canonical transformation is defined as a change of phase-space variables that preserves the symplectic expression of the phase-space Lagrangian, i.e. $\Omega_C = D_C^T \omega D_C = \omega$ (Goldstein et al., 2001, chapter 9.4). A non-canonical transformation will implicitly preserve the symplectic structure but mix-up the writing.

We see that $\det \Omega = (\det D)^2 > 0$. Therefore, the inverse Π is guaranteed to exist. Namely,

$$\Pi = (D^{-1})^T \omega^{-1} D^{-1} \quad \text{or} \quad \Pi^{\alpha\beta} = \frac{\partial z^\alpha}{\partial Z^\mu} \sigma^{\mu\nu} \frac{\partial z^\beta}{\partial Z^\nu} \quad (\text{A.54})$$

where $\sigma = \omega^{-1} = -\omega$ and $(D^{-1})^\alpha_\beta = \frac{\partial z^\alpha}{\partial Z^\beta}$ the Jacobian matrix of the transformation from non-canonical to canonical coordinates.

It is interesting to notice from (A.54) that Π is also the matrix formed by the *Poisson brackets* of the new coordinates

$$\Pi^{\alpha\beta} = \frac{\partial z^\alpha}{\partial q^i} \frac{\partial z^\beta}{\partial p_i} - \frac{\partial z^\beta}{\partial q^i} \frac{\partial z^\alpha}{\partial p_i} = [z^\alpha, z^\beta] \quad (\text{A.55})$$

Hence, the Poisson brackets of any two functions f and g can now be expressed in the new coordinate system as

$$[f, g] = \partial_\alpha f \Pi^{\alpha\beta} \partial_\beta g \quad (\text{A.56})$$

and again, a canonical transformation is such that the Poisson brackets are purely symplectic, i.e. $\Pi_C = \sigma$. We now realize that the equations of motion (C.12) are the full time-derivative of the coordinates under the action of the Hamiltonian flow, i.e.

$$\dot{z}^\alpha = [z^\alpha, H] + \partial_t z^\alpha \quad (\text{A.57})$$

This confirms that there is no loss of structure in the change of coordinates and all properties of the Hamiltonian formalism are retained.

A.2.3 Liouville theorem and other properties

The important Liouville theorem is still valid after a non-canonical phase-space transformation, as shown hereafter. From (A.51) and (A.53) we conclude that Ω is a 2-covariant anti-symmetric tensor. It can be represented by a differential 2-form $\Omega = \frac{1}{2}\Omega_{\alpha\beta} dz^\alpha \wedge dz^\beta$. We notice that $\Omega = d\Lambda = d(\Lambda_\alpha dz^\alpha)$ by construction, i.e. Ω is an exact form. Since $d^2 = 0$, we have $d\Omega = 0$, i.e. Ω is a closed form. This is a useful property, equivalent to stating the following Jacobi identity

$$\partial_\alpha \Omega_{\beta\gamma} + \partial_\beta \Omega_{\gamma\alpha} + \partial_\gamma \Omega_{\alpha\beta} = 0. \quad (\text{A.58})$$

This equation can be inverted to involve the Poisson matrix. Starting from $\Pi^{\alpha\beta}\Omega_{\beta\gamma} = \delta_\gamma^\alpha$, we have

$$\partial_\mu \Pi^{\alpha\beta}\Omega_{\beta\gamma} + \Pi^{\alpha\beta}\partial_\mu \Omega_{\beta\gamma} = 0 \quad \Rightarrow \quad \partial_\mu \Pi^{\alpha\delta} = -\Pi^{\alpha\beta}\partial_\mu \Omega_{\beta\gamma}\Pi^{\gamma\delta} \quad (\text{A.59})$$

and contracting (A.58) with $\Pi^{\mu\alpha}\Pi^{\nu\beta}\Pi^{\sigma\gamma}$, we find

$$\Pi^{\mu\alpha}\partial_\alpha \Pi^{\nu\sigma} + \Pi^{\nu\alpha}\partial_\alpha \Pi^{\sigma\mu} + \Pi^{\sigma\alpha}\partial_\alpha \Pi^{\mu\nu} = 0 \quad (\text{A.60})$$

It is not difficult to show that this identity corresponds to the well-known property of Poisson brackets, which is one of the defining properties of a Lie algebra

$$[f, [g, h]] + [g, [h, f]] + [h, [f, g]] = 0 \quad (\text{A.61})$$

for any functions f, g and h .

We will use the above identities to prove Liouville theorem for non-canonical coordinates. That the dynamics satisfy Liouville theorem is an advantage when solving the problem numerically. It basically states that phase-space volume is conserved under Hamiltonian flow. Another way of phrasing it is that the Hamiltonian flow is *incompressible*

$$\text{“div } v\text{”} = (\partial_q, \partial_p, \partial_t) \cdot (\dot{q}, \dot{p}, \dot{t}) = \frac{\partial \dot{q}}{\partial t} + \frac{\partial \dot{q}}{\partial q} + \frac{\partial \dot{p}}{\partial p} = \frac{\partial^2 H}{\partial q \partial p} - \frac{\partial^2 H}{\partial p \partial q} = 0 \quad (\text{A.62})$$

Switching to non-canonical coordinates, the divergence is adjusted to “div v ” = $\frac{1}{\mathcal{J}} \frac{\partial}{\partial z^M} (\mathcal{J} v^M)$, where $\mathcal{J} = \det D = \sqrt{\Omega}$ is the Jacobian of the transformation from canonical to non-canonical coordinates. Liouville theorem is then

$$\frac{\partial \sqrt{\Omega}}{\partial t} + \frac{\partial}{\partial z^\alpha} (\sqrt{\Omega} \dot{z}^\alpha) = \frac{1}{2\sqrt{\Omega}} \frac{\partial \Omega}{\partial t} + \frac{1}{2\sqrt{\Omega}} \frac{\partial \Omega}{\partial z^\alpha} \dot{z}^\alpha + \sqrt{\Omega} \frac{\partial \dot{z}^\alpha}{\partial z^\alpha} = 0 \quad (\text{A.63})$$

Even if this equation is justified by the properties of coordinate transformations, it is instructive to check it explicitly.

First, we express the derivatives of Ω . Starting with the relation between the determinant and

Appendix A. Mathematical complements

trace of a matrix, $\ln \det M = \text{tr} \ln M$ we derive

$$\frac{\partial \Omega}{\partial z^\alpha} = \Omega \Pi^{\beta\gamma} \partial_\alpha \Omega_{\gamma\beta} = -\Omega \Pi^{\beta\gamma} \partial_\alpha \Omega_{\beta\gamma} \quad (\text{A.64})$$

$$\frac{\partial \Omega}{\partial t} = -2\Omega \Pi^{\alpha\beta} \frac{\partial^2 \Lambda_\beta}{\partial z^\alpha \partial t} \quad (\text{A.65})$$

Then, we unfold $\partial_\alpha \dot{z}^\alpha$ using equations of motion (C.12) and identity (A.59)

$$\begin{aligned} \frac{\partial \dot{z}^\alpha}{\partial z^\alpha} &= \partial_\alpha \Pi^{\alpha\beta} (\partial_\beta H + \partial_t \Lambda_\beta) + \Pi^{\alpha\beta} \frac{\partial^2 \Lambda_\beta}{\partial z^\alpha \partial t} \\ &= -\Pi^{\alpha\gamma} \partial_\alpha \Omega_{\gamma\delta} \underbrace{\Pi^{\delta\beta} (\partial_\beta H + \partial_t \Lambda_\beta)}_{\dot{z}^\delta} + \Pi^{\alpha\beta} \frac{\partial^2 \Lambda_\beta}{\partial z^\alpha \partial t} \end{aligned}$$

and after re-ordering and relabeling indices, we have

$$\frac{\partial \dot{z}^\alpha}{\partial z^\alpha} = -\frac{1}{2} \Pi^{\beta\gamma} (\partial_\beta \Omega_{\gamma\alpha} + \partial_\gamma \Omega_{\alpha\beta}) \dot{z}^\alpha + \Pi^{\alpha\beta} \frac{\partial^2 \Lambda_\beta}{\partial z^\alpha \partial t} \quad (\text{A.66})$$

Gathering and plugging all pieces from (A.64-A.66) into (A.63) shows the validity of Liouville theorem for non-canonical coordinates

$$-\cancel{\sqrt{\Omega} \Pi^{\alpha\beta} \frac{\partial^2 \Lambda_\beta}{\partial z^\alpha \partial t}} - \frac{1}{2} \sqrt{\Omega} \Pi^{\beta\gamma} (\partial_\alpha \Omega_{\beta\gamma} + \partial_\beta \Omega_{\gamma\alpha} + \partial_\gamma \Omega_{\alpha\beta}) \dot{z}^\alpha + \cancel{\sqrt{\Omega} \Pi^{\alpha\beta} \frac{\partial^2 \Lambda_\beta}{\partial z^\alpha \partial t}} = 0 \quad (\text{A.67})$$

Notice how Jacobi identity (A.58) enters in the final step of the proof.

Finally, we may think of $\mathcal{J} = \sqrt{\Omega}$ as a *phase-space density* in the sense that $\sqrt{\Omega} dz^{2N} = dq^N dp^N$ is a phase-space volume with well-behaved time-evolution.

B MHD equilibria

B.1 Axisymmetric representations

B.1.1 Analytic Solov'ev equilibrium

Solov'ev equilibrium is an axisymmetric solution of the Grad-Shafranov equation in the particular case where the current profile F is constant and the pressure profile p is a linear function of the poloidal flux Ψ (Solov'ev, 1968), namely

$$F = B_0 R_0 \qquad \mu_0 p(\Psi) = \frac{1 + e^2}{a^2 R_0^2 e^2} 2\Psi_b(\Psi_b - \Psi)$$

where Ψ_b is the poloidal flux at the last closed flux surface, R_0 the major radius, B_0 the magnetic field strength at the magnetic axis, μ_0 the vacuum permeability, a the minor radius and e the elongation. Given these particular profiles, the Grad-Shafranov equation admits the following solution for the poloidal magnetic flux as a function of cylindrical coordinates

$$\Psi(R, Z) = \frac{\Psi_b}{a^2 R_0^2} \left[\frac{(R^2 - R_0^2)^2}{4} + \frac{R^2 Z^2}{e^2} \right].$$

Recognising the equation of an ellipse, it is reasonable to define the radial variable $\rho \in [0, 1]$ as $\rho^2 = \Psi/\Psi_b$ and the poloidal angle θ such that

$$R^2 = R_0^2 + 2aR_0\rho \cos\theta \qquad Z = \frac{eaR_0}{R}\rho \sin\theta.$$

Letting (ρ, θ, ϕ) define the new curvilinear coordinate system, the Jacobian is expressed as

$$\sqrt{g} \stackrel{(A.36)}{=} -ea^2\rho R_0 \frac{R_0}{R}.$$

The Jacobian being negative means that the chosen coordinates define a left-handed system.

First derivatives, that are useful to construct the metric tensor, are written as

$$\begin{aligned} \frac{\partial R}{\partial \rho} &= \frac{a_0 R_0}{R} \cos\theta & \frac{\partial R}{\partial \theta} &= -\frac{Z}{e} \\ \frac{\partial Z}{\partial \rho} &= \frac{a_0 R_0}{R} \left(e \sin\theta - \frac{Z}{R} \cos\theta \right) & \frac{\partial Z}{\partial \theta} &= \frac{\rho a_0 R_0}{R} \left(e \cos\theta + \frac{Z}{R} \sin\theta \right). \end{aligned}$$

Second derivatives, that enter the Christoffel symbol and the variation of the metric tensor,

Appendix B. MHD equilibria

are expressed as

$$\frac{\partial^2 R}{\partial \rho^2} = -\frac{1}{R} \left(\frac{\partial R}{\partial \rho} \right)^2 \quad \frac{\partial^2 R}{\partial \theta^2} = -\frac{1}{e} \frac{\partial Z}{\partial \theta} \quad \frac{\partial^2 R}{\partial \theta \partial \rho} = -\frac{1}{e} \frac{\partial Z}{\partial \rho}$$

and

$$\begin{aligned} \frac{\partial^2 Z}{\partial \rho^2} &= \frac{e a_0 R_0 \sin \theta}{R^2} \frac{\partial R}{\partial \rho} \left(-2 + 3 \frac{\rho}{R} \frac{\partial R}{\partial \rho} \right) \\ \frac{\partial^2 Z}{\partial \theta^2} &= -Z + 3 \rho \cos \theta \frac{Z}{R} \frac{\partial R}{\partial \rho} + \frac{3}{e^2} \frac{Z^3}{R^2} \\ \frac{\partial^2 Z}{\partial \rho \partial \theta} &= e \frac{\partial R}{\partial \rho} + e \rho \frac{\partial^2 R}{\partial \rho^2} + 2 \frac{Z}{R} \frac{a_0 R_0 \sin \theta}{R} - \frac{3}{e} \frac{Z^2}{R^2} \frac{\partial R}{\partial \rho}. \end{aligned}$$

The axisymmetric magnetic field $\mathbf{B} = F \nabla \phi + \nabla \Psi \times \nabla \phi$ is thus written

$$\mathbf{B} = B_0 R_0 \nabla \phi - 2 \Psi_b \rho \nabla \phi \times \nabla \rho = \frac{B_0 R_0}{R^2} \mathbf{e}_\phi - \frac{2 \Psi_b \rho}{\sqrt{g}} \mathbf{e}_\theta$$

such that the covariant, contravariant and wedge components of the field required in the equations of motion are

$$\begin{aligned} B_\phi &= B_0 R_0 & B^\phi &= \frac{B_0 R_0}{R^2} & W^\phi &= -B_0 e a^2 \rho \frac{R_0^3}{R^3} \\ B_\theta &= g_{\theta\theta} B^\theta & B^\theta &= \frac{2 \Psi_b R}{e a^2 R_0^2} & W^\theta &= -2 \Psi_b \rho \\ B_\rho &= g_{\rho\rho} B^\rho & B^\rho &= 0 & W^\rho &= 0 \end{aligned}$$

where

$$\begin{aligned} g_{\rho\theta} &= -\rho \frac{a_0^2 R_0^2}{R^2} \left[\left(1 - e^2 + \frac{Z^2}{R^2} \right) \cos \theta \sin \theta + e \frac{Z}{R} (1 - 2 \sin^2 \theta) \right] \\ g_{\theta\theta} &= \rho^2 \frac{a_0^2 R_0^2}{R^2} \left[e^2 + \left(1 - e^2 + \frac{Z^2}{R^2} \right) \sin^2 \theta + 2e \frac{Z}{R} \sin \theta \cos \theta \right] \end{aligned}$$

Because the current profile F is constant, $\nabla \times \mathbf{B} = K^\phi \nabla \rho \times \nabla \theta$. From the fact that the magnetic field satisfies MHD force balance, $(\nabla \times \mathbf{B}) \times \mathbf{B} = \mu_0 \nabla p = -\frac{1+e^2}{e^2 a^2 R_0^2} 4 \Psi_b^2 \rho \nabla \rho$, the components of $\nabla \times \mathbf{B}$ are

$$K^\rho = 0 \quad K^\theta = 0 \quad K^\phi = \frac{1+e^2}{e} \frac{2 \Psi_b \rho}{R}$$

Notice that this means that the toroidal current $J^\phi = (\nabla \times \mathbf{B}) \cdot \nabla \phi = K^\phi / \sqrt{g} = -2 \Psi_b (1 + e^2) / e^2 a^2 R_0^2$ is negative for a positively oriented poloidal field ($\Psi_b > 0$). This affects the interpretation of co-passing and counter-passing particles.

Finally, the magnetic field strength (square) is expressed as

$$B^2 = \frac{B_0^2 R_0^2}{R^2} + \frac{4\Psi_b^2 \rho^2}{e^2 a^2 R_0^2} \left[e^2 + \left(1 - e^2 + \frac{Z^2}{R^2} \right) \sin^2 \theta + 2e \frac{Z}{R} \sin \theta \cos \theta \right]$$

and its relevant derivatives

$$\begin{aligned} \frac{\partial B^2}{\partial \rho} = & -2a_0 R_0 \cos \theta \left(\frac{B_0 R_0}{R^2} \right)^2 + \frac{8\Psi_b^2 \rho}{e^2 a_0^2 R_0^2} \left[e^2 - 2 \frac{Z^2}{R^2} \right. \\ & \left. + \left(1 - e^2 + 4 \frac{Z^2}{R^2} \right) \sin^2 \theta + \frac{1}{e} \frac{Z}{R} \left(3e^2 - 2 \frac{Z^2}{R^2} \right) \cos \theta \sin \theta \right] \end{aligned}$$

and

$$\begin{aligned} \frac{\partial B^2}{\partial \theta} = & 2\rho a_0 R_0 \sin \theta \left(\frac{B_0 R_0}{R^2} \right)^2 + \frac{8\Psi_b^2 \rho}{e^2 a_0^2 R_0^2} \left[2e \frac{Z}{R} \right. \\ & \left. + \left(1 - e^2 + 4 \frac{Z^2}{R^2} \right) \cos \theta \sin \theta - \frac{1}{e} \frac{Z}{R} \left(3e^2 - 2 \frac{Z^2}{R^2} \right) \sin^2 \theta \right]. \end{aligned}$$

B.1.2 Axisymmetric straight field-line coordinates (MINERVA, PEST)

From the general representation of axisymmetric equilibrium magnetic fields, $\mathbf{B} = F(\bar{\Psi})\nabla\zeta + \nabla\zeta \times \nabla\Psi$ where the toroidal angle is the reversed geometric angle $\zeta = -\phi$, the radial variable is chosen as $\bar{\Psi} = \Psi/\Psi_e$ (poloidal magnetic flux) and the poloidal angle θ is defined such that the coordinate system is field-aligned, i.e. that the local pitch of the field is the q-profile flux function

$$\frac{\mathbf{B} \cdot \nabla\zeta}{\mathbf{B} \cdot \nabla\theta} = \frac{F|\nabla\zeta|^2}{\Psi_e(\nabla\zeta \times \nabla\bar{\Psi}) \cdot \nabla\theta} = \frac{F\sqrt{g}}{\Psi_e R^2} \equiv q(\bar{\Psi}).$$

Reversing the toroidal angle ensures that the coordinate system $(\bar{\Psi}, \theta, \zeta)$ is right-handed when F , q and Ψ_e are positive profiles. The jacobian of the coordinate transformation is thus $\sqrt{g} = \frac{q}{F} \Psi_e R^2 > 0$.

The contravariant components of the magnetic field are

$$B^\theta = \mathbf{B} \cdot \nabla\theta = \frac{\Psi_e}{\sqrt{g}} = \frac{F}{qR^2} \qquad B^\zeta = \mathbf{B} \cdot \nabla\zeta = q \frac{\Psi_e}{\sqrt{g}} = \frac{F}{R^2}.$$

Since $\nabla\zeta = \frac{\sqrt{g}}{R^2} \nabla\bar{\Psi} \times \nabla\theta = \frac{q\Psi_e}{F} \nabla\bar{\Psi} \times \nabla\theta$, the magnetic field is conveniently expressed in the wedge-representation as

$$\mathbf{B} = q\Psi_e \nabla\bar{\Psi} \times \nabla\theta + \Psi_e \nabla\zeta \times \nabla\bar{\Psi} = \Psi_e \nabla\bar{\Psi} \times \nabla(q\theta - \zeta)$$

and, up to a gauge choice, the vector potential is

$$\mathbf{A} = Q\nabla\theta - \Psi\nabla\zeta$$

Appendix B. MHD equilibria

where Q is the integral of the q -profile in Ψ , i.e. $\frac{dQ}{d\Psi} = \Psi_e Q' = q$.

The covariant components are $B_\zeta = F$, $B_\theta = g_{\theta\theta} B^\theta$ and $B_{\bar{\Psi}} = g_{\bar{\Psi}\theta} B^\theta$, where the metric elements are computed as

$$g_{\bar{\Psi}\theta} = \frac{\partial R}{\partial \bar{\Psi}} \frac{\partial R}{\partial \theta} + \frac{\partial Z}{\partial \bar{\Psi}} \frac{\partial Z}{\partial \theta} \quad g_{\theta\theta} = \left(\frac{\partial R}{\partial \theta} \right)^2 + \left(\frac{\partial Z}{\partial \theta} \right)^2.$$

Concerning $\nabla \times \mathbf{B} = -F' \nabla \zeta \times \nabla \bar{\Psi} + K^\zeta \nabla \bar{\Psi} \times \nabla \theta$, the MHD force balance equation $(\nabla \times \mathbf{B}) \times \mathbf{B} = \mu_0 \nabla p = \mu_0 p' \nabla \bar{\Psi}$ is invoked to yield

$$K^{\bar{\Psi}} = 0 \quad K^\theta = -F' \quad K^\zeta = -q \left(F' + \mu_0 p' \frac{R^2}{F} \right)$$

where $p(\bar{\Psi})$ is the pressure profile and μ_0 the vacuum permeability.

The field strength is calculated as

$$B = \sqrt{\frac{F^2}{R^2} + g_{\theta\theta} (B^\theta)^2} = \frac{F}{R} \sqrt{1 + \frac{g_{\theta\theta}}{q^2 R^2}}$$

and its derivatives as

$$\begin{aligned} \frac{\partial B}{\partial \bar{\Psi}} &= \left(\frac{F'}{F} - \frac{\partial R}{\partial \bar{\Psi}} \frac{1}{R} \right) B + \frac{(B^\theta)^2}{B} \left[\frac{1}{2} \frac{\partial g_{\theta\theta}}{\partial \bar{\Psi}} - g_{\theta\theta} \left(\frac{q'}{q} + \frac{\partial R}{\partial \bar{\Psi}} \frac{1}{R} \right) \right] \\ \frac{\partial B}{\partial \theta} &= -\frac{\partial R}{\partial \theta} \frac{1}{R} B + \frac{(B^\theta)^2}{B} \left(\frac{1}{2} \frac{\partial g_{\theta\theta}}{\partial \theta} - g_{\theta\theta} \frac{\partial R}{\partial \theta} \frac{1}{R} \right). \end{aligned}$$

where

$$\frac{1}{2} \frac{\partial g_{\theta\theta}}{\partial \bar{\Psi}} = \frac{\partial R}{\partial \theta} \frac{\partial^2 R}{\partial \bar{\Psi} \partial \theta} + \frac{\partial Z}{\partial \theta} \frac{\partial^2 Z}{\partial \bar{\Psi} \partial \theta} \quad \frac{1}{2} \frac{\partial g_{\theta\theta}}{\partial \theta} = \frac{\partial R}{\partial \theta} \frac{\partial^2 R}{\partial \theta^2} + \frac{\partial Z}{\partial \theta} \frac{\partial^2 Z}{\partial \theta^2}$$

The q -profile, the current profile and the pressure profile, as well as the geometry of flux surfaces and the mapping to cylindrical coordinates, have to be prescribed. MINERVA is an example of a stability code providing a Fourier decomposition of those fields, which is then interpolated in VENUS-LEVIS with the spline-Fourier technique described in section 4.2.

B.2 3D representations with nested flux surfaces

B.2.1 VMFC/ANIMEC coordinates

VMFC/ANIMEC coordinates are flux coordinates (s, u, v) , where $s = \Phi/\Phi_b$ is the radial variable proportional to the toroidal magnetic flux, u the poloidal angle and $v = \phi$ corresponds to the geometrical toroidal angle. The coordinate system is neither orthogonal nor straight, but it has the property that the number of Fourier modes representing the MHD equilibrium is minimum. The magnetic field is deduced from the following vector potential in terms of flux

functions $\Phi(s) = \Phi_b s$ and $\Psi(s)$ and the additional field $\lambda(s, u, v)$

$$\mathbf{A} = \lambda(s, u, v) \nabla s + \Phi \nabla u - \Psi \nabla v.$$

In the wedge representation, the magnetic field becomes via

$$\mathbf{B} = \nabla \times \mathbf{A} = (\Psi' + \partial_v \lambda) \nabla v \times \nabla s + (\Phi' - \partial_u \lambda) \nabla s \times \nabla u.$$

The q -profile is thus given by $q(s) = \langle B^v / B^u \rangle = \Phi' / \Psi'$, where $\langle . \rangle$ means flux-surface average.

The output of VMEC/ANIMEC readily provides the mapping to cylindrical coordinates in the form

$$R(s, u, v) = \sum_{mn} R_{mn}(s) \cos(mu - nv)$$

$$Z(s, u, v) = \sum_{mn} Z_{mn}(s) \sin(mu - nv)$$

which is used in VENUS-LEVIS to calculate various elements of the metric via the results of section A.1.3. The covariant and contravariant components of the magnetic field B^u, B^v, B_s, B_u and B_v , as well as the magnetic field strength B , are similarly decomposed in Fourier series. VMEC/ANIMEC output includes cosine based functions $B_{mn}, B_{mn}^u, B_{mn}^v, B_{u,mn}, B_{v,mn}, R_{mn}$ and sine based functions $B_{s,mn}, Z_{mn}$ and also provides flux functions such as the iota profile $\iota(s)$ and the toroidal magnetic flux $\Psi'(s)$. Remaining quantities required in the equations of motion are derived without difficulty via the spline-Fourier algorithm of section 4.2.

B.3 Stellarator symmetry jargon

The condition of stellarator symmetry is an adaptation to toroidal systems of the concepts of parity and time-reversal. Let us consider the discrete transformation on the cylindrical coordinates

$$I: (R, \phi, Z) \rightarrow (R, -\phi, -Z) \tag{B.1}$$

and its action on an arbitrary field (pullback operation) as

$$(IM)(R, \phi, Z) = (\mathbf{M} \circ I)(R, \phi, Z) = \mathbf{M}(R, -\phi, -Z). \tag{B.2}$$

An important property of this transformation is, by virtue of the definition of partial derivatives for a given function f

$$(\partial_R f)(R, \phi, Z) = \lim_{h \rightarrow 0} \frac{f(R+h, \phi, Z) - f(R, \phi, Z)}{h},$$

Appendix B. MHD equilibria

that I commutes with the radial partial derivative

$$\begin{aligned} (I(\partial_R f))(R, \phi, Z) &= (\partial_R f)(R, -\phi, -Z) = \lim_{h \rightarrow 0} \frac{f(R+h, -\phi, -Z) - f(R, -\phi, -Z)}{h} \\ &= \lim_{h \rightarrow 0} \frac{(If)(R+h, \phi, Z) - (If)(R, \phi, Z)}{h} = (\partial_R(If))(R, \phi, Z) \end{aligned}$$

but anti-commutes with the toroidal and vertical partial derivative

$$\begin{aligned} (I(\partial_\phi f))(R, \phi, Z) &= (\partial_\phi f)(R, -\phi, -Z) = \lim_{h \rightarrow 0} \frac{f(R, -\phi+h, -Z) - f(R, -\phi, -Z)}{h} \\ &= \lim_{h \rightarrow 0} \frac{(If)(R, \phi-h, Z) - (If)(R, \phi, Z)}{h} = \lim_{h \rightarrow 0} \frac{(If)(R, \phi+h, Z) - (If)(R, \phi, Z)}{-h} \\ &= -(\partial_R(If))(R, \phi, Z) \end{aligned}$$

(and similarly for ∂_Z). The commutation of partial derivatives with the transformation I is summarised as

$$I\partial_R = \partial_R I \qquad I\partial_\phi = -\partial_\phi I \qquad I\partial_Z = -\partial_Z I. \quad (\text{B.3})$$

Then, the gradient operation $\nabla f = \partial_R f \nabla R + \partial_\phi f \nabla \phi + \partial_Z f \nabla Z$ becomes

$$I\nabla f = (\partial_R If)(I\nabla R) - (\partial_\phi If)(I\nabla \phi) - (\partial_Z If)(I\nabla Z)$$

The curl operation $\nabla \times \mathbf{B} = (\partial_\phi B_Z - \partial_Z B_\phi) \nabla \phi \times \nabla Z + (\partial_Z B_R - \partial_R B_Z) \nabla Z \times \nabla R + (\partial_R B_\phi - \partial_\phi B_R) \nabla R \times \nabla \phi$

$$I\nabla \times \mathbf{B} = -(\partial_\phi IB_Z - \partial_Z IB_\phi) RI\mathbf{e}_R + (-\partial_Z IB_R - \partial_R IB_Z) RI\mathbf{e}_\phi + (\partial_R IB_\phi + \partial_\phi IB_R) RI\mathbf{e}_Z$$

In the jargon of parity transformations and their effect on various tensor objects, we define

a “**stellarator symmetric (SS) scalar**” a function f such that respects

$$If = f \iff f(R, -\phi, -Z) = f(R, \phi, Z). \quad (\text{B.4})$$

The covariant components of the gradient $\nabla f = \partial_R f \nabla R + \partial_\phi f \nabla \phi + \partial_Z f \nabla Z$ automatically form what is called a “SS polar-vector”

$$I\partial_R f = \partial_R f \qquad I\partial_\phi f = -\partial_\phi f \qquad I\partial_Z f = -\partial_Z f,$$

a “**SS polar-vector**” a vector field respecting

$$I[V_R, V_\phi, V_Z] = [V_R, -V_\phi, -V_Z]. \quad (\text{B.5})$$

Because the metric elements $g_{ij} = \text{diag}(1, R^2, 1)$ are SS scalars, the contravariant components of a SS polar-vector also satisfy

$$I[V^R, V^\phi, V^Z] = [V^R, -V^\phi, -V^Z].$$

The contraction of two SS polar-vectors \mathbf{V} and \mathbf{W} is a SS scalar

$$I\mathbf{V} \cdot \mathbf{W} = IV_R IW^R + IV_\phi IW^\phi + IV_Z IW^Z = V_R W^R + V_\phi W^\phi + V_Z W^Z = \mathbf{V} \cdot \mathbf{W}.$$

The vector product of two SS polar-vectors \mathbf{V} and \mathbf{W} is also a SS polar-vector

$$I[\mathbf{V} \times \mathbf{W}]_{R,\phi,Z} = [IV_\phi IW_Z - IV_Z IW_\phi, IV_Z IW_R - IV_R IW_Z, IV_R IW_\phi - IV_\phi IW_R] \quad (\text{B.6})$$

$$= [V_\phi W_Z - V_Z W_\phi, -(V_Z W_R - V_R W_Z), -(V_R W_\phi - V_\phi W_R)]. \quad (\text{B.7})$$

The curl of a SS polar-vector $\nabla \times \mathbf{V}$ is also a SS polar-vector (∇ acting like a polar-vector)

$$I[\nabla \times \mathbf{V}]_{R,\phi,Z} = [I\partial_\phi V_Z - I\partial_Z V_\phi, I\partial_Z V_R - I\partial_R V_Z, I\partial_R V_\phi - I\partial_\phi V_R] \quad (\text{B.8})$$

$$= [\partial_\phi V_Z - \partial_Z V_\phi, -\partial_Z V_R + \partial_R V_Z, -\partial_R V_\phi + \partial_\phi V_R], \quad (\text{B.9})$$

a “SS pseudo-scalar” a function g such that

$$Ig = -g \iff g(R, -\phi, -Z) = -g(R, \phi, Z). \quad (\text{B.10})$$

The covariant components of the gradient ∇g forms what is called a “SS axial-vector”

$$I\partial_R g = -\partial_R g \quad I\partial_\phi g = \partial_\phi g \quad I\partial_Z g = \partial_Z g,$$

a “SS axial-vector” a vector field respecting

$$I[J_R, J_\phi, J_Z] = [-J_R, J_\phi, J_Z] = -[J_R, -J_\phi, -J_Z] \quad \text{or} \quad I[J^R, J^\phi, J^Z] = [-J^R, J^\phi, J^Z]. \quad (\text{B.11})$$

The contraction of two SS axial-vectors \mathbf{B} and \mathbf{J} is a SS scalar

$$I\mathbf{J} \cdot \mathbf{B} = IJ_R IB^R + IJ_\phi IB^\phi + IJ_Z IB^Z = J_R B^R + J_\phi B^\phi + J_Z B^Z = \mathbf{J} \cdot \mathbf{B}.$$

The contraction of a SS axial-vector \mathbf{B} and a SS polar-vector \mathbf{E} is a SS pseudo-scalar

$$I\mathbf{E} \cdot \mathbf{B} = IE_R IB^R + IE_\phi IB^\phi + IE_Z IB^Z = -E_R B^R - E_\phi B^\phi - E_Z B^Z = -\mathbf{E} \cdot \mathbf{B}.$$

The vector product of two SS axial-vectors \mathbf{B} and \mathbf{J} is a SS polar-vector

$$I[\mathbf{J} \times \mathbf{B}]_{R,\phi,Z} = [IJ_\phi IB_Z - IJ_Z IB_\phi, IJ_Z IB_R - IJ_R IB_Z, IJ_R IB_\phi - IJ_\phi IB_R] \quad (\text{B.12})$$

$$= [J_\phi B_Z - J_Z B_\phi, -(J_Z B_R - J_R B_Z), -(J_R B_\phi - J_\phi B_R)]. \quad (\text{B.13})$$

The vector product of a SS axial-vector \mathbf{B} and a SS polar-vector \mathbf{E} is a axial-vector

$$I[\mathbf{E} \times \mathbf{B}]_{R,\phi,Z} = [IE_\phi IB_Z - IE_Z IB_\phi, IE_Z IB_R - IE_R IB_Z, IE_R IB_\phi - IE_\phi IB_R] \quad (\text{B.14})$$

$$= [-E_\phi B_Z + E_Z B_\phi, E_Z B_R - E_R B_Z, E_R B_\phi - E_\phi B_R]. \quad (\text{B.15})$$

Appendix B. MHD equilibria

Similarly, the curl of a SS axial-vector is an axial-vector

$$I[\nabla \times \mathbf{B}]_{R,\phi,Z} = [I\partial_\phi B_Z - I\partial_Z B_\phi, I\partial_Z B_R - I\partial_R B_Z, I\partial_R B_\phi - I\partial_\phi B_R] \quad (\text{B.16})$$

$$= [\partial_\phi B_Z - \partial_Z B_\phi, -\partial_Z B_R + \partial_R B_Z, -\partial_R B_\phi + \partial_\phi B_R]. \quad (\text{B.17})$$

C Orbit equations

C.1 Relativistic non-canonical phase-space Lagrangian Guiding-centre Drift Equations

In this section, the guiding-centre equations are derived in general curvilinear (non-canonical) coordinates from the relativistic guiding-centre phase-space Lagrangian (Brizard and Chan, 1999; Grebogi, 1985)

$$L_{GC}(\mathbf{X}, p_{\parallel}; \mu, \zeta; t) = \left(q\mathbf{A} + p_{\parallel} \frac{\mathbf{B}}{B} \right) \cdot \dot{\mathbf{X}} + \frac{m}{q} \mu \dot{\zeta} - H_{GC} \quad (\text{C.1})$$

where \mathbf{X} is the position of the guiding centre, q and m the charge and mass of the considered particle, $p_{\parallel} = m\gamma v_{\parallel}$ its relativistic momentum along the field-line, ζ the ignorable variable characterizing the gyro-angle, $\mu = p_{\perp}^2 / 2mB$ the (adiabatically) conserved magnetic moment associated with the fast gyro-motion, $\mathbf{A}(\mathbf{X}, t)$ and $\mathbf{B}(\mathbf{X}, t) = \nabla \times \mathbf{A}$ the magnetic vector potential and magnetic field. The guiding-centre Hamiltonian is given by

$$H_{GC}(\mathbf{X}, p_{\parallel}; \mu; t) = mc^2 \gamma + q\Phi \quad \gamma = \frac{1}{\sqrt{1 - \frac{v^2}{c^2}}} = \sqrt{1 + \frac{2\mu B}{mc^2} + \frac{p_{\parallel}^2}{m^2 c^2}} \quad (\text{C.2})$$

and $\Phi(\mathbf{X}, t)$ the electrostatic potential.

The form of phase-space Lagrangian (C.1) is interesting; the first part is written as the scalar product of two spatial vectors. It indicates it is possible to preserve the vector notation throughout the computation. It also means that the solution can be expressed without specifying the choice of spatial coordinates.

In the presence of anisotropy, it is customary to express the free current density \mathbf{K} and the *magnetic field intensity* \mathbf{H} , connected one to another by $\nabla \times \mathbf{H} = \mathbf{K}$. The relation between \mathbf{B} and \mathbf{H} is modelled by $\mathbf{H} = \sigma \mathbf{B}$, where $\sigma(\mathbf{X}, B)$ is the permittivity of the medium. This description is adequate to embed the fire-hose stability criterion (Grad, 1966)

$$\sigma(s, B) \equiv 1 - \frac{\mu_0}{B} \frac{\partial P_{\parallel}}{\partial B} \Big|_s = 1 - \frac{\mu_0 (P_{\parallel} - P_{\perp})}{B^2} > 0 \quad (\text{C.3})$$

and the mirror stability criterion

$$\tau(s, B) \equiv \frac{\partial(\sigma B)}{\partial B} \Big|_s = 1 + \frac{\mu_0}{B} \frac{\partial P_{\perp}}{\partial B} \Big|_s > 0 \quad (\text{C.4})$$

where $P_{\parallel}(P_{\perp})$ is the parallel(perpendicular) background pressure (Grad, 1966).

Appendix C. Orbit equations

Instead of the parallel momentum p_{\parallel} , it is convenient to use some sort of parallel *gyro-radius* in order to make the magnetic field intensity appear explicitly. It is proportional to the distance along the field-lines covered by the guiding-centre over a gyro-period (anisotropy included).

$$\rho_{\parallel} = \frac{p_{\parallel}}{qH} = \frac{v_{\parallel}}{\sigma\omega_c} \iff v_{\parallel}(\mathbf{X}, \rho_{\parallel}; \mu; t) = \rho_{\parallel} \frac{qH}{m\gamma} \quad (\text{C.5})$$

Adjusting the guiding-centre Lagrangian to the new coordinates and normalizing by q yields

$$l(\mathbf{X}, \rho_{\parallel}, t) = (\mathbf{A} + \rho_{\parallel} \mathbf{H}) \cdot \dot{\mathbf{X}} - h = \mathbf{A}^* \cdot \dot{\mathbf{X}} - h \quad (\text{C.6})$$

with

$$h = \frac{m}{q} c^2 \gamma + \Phi, \quad \gamma = \sqrt{1 + \frac{2\mu B}{mc^2} + \frac{q^2 \rho_{\parallel}^2 H^2}{m^2 c^2}}. \quad (\text{C.7})$$

Equations (C.1-C.7) are a coordinate-free generalisation of the treatment of Cary and Brizard (2009), with the additional dependency of anisotropy and relativistic effects.

Since ρ_{\parallel} (formally p_{\parallel}) does not have a $\dot{\rho}_{\parallel}$ term in the Lagrangian, its redefinition does not affect the structure of the equations of motion¹. Many authors (Cooper et al., 2007; Hirvijoki et al., 2012; White and Chance, 1984; White et al., 1982) have made use of this property in order to include $\delta A_{\parallel}(\mathbf{X}, t)$ perturbations, defining for example $\rho_c = \rho_{\parallel} + \delta A_{\parallel}/H$. This trick is only valid if the perturbations are much smaller than the original axisymmetric magnetic field (for the static application of interest here). Indeed, the main assumption of guiding-centre physics is that particles gyrate rapidly around the field-lines traced out by the total magnetic field. If the perturbations are large, the direction of the total field can become very different from the original equilibrium and the guiding-centre derivation is inconsistent from the start (perturbations are stored only in the vector potential but not in the direction of reference for velocity space). In this derivation, \mathbf{A} is recognized as the full 3D vector potential, implicitly including equilibrium and perturbations, if any. \mathbf{A} (and thus \mathbf{B}) is assumed to vary smoothly in space and slowly in time, according to the guiding-centre approximation. Adding faster and finer perturbations is only possible if the guiding-centre Lagrangian is expanded at higher-order in Larmor radius (5D, gyrokinetics) or if the full Lorentz equations (6D) are considered. The formalism presented here is compatible with time-varying electromagnetic fields in general, but is applied to saturated equilibria such as the internal kink in section 5.1.1 and RMPs in section 6.3, where \mathbf{A} describes the vector potential of a 3D magnetic equilibrium configuration from VMEC or other equilibrium codes.

The Euler-Lagrange equations of (C.6) based on coordinates $z^{\alpha} = (z^0, z^i) = (\rho_{\parallel}, \mathbf{X})$ can be arranged as

$$\Omega_{\alpha\beta} \dot{z}^{\beta} = \partial_{\alpha} h + \partial_t A_{\alpha}^* \quad (\text{C.8})$$

¹If there was a $\Lambda \dot{\rho}_{\parallel}$ term in the Lagrangian, the change of coordinate defined by $\rho_{\parallel} = f(\rho_{new}, \mathbf{X}, t)$ would imply $\dot{\rho}_{\parallel} = \rho_{new} \partial_{\rho_{new}} f + \dot{\mathbf{X}} \nabla f + \partial_t f$. These extra terms would be distributed to the spatial variables affecting their equations of motion.

C.1. Relativistic non-canonical phase-space Lagrangian Guiding-centre Drift Equations

where the anti-symmetric tensor $\Omega_{\alpha\beta} = \partial_\alpha A_\beta^* - \partial_\beta A_\alpha^*$ is the Lagrange brackets of non-canonical coordinates

$$\Omega_{\alpha\beta} = \begin{array}{cc} & \begin{array}{c} 1 \times 1 \\ 1 \times 3 \\ 3 \times 3 \end{array} \\ \begin{array}{c} 3 \\ \times \\ 1 \end{array} & \begin{pmatrix} 0 & \partial_{\rho_{\parallel}} A_j^* \\ -\partial_{\rho_{\parallel}} A_i^* & \partial_i A_j^* - \partial_j A_i^* \end{pmatrix} = \begin{pmatrix} 0 & H_j \\ -H_i & B^{*k} \varepsilon_{kij} \end{pmatrix} \end{array} \quad (\text{C.9})$$

where $\varepsilon_{ijk} = \sqrt{g} \varepsilon_{ijk}$ is the Levi-Civita tensor, $\sqrt{g} = [\nabla z^1 \cdot (\nabla z^2 \times \nabla z^3)]^{-1}$ is the Jacobian of the spatial coordinate system and $\mathbf{B}^* = \nabla \times \mathbf{A}^* = \mathbf{B} + \rho_{\parallel} \mathbf{K}$ the modified magnetic field.

$\sqrt{\Omega}$ is the Jacobian of the transformation from canonical to non-canonical coordinates, a measure of *phase-space density* in the sense that $m q \sqrt{\Omega} dz^3 d\rho_{\parallel} d\mu d\zeta = dq^3 dp^3$ is an infinitesimal volume of phase-space. The evolution of phase-space under the Hamiltonian flow, and that of $\sqrt{\Omega}$, is well-defined by Liouville equation,

$$\frac{\partial \sqrt{\Omega}}{\partial t} + \frac{\partial}{\partial z^\alpha} (\sqrt{\Omega} \dot{z}^\alpha) = 0 \quad (\text{C.10})$$

which is important for establishing a Vlasov equation and essential for the numerical implementation of a consistent weighting scheme in a full- f or delta- f PIC approach.

To express $\sqrt{\Omega}$ without effort, the following reasoning is applied. The determinant of any anti-symmetric matrix is equal the square of its Pfaffian², $\det \Omega = \text{pf}(\Omega)^2$. Written as a p-form, $\Omega = \frac{1}{2} \Omega_{\alpha\beta} dz^\alpha \wedge dz^\beta$ and its Pfaffian is related by $\frac{\Omega^2}{2} = \text{pf}(\Omega) dz^0 \wedge dz^1 \wedge dz^2 \wedge dz^3$. Thus,

$$\text{pf}(\Omega) = \sqrt{\Omega} = \frac{1}{2} (\partial_\alpha A_\beta^*) (\partial_\gamma A_\delta^*) \varepsilon^{\alpha\beta\gamma\delta} = (\partial_0 A_i^*) (\partial_j A_k^*) \varepsilon^{ijk} = H_i [\nabla \times \mathbf{A}^*]^i \sqrt{g} = \mathbf{H} \cdot \mathbf{B}^* \sqrt{g} = \sigma B B_{\parallel}^* \sqrt{g}. \quad (\text{C.11})$$

Phase-space density (i.e. $\sqrt{\Omega}$) can become zero in two ways: the spatial coordinate system is singular at some point (polar coordinates) or $\rho_{\parallel} K_{\parallel}$ starts competing with B . In the first case, a change of coordinates will remove the singularity (pseudo-Cartesian coordinates) but in the second, it means that Larmor radius corrections are of the same order as the magnetic field strength and that the guiding-centre approximation breaks down.

Finding the inverse of Ω , namely Π the *Poisson brackets* (Arnol'd, 1989) such that $\Pi^{\alpha\beta} \Omega_{\beta\gamma} = \delta_\gamma^\alpha$, permits the equations of motion to be written as³

$$\dot{z}^\alpha = \Pi^{\alpha\beta} (\partial_\beta h + \partial_t A_\beta^*). \quad (\text{C.12})$$

²The Pfaffian is a polynomial of the entries of anti-symmetric $2n \times 2n$ matrices. The determinant of any anti-symmetric matrix A is equal to the square of its Pfaffian, $\det A = \text{pf}(A)^2$ (Muir, 1882). In the context of differential forms, one can associate to A a bi-vector $\omega = \frac{1}{2} A_{ij} e^i \wedge e^j$, where (e^1, \dots, e^{2n}) is a basis of \mathbb{R}^{2n} . The Pfaffian is then defined as $\frac{\omega^n}{n!} = \text{pf}(A) e^1 \wedge \dots \wedge e^{2n}$.

³In the end, it is equivalent to the expression $\dot{z}^\alpha = [z^\alpha, H] + \partial_t z^\alpha$, i.e. the evolution of the non-canonical variables in the Hamilton picture.

Appendix C. Orbit equations

Inverting the Lagrange matrix is possible only if its determinant Ω is non-zero. Π is verified to be

$$\Pi^{\alpha\beta} = \frac{1}{\mathbf{H} \cdot \mathbf{B}^*} \begin{pmatrix} 0 & -B^{*j} \\ B^{*i} & -H_k \epsilon^{kij} \end{pmatrix} \quad (\text{C.13})$$

where $\epsilon^{ijk} = \epsilon^{ijk} / \sqrt{g}$ the contravariant components of the Levi-Civita tensor. Thanks to Π , the equations of motion in general coordinates become

$$\dot{z}^\alpha = \begin{pmatrix} \dot{\rho}_{\parallel} \\ \dot{X}^i \end{pmatrix} = \Pi \begin{pmatrix} \partial_{\rho_{\parallel}} h \\ \partial_j h + \partial_t A_j^* \end{pmatrix} \quad (\text{C.14})$$

where

$$\partial_{\rho_{\parallel}} h = \frac{\rho_{\parallel} q}{m\gamma} H^2 = v_{\parallel} H \quad \text{and} \quad \partial_i h + \partial_t A_i^* = \frac{\mu}{q\gamma} \partial_i B + v_{\parallel} \rho_{\parallel} \partial_i (\sigma B) - E_i + \rho_{\parallel} \partial_t B_i \equiv -E_i^* \quad (\text{C.15})$$

the modified electric field. Finally, the guiding-centre drift equations in general coordinates are written

$$\dot{\rho}_{\parallel} = \frac{E_j^* B^{*j}}{H_l B^{*l}} = \frac{E_j^* W^{*j}}{H_l W^{*l}} = \frac{\mathbf{E}^* \cdot \mathbf{B}^*}{H B_{\parallel}^*} \quad (\text{C.16})$$

$$\dot{X}^i = v_{\parallel} \frac{H B^{*i}}{H_l B^{*l}} + \frac{\epsilon^{ijk}}{\sqrt{g}} \frac{H_k E_j^*}{H_l B^{*l}} = v_{\parallel} \frac{H W^{*i}}{H_l W^{*l}} + \epsilon^{ijk} \frac{H_k E_j^*}{H_l W^{*l}} = \left[v_{\parallel} \frac{\mathbf{B}^*}{B_{\parallel}^*} + \frac{\mathbf{E}^* \times \mathbf{b}}{B_{\parallel}^*} \right]^i \quad (\text{C.17})$$

where $W^i(X^i, t) = B^i \sqrt{g}$ is a notation for the components of the magnetic field in the so-called *wedge-representation*, where $\mathbf{B} = W^i \frac{\epsilon_{ijk}}{2} \nabla X^j \times \nabla X^k$. These equations for (ρ_{\parallel}, X^i) are consistent with (Littlejohn, 1983) and a generalisation of previous work (Cooper et al., 2011a). The main features of drift theory are easily recognisable. At lowest order, the motion is along the field-lines, as seen in the $v_{\parallel} \mathbf{B}/B$ term. The electric field induces a $\mathbf{E} \times \mathbf{B}$ drift, the gradients of B induce a $\mathbf{B} \times \nabla B$ drift and the time-variation a $\mathbf{B} \times \partial_t \mathbf{B}$ drift. The so-called curvature drift appears in the $\nabla \times \mathbf{B}$ term.

The contravariant (upper index as in B^i) and covariant (lower index as in H_i) components of each field, as well as the coordinate transformation and the metric elements, are provided separately from the equations of motions. The coordinate system is in effect determined a posteriori. This makes the representation of the electromagnetic field interchangeable and not limited to toroidal geometry. The list of quantities required by the above guiding-centre equations is W^i , H_i , E_i , $\partial_i B$, $\partial_t H_i$ and $K^i = \sqrt{g} [\nabla \times \mathbf{B}]^i$. A selection of field representations in flux coordinates was shown in the section B.1.

C.1.1 Guiding-centre Drift Equations in straight field-line coordinates

The GCDE derived in work by White and Zakharov (2003); White and Chance (1984) and previous work by Cooper et al. (2011a) using canonical coordinates are recovered in this sec-

C.1. Relativistic non-canonical phase-space Lagrangian Guiding-centre Drift Equations

tion, considering the time-independent anisotropic MHD equilibrium expressed in Boozer coordinates. This is an algebraic exercise that shows how the phase-space Lagrangian technique applies to a specific choice of coordinates. The same notation and assumptions as in section 2.3.3 are used. We only let the covariant representation of the magnetic field contain the anisotropy

$$\mathbf{H} = \sigma \mathbf{B} = H_s(s, \theta, \varphi) \nabla s + \mathcal{J}(s) \nabla \theta - \mathcal{I}(s) \nabla \varphi \quad (\text{C.18})$$

where \mathbf{H} is the magnetic intensity, $s = \Phi/\Phi_b$ the radial flux label proportional to the toroidal flux, θ and φ are the poloidal and toroidal angles, $\mathcal{J} = \mu_0 J$ and $\mathcal{I} = \mu_0 I$ are respectively toroidal and poloidal current fluxes, and the permittivity $\sigma(s, B)$ satisfies the fire-hose stability criterion and the mirror stability criterion (Grad, 1966). The magnetic field is written in contravariant components in terms of flux functions $\Psi(s)$ and $\Phi(s)$ as in equation (2.13).

$$\mathbf{B} = \nabla \varphi \times \nabla \Psi + \nabla \Phi \times \nabla \theta = \frac{1}{\sqrt{g}} \left(\Psi' \mathbf{e}^\theta + \Phi' \mathbf{e}^\varphi \right) \quad (\text{C.19})$$

The scalar product between the magnetic field and the magnetic intensity (contraction of covariant and contravariant representations) has a simple dependency

$$\mathbf{H} \cdot \mathbf{B} = \frac{\mathcal{J} \Psi' - \mathcal{I} \Phi'}{\sqrt{g}} = \sigma B^2 > 0. \quad (\text{C.20})$$

The current is computed as

$$\nabla \wedge \mathbf{H} = \mathcal{J}' \nabla s \wedge \nabla \theta + \mathcal{I}' \nabla \varphi \wedge \nabla s + \nabla H_s \wedge \nabla s = \frac{1}{\sqrt{g}} \left[(\mathcal{J}' + \partial_\varphi H_s) \mathbf{e}^\theta + (\mathcal{I}' - \partial_\theta H_s) \mathbf{e}^\varphi \right] \quad (\text{C.21})$$

such that

$$\mathbf{B}^* = \mathbf{B} + \rho_{\parallel} \nabla \wedge \mathbf{H} = \frac{1}{\sqrt{g}} \left[(\Psi' + \rho_{\parallel} \mathcal{J}' + \rho_{\parallel} \partial_\varphi H_s) \mathbf{e}^\theta + (\Phi' + \rho_{\parallel} \mathcal{I}' - \rho_{\parallel} \partial_\theta H_s) \mathbf{e}^\varphi \right] \quad (\text{C.22})$$

and

$$\sqrt{\Omega} = \sqrt{g} \mathbf{H} \cdot \mathbf{B}^* = \mathcal{J} \Psi' - \mathcal{I} \Phi' + (\rho_{\parallel} \mathcal{J} \mathcal{J}' - \mathcal{I} \mathcal{I}' + \mathcal{J} \partial_\varphi H_s + \mathcal{I} \partial_\theta H_s) \quad (\text{C.23})$$

The modified electric field is

$$-\mathbf{E}^* = \frac{\mu}{q\gamma} \nabla B + v_{\parallel} \rho_{\parallel} \nabla(\sigma B) = \underbrace{\left(\frac{\mu}{q\gamma} + v_{\parallel} \rho_{\parallel} \tau \right)}_{C_B} \nabla B + v_{\parallel} \rho_{\parallel} B \left. \frac{\partial \sigma}{\partial s} \right|_B \nabla s \quad (\text{C.24})$$

Appendix C. Orbit equations

Collecting all pieces, the Boozer coordinate equations of motion of a particle in anisotropic MHD plasma at equilibrium are

$$\dot{\rho}_{\parallel} = -\frac{C_B}{\sqrt{\Omega}} \left[\partial_{\theta} B (\Psi' + \rho_{\parallel} \mathcal{J}' + \rho_{\parallel} \partial_{\varphi} H_s) + \partial_{\varphi} B (\Phi' + \rho_{\parallel} \mathcal{J}' - \rho_{\parallel} \partial_{\theta} H_s) \right] \quad (\text{C.25a})$$

$$\dot{s} = \nabla s \cdot \dot{\mathbf{X}} = \frac{C_B}{\sqrt{\Omega}} (\mathcal{J} \partial_{\varphi} B + \mathcal{J} \partial_{\theta} B) \quad (\text{C.25b})$$

$$\dot{\theta} = \nabla \theta \cdot \dot{\mathbf{X}} = \frac{1}{\sqrt{\Omega}} \left[v_{\parallel} \sigma B \left(\Psi' + \rho_{\parallel} \mathcal{J}' + \rho_{\parallel} \partial_{\varphi} H_s - \rho_{\parallel} \mathcal{J} \left. \frac{\partial \ln \sigma}{\partial s} \right|_B \right) - C_B (\mathcal{J} \partial_s B + H_s \partial_{\varphi} B) \right] \quad (\text{C.25c})$$

$$\dot{\varphi} = \nabla \varphi \cdot \dot{\mathbf{X}} = \frac{1}{\sqrt{\Omega}} \left[v_{\parallel} \sigma B \left(\Phi' + \rho_{\parallel} \mathcal{J}' - \rho_{\parallel} \partial_{\theta} H_s - \rho_{\parallel} \mathcal{J} \left. \frac{\partial \ln \sigma}{\partial s} \right|_B \right) - C_B (\mathcal{J} \partial_s B - H_s \partial_{\theta} B) \right] \quad (\text{C.25d})$$

Bibliography

- S. Abdullaev. *Magnetic Stochasticity in Magnetically Confined Fusion Plasmas: Chaos of Field Lines and Charged Particle Dynamics*. Springer Series on Atomic, Optical, and Plasma Physics. Springer, 2013. ISBN 9783319018904.
- N. Aiba, S. Tokuda, M. Furukawa, P. Snyder, and M. Chu. Minerva: Ideal MHD stability code for toroidally rotating tokamak plasmas. *Computer Physics Communications*, 180(8):1282 – 1304, 2009.
- N. Aiba, J. Shiraishi, and M. Hirota. Impact of plasma rotation on the linear physics of resistive wall modes in tokamaks. *Plasma Physics and Controlled Fusion*, 55(7):074002, 2013.
- M. Albergante. *Interaction Between Fast Ions and Microturbulence in Thermonuclear Devices*. PhD thesis, EPFL, Lausanne, 2011.
- M. Albergante, A. Fasoli, J. Graves, S. Brunner, and W. Cooper. Assessment of turbulent beam ion redistribution in tokamaks through velocity space-dependent gyrokinetic analyses. *Nuclear Fusion*, 52(9):094016, 2012.
- D. Anderson, W. Cooper, R. Gruber, S. Merazzi, and U. Schwenn. Methods for the efficient calculation of the MHD stability properties of magnetically confined fusion plasmas. *International Journal of High Performance Computing Applications*, 4(3):34–47, 1990.
- V. Arnol'd. *Mathematical Methods of Classical Mechanics*. Graduate Texts in Mathematics. Springer, 1989. ISBN 9780387968902.
- O. Asunta, S. Äkäslompolo, T. Kurki-Suonio, T. Koskela, S. Sipilä, A. Snicker, M. García-Muñoz, and t. A. U. Team. Simulations of fast ion wall loads in ASDEX upgrade in the presence of magnetic perturbations due to ELM-mitigation coils. *Nuclear Fusion*, 52(9):094014, 2012.
- A. Y. Aydemir. A unified Monte Carlo interpretation of particle simulations and applications to non-neutral plasmas. *Physics of Plasmas (1994-present)*, 1(4):822–831, 1994.
- A. Baños. The guiding centre approximation in lowest order. *Journal of Plasma Physics*, 1: 305–316, 8 1967.
- E. V. Belova, N. N. Gorelenkov, and C. Z. Cheng. Self-consistent equilibrium model of low aspect-ratio toroidal plasma with energetic beam ions. *Physics of Plasmas (1994-present)*, 10(8):3240–3251, 2003.
- T. M. Bird and C. C. Hegna. A model for microinstability destabilization and enhanced transport in the presence of shielded 3D magnetic perturbations. *Nuclear Fusion*, 53(1): 013004, 2013.

Bibliography

- A. H. Boozer. Guiding center drift equations. *Physics of Fluids*, 23(5):904–908, 1980.
- A. H. Boozer. Plasma equilibrium with rational magnetic surfaces. *Physics of Fluids (1958-1988)*, 24(11):1999–2003, 1981.
- A. H. Boozer. Establishment of magnetic coordinates for a given magnetic field. *Physics of Fluids*, 25(3):520–521, 1982.
- A. H. Boozer and G. Kuo-Petravic. Monte Carlo evaluation of transport coefficients. *Physics of Fluids (1958-1988)*, 24(5):851–859, 1981.
- H.-S. Bosch and G. Hale. Improved formulas for fusion cross-sections and thermal reactivities. *Nuclear Fusion*, 32(4):611, 1992.
- A. J. Brizard. Nonlinear gyrokinetic Vlasov equation for toroidally rotating axisymmetric tokamaks. *Physics of Plasmas (1994-present)*, 2(2):459–471, 1995.
- A. J. Brizard. Variational principle for nonlinear gyrokinetic Vlasov–Maxwell equations. *Physics of Plasmas (1994-present)*, 7(12):4816–4822, 2000.
- A. J. Brizard and A. A. Chan. Nonlinear relativistic gyrokinetic Vlasov–Maxwell equations. *Physics of Plasmas (1994-present)*, 6(12):4548–4558, 1999.
- A. J. Brizard and T. S. Hahm. Foundations of nonlinear gyrokinetic theory. *Rev. Mod. Phys.*, 79:421–468, Apr 2007.
- D. Brunetti, J. Graves, W. Cooper, and D. Terranova. Ideal saturated MHD helical structures in axisymmetric hybrid plasmas. *Nuclear Fusion*, 54(6):064017, 2014.
- D. Brunetti, J. Graves, W. Cooper, and D. Terranova. Fast growing resistive two fluid instabilities in hybrid-like tokamak configuration. *Plasma Physics and Controlled Fusion*, accepted, 2015.
- J. W. Burby, J. Squire, and H. Qin. Automation of the guiding center expansion. *Physics of Plasmas (1994-present)*, 20(7):072105, 2013.
- B. Cambon, X. Leoncini, M. Vittot, R. Dumont, and X. Garbet. Chaotic motion of charged particles in toroidal magnetic configurations. *Chaos: An Interdisciplinary Journal of Nonlinear Science*, 24(3):033101, 2014.
- J. M. Canik, R. Maingi, T. E. Evans, R. E. Bell, S. P. Gerhardt, B. P. LeBlanc, J. Manickam, J. E. Menard, T. H. Osborne, J.-K. Park, S. F. Paul, P. B. Snyder, S. A. Sabbagh, H. W. Kugel, and E. A. Unterberg. On demand triggering of edge localized instabilities using external nonaxisymmetric magnetic perturbations in toroidal plasmas. *Phys. Rev. Lett.*, 104:045001, Jan 2010.
- J. M. Canik, S. P. Hirshman, R. Sanchez, R. Maingi, J.-W. Ahn, R. E. Bell, A. Diallo, S. P. Gerhardt, B. P. LeBlanc, J. E. Menard, J.-K. Park, M. Podesta, and S. A. Sabbagh. First use of three-dimensional equilibrium, stability and transport calculations for interpretation of ELM triggering with magnetic perturbations in NSTX. *Nuclear Fusion*, 52(5):054004, 2012.

- B. W. Carroll, D. A. Ostlie, and M. Friedlander. *An introduction to modern astrophysics*, volume 523. Addison-Wesley New York, 1996.
- J. R. Cary and A. J. Brizard. Hamiltonian theory of guiding-center motion. *Rev. Mod. Phys.*, 81: 693–738, May 2009.
- J. R. Cary and R. G. Littlejohn. Noncanonical hamiltonian mechanics and its application to magnetic field line flow. *Annals of Physics*, 151(1):1 – 34, 1983.
- J. R. Cary, C. L. Hedrick, and J. S. Tolliver. Orbits in asymmetric toroidal magnetic fields. *Physics of Fluids*, 31(6):1586–1600, 1988.
- M. Cecconello, M. Turnyanskiy, S. Conroy, G. Ericsson, E. Ronchi, S. Sangaroon, R. Akers, I. Fitzgerald, A. Cullen, and M. Weiszlog. A neutron camera system for MASTa). *Review of Scientific Instruments*, 81(10):10D315, 2010.
- M. Cecconello, S. Sangaroon, M. Turnyanskiy, S. Conroy, I. Wodniak, R. J. Akers, G. Ericsson, and the MAST Team. Observation of fast ion behaviour with a neutron emission profile monitor in MAST. *Nuclear Fusion*, 52(9):094015, 2012.
- I. Chapman, W. Cooper, J. Graves, M. Gryaznevich, R. Hastie, T. Hender, D. Howell, M.-D. Hua, G. Huysmans, D. Keeling, Y. Liu, H. Meyer, C. Michael, S. Pinches, S. Saarelma, S. Sabbagh, and the MAST Team. Macroscopic stability of high beta MAST plasmas. *Nuclear Fusion*, 51(7):073040, 2011.
- I. T. Chapman, M. D. Hua, S. D. Pinches, R. J. Akers, A. R. Field, J. P. Graves, R. J. Hastie, C. A. Michael, and the MAST Team. Saturated ideal modes in advanced tokamak regimes in MAST. *Nuclear Fusion*, 50(4):045007, 2010.
- I. T. Chapman, A. Kirk, C. J. Ham, J. R. Harrison, Y. Q. Liu, S. Saarelma, R. Scannell, A. J. Thornton, M. Becoulet, F. Orain, W. A. Cooper, S. Pamela, and M. Team. Towards understanding edge localised mode mitigation by resonant magnetic perturbations in MAST. *Physics of Plasmas*, 20(5):056101, 2013.
- B. V. Chirikov. A universal instability of many-dimensional oscillator systems. *Physics Reports*, 52(5):263 – 379, 1979.
- M. S. Chu, L. L. Lao, M. J. Schaffer, T. E. Evans, E. J. Strait, Y. Q. Liu, M. J. Lanctot, H. Reimerdes, Y. Liu, T. A. Casper, and Y. Gribov. Response of a resistive and rotating tokamak to external magnetic perturbations below the Alfvén frequency. *Nuclear Fusion*, 51(7):073036, 2011.
- J. Connor and J. Cordey. Effects of neutral injection heating upon toroidal equilibria. *Nuclear Fusion*, 14(2):185, 1974.
- G. A. Cooper et al. Exact canonical drift Hamiltonian formalism with pressure anisotropy and finite perturbed fields. *Physics of Plasmas*, 14(10):102506, 2007.
- W. A. Cooper, S. E. i Margalet, S. J. Allfrey, J. Kißlinger, H. F. G. Wobig, Y. Narushima, S. Okamura, C. Suzuki, K. Y. Watanabe, K. Yamazaki, and M. Y. Isaev. Magnetohydrodynamic stability of free-boundary quasi-axisymmetric stellarator equilibria with finite bootstrap current. *Fusion Science and Technology*, 46(2):365 – 377, 2004.

Bibliography

- W. A. Cooper, S. P. Hirshman, P. Merkel, J. P. Graves, J. Kisslinger, H. F. G. Wobig, Y. Narushima, S. Okamura, and K. Y. Watanabe. Three-dimensional anisotropic pressure free boundary equilibria. *Computer Physics Communications*, 180(9):1524–1533, 2009.
- W. A. Cooper, J. P. Graves, A. Pochelon, O. Sauter, and L. Villard. Tokamak Magnetohydrodynamic Equilibrium States with Axisymmetric Boundary and a 3D Helical Core. *Physical Review Letters*, 105(035003):035003, 2010.
- W. A. Cooper, J. P. Graves, S. Brunner, and M. Y. Isaev. Full-Field Drift Hamiltonian Particle Orbit in 3D Geometry. *Plasma Physics and Controlled Fusion*, 53:024001, 2011a.
- W. A. Cooper, J. P. Graves, O. Sauter, I. T. Chapman, M. Gobbin, L. Marrelli, P. Martin, I. Predebon, and D. Terranova. Magnetohydrodynamic properties of nominally axisymmetric systems with 3d helical core. *Plasma Physics and Controlled Fusion*, 53(7):074008, 2011b.
- W. A. Cooper, J. P. Graves, O. Sauter, I. T. Chapman, M. Gobbin, L. Marrelli, P. Martin, I. Predebon, and D. Terranova. Magnetohydrodynamic properties of nominally axisymmetric systems with 3d helical core. *Plasma Physics and Controlled Fusion*, 53(7):074008, 2011c.
- M. de Rover, N. J. Lopes Cardozo, and A. Montvai. Hamiltonian description of the topology of drift orbits of relativistic particles in a tokamak. *Physics of Plasmas (1994-present)*, 3(12):4468–4477, 1996.
- S. Dettrick, S. Lloyd, H. Gardner, R. Dewar, and S. Painter. Particle orbits and drift surfaces in a heliac. *Nuclear Fusion*, 38(7):1001, 1998.
- R. Dewar and S. Hudson. Stellarator symmetry. *Physica D: Nonlinear Phenomena*, 112(1–2):275 – 280, 1998.
- R. L. Dewar, M. J. Hole, M. McGann, R. Mills, and S. R. Hudson. Relaxed plasma equilibria and entropy-related plasma self-organization principles. *Entropy*, 10(4):621–634, 2008.
- W. D’Haeseleer. *Flux coordinates and magnetic field structure: a guide to a fundamental tool of plasma structure*. Springer series in computational physics. Springer-Verlag, 1991.
- A. J. Dragt and J. M. Finn. Insolubility of trapped particle motion in a magnetic dipole field. *Journal of Geophysical Research*, 81(13):2327–2340, 1976.
- T. E. Evans, R. A. Moyer, P. R. Thomas, J. G. Watkins, T. H. Osborne, J. A. Boedo, E. J. Doyle, M. E. Fenstermacher, K. H. Finken, R. J. Groebner, M. Groth, J. H. Harris, R. J. La Haye, C. J. Lasnier, S. Masuzaki, N. Ohyaabu, D. G. Pretty, T. L. Rhodes, H. Reimerdes, D. L. Rudakov, M. J. Schaffer, G. Wang, and L. Zeng. Suppression of large edge-localized modes in high-confinement DIII-D plasmas with a stochastic magnetic boundary. *Phys. Rev. Lett.*, 92:235003, Jun 2004.
- T. E. Evans, R. A. Moyer, K. H. Burrell, M. E. Fenstermacher, I. Joseph, A. W. Leonard, T. H. Osborne, G. D. Porter, M. J. Schaffer, P. B. Snyder, P. R. Thomas, J. G. Watkins, and W. P. West. Edge stability and transport control with resonant magnetic perturbations in collisionless tokamak plasmas. *Nature Physics*, 2(6):419–423, 2006.

- N. M. Ferraro. Calculations of two-fluid linear response to non-axisymmetric fields in tokamak(s). *Physics of Plasmas (1994-present)*, 19(5):056105, 2012.
- O. Fischer et al. Neoclassical transport and alpha particle confinement in novel 3-D reactor systems. *Nuclear Fusion*, 42(7):817, 2002.
- E. Frieman and M. Rotenberg. On hydromagnetic stability of stationary equilibria. *Rev. Mod. Phys.*, 32:898–902, 1960.
- M. Garcia-Munoz, S. Äkäslompolo, O. Asunta, J. Boom, X. Chen, I. Classen, R. Dux, T. Evans, S. Fietz, R. Fisher, C. Fuchs, B. Geiger, M. Hoelzl, V. Igoshine, Y. Jeon, J. Kim, J. Kim, B. Kurzan, N. Lazanyi, T. Lunt, R. McDermott, M. Nocente, D. Pace, T. Rhodes, M. Rodriguez-Ramos, K. Shinohara, W. Suttrop, M. V. Zeeland, E. Viezzer, M. Willensdorfer, E. Wolfrum, the ASDEX Upgrade, DIII-D, and K. Teams. Fast-ion redistribution and loss due to edge perturbations in the ASDEX upgrade, DIII-D and KSTAR tokamaks. *Nuclear Fusion*, 53(12):123008, 2013a.
- M. Garcia-Munoz, S. Äkäslompolo, P. de Marne, M. G. Dunne, R. Dux, T. E. Evans, N. M. Ferraro, S. Fietz, C. Fuchs, B. Geiger, A. Herrmann, M. Hoelzl, B. Kurzan, N. Lazanyi, R. M. McDermott, M. Nocente, D. C. Pace, M. Rodriguez-Ramos, K. Shinohara, E. Strumberger, W. Suttrop, M. A. V. Zeeland, E. Viezzer, M. Willensdorfer, and E. Wolfrum. Fast-ion losses induced by ELMs and externally applied magnetic perturbations in the ASDEX upgrade tokamak. *Plasma Physics and Controlled Fusion*, 55(12):124014, 2013b.
- H. Goldstein, C. P. Poole, and J. L. Safko. *Classical Mechanics (3rd Edition)*. Addison-Wesley, 3 edition, June 2001. ISBN 0201657023.
- R. J. Goldston, R. B. White, and A. H. Boozer. Confinement of high-energy trapped particles in tokamaks. *Phys. Rev. Lett.*, 47:647–649, Aug 1981.
- H. Grad. Velocity gradient instability. *Physics of Fluids (1958-1988)*, 9(3):498–513, 1966.
- H. Grad. Toroidal containment of a plasma. *Physics of Fluids (1958-1988)*, 10(1):137–154, 1967.
- J. P. Graves, D. Brunetti, I. T. Chapman, W. A. Cooper, H. Reimerdes, F. Halpern, A. Pochelon, O. Sauter, the TCV team, and the MAST team. Magnetohydrodynamic helical structures in nominally axisymmetric low-shear tokamak plasmas. *Plasma Physics and Controlled Fusion*, 55(1):014005, 2013.
- C. Grebogi. Relativistic ponderomotive hamiltonian of two interacting electromagnetic waves. *Phys. Rev. A*, 31:914–920, Feb 1985.
- Ø. Grøn and S. Hervik. *Einstein's General Theory of Relativity: With Modern Applications in Cosmology*. Springer, 2007. ISBN 9780387691992.
- J. Hammersley and D. Handscomb. *Monte Carlo Methods*. Monographs on Statistics and Applied Probability. Springer Netherlands, 1964. ISBN 9789400958210.
- K. Harafuji, T. Hayashi, and T. Sato. Computational study of three-dimensional magnetohydrodynamic equilibria in toroidal helical systems. *Journal of Computational Physics*, 81(1):169 – 192, 1989.

Bibliography

- S. R. Haskey, M. J. Lanctot, Y. Q. Liu, J. M. Hanson, B. D. Blackwell, and R. Nazikian. Linear ideal MHD predictions for $n=2$ non-axisymmetric magnetic perturbations on DIII-D. *Plasma Physics and Controlled Fusion*, 56(3):035005, 2014.
- P. Helander, C. G. Gimblett, R. J. Hastie, and K. G. McClements. The influence of fast ions on the magnetohydrodynamic stability of negative shear profiles. *Physics of Plasmas (1994-present)*, 4(6):2181–2187, 1997.
- M. Heyn, I. Ivanov, S. Kasilov, W. Kernbichler, A. Loarte, V. Nemov, and A. Runov. On the confinement of passing alpha particles in a tokamak-reactor with resonant magnetic field perturbations shielded by plasma currents. *Nuclear Fusion*, 52(5):054010, 2012.
- S. Hirshman, W. van RIJ, and P. Merkel. Three-dimensional free boundary calculations using a spectral Green's function method. *Computer Physics Communications*, 43(1):143 – 155, 1986a.
- S. P. Hirshman and J. C. Whitson. Steepest-descent moment method for three-dimensional magnetohydrodynamic equilibria. *Physics of Fluids*, 26(12):3553–3568, 1983.
- S. P. Hirshman, K. C. Shaing, W. I. van Rij, C. O. Beasley, and E. C. Crume. Plasma transport coefficients for nonsymmetric toroidal confinement systems. *Physics of Fluids (1958-1988)*, 29(9):2951–2959, 1986b.
- S. P. Hirshman, R. Sanchez, and C. R. Cook. SIESTA: A scalable iterative equilibrium solver for toroidal applications. *Physics of Plasmas (1994-present)*, 18(6):062504, 2011.
- E. Hirvijoki, A. Snicker, T. Korpilo, P. Lauber, E. Poli, M. Schneller, and T. Kurki-Suonio. Alfvén eigenmodes and neoclassical tearing modes for orbit-following implementations. *Computer Physics Communications*, 183(12):2589 – 2593, 2012.
- E. Hirvijoki, A. Brizard, A. Snicker, and T. Kurki-Suonio. Monte Carlo implementation of a guiding-center Fokker-Planck kinetic equation. *Physics of Plasmas (1994-present)*, 20(9):092505, 2013.
- M.-D. Hua, I. T. Chapman, S. D. Pinches, R. J. Hastie, and the MAST team. Saturated internal instabilities in advanced-tokamak plasmas. *EPL (Europhysics Letters)*, 90(5):55001, 2010.
- S. R. Hudson, R. L. Dewar, M. J. Hole, and M. McGann. Non-axisymmetric, multi-region relaxed magnetohydrodynamic equilibrium solutions. *Plasma Physics and Controlled Fusion*, 54(1):014005, 2012.
- G. T. A. Huysmans, S. Pamela, E. v. d. Plas, and P. Ramet. Non-linear MHD simulations of edge localized modes (ELMs). *Plasma Physics and Controlled Fusion*, 51(12):124012, 2009.
- S. C. Jardin, N. Ferraro, X. Luo, J. Chen, J. Breslau, K. E. Jansen, and M. S. Shephard. The M3D-C1 approach to simulating 3D 2-fluid magnetohydrodynamics in magnetic fusion experiments. *Journal of Physics: Conference Series*, 125(1):012044, 2008.
- M. Jucker, J. P. Graves, W. A. Cooper, and T. Johnson. Ion cyclotron resonance heating with consistent finite orbit widths and anisotropic equilibria. *Plasma Physics and Controlled Fusion*, 53(5):054010, 2011.

- M. Jucker, W. Cooper, and J. Graves. Integrated modelling of ICRH in a quasi-axisymmetric stellarator. *Nuclear Fusion*, 52(1):013015, 2012.
- K. Kim, J.-K. Park, G. J. Kramer, and A. H. Boozer. δf Monte Carlo calculation of neoclassical transport in perturbed tokamaks. *Physics of Plasmas*, 19(8):082503, 2012.
- A. Kirk, E. Nardon, R. Akers, M. Bécoulet, G. D. Temmerman, B. Dudson, B. Hnat, Y. Liu, R. Martin, P. Tamain, D. Taylor, and the MAST team. Resonant magnetic perturbation experiments on MAST using external and internal coils for ELM control. *Nuclear Fusion*, 50(3):034008, 2010.
- M. A. Kovanen and W. G. F. Core. HECTOR: A code for the study of charged particles in axisymmetric tokamak plasmas. *Journal of Computational Physics*, 105(1):14 – 23, 1993.
- G. J. Kramer, R. V. Budny, A. Bortolon, E. D. Fredrickson, G. Y. Fu, W. W. Heidbrink, R. Nazikian, E. Valeo, and M. A. V. Zeeland. A description of the full-particle-orbit-following SPIRAL code for simulating fast-ion experiments in tokamaks. *Plasma Physics and Controlled Fusion*, 55(2):025013, 2013.
- J. A. Krommes. Nonlinear gyrokinetics: a powerful tool for the description of microturbulence in magnetized plasmas. *Physica Scripta*, 2010(T142):014035, 2010.
- J. A. Krommes and A. H. Reiman. Plasma equilibrium in a magnetic field with stochastic regions. *Physics of Plasmas (1994-present)*, 16(7):072308, 2009.
- M. D. Kruskal and R. M. Kulsrud. Equilibrium of a magnetically confined plasma in a toroid. *Physics of Fluids (1958-1988)*, 1(4):265–274, 1958.
- T. Kurki-Suonio, O. Asunta, T. Hellsten, V. Hynönen, T. Johnson, T. Koskela, J. Lönnroth, V. Parail, M. Roccella, G. Saibene, A. Salmi, and S. Sipilä. ASCOT simulations of fast ion power loads to the plasma-facing components in ITER. *Nuclear Fusion*, 49(9):095001, 2009.
- L. Lao, H. S. John, R. Stambaugh, A. Kellman, and W. Pfeiffer. Reconstruction of current profile parameters and plasma shapes in tokamaks. *Nuclear Fusion*, 25(11):1611, 1985.
- F. Lekien and J. Marsden. Tricubic interpolation in three dimensions. *International Journal for Numerical Methods in Engineering*, 63(3):455–471, 2005.
- Y. Liang, H. R. Koslowski, P. R. Thomas, E. Nardon, B. Alper, P. Andrew, Y. Andrew, G. Arnoux, Y. Baranov, M. Bécoulet, M. Beurskens, T. Biewer, M. Bigi, K. Crombe, E. De La Luna, P. de Vries, W. Fundamenski, S. Gerasimov, C. Giroud, M. P. Gryaznevich, N. Hawkes, S. Hotchin, D. Howell, S. Jachmich, V. Kiptily, L. Moreira, V. Parail, S. D. Pinches, E. Rachlew, and O. Zimmermann. Active control of type-I edge-localized modes with $n = 1$ perturbation fields in the JET tokamak. *Phys. Rev. Lett.*, 98:265004, 2007.
- Y. Liang, P. Lomas, I. Nunes, M. Gryaznevich, M. N. A. Beurskens, S. Brezinsek, J. W. Coenen, P. Denner, T. Eich, L. Frassinetti, S. Gerasimov, D. Harting, S. Jachmich, A. Meigs, J. Pearson, M. Rack, S. Saarelma, B. Sieglin, Y. Yang, L. Zeng, and J.-E. Contributors. Mitigation of type-I ELMs with $n = 2$ fields on JET with ITER-like wall. *Nuclear Fusion*, 53(7):073036, 2013.

Bibliography

- A. Lichtenberg and M. Lieberman. *Regular and Chaotic Dynamics*. Applied Mathematical Sciences. Springer New York, 2010. ISBN 9781441931009.
- R. G. Littlejohn. A guiding center hamiltonian: A new approach. *Journal of Mathematical Physics*, 20(12):2445–2458, 1979.
- R. G. Littlejohn. Hamiltonian formulation of guiding center motion. *Physics of Fluids*, 24(9): 1730–1749, 1981.
- R. G. Littlejohn. Hamiltonian perturbation theory in noncanonical coordinates. *Journal of Mathematical Physics*, 23(5):742–747, 1982.
- R. G. Littlejohn. Variational principles of guiding centre motion. *Journal of Plasma Physics*, 29: 111–125, 1 1983.
- R. G. Littlejohn. Phase anholonomy in the classical adiabatic motion of charged particles. *Phys. Rev. A*, 38:6034–6045, Dec 1988.
- Y. Liu, A. Kirk, Y. Gribov, M. Gryaznevich, T. Hender, and E. Nardon. Modelling of plasma response to resonant magnetic perturbation fields in MAST and ITER. *Nuclear Fusion*, 51 (8):083002, 2011.
- Y. Q. Liu, A. Kirk, Y. Sun, P. Cahyna, I. T. Chapman, P. Denner, G. Fishpool, A. M. Garofalo, J. R. Harrison, E. Nardon, and the MAST team. Toroidal modeling of plasma response and resonant magnetic perturbation field penetration. *Plasma Physics and Controlled Fusion*, 54(12):124013, 2012.
- H. Lütjens, J.-F. Luciani, D. Leblond, F. Halpern, and P. Maget. Non-linear modeling of core MHD in tokamaks. *Plasma Physics and Controlled Fusion*, 51(12):124038, 2009.
- R. J. McKay, K. G. McClements, A. Thyagaraja, and L. Fletcher. Test-particle simulations of collisional impurity transport in rotating spherical tokamak plasmas. *Plasma Physics and Controlled Fusion*, 50(6):065017, 2008.
- J. D. Meiss and R. D. Hazeltine. Canonical coordinates for guiding center particles. *Physics of Fluids B: Plasma Physics (1989-1993)*, 2(11):2563–2567, 1990.
- J. Menard, R. Bell, E. Fredrickson, D. Gates, S. Kaye, B. LeBlanc, R. Maingi, S. Medley, W. Park, S. Sabbagh, A. Sontag, D. Stutman, K. Tritz, W. Zhu, and the NSTX Research Team. Internal kink mode dynamics in high-beta NSTX plasmas. *Nuclear Fusion*, 45(7):539, 2005.
- J. E. Menard, R. E. Bell, D. A. Gates, S. M. Kaye, B. P. LeBlanc, F. M. Levinton, S. S. Medley, S. A. Sabbagh, D. Stutman, K. Tritz, and H. Yuh. Observation of instability-induced current redistribution in a spherical-torus plasma. *Phys. Rev. Lett.*, 97:095002, Aug 2006.
- D. Mikkelsen. Approximation for non-resonant beam target fusion reactivities. *Nuclear Fusion*, 29(7):1113, 1989.
- G. H. Miley and H. H. Towner, editors. *Reactivities for two-component fusion calculations*, 1975.

- K. Miyamoto. *Plasma Physics for Nuclear Fusion*. The MIT Press, 1989.
- A. I. Morozov and L. S. Solov'ev. Motion of Charged Particles in Electromagnetic Fields. *Reviews of Plasma Physics*, 2:201, 1966.
- P. J. Morrison. Magnetic field lines, hamiltonian dynamics, and nontwist systems. *Physics of Plasmas (1994-present)*, 7(6):2279–2289, 2000.
- R. A. Moyer, M. A. V. Zeeland, D. M. Orlov, A. Wingen, T. E. Evans, N. M. Ferraro, J. M. Hanson, R. Nazikian, M. R. Wade, and L. Zeng. Measurement of plasma boundary displacement by $n = 2$ magnetic perturbations using imaging beam emission spectroscopy. *Nuclear Fusion*, 52(12):123019, 2012.
- T. Muir. *A treatise on the theory of determinants*. Macmillan, 1882.
- E. Nardon, A. Kirk, R. Akers, M. Bécoulet, P. Cahyna, G. D. Temmerman, B. Dudson, B. Hnat, Y. Q. Liu, R. Martin, H. Meyer, P. Tamain, D. Taylor, D. Temple, and the MAST Team. Edge localized mode control experiments on MAST using resonant magnetic perturbations from in-vessel coils. *Plasma Physics and Controlled Fusion*, 51(12):124010, 2009.
- T. G. Northrop and J. A. Rome. Extensions of guiding center motion to higher order. *Physics of Fluids (1958-1988)*, 21(3):384–389, 1978.
- NRL Plasma Formulary. Plasma physics division. *Naval Research Laboratory*, 2009.
- N. Oyama, H. Urano, K. Shinohara, M. Honda, T. Takizuka, N. Hayashi, Y. Kamada, and the JT-60 Team. Effects of local toroidal field ripples due to test blanket modules for ITER on radial transport of thermal ions. *Nuclear Fusion*, 52(11):114013, 2012.
- A. Pankin, D. McCune, R. Andre, G. Bateman, and A. Kritz. The tokamak monte carlo fast ion module NUBEAM in the national transport code collaboration library. *Computer Physics Communications*, 159(3):157 – 184, 2004.
- A. Pataki, A. J. Cerfon, J. P. Freidberg, L. Greengard, and M. O'Neil. A fast, high-order solver for the Grad–Shafranov equation. *Journal of Computational Physics*, 243(0):28 – 45, 2013.
- D. Pfefferlé and M. Albergante. VENUS-LEVIS documentation. *CRPP software*, 2015.
- D. Pfefferlé, J. Graves, W. Cooper, C. Misev, I. Chapman, M. Turnyanskiy, and S. Sangaroon. NBI fast ion confinement in the helical core of MAST hybrid-like plasmas. *Nuclear Fusion*, 54(6):064020, 2014.
- D. Pfefferlé, J. Graves, and W. Cooper. Hybrid guiding-centre/full-orbit simulations in non-axisymmetric magnetic geometry exploiting general criterion for guiding-centre accuracy. *Plasma Physics and Controlled Fusion*, accepted, 2015a.
- D. Pfefferlé, C. Misev, W. A. Cooper, and J. P. Graves. Impact of RMP magnetic field simulation models on fast ion losses. *Nuclear Fusion*, 55(1):012001, 2015b.

Bibliography

- S. D. Pinches, L. C. Appel, J. Candy, S. E. Sharapov, H. L. Berk, D. Borba, B. N. Breizman, T. C. Hender, K. I. Hopcraft, G. T. A. Huysmans, and W. Kerner. The HAGIS self-consistent nonlinear wave-particle interaction model. *Computer Physics Communications*, 111(1-3): 133 – 149, 1998.
- F. Porcelli, R. Stankiewicz, W. Kerner, and H. L. Berk. Solution of the drift-kinetic equation for global plasma modes and finite particle orbit widths. *Physics of Plasmas (1994-present)*, 1 (3):470–480, 1994.
- H. Reimerdes, I. Furno, F. Hofmann, A. Martynov, A. Pochelon, and O. Sauter. Sawtooth behaviour in highly elongated TCV plasmas. *Plasma Physics and Controlled Fusion*, 48(11): 1621, 2006.
- J. Rome. Orbit topology in conventional stellarators in the presence of electric fields. *Nuclear Fusion*, 35(2):195, 1995.
- R. Saucier. *Computer Generation of Statistical Distributions*. Storming Media, 2000. ISBN 9781423540281.
- O. Schmitz, T. E. Evans, M. E. Fenstermacher, H. Frerichs, M. W. Jakubowski, M. J. Schaffer, A. Wingen, W. P. West, N. H. Brooks, K. H. Burrell, J. S. deGrassie, Y. Feng, K. H. Finken, P. Gohil, M. Groth, I. Joseph, C. J. Lasnier, M. Lehnen, A. W. Leonard, S. Mordijck, R. A. Moyer, A. Nicolai, T. H. Osborne, D. Reiter, U. Samm, K. H. Spatschek, H. Stoschus, B. Unterberg, E. A. Unterberg, J. G. Watkins, R. Wolf, t. D. Teams, and TEXTOR. Aspects of three dimensional transport for ELM control experiments in ITER-similar shape plasmas at low collisionality in DIII-D. *Plasma Physics and Controlled Fusion*, 50(12):124029, 2008.
- S. Shafiee and E. Topal. When will fossil fuel reserves be diminished? *Energy Policy*, 37(1):181 – 189, 2009.
- K. Shinohara, K. Tani, T. Oikawa, S. Putvinski, M. Schaffer, and A. Loarte. Effects of rippled fields due to ferritic inserts and ELM mitigation coils on energetic ion losses in a 15MA inductive scenario in ITER. *Nuclear Fusion*, 52(9):094008, 2012.
- D. Slaughter. Fusion reactivities for several beam and target ion distributions. *Journal of Applied Physics*, 54(3), 1983.
- L. S. Solov'ev. The Theory of Hydromagnetic Stability of Toroidal Plasma Configurations. *Soviet Journal of Experimental and Theoretical Physics*, 26:400, Feb. 1968.
- D. Spong. Energetic particle transport and alfvén instabilities in compact stellarators. *Plasma Physics and Fusion Technology*, 2006.
- D. A. Spong. Three-dimensional effects on energetic particle confinement and stability. *Physics of Plasmas (1994-present)*, 18(5):056109, 2011.
- D. F. H. Start, J. G. Cordey, and E. M. Jones. The effect of trapped electrons on beam driven currents in toroidal plasmas. *Plasma Physics*, 22(4):303, 1980.

- W. Suttrop, L. Barrera, A. Herrmann, R. M. McDermott, T. Eich, R. Fischer, B. Kurzan, P. T. Lang, A. Mlynek, T. Pütterich, S. K. Rathgeber, M. Rott, T. Vierle, E. Viezzer, M. Willensdorfer, E. Wolfrum, I. Zammuto, and t. A. U. Team. Studies of edge localized mode mitigation with new active in-vessel saddle coils in ASDEX upgrade. *Plasma Physics and Controlled Fusion*, 53(12):124014, 2011a.
- W. Suttrop, T. Eich, J. C. Fuchs, S. Günter, A. Janzer, A. Herrmann, A. Kallenbach, P. T. Lang, T. Lunt, M. Maraschek, R. M. McDermott, A. Mlynek, T. Pütterich, M. Rott, T. Vierle, E. Wolfrum, Q. Yu, I. Zammuto, H. Zohm, and undefined. First observation of edge localized modes mitigation with resonant and nonresonant magnetic perturbations in ASDEX upgrade. *Physical Review Letters*, 106(22):225004, 2011b.
- Y. Suzuki, N. Nakajima, K. Watanabe, Y. Nakamura, and T. Hayashi. Development and application of HINT2 to helical system plasmas. *Nuclear Fusion*, 46(11):L19, 2006.
- K. Tani, M. Azumi, H. Kishimoto, and S. Tamura. Effect of toroidal field ripple on fast ion behavior in a tokamak. *Journal of the Physical Society of Japan*, 50(5):1726–1737, 1981.
- K. Tani, K. Shinohara, T. Oikawa, H. Tsutsui, S. Miyamoto, Y. Kusama, and T. Sugie. Effects of ELM mitigation coils on energetic particle confinement in ITER steady-state operation. *Nuclear Fusion*, 52(1):013012, 2012.
- J. B. Taylor. Relaxation of toroidal plasma and generation of reverse magnetic fields. *Phys. Rev. Lett.*, 33:1139–1141, Nov 1974.
- L. H. Thomas. Elliptic problem in linear difference equations over a network. *Watson Sci. Comp. Lab. Rep.*, 1949.
- A. D. Turnbull. Plasma response models for non-axisymmetric perturbations. *Nuclear Fusion*, 52(5):054016, 2012.
- A. D. Turnbull, N. M. Ferraro, V. A. Izzo, E. A. Lazarus, J.-K. Park, W. A. Cooper, S. P. Hirshman, L. L. Lao, M. J. Lanctot, S. Lazerson, Y. Q. Liu, A. Reiman, and F. Turco. Comparisons of linear and nonlinear plasma response models for non-axisymmetric perturbations. *Physics of Plasmas (1994-present)*, 20(5):056114, 2013.
- S. Wang. Canonical hamiltonian theory of the guiding-center motion in an axisymmetric torus, with the different time scales well separated. *Physics of Plasmas (1994-present)*, 13(5):052506, 2006.
- R. White and L. E. Zakharov. Hamiltonian guiding center equations in toroidal magnetic configurations. *Physics of Plasmas (1994-present)*, 10(3):573–576, 2003.
- R. B. White and M. S. Chance. Hamiltonian guiding center drift orbit calculation for plasmas of arbitrary cross section. *Physics of Fluids*, 27(10):2455–2467, 1984.
- R. B. White, A. H. Boozer, and R. Hay. Drift hamiltonian in magnetic coordinates. *Physics of Fluids*, 25(3):575–576, 1982.

Bibliography

- R. B. White, G. Spizzo, and M. Gobbin. Guiding center equations of high accuracy. *Plasma Physics and Controlled Fusion*, 55(11):115002, 2013.
- A. Wingen, S. Abdullaev, K. Finken, M. Jakubowski, and K. Spatschek. Influence of stochastic magnetic fields on relativistic electrons. *Nuclear Fusion*, 46(11):941, 2006.
- M. A. V. Zeeland, N. M. Ferraro, W. W. Heidbrink, G. J. Kramer, D. C. Pace, X. Chen, T. E. Evans, R. K. Fisher, M. Garcia-Munoz, J. M. Hanson, M. J. Lanctot, L. L. Lao, R. A. Moyer, R. Nazikian, and D. M. Orlov. Modulation of prompt fast-ion loss by applied $n=2$ fields in the DIII-D tokamak. *Plasma Physics and Controlled Fusion*, 56(1):015009, 2014.

Acronyms

ASDEX Axially Symmetric Divertor Experiment.

AUG Axially Symmetric Divertor Experiment (ASDEX) Upgrade.

CCFE Culham Centre for Fusion Energy.

CPU Computer Processing Unit.

DND Double Null Diverted.

ELM Edge Localised Mode.

GCDE Guiding-centre Drift Equations.

GPU Graphics Processing Unit.

ICRH Ion Cyclotron Resonance Heating.

ITER International Thermonuclear Experimental Reactor.

JET Joint European Torus.

LLM Long-Lived Mode.

MAST Mega-Ampère Spherical Tokamak.

MHD MagnetoHydroDynamics.

NBI Neutral Beam Injection.

NSTX National Spherical Tokamak eXperiment.

PIC Particle-In-Cell.

PINI Positive Ion Neutral Injector.

RMP Resonant Magnetic Perturbation.

RWM Resistive Wall Mode.

SND Single Null Diverted.

TAE Toroidal Alfvén Eigenmode.

TBM Test Blanket Module.

TCV Tokamak à Configuration Variable.

W7X Wendelstein-7X.

Acknowledgements

The last four years have been so much more than an intellectually exhilarating and fulfilling period; the thesis was an unforgettably enriching human experience which has profoundly influenced the person I have become. The following acknowledgements are a humble attempt to convey my gratitude to the people who accompanied me on this journey and contributed to its successful outcome.

First, I would like to thank my supervisors Tony and Jon for their great support and guidance. I feel particularly honoured by their availability for discussion and their encouragement for exploration and self-expression. I would also like to thank them for valuable help and advice in writing the present manuscript as well as the related publications.

I would like to thank the members of the thesis jury Per, Yueqiang and Stefano for reading the manuscript with such attention and consideration. Their suggestions and comments have considerably improved this document.

I would like to thank the managers of CRPP, namely Ambrogio, Quang, Paolo and Yves for providing such a privileged working environment. The opportunities for mobility to CCFE (UK) and JAEA (Japan) as well as participation to several conferences have undeniably boosted my motivation and inspired me to make every effort to contribute. I am also grateful to CRPP seniors Stefan, Laurent, Olivier, Minh, Ivo, Jo, Laurie, Basil for insightful discussions and coaching. The assistance of Edith, Roxane, Heidi, Christian, Pierre with administrative tasks and hardware concerns was appreciated.

I would like to thank my Japanese colleague Nobuyuki-san for such a scientifically fruitful and culturally enriching collaboration. It was an honour to learn, discuss ideas and share thoughts with him and his colleague Matsuyama-san. I was deeply touched by the hospitality of Nobuyuki-san and of his wife during my stay in Rokkasho. ありがとうございます。

I am indebted to Ian for bringing many ideas and open questions to my attention as well as for providing valuable data from the MAST and JET experiments. His trust and support were greatly appreciated. I am also grateful to colleagues around the world, namely Mikhail, Maxim, Siri, Gerrit, Luca, Lee, Benedikt, Thimothée, Josephine for suggestions, discussions and exchange of thoughts.

It was a pleasure to work with competent as well as genuinely fun colleagues within the MHD group. Special thanks to Mattia for his mentorship, Daniele for his improvised MHD lectures, Cyril for his significant contribution to the code, Jonathan for his help on some tricky details (as well as the occasional place to stay). I wish the newcomers Madhu, Hamish and Samuel the best of luck. I also thank colleagues and now good friends Julien and Alexandre, who were always available for discussion and/or humorous interruptions.

Acknowledgements

I would like to thank all fellow PhD students and postdocs for the collaborative and joyful atmosphere that is perpetuated at CRPP. I will always remember the enthusiasm of our discussions at coffee break, the fervour at our soccer games, the smiles and laughs at our aperos, etc... Special thanks to Karim, Joaquim, Federicos, Thibaut, Sébastien, Vincent, Fabios, Falk, Loïc, Kyle, Kees, David, Annamaria, Bogdan, Lucia, Josef, Claudio, Andreas, Antoine, Gabriele, Christian, Wouter, Christoph, Himank, Joan, Paola, Umar, Emmanuel, Jérémy and whoever I am forgetting.

J'aimerais adresser mes sincères remerciements à mes amis (du Valais ou d'ailleurs), qui me soutiennent avec le coeur depuis bien des années. Je pense notamment à Nicolas et Valentine, Alex, Matthieu, Patrick, Émilies, Gâelle et Alex, Philippe et Isa, Célien et Yannick, Mexico et Anni, Jonathan, Thierry, Benoît, Fred, Yves et Julie, Gilles, et à d'autres encore...

I will never be able to thank my parents enough for their unconditional support, encouragement, love and affection. I am grateful to my (extended) family for feeding my mind with positive thoughts and my stomach with amazing food. Tante grazie alla famiglia italiana per avermi sostenuto, non solo con le parole incoraggianti ma anche con dei piatti irresistibili.

Finally, I would like to express my deepest gratitude to my wife who has not only critically read the manuscript and provided extremely useful feedback, but has been a firm foothold in reality as well as an infinite source of courage and energy. This thesis would certainly not have been possible without her loving support.

Lausanne, April 9, 2015

D. P.



David Pfefferlé

Av. Tourbillon 76B
1950 Sion (VS)
Switzerland

+41 79 503 35 88

david.pfefferle@epfl.ch

Citizenship Swiss/Australian
DOB November 18, 1985 (29 years old)
Married

MSc in Physics EPFL

PROFILE

Having studied a wide range of fields in physics out of sheer curiosity, I am passionately applying my solid problem solving skills in scientific research for fusion, while deepening my understanding of plasma physics.

EDUCATION

PH.D CANDIDATE in plasma physics

2011 - present

Centre de Recherches en Physique des Plasmas (CRPP-EPFL), Lausanne, Switzerland

- Provisional thesis title: "*Energetic ion dynamics and confinement in 3D saturated MHD configurations*", development of orbit following code VENUS-LEVIS using coordinate independent equations of motion and field representation. Under the direction of Dr. Wilfred A. Cooper and Jonathan P. Graves

MASTER of Science in theoretical particle physics

2008 - 2010

Swiss Institute of Technology (EPFL), Lausanne, Switzerland

- Thesis title: "*EWSB from a discrete extra dimension*", composite Higgs model as a pseudo-Goldstone boson of a 5D gauge theory on a segment with symmetry breaking boundary conditions. Under the direction of Prof. Riccardo Rattazzi

BACHELOR of Science in physics

2005 - 2008

Swiss Institute of Technology (EPFL), Lausanne, Switzerland

SECONDARY EDUCATION majoring in physics/applied mathematics

2000 - 2005

Lycée-Collège de la Planta, Sion, Switzerland

- Final project for graduation : "*The missing mass of the universe or the obesity of darkness*"

HONORS AND AWARDS

531st WEH poster prize issued by Wilhelm und Else Hereaus Stiftung, Bad Honnef, Germany

2013

Excellency Scholarship issued by Swiss Institute of Technology (EPFL), Lausanne, Switzerland in recognition of outstanding academic performance during Bachelors Degree

2009

TP prize issued by Swiss Institute of Technology (EPFL), Lausanne, Switzerland for innovative practical work and high quality reports

2008

Valais physics prize issued by Lycée-Collège de la Planta and Raiffeisen Bank, Sion, Switzerland for highest grades in physics at secondary school

2005

EXTRA-CURRICULA EXPERIENCE

MOBILITY TRIP to Japan Atomic Energy Agency, Rokkasho, Japan

2014

- Interface between stability code MINERVA and orbit solver VENUS-LEVIS for hybrid kinetic-MHD simulations in the presence of plasma rotation

TEACHING ASSISTANT at Swiss Institute of Technology (EPFL), Lausanne, Switzerland

- Principal assistant for General Physics class by Prof. Paolo Ricci: conception of undergraduate exercises and exam material

2013 - present

- Co-supervision and co-direction of masters student

2012 - 2013

- Tutoring and front-lessons in general physics, thermodynamics, fluid dynamics, electromagnetism and numerical physics for undergraduate students

2008 - 2012

MOBILITY TRIP to Culham Centre for Fusion Energy, Culham, UK

2012

- Modelling and simulations of the MAST neutral beam injection system, implementation of a virtual diagnostic for neutron emission in VENUS-LEVIS and comparison with experimental data

IT MANAGER at Pfefferlé & Cie SA, Sion, Switzerland

2010 – 2011

- Resource allocation and maintenance, online strategy and marketing, IT consultant, e-shop deployment, design and development of multilingual website www.pfefferle.ch

WORKSHOP at CERN, Meyrin, Switzerland

2009

- Participation in seminar: “Standard Model & Beyond Standard Model physics at LHC”

LANGUAGES

English / French

Mother tongue

German

Advanced certificate (C1)

Italian

Spoken (B1)

COMPUTER SKILLS

Scientific software

Matlab, Mathematica, MPICH2, HDF5, LaTeX

Programming languages

FORTRAN, C++, HTML, PHP, CSS, MySQL, Java, Bash

INTERESTS

Active sport

Tennis, cycling, golf, rock-climbing, ski-touring

Hobbies

Classical/jazz music, digital photography, Afro-Cuban dances

LIST OF PUBLICATONS

FIRST AUTHOR

- D. Pfefferlé et al., “Hybrid guiding-centre/full-orbit simulations in non-axisymmetric magnetic geometry exploiting general criterion for guiding-centre accuracy”, Plasma Physics and Controlled Fusion (submitted, 2014)
- D. Pfefferlé et al., “Impact of RMP magnetic field simulation models on fast ion losses”, Nuclear Fusion 55 (1) p.012001 (2014)
- D. Pfefferlé et al., “VENUS-LEVIS and its spline-Fourier interpolation of 3D toroidal magnetic field representation for guiding-centre and full-orbit simulations of charged energetic particles”, Computer Physics Communications 185 (12) p.3127-3140 (2014)
- D. Pfefferlé et al., “NBI fast ion confinement in the helical core of MAST hybrid-like plasmas”, Nuclear Fusion 54 (6) p.064020 (2014)

CO-AUTHOR

- W. A. Cooper et al., “An approximate single fluid 3-dimensional magnetohydrodynamic equilibrium model with toroidal flow”, Plasma Physics and Controlled Fusion 56 (9) p.094004 (2014)
- W. A. Cooper et al., “Bifurcated Helical Core Equilibrium States in Tokamaks”, Nuclear Fusion 53 (7) p.073021 (2013)

CONFERENCE PROCEEDINGS

- D. Pfefferlé et al., “Fast ion transport in 3D saturated MHD configurations”, contributed talk at MHD Workshop, Auburn (USA, 2014)
- D. Pfefferlé et al., “Linear hybrid kinetic-MHD model of rotating plasmas via the interface of MINERVA stability and VENUS-LEVIS delta-f PIC codes”, contributed poster at APS conference on Plasma Physics, New Orleans (USA, 2014)
- D. Pfefferlé et al., “Fast ion transport during large scale saturated MHD activity”, invited talk at Theory of Fusion Plasmas conference, Varenna (Italy, 2014)
- D. Pfefferlé et al., “Fast ion redistribution in helical tokamak equilibrium states and RMP from PIC full-f calculations”, contributed poster at 40th EPS on Plasma Physics, Espoo (Finland, 2013)
- D. Pfefferlé et al., “Full-f calculations of fast ion distributions in helical tokamak equilibrium states and numerical challenges”, contributed poster at 531st Wilhelm and Else Heraeus Seminar on 3D versus 2D in Hot Plasmas, Bad Honnef (Germany, 2013)
- D. Pfefferlé et al., “Exploitation of a general-coordinate guiding centre code for the redistribution of fast ions in deformed hybrid tokamak equilibria”, contributed poster at the Theory of Fusion Plasmas conference, Varenna (Italy) and Journal of Physics Conference Series (401) p. 012020 (2012)
- D. Pfefferlé et al., “Hamiltonian Phase-space Guiding-Centre Drift Equations”, contributed poster at the Swiss Physics Society conference on plasma physics, Lausanne (Switzerland, 2011)